



HAL
open science

Development of anticorrosive Zn-based alloy coatings for cold formed steel body parts

Florian Claudel

► **To cite this version:**

Florian Claudel. Development of anticorrosive Zn-based alloy coatings for cold formed steel body parts. Materials. Université de Lorraine, 2019. English. NNT : 2019LORR0264 . tel-02558306

HAL Id: tel-02558306

<https://hal.univ-lorraine.fr/tel-02558306>

Submitted on 14 Dec 2021

HAL is a multi-disciplinary open access archive for the deposit and dissemination of scientific research documents, whether they are published or not. The documents may come from teaching and research institutions in France or abroad, or from public or private research centers.

L'archive ouverte pluridisciplinaire **HAL**, est destinée au dépôt et à la diffusion de documents scientifiques de niveau recherche, publiés ou non, émanant des établissements d'enseignement et de recherche français ou étrangers, des laboratoires publics ou privés.



AVERTISSEMENT

Ce document est le fruit d'un long travail approuvé par le jury de soutenance et mis à disposition de l'ensemble de la communauté universitaire élargie.

Il est soumis à la propriété intellectuelle de l'auteur. Ceci implique une obligation de citation et de référencement lors de l'utilisation de ce document.

D'autre part, toute contrefaçon, plagiat, reproduction illicite encourt une poursuite pénale.

Contact : ddoc-theses-contact@univ-lorraine.fr

LIENS

Code de la Propriété Intellectuelle. articles L 122. 4

Code de la Propriété Intellectuelle. articles L 335.2- L 335.10

http://www.cfcopies.com/V2/leg/leg_droi.php

<http://www.culture.gouv.fr/culture/infos-pratiques/droits/protection.htm>

École Doctorale CM2P (Chimie – Mécanique – Matériaux – Physique)

THÈSE

Pour l'obtention du titre de:

DOCTEUR DE L'UNIVERSITÉ DE LORRAINE

Spécialité : Science des Matériaux

Présentée par :

FLORIAN CLAUDEL

Development of anticorrosive Zn-based alloy coatings for cold formed steel body parts

Soutenance publique prévue à Metz le 16 Octobre 2019 devant le jury composé de :

László PÉTER	Directeur de recherche Wigner Research Centre for Physics, Hungarian Academy of Sciences Budapest – Hongrie	Rapporteur
Catherine SAVALL	Maître de conférences HDR LASIE, Université de La Rochelle La Rochelle – France	Rapporteur
Angéline POULON- QUINTIN	Maître de conférences HDR ICMCB, Université de Bordeaux Bordeaux – France	Examinatrice
Juan CREUS	Professeur LASIE, Université de la Rochelle La Rochelle – France	Examineur
Albert TIDU	Professeur LEM3, Université de Lorraine Metz – France	Examineur
Nicolas STEIN	Maître de conférences HDR IJL, Université de Lorraine Metz – France	Directeur de thèse
Nathalie ALLAIN	Professeur LEM3, Université de Lorraine Metz – France	Co-directrice de thèse
Damien CLOSE	Dr.-Ing. Daimler AG Sindelfingen – Allemagne	Invité

According to the requirements of the doctorate school CM2P, the thesis being written in English, an extended summary was written in French. Furthermore, to offer a better understanding of this work, the general introduction, the aim of the study and experimental approach as well as the introduction and conclusion of the chapters 3, 4 and 5 were translated in French.

Conformément aux exigences de l'école doctorale CM2P, la thèse étant rédigée en anglais, un résumé étendu a été rédigé en français. De plus et afin d'offrir la meilleure compréhension possible de ce travail, l'introduction générale, le but de l'étude et approche expérimentale ainsi que l'introduction et la conclusion des chapitres 3, 4 et 5 ont également été rédigés en français.

This work was part of an industrial research project in cooperation with the Daimler AG (Sindelfingen, Germany) and was carried out between the Institut Jean Lamour (IJL) and the Laboratoire d'Études des Microstructures et de Mécanique des Matériaux (LEM3) both affiliated to the Université de Lorraine.

I would like to express my sincere gratitude to Prof. Nathalie Allain, Prof. Albert Tidu and especially to Dr. Nicolas Stein for their continuous support during this whole PhD thesis and their deep implication in this project, as well as their various inputs and feedbacks on the scientific and technical challenges I encountered during this work. I will long remember our endless meetings trying to understand our results. And of course, not to forget the time they involved during the final writings of the manuscript, with their extremely valuable comments and remarks, despite the call of the summer holidays.

My special thanks go to Nicolas for his unfailing supervision and support during this project, his incredible dedication and passion for his job as well as his immense knowledge.

I would also like to particularly thank Dr. Damien Close for his incredible support at Daimler during this PhD. From my early days at Daimler, up to the end you were always there with the most helpful tips and tricks on the academic and industrial environments where I was continuously involved. Also a car freak, you were also there to share my passion for cars. I will long remember our brainstorming meetings and our not always so crazy ideas and patents applications. I will also definitely miss our drives in the Black Forest!

Of course, all this would not have been possible without the efforts of Dr. Régis Lallement and Mr. Felix Raschke, as well as Mr. Roland Bachmann who put this project together and gave me the opportunity to work on this topic.

I would like also to thank Prof. László Péter, Dr. Catherine Savall, Dr. Angéline Poulon-Quintin and Prof. Juan Creus for being part of my thesis committee as well as for their helpful comments on the manuscript and on the presentation.

I am also extremely thankful to my colleagues from the IJL and LEM3 for their friendliness and their help during the various experiments I performed. Some special thanks go to Dr. Julien Guyon for his expertise on the FIB and EBSD experiments, Aurianne Mandrelli for optimizing the preparation of our samples before analysis, and Dr. Sébastien Diliberto for his input and tips on the XRD analyses. I also would like to thank my colleagues of the RD/KSO, TF/VBT and TF/VWT, Mrs. Carmen Schmidt, Mr. Thomas Richter and especially Dr. Michael Bayer for sharing his immense knowledge.

I would like to thank also Alexander Wolotschai, Sébastien Weibel, Hidajete Tidona, Nicolas Hajczak, Julien Mertz, Aurélien Henry, Johannes Rominger and Aurélie Valli for their support during the experiments.

Un très grand merci à ma famille, à mes parents ainsi qu'à mon frère Laurick pour leur soutien au cours de toute ses années d'études. Ils m'ont permis d'être là où je suis aujourd'hui.

Und meinen herzlichen Dank an Maria, für deine Liebe, deine Unterstützung und dein Verständnis während der Promotion. Ohne dich wäre es nicht möglich gewesen.

Wer rastet, der rostet

When I rest, I rust

LAY SUMMARY

Electrodeposition of alternative Zn-based coatings for the corrosion protection of cold formed automotive body parts

While numerous coatings are currently used for the corrosion protection of cold formed automotive body parts, steelmakers as well as automotive manufacturers conduct continuous research in order to improve the performance of the deposits. The literature research conducted in this study revealed a large amount of solutions investigated at the laboratory scale with on the other hand only a few coatings system going into mass-production.

The present work is therefore focused on the development and the characterization of alternative Zn-Mn alloy coatings. Various electrodeposition methods and process parameters were studied in order to determine the optimal conditions for the manufacturing of the deposits. In order to define the suitability of the deposits for an application in the automotive industry, various aspects of the coatings such as their corrosion resistance, cold formability, suitability for painting processes, etc. were also investigated in this work.

It appeared that Zn-Mn deposits obtained via pulse electrodeposition presented better anticorrosive behaviour than traditional deposits as well as interesting cold forming properties.

KEYWORDS

Coatings – Electrodeposition – Zinc alloys – Corrosion – Materials characterization

RÉSUMÉ VULGARISÉ

Électrodéposition de nouveaux revêtements à base de Zn pour la protection contre la corrosion de pièces de carrosserie embouties à froid

Alors que de nombreux revêtements sont actuellement utilisés pour la protection contre la corrosion de pièces de carrosserie embouties à froid, les aciéristes ainsi que les constructeurs automobiles mènent une recherche permanente afin d'améliorer la performance des revêtements. La littérature conduite dans cette étude a révélé une importante quantité de solutions étudiées à l'échelle laboratoire avec seulement quelques systèmes de revêtements aboutissant à l'échelle industrielle.

Le travail actuel vise le développement et la caractérisation de nouveaux alliages de Zn-Mn. Divers paramètres d'électrolyse ont été étudié afin de déterminer les conditions optimales de déposition. Afin de définir l'aptitude des films à une utilisation dans l'industrie automobile, divers aspects tels que la résistance à la corrosion, le comportement lors de la mise en forme et l'aptitude aux opérations de peinture ont été déterminées.

Il est apparu que les revêtements de Zn-Mn obtenus par électrodéposition impulsionnelle présentaient un meilleur comportement anticorrosif que les produits traditionnels ainsi que des propriétés de mise en forme intéressantes.

MOTS-CLES

Revêtements – Électrodéposition – Alliages de Zinc – Corrosion – Caractérisation des matériaux

FULL SUMMARY

Electrodeposition of alternative Zn-based coatings for the corrosion protection of cold formed automotive body parts

Numerous coating systems are traditionally used by the automotive manufacturers for the corrosion protection of cold formed steel body parts. Steelmakers as well as automotive manufacturers conducted numerous research studies in order to enhance the properties of anticorrosive coatings. According to the reference literature, various approaches and possible solutions were suggested over the past decades. However, only a few systems were able to go into serial production.

The objective of the present doctorate thesis is to develop and characterize alternative anticorrosive coatings based on Zn-alloys for the corrosion protection of cold formed steel components used for automotive body parts. On the basis of a thorough literature review, two interesting approaches were considered and consisting in the pulse electrodeposition of Zn-Mn and ZnMn-Al₂O₃ coatings. The deposits were comprehensively characterized in order to determine their chemical composition, morphology, microstructure as well as their crystallographic properties. The suitability of these new deposits was then assessed based on their anticorrosive behaviour, cold formability and paintability in comparison to commercialized products.

Using pulse electrodeposition permitted to deposit monophasic, pore-free and compact Zn-Mn alloys containing about 15 wt.% Mn at high current efficiencies. Electrodeposition on various substrates up to sizes of 100 x 200 mm² exposed a stable and reproducible deposition process.

Electrochemical experiments as well as accelerated corrosion tests revealed a particularly promising anticorrosive performance of the Zn-Mn alloys. A substantial improvement in the time before red rust appearance as well as a significant decrease of the corrosion rate were observed in comparison to the traditional Zn deposits. Analyses of the cold formability also exposed a promising behaviour of the Zn-Mn deposits. While a slight increase of the hardness was observed in comparison to the Zn coatings, a lower crack density was observed on the Zn-Mn deposits after tensile experiments. Preliminary phosphating and painting tests revealed the good suitability of the Zn-Mn alloys for phosphating and painting processes with the formation of a dense and homogeneous phosphate crystals network and the successful deposition of a homogeneous and pore-free electrophoretic paint layer, respectively. However, some challenges were identified with Zn-Mn deposits presenting some unsatisfactory properties when immersed in chloride-containing environments. Furthermore, pores were detected close to the deposit – substrate interface.

With the aim to solve these issues, the deposition of ZnMn-Al₂O₃ composite coatings was considered. The impact of the particles, stirring and electric parameters were investigated with a particular attention given to the homogeneous distribution of the particles in the metallic matrix. Using optimized deposition parameters, homogeneous, compact and monophasic composite coatings containing about 15 wt.% Mn were obtained at high faradaic efficiencies. Further analyses revealed the presence of particles on the surface as well as at the substrate – deposit interface. First mechanical tests revealed some interesting properties of the composite coatings with a substantial increase of the coating hardness. Electrochemical experiments also revealed some promising insights on the corrosion behaviour of the ZnMn-Al₂O₃ deposits.

RÉSUMÉ

Électrodéposition de nouveaux revêtements à base de Zn pour la protection contre la corrosion de pièces de carrosserie embouties à froid

De nombreux revêtements sont traditionnellement utilisés par les constructeurs automobiles pour la protection contre la corrosion de pièces de carrosserie embouties à froid. Les aciéristes ainsi que les constructeurs ont effectué de nombreuses études afin d'améliorer les propriétés des revêtements anticorrosifs. D'après la littérature, diverses solutions et approches ont été suggérées au cours des dernières décennies. Cependant, seulement quelques systèmes ont pu aboutir à une production en série.

L'objectif de la thèse de doctorat présentée ici est de développer et caractériser de nouveaux revêtements anticorrosifs à base d'alliages de zinc pour la protection contre la corrosion de composants en acier mis en forme à froid. Sur la base d'une revue de la littérature détaillée, deux approches d'intérêt ont été considérées, consistant en l'électrodéposition impulsionsnelle de dépôts de Zn-Mn et de ZnMn-Al₂O₃. Les revêtements ont été caractérisés en termes de composition chimique, morphologie, microstructure ainsi que leurs caractéristiques cristallographiques. L'aptitude des revêtements à une application dans l'industrie a ensuite été évaluée sur la base du comportement en corrosion, de la formabilité à froid et l'aptitude aux opérations de peintures en comparaison à des produits commerciaux.

L'utilisation de l'électrodéposition impulsionsnelle a permis d'obtenir des revêtements de Zn-Mn monophasés, absent de porosités et compacts, présentant une teneur en Mn avoisinant les 15 m.% avec un fort rendement. L'électrodéposition sur des substrats allant jusqu'à des surfaces de 100 x 200 mm² a révélé un procédé de déposition stable et reproductible.

Des mesures électrochimiques ainsi des tests de corrosion accélérés ont révélé une performance anticorrosive des alliages de Zn-Mn particulièrement intéressante. Une amélioration substantielle du temps d'apparition de la rouille rouge ainsi qu'une diminution significative de la vitesse de corrosion ont pu être observées en comparaison avec les revêtements traditionnels. Des analyses de la mise en forme à froid ont également montré un comportement prometteur des dépôts de Zn-Mn. Alors qu'une légère augmentation de la dureté est apparue par rapport aux dépôts de Zn, une plus faible densité de fissures a été observée sur les revêtements de Zn-Mn après des essais de traction. Des premiers tests de phosphatation et peinture ont démontré la bonne aptitude des revêtements pour ces procédés avec la formation d'un dense et homogène réseau de cristaux de phosphate ainsi que la déposition d'une couche de peinture électrophorèse homogène et absente de porosités. Cependant, certaines limitations ont été identifiées avec notamment des propriétés insatisfaisantes des revêtements lors d'une immersion en milieu chloré. De plus, des porosités ont pu être observées à proximité de l'interface entre le dépôt et le substrat.

Dans le but de résoudre ces problèmes, l'électrodéposition de revêtements composites ZnMn-Al₂O₃ a été considérée. L'impact des particules, de l'agitation et des paramètres électriques ont été étudiés avec une attention particulière portée sur la distribution homogène des particules dans la matrice métallique. Avec des paramètres de déposition optimisés, des dépôts composites homogènes, compacts et monophasiques contenant jusqu'à 15 m.% de Mn ont pu être obtenus avec de forts rendements. Des analyses poussées ont aussi révélé la présence de particules sur la surface ainsi qu'à l'interface substrat - film. Des premiers essais mécaniques ont montré une augmentation non négligeable de la dureté des dépôts composites. Des mesures électrochimiques ont également donné un aperçu très prometteur sur le comportement anticorrosif des revêtements ZnMn-Al₂O₃.

Table of content

Table of content.....	13
Abbreviations	18
Introduction (EN)	21
Introduction (FR).....	23
1. State of the art: current and alternative coatings for corrosion protection of automotive steel parts and definition of alternative coating systems	25
1.1. Corrosion and corrosion protection of car bodies: a general introduction	25
1.1.1. Corrosion of car bodies	26
1.1.2. Corrosion protection of car bodies	29
1.1.3. Assessment of the corrosion performance in the industry.....	31
1.2. Properties of the current Zn-based coatings	34
1.2.1. Anticorrosive properties of Zn-based coatings.....	36
1.2.2. Mechanical properties	42
1.3. Comparative review of commercial coatings for the automotive industry.....	44
1.4. Alternative coating systems and promising solutions	45
1.4.1. Identification of promising coating systems.....	46
1.4.2. Properties of Zn-Mn-based coatings	46
1.5. Deposition processes of Zn-Mn-based coatings.....	47
1.5.1. Hot-Dip Galvanizing – HDG.....	47
1.5.2. Physical Vapor Deposition – PVD.....	49
1.5.3. Electrodeposition.....	49
1.5.4. Conclusion.....	53
1.6. Particular case of Zn-based metal matrix coatings reinforced by particles	53
1.6.1. Interest of Zn-based metal matrix coatings	53
1.6.2. Mechanisms of particle codeposition	54
1.6.3. Effect of the zeta (ζ) – potential	57
1.6.4. Influence of electrolyte composition	58
1.6.5. Influence of particle size	58
1.6.6. Impact of the stirring conditions.....	58
1.6.7. Effect of the deposition mode and influence of the electrical parameters.....	59
1.6.8. Conclusion.....	59
1.7. Aim of the study and experimental approach (EN) – But de l'étude et approche expérimentale (FR).....	60
2. Materials and experimental methods.....	63
2.1. Procedure.....	63

Table of content

2.2.	Electrochemical setups	64
2.2.1.	Electrolytes	64
2.2.2.	Electrodeposition setups	64
2.2.3.	Characterization of the plating bath	67
2.3.	Preparation of the samples for metallographic analyses	68
2.3.1.	Mechanical polishing	68
2.3.2.	Ni-coating	68
2.3.3.	Focused Ion Beam – FIB	69
2.3.4.	Ion polishing	69
2.4.	Microstructural and chemical analyses of the coatings	69
2.4.1.	Optical microscopy	69
2.4.2.	Scanning Electron Microscopy – SEM	69
2.4.3.	Energy Dispersive Spectroscopy – EDS	70
2.4.4.	Electron BackScatter Diffraction – EBSD	70
2.4.5.	Transmission Electron Microscopy – TEM	71
2.4.6.	X-Ray Diffraction – XRD	72
2.4.7.	Confocal microscopy	72
2.5.	Electrochemical and accelerated corrosion tests	73
2.5.1.	Galvanostatic dissolution – GVA	73
2.5.2.	Linear Scan Voltammetry – LSV for corrosion experiments	74
2.5.3.	Continuous Salt Spray Test – SST	75
2.5.4.	Cyclic Corrosion Test – CCT	76
2.5.5.	Image analysis	76
2.5.6.	Removal of the corrosion products	77
2.6.	Post-processing: phosphating and electrocoating	77
2.6.1.	Phosphating process	77
2.6.2.	Electrophoretic coating process	78
2.6.3.	Corrosion tests with phosphate and electrocoating	78
2.7.	Mechanical tests	78
2.7.1.	Hardness test	78
2.7.2.	Tensile test	78
2.7.3.	Bending test	79
2.8.	Materials	80
2.8.1.	Steel substrate	80
2.8.2.	Commercial coatings	83
2.8.3.	Al ₂ O ₃ particles	86

2.9.	Experimental approach and deposition parameters	88
3.	Study, deposition and characterization of advanced Zn-Mn coatings	90
3.1.	Aim and procedure (EN) – But et procédure (FR)	90
3.2.	Preliminary study of the deposition under continuous currents	92
3.2.1.	Study of the electrodeposition system	92
3.2.2.	Transfer from potentiostatic to galvanostatic mode	93
3.2.3.	Crystallography and texture of the deposits	98
3.2.4.	Microstructure of the deposits	100
3.2.5.	Discussion and conclusion	105
3.3.	Towards new properties: study of the electrodeposition under pulse current	105
3.3.1.	Preliminary modelling of the pulse electrodeposition	106
3.3.2.	Influence on the composition	109
3.3.3.	Efficiency	111
3.3.4.	Influence on the morphology	112
3.3.5.	Influence on the microstructure	115
3.3.6.	Influence on the crystallography and texture	119
3.3.7.	Discussion and conclusion	127
3.4.	Definition of the optimal parameters	127
3.5.	Up-scaling and reproducibility	128
3.5.1.	Up-scaling	128
3.5.2.	Reproducibility	131
3.5.3.	Edge effect	132
3.5.4.	Conclusion	137
3.6.	Conclusion and outlook on the deposition of Zn-Mn (EN) – Conclusion et perspectives sur la déposition du Zn-Mn (FR)	137
4.	Suitability of the pulse Zn-Mn deposits for automotive application	141
4.1.	Aim and procedure (EN) – But et procédure (FR)	141
4.2.	Corrosion resistance	142
4.2.1.	Electrochemical properties	143
4.2.2.	Anticorrosive behaviour under accelerated corrosion tests	144
4.2.3.	Corrosion mechanisms and corrosion products analysis	148
4.2.4.	Comparison with commercial coatings	158
4.2.5.	Conclusion	163
4.3.	Forming behaviour	163
4.3.1.	Hardness	164
4.3.2.	Adhesion of the coatings with the steel substrate	165
4.3.3.	Comparison with commercial coatings	168

Table of content

4.3.4.	Conclusion.....	171
4.4.	Paintability	171
4.4.1.	Analysis of the phosphate conversion layer	171
4.4.2.	Corrosion resistance of the painted samples.....	172
4.4.3.	Comparison with commercial coatings	174
4.4.4.	Conclusion.....	176
4.5.	Overall performance (EN) – Performance globale (FR)	176
5.	Towards new coating systems: electrodeposition of ZnMn-Al ₂ O ₃ composite coatings.....	183
5.1.	Aim and procedure (EN) – But et procédure (FR).....	183
5.2.	Preliminary study of the electroplating bath	185
5.2.1.	Dispersion and stability of the plating bath.....	185
5.2.2.	Study of the electrochemical system	189
5.2.3.	Discussion and conclusion	192
5.3.	Electrodeposition of ZnMn-Al ₂ O ₃ coatings under pulse currents	192
5.3.1.	Characterization of the metallic matrix	193
5.3.2.	Mechanisms of particle incorporation	197
5.3.3.	Discussion and conclusion	203
5.4.	Perspectives on the anticorrosive properties of ZnMn-Al ₂ O ₃ deposits	204
5.4.1.	Hardness	204
5.4.2.	Electrochemical properties	206
5.4.3.	Conclusion and discussion	207
5.5.	Conclusion and outlook on the deposition of ZnMn-Al ₂ O ₃ coatings (EN) – Conclusion et perspectives sur la deposition de revêtements ZnMn-Al ₂ O ₃ (FR).....	207
Summary and outlook (EN)		211
Résumé et perspectives (FR).....		218
Appendix		225
Appendix 1: Promising coating systems		225
	Zn-Co-Fe alloys.....	225
	High entropy alloys – HEA.....	226
	Zn-Mo and Zn-Mn-Mo alloys	226
	Zn-Mn with Ce-containing nanoparticles.....	227
	Zn-Mn with active nanocontainers	228
Appendix 2: Mathematical models describing the behavior of metal electrodeposition with inclusion of particles		229
Appendix 3: Numerical modeling of the cell geometries.....		230
Appendix 4: Transmission Electron Microscopy – TEM.....		234
References		235

Table of content

Abbreviations

δ_N	thickness of the Nernst layer
δ_p	thickness of the pulsating diffusion layer
δ_s	thickness of the stationary diffusion layer
ζ	zeta potential
γ	Duty cycle
3-HB	3-hydroxybenzaldehyde
4-HB	4-hydroxybenzaldehyde
AAS	Atomic absorption spectroscopy
AASS	Acetic acid salt spray test
ACT	Accelerated corrosion test
ASTM	American society for testing materials
BCC	Body centered cubic
BEV	Battery electric vehicle
BIW	Body-in-white
BSE	Backscattered electrons
BTA	Benzotriazole
CASS	Copper-accelerated acetic acid salt spray test
CC	Continuous current
CCT	Cyclic corrosion test
COD	Crystallography open database
CP	Continuous plating
CPC	Cetyl pyridinium chloride
CR	Corrosion rate
CTAB	Cetyl trimethyl ammonium bromide
CTAC	Cetyl trimethyl ammonium chloride
DLS	Dynamic light scattering
DIN	Deutsche Institut für Normung (german institute for standardization)
E_{corr}	Corrosion potential
EBSD	Electron backscatter diffraction
ECC1	Essai de corrosion cyclique 1 / cyclic corrosion test 1 (Renault)
EDL	Electrical double layer
EDS	Energy dispersive spectroscopy
EDTA	Ethylenediaminetetraacetic acid
EG	Electrogalvanized
EIS	Electrochemical impedance spectroscopy
EMF	Electromotive force
EN	European Norm (european committee for standardization)
Euro NCAP	European new car assessment programme
EW	Equivalent weight
F	Faraday constant, 96500 s.A.mol ⁻¹
F	Frequency
FCC	Face centered cubic
FE-SEM	Field emission scanning electron microscopy
FEG	Field emission gun
FEM	Finite elements method
FIB	Focused ion beam
GA	Galvanized
GDOES	Glow discharge optical emission spectroscopy
GI	Galvanized
GM	General Motors

Abbreviations

GVA	Galvanostatic dissolution, coulometry
HCP	Hexagonal close-packed
HDG	Hot-dip galvanized
HEA	High entropy alloy
HER	Hydrogen evolution reaction
HM	Hydromagnesite
HSB	Hue, saturation, brightness
HZ	Hydrozincite – zinc hydroxycarbonate
j_a	Average current density
j_p	Peak current density
j_{LIM}	Limiting current density
$j_{p,LIM}$	Pulse limiting current density
IBAD	Ion beam assisted deposition
i_{corr}	Corrosion current density
IF	Interstitial-free
IPF	Inverse Pole Figure
ISO	International organization for standardization
JCPDS	Joint committee on powder diffraction standards
E-coat	Cathodic dip painting
KWT-DC	Klimawechseltest Daimler Chrysler / Alternating climate test
LDH	Layered double hydroxide
LMIS	Liquid metal ion source
LSV	Linear scan voltammetry
LME	Liquid metal embrittlement
MC	Magnesium carbonate
MeKo-S	Mercedes-Benz corrosion test, static
MeKo-D	Mercedes-Benz corrosion test, dynamic
MH	Magnesium hydroxide
MHC	Magnesium hydroxycarbonate
MMC	Metal matrix composite
MZ	Commercial denomination for Mg-Zn coatings
NHTSA	National highway traffic safety administration
NND	N,N-dimethyl dodecyl amine
NSS	Neutral salt spray test
OCP	Open circuit potential
OCP	Overall corrosion performance
PAA	poly(acrylic acid)
PC	Pulse current
PCI	Perforation corrosion index
PDAD	poly(diallyldimethylammonium chloride)
PE	Primary electrons
PEG	Polyethylene glycol
PosMAC	Zn-Al-Mg coating (Posco)
PV1210	Climate corrosion test cycle (Volkswagen Group)
PVD	Physical vapor deposition
RPC	Reversed pulse current
S_a	Mean roughness
S_{max}	Maximal roughness
S_z	Roughness height
SAE	Society of automotive engineers
SCE	Saturated reference electrode
SDS	Sodium dodecyl sulfate
SE	Secondary electrons

Abbreviations

SEM	Scanning electron microscopy
SESI	Secondary electrons secondary ions
SHE	Standard hydrogen electrode
SLS	Sodium lauryl sulfate
SPC	Superimposed pulse current
SST	Salt spray test
SZCH	Sodium zinc carbonate hydrate
t_{ch}	Charging time
t_{disch}	Discharging time
t_{on}	Pulse duration, ON-time
t_{off}	Relaxation time, OFF-time
TCA	Thiocarbamide
TEM	Transmission electron microscopy
TKD	Transmission Kikuchi diffraction
UTS	Ultimate tensile strength
UV	Ultra-violet
VDA	Verband der Automobilindustrie (german association of the automotive industry)
VICT	Volvo indoor corrosion test
WDS	Wavelength dispersive X-ray spectroscopy
XPS	X-ray photoelectron spectroscopy
XRD	X-ray diffractometry
Z	Commercial denomination for hot-dig galvanized Zn coatings
ZA	Commercial denomination for Zn-Al coatings (Galfan)
ZAM	Commercial denomination for Zn-Al-Mg coatings
ZE	Commercial denomination for electrogalvanized Zn coatings
ZF	Commercial denomination for Zn-Fe coatings
ZHC	Simonkollite – zinc hydroxychloride
ZHS	Zinc hydroxysulfate
ZM	Commercial denomination for Zn-Mg coatings
ZSC	Gordaite

Introduction (EN)

Automotive manufacturers face constant challenges for the conception and the production of modern passenger vehicles, and especially in relation to the chassis and body work. On one side, the constant strive for weight reduction related to new environmental regulations is often managed by the development and use of new lightweight materials, designs and assemblies. In contrast to this lightening of the structure, manufacturers still need to meet, in the event of a crash, demanding safety ratings and severe requirements of safety institutes such as the Euro NCAP or the NHTSA.

In order to provide an optimal protection of the passengers in the event of a crash, the vehicle and especially the body-in-white have to be specifically designed. These safety requirements mean that even in a struggle for lighter structures, the use of various steels is still predominant for the body-in-white. On the one side, a rigid structure consisting mostly of hot formed steel presenting high yield strength is required to form a non-deformable shell around the passengers. On the other side, the use of softer cold formed steels is also necessary for given components that need to crumple and adsorb the energy created during a crash. These cold formed steels offer various properties and are therefore found in numerous places from reinforcements of the chassis to the bodywork.

Various forms of corrosion are likely to arise on the body-in-white or on the chassis of passenger vehicles. Corrosion may originate due to a contact between different materials or due to some defects or inhomogeneities on a single material. As a result, numerous solutions are routinely implemented by automotive manufacturers. These solutions may consist in the specific design of a single component, in a specific assembly and sealing solution between various components, and in the correct selection and application of a coating system. Depending on the component and its location on the vehicle, this coating system comprises at least a sacrificial metallic layer, a phosphate conversion layer and an electrophoretic coating.

This doctorate thesis is part of a collaborative project between the automotive manufacturer Daimler AG and the University of Lorraine, which objective is to develop and characterize alternative anticorrosive coatings for the sacrificial protection of steel-based components for the chassis and bodywork of passenger vehicles. The suitability of these newly developed deposits for an application in the automotive industry will be based on an assessment of the performance in comparison to commercialized products.

The problematic of corrosion of steel components was over the past decades of significant interest for automotive manufacturers and steel producers. As a result, a large amount of approaches and possible solutions were reviewed in a literature study presented in chapter 1. This chapter covers the technical solutions implemented in the automotive industry for the corrosion protection of steel components, the various coating systems provided by the steel producers and an overview of alternative deposits only considered at the laboratory scale.

On the basis of this literature review, numerous alternative concepts could be proposed and two approaches have been considered in this thesis:

- The pulse electrodeposition of Zn-Mn alloy coatings
- The pulse electrodeposition of Zn-Mn- Al_2O_3 composite coatings

A description of the experimental approach and characterization methods used for the development, electrodeposition and characterization of the coatings is described in chapter 2. A specific aspect of this work is the characterization of the deposits at both laboratory and industrial scales, requiring a large variety of techniques in various fields.

The deposition and the characterization of the Zn-Mn coatings are presented in chapter 3. While the deposition of the Zn-Mn alloys under continuous currents will be of interest in a preliminary study, a particular attention will be given to the influence of the pulse parameters on the composition, morphology, microstructure, crystallography and texture of the deposits. Based on those investigations, optimal deposition parameters will be identified corresponding to deposits presenting the most promising characteristics such as the Mn content, the crystallography, the porosity and so on.

The suitability of those newly developed Zn-Mn pulse electrodeposits for an application in the automotive industry will be investigated in chapter 4. Numerous aspects of the deposits such as their corrosion resistance under various corrosive environments, forming behaviour, adhesive properties, hardness and suitability for phosphating and painting operations will be considered. On the basis of these experiments carried out at the laboratory and at the industrial scale, the performance of the Zn-Mn deposits will be assessed in comparison to commercial coatings already in use in the automotive industry.

In order to try to further optimize the properties and the performance of the Zn-Mn deposits, the codeposition of Al_2O_3 particles inside a Zn-Mn metallic matrix is considered in chapter 5. In this chapter, a particular interest will be given to the dispersion of the particles in the plating bath. In addition, the mechanisms of incorporation of the particles and their influence on the properties of Zn-Mn metallic matrix will be studied.

In order to conclude this work, some perspectives and some interesting research tracks for the further development of anticorrosive coatings will be discussed.

Introduction (FR)

Les constructeurs d'automobiles font constamment face à de nombreux challenges lors de la conception et de la production de véhicules de tourisme modernes, en particulier concernant le châssis et la carrosserie des véhicules. D'un côté, l'effort constant pour diminuer le poids des véhicules, en relation avec les nouvelles normes environnementales est souvent résolu par le développement et l'utilisation de nouveaux matériaux, concepts et assemblages légers. En opposition à cette recherche pour l'allègement des structures, les constructeurs sont toujours requis de respecter en cas de crash les normes de sécurité d'instituts tels que l'Euro NCAP ou le NHTSA.

Afin de permettre une protection optimale des passagers en cas de crash, le véhicule et en particulier la caisse en blanc doivent être conçus spécifiquement. Ces exigences de sécurité signifient que même avec une recherche de légèreté toujours plus importante, l'utilisation de différents alliages d'aciers reste toujours largement prédominante pour la caisse en blanc. D'un côté, une structure rigide consistant en grande majorité d'aciers formés à chaud et présentant une limite d'élasticité élevée est requise pour obtenir un compartiment indéformable pour les passagers. D'un autre côté, l'utilisation d'aciers plus ductiles mis en forme à froid est également nécessaire pour certains composants des zones tampons qui doivent se déformer afin d'absorber l'énergie créée lors d'un accident. Ces aciers mis en forme à froid offrent de nombreuses propriétés et sont de ce fait utilisés à divers emplacements du véhicule, du renforcement du châssis jusqu'à la carrosserie.

De nombreuses formes de corrosion sont susceptibles de survenir sur la caisse en blanc ou sur le châssis des véhicules. La corrosion de structures métalliques peut provenir, suite à leur exposition à un milieu environnant oxydant, au contact entre deux matériaux différents, de défauts (impuretés, porosités, etc.) ou encore d'inhomogénéités sur un matériau unique. De ce fait, de nombreux remèdes sont couramment implémentés par les constructeurs automobiles. Ils peuvent consister en une conception spécifique d'un composant, un assemblage spécifique ainsi qu'une étanchéité entre plusieurs composants, et dans une sélection appropriée de plusieurs revêtements. En fonction du composant et de sa localisation sur le véhicule, ces revêtements sont constitués d'au moins une couche métallique sacrificielle, une couche de phosphate métallique ainsi que d'un revêtement obtenu par électrophorèse.

Cette thèse de doctorat fait partie d'un projet collaboratif entre le constructeur automobile Daimler AG et l'université de Lorraine, avec pour objectif de développer et caractériser de nouveaux revêtements anticorrosifs pour la protection sacrificielle de pièces en acier pour le châssis et la carrosserie de véhicules de tourisme. L'aptitude de ces nouveaux revêtements pour une application dans l'industrie automobile sera basée sur une évaluation de leurs performances anticorrosives et mécaniques en comparaison avec les produits commerciaux.

La problématique de la corrosion des aciers a été au cours des dernières décennies d'un intérêt capital pour les constructeurs automobiles et les aciéristes. De ce fait, de nombreuses solutions et approches ont été présentées dans la section état de l'art du chapitre 1. Ce chapitre couvre différentes solutions techniques implémentée dans l'industrie automobile pour la protection contre la corrosion du châssis et de la carrosserie, les différents revêtements commercialisés par les aciéristes ainsi qu'une vue d'ensemble des revêtements alternatifs étudiés à l'échelle du laboratoire.

Sur la base de cet état de l'art, divers concepts novateurs ont pu être proposés, avec deux approches retenues dans le cadre de cette thèse de doctorat et qui consistent en :

- L'électrodéposition impulsionnelle de revêtements Zn-Mn
- L'électrodéposition impulsionnelle de revêtements composites Zn-Mn-Al₂O₃

Une description des méthodes d'électrodéposition et de caractérisation des revêtements est décrite dans le chapitre 2. Un aspect particulier de ce travail réside dans la caractérisation des revêtements aux échelles de laboratoire et industrielles, ce qui requiert un large panel de techniques dans des domaines variés.

La déposition et la caractérisation des revêtements de Zn-Mn est présentée dans le chapitre 3. Alors que la déposition des alliages de Zn-Mn sous courants continus sera envisagée dans une étude préliminaire, une attention particulière sera portée à l'influence des paramètres du courant impulsionnel sur la composition, morphologie, microstructure, cristallographie et texture des revêtements. De plus, une étude de l'interface entre le dépôt et le substrat sera effectuée. Sur la base de ces recherches, des paramètres de déposition optimaux seront identifiés, correspondant aux revêtements possédant les propriétés les plus prometteuses.

L'aptitude de ces nouveaux revêtements de Zn-Mn impulsionnels pour une application dans l'industrie automobile sera étudiée dans le chapitre 4. Divers aspects des revêtements tel que leur résistance à la corrosion sous des environnements variés, leur comportement lors de la mise en forme, leur propriétés d'adhésion, leur dureté et leur aptitude aux opérations de phosphatation et de peinture électrophorèse seront analysés. À partir de ces expériences effectuées aussi bien à l'échelle laboratoire qu'à l'échelle industrielle, la performance des dépôts de Zn-Mn sera définie en comparaison aux revêtements commerciaux déjà utilisés dans l'industrie automobile.

Dans le but d'optimiser davantage les propriétés et la performance des revêtements de Zn-Mn, la codéposition de nanoparticules d' Al_2O_3 dans une matrice métallique de Zn-Mn sont analysée dans le chapitre 5. Dans ce chapitre, un intérêt particulier sera porté à la dispersion des particules dans l'électrolyte. De plus, les mécanismes d'incorporation des particules ainsi que leur influence sur certaines propriétés de la matrice métallique Zn-Mn sera étudiée.

Afin de conclure ces travaux, des perspectives et des directions de recherche permettant de développer davantage les revêtements métalliques anticorrosifs seront discutées.

1. State of the art: current and alternative coatings for corrosion protection of automotive steel parts and definition of alternative coating systems

This first introductory chapter aims to define the problematic of corrosion of body parts in the automotive industry as well as the current and alternative solutions aiming to hinder the progress of corrosion. It takes the form of a state of the art on the technical knowledge in the modern automotive industry with an outlook towards the current research on alternative coatings.

In the first section 1.1, the general problematic as seen by the automotive industry will be treated. The different materials used for the construction of the vehicles chassis and body will be detailed. The various corrosion phenomenon occurring on vehicles will be presented as well as the technical solutions commonly used to act against corrosion and to anticipate it. The second section 1.2 will be focused on the actually commercialized Zn-based coatings. Their anticorrosive and mechanical properties will be detailed and the different products will be compared based on the literature. These commercial coatings will be compared in section 1.3 and the required specifications for the coatings will be given. In the last sections 1.4, 1.5 and 1.6, a review of alternative Zn-based coatings will be carried out. Promising coating systems and solutions will be detailed with focus on their properties and manufacturing processes.

Ce premier chapitre introductif a pour objectif de définir la problématique de corrosion de la carrosserie dans l'industrie automobile ainsi que les solutions actuelles et alternatives visant à réduire les différentes formes de corrosion. Un état de l'art des connaissances est ainsi dressé dans l'industrie automobile, avec une ouverture sur les recherches actuelles conduites sur des revêtements alternatifs.

Dans la première section 1.1, la problématique générale de la corrosion dans l'automobile sera abordée. Les différents matériaux utilisés pour la construction du châssis et de la carrosserie des véhicules seront détaillés. Les différents phénomènes de corrosion prenant place dans les véhicules seront traités ainsi que les solutions techniques habituellement utilisées pour lutter contre la corrosion et la prévenir. La section 1.2 sera consacrée aux revêtements actuels à base de zinc. Les propriétés anticorrosives et mécaniques de ces alliages seront détaillées et comparés sur la base de la littérature. Ces dépôts commerciaux seront ensuite comparés dans la section 1.3 et le cahier des charges pour les revêtements y sera détaillé. Dans les dernières parties 1.4, 1.5 et 1.6, une analyse de la littérature concernant des revêtements à base de zinc présentant une alternative aux produits actuels sera conduite. Les solutions les plus prometteuses seront décrites avec un intérêt particulier pour leurs propriétés ainsi que leurs procédés de dépôt.

1.1. Corrosion and corrosion protection of car bodies: a general introduction

Since its debut in 1886 with the invention of the automobile [1], the construction and design of automobiles was subjected to drastic changes (Fig.1). These mutations have been brought by improvements of the structural safety, increase of the inner space, proliferation of the standard and/or optional equipment and electronics; all leading to an increase of the curb weight. Automotive manufacturers however managed to contain these uptakes by developing and using new lightweight design and materials. This strive for weight reduction is also related to the actual environmental regulations and to the global effort to lower global warming. Reducing the weight of the vehicles is in all cases beneficial for their consumption. Moreover, the development of battery electric vehicles (BEV) leads to further weight uptakes due to the batteries, electronics and reinforcements [2] making lightweight constructions even more important.

For example, the Mercedes-Benz C-Class showed in the last 30 years a 35 % increase of its curb weight while the weight of the bodyshell (Body-In-White plus chassis) only showed an 8 % increase. These

reductions are mainly achieved through development and appropriate choice of materials, but also through lightweight construction and well-chosen assemblies.

On opposition to the weight reductions, automotive manufacturers still have to provide optimal protection for the passengers of the vehicles. They must provide constructions and materials with high performance in crash in order to meet the strict requirements of safety programs like the Euro NCAP or the NHTSA [3, 4].



Fig.1: 1886-2011, evolution of the automobile from the „Benz Patent Motorwagen” (left) to the 2011 A-class concept (right), from [5]

In order to combine the lightweight design and an optimal protection of the passengers, various materials are generally mixed when designing the Body-In White (BIW) of vehicles. An overview of the different materials used in the 2014 Mercedes-Benz C-Class is presented in Fig.2. Steels are still predominant in the base construction, representing about 60 % of a traditional family vehicle [6]. Numerous steel grades are traditionally used in the construction of the BIW. These steels can be distinguished between cold and hot formed steels. The search for weight reduction has led recently to the development of alternative materials such as aluminium, magnesium and composites, with a clear preference of the manufacturers for aluminium due to its lower costs [6] (Fig.2).

The work conducted in the framework of this thesis will be focused on cold formed steel components, described later in section 2.8.1.

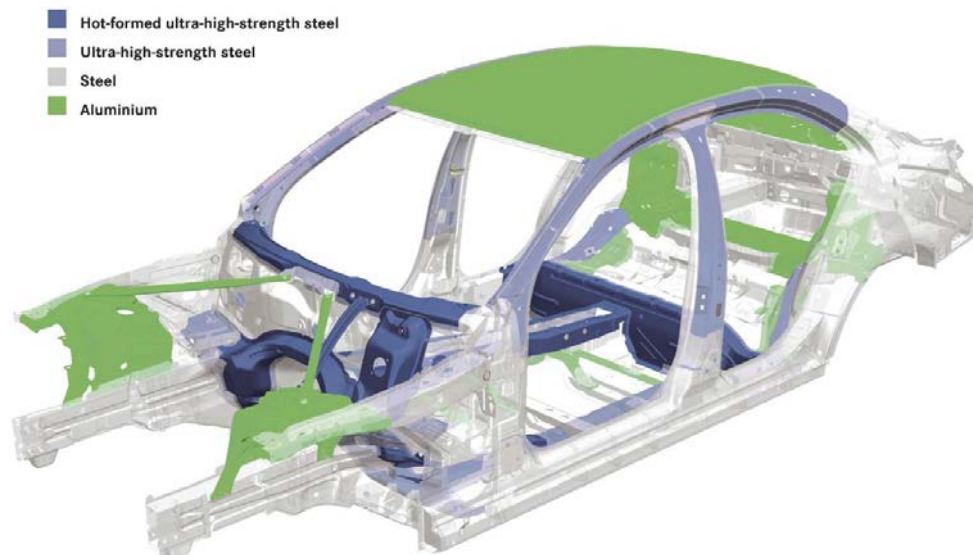


Fig.2: Distribution of materials in the bodyshell of cars, example of the 2014 Mercedes-Benz C-Class, from [7]

1.1.1. Corrosion of car bodies

Corrosion is defined as the electrochemical reaction between a metal and its environment, impacting the properties of the metal. So that this electrochemical reaction can occur, the presence of an electronic (the metal) and an ionic medium (the electrolyte) are required. The anodic and cathodic

reactions can take place on the same metal and form a micro corrosion cell or can be separated forming then a macro corrosion cell.

Six different forms of corrosion can be distinguished for the car bodies [8]:

- generalized (or uniform) corrosion
- galvanic corrosion
- crevice corrosion
- pitting corrosion
- intergranular corrosion
- stress cracking corrosion

These types of corrosion are, depending on the coating system, the environment and the chemistry, more or less likely to occur. In the case of zinc-based alloys coated steels, the most common forms of corrosion are generalized, galvanic, pitting and inter-granular corrosion, further described in the following sections.

Generalized corrosion

Generalized corrosion occurs in presence of micro corrosion cells due to differences of potential on a same metal or alloy as illustrated in Fig.3. These defects are created by local imperfections on the surface of the material such as point defects, dislocations, grain boundaries, inclusions or by the roughness of the surface. Because of the usually high number and regular distribution of these defects on the metallic surface, this type of corrosion is relatively homogeneous and has little structural impact on the material [8].

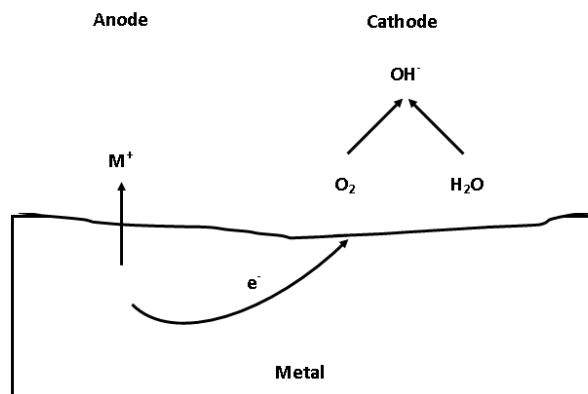


Fig.3: Schematic of generalized corrosion of metals

Galvanic corrosion

Galvanic cells are formed when two different metals or alloys are electrically connected. Due to the difference in corrosion potential between the two materials, a current called galvanic current flows between the latter (Fig.4). During galvanic corrosion, the thermodynamic reversible potentials of the metals determines the polarity and the current flow direction between both electrodes. The metal with the highest corrosion potential in the electromotive force (EMF) series is the cathode while the metal with the lowest potential is the anode and will therefore be preferentially corroded. In addition to the potential difference, numerous factors can impact galvanic corrosion. In fact, alloying or heat treatment can induce changes in the corrosion potential. The presence of a passive film or corrosion products can also interfere with the galvanic process as well as the properties of the electrolyte [8]. In the case of a

Zn-coated steel substrate, the substrate is protected through a barrier effect and a galvanic effect. The barrier protection represents the “physical” layer isolating the substrate from outer aggressions. According to the galvanic effect, zinc acts as a sacrificial anode because of its corrosion potential lower than that of steel. It forms as a result a so-called sacrificial or cathodic protection.

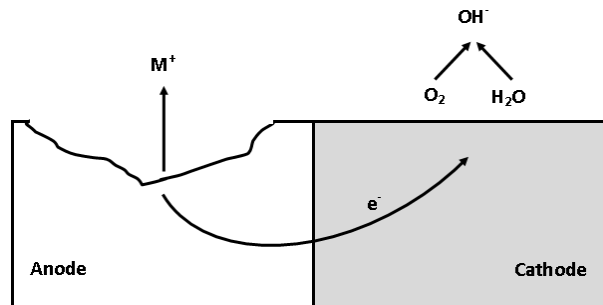


Fig.4: Schematic of galvanic corrosion

Pitting corrosion

Pitting corrosion is the localized corrosion of a material, leading to the formation of holes and cavities. A strongly heterogeneous distribution of the anodic and cathodic sites at the surface of the metal, particularly with an anodic site isolated in a cathodic environment, will be likely to form a starting point for pitting corrosion. The anodic site will be preferentially oxidized resulting in an attack in depth and the rapid perforation of the metal [8].

In the general case of corrosion in solutions, the pitting mechanism of metals only takes place after breakdown of the passivated surface. This breakdown is linked to the presence of chloride ions in the solution, the local pH of the solution and the electrode potential [8]. An increase of the amount of chloride ions together with a decrease of the pH will lead to an acceleration of the pitting process. On the contrary, if the dissolution rate stays low, the local pH of the electrolyte will be able to regulate itself, re-passivation will occur and the pitting mechanism will be interrupted. This form of corrosion is considered as critical due to the structural damages it causes and the resulting possibility for catastrophic failure. Pitting corrosion can lead to deep and narrow pits cutting through the coating, or subsurface corrosion. Moreover, the occurrence of corrosion pits can be difficult to detect due to the presence of corrosion products filling and covering the pits.

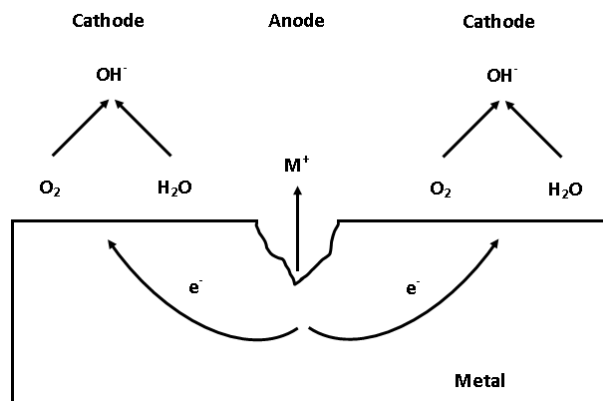


Fig.5: Schematic of the pitting corrosion

Intergranular corrosion

Intergranular corrosion is the localized corrosion occurring at the grain boundaries. Typically, intergranular corrosion is due to different electrochemical behaviour of the phases at the grain boundaries, encountered in the case of multiple phase alloys or instable solid solutions, and originates from segregation effects. Because these impurities, defects and specific phases are more likely to be found at the grain boundaries, this form of corrosion is less likely to affect not only the bulk material [8] but also the coatings.

In the case of zinc-based alloys coatings, the intergranular corrosion was mostly observed for zinc alloyed with aluminium, particularly in the case of warm-humid environments [8]. In this case, Al-rich phases are formed at the grain boundaries and due to the lower potential of Al will tend to be preferentially corroded. The presence of other elements with low solubility in Zn such as Bi, Cd, Hg, In, Na, Pb, Sn or Tl will also lead to solid precipitates at the grain boundaries. The presence of these impurities will further increase the separation between the anodic and cathodic sites and therefore will further increase the corrosion rate at the grain boundaries [8]. Another theory, proposed by Devillers and Niessen [8], suggests that formation of hydroxide ions OH^- occurs at the alkaline grain boundary, caused by the cathodic reduction of hydrogen. This reaction takes place in parallel to the preferential dissolution of the anodic grain boundary [8]. The damages caused by this form of corrosion are difficult to observe and are mainly evaluated through metallographic analyses. The effects can vary from losses of ductility and / or strength of the metal (or alloy) to a complete failure.

1.1.2. Corrosion protection of car bodies

It was demonstrated in the previous section that a large number of corrosion forms might arise on the BIW of passenger vehicles. This may occur due to a specific assembly such as in the case of galvanic corrosion, or due to the material himself such as in the cases of generalized, pitting or intergranular corrosion. Automotive manufacturers therefore developed over the last years various technical solutions in order to hinder the occurrence of corrosion. These measures concern the construction and the assembly of the components, and the correct material selection permitting to obtain a protective layer system.

Construction

The first measure that guarantee a good corrosion protection of the car bodies concerns the design of appropriate constructions for components to ensure that the geometry and the assembly of the components limit the exposure to corrosive environment. For components or assemblies presenting cavities, as depicted in the Fig.6a, the needs for gaps or holes letting water flow in and out is recommended. Moreover, entries and outlets in cavities allow aeration. The amount of horizontal surfaces also needs to be limited, in order to reduce the stagnation of water. The case of flanges is also of particular concern during the development, as illustrated in Fig.6b. Overlap of two sheets can lead in some cases to accumulation of water and earlier corrosion.

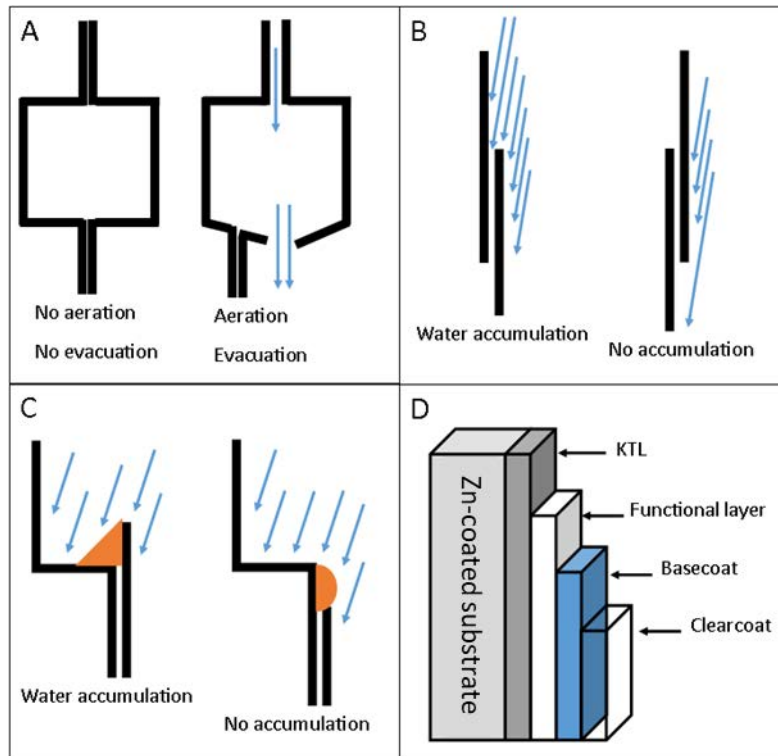


Fig.6: Corrosion protection of car bodies, examples of inappropriate and appropriate construction (a), assembly (b), sealing (c) and coating (d)

Assembly and sealing

As an appropriate design of the geometry is not sufficient to ensure the full sealing of the bodyshell, the use of proper assemblies, sealants, wax and adhesives is required. Adhesives are used to join two plates in the case of overlapping, preventing the entry of water between the sheets, as schematized in Fig.6c. Because of the hydrophobic nature of the wax, repelling water, the inner-surface of the components presenting cavities can also be sprayed. Sealants are used in order to complete the sealing of the components, they are used for example at the interface between a steel plate and adhesives.

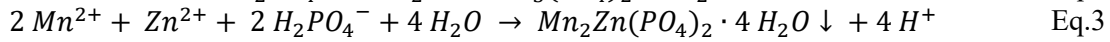
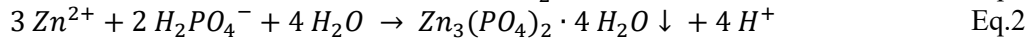
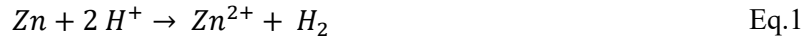
Coating systems

Once the design and the assembling of the components are validated, the materials and particularly their coating systems, as depicted in Fig.6d need to be defined according to commercial availability, price, performance, processability and location in the car.

The first protective measure consists in coating the steel substrate with a less noble metal or alloy in order to ensure a sacrificial protection. This first coating step is performed by steel manufacturers and is in most cases the only coating step performed before forming and assembling of the BIW. If the coating is damaged and the substrate is exposed, the protective layer will preferentially corrode and the substrate will be protected. In the last decades, cadmium-containing coatings were widely used in the automotive industry because of their excellent corrosion resistance. Due to its toxicity, the use of cadmium is now restricted by environmental regulations and cannot be used as coating anymore [9]. Numerous researches were conducted over the past years in order to find a replacement to cadmium coatings. Coatings that are now found in the industry are composed of aluminium-silicon (Al-Si), pure zinc (Zn), zinc-aluminium (Zn-Al), zinc-aluminium-magnesium (Zn-Al-Mg), zinc-iron (Zn-Fe), zinc-magnesium (Zn-Mg) and zinc-nickel (Zn-Ni).

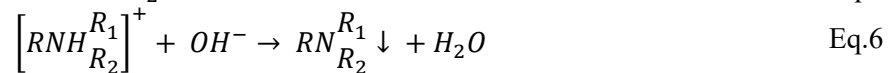
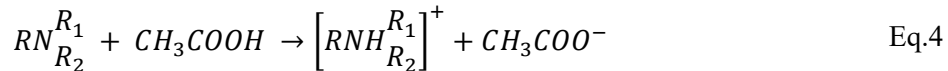
In order to further increase corrosion protection, the metallic coated substrates are successively treated by phosphate conversion coating and by cathaphoresis, or cationic electrophoresis (E-coat) [10]. Prior to the cathaphoresis, the samples are pre-treated and coated with a phosphate conversion coating, also called phosphating [11].

The phosphating process consists in treating chemically a metallic surface in order to produce a hard, electrically isolating coating with a good adherence to the underlying metal. The particularly good adhesive properties of the phosphate layer are due to the topochemical reaction occurring during the deposition [11]. When the metallic substrate is introduced into the phosphate solution the metal is dissolved by the free phosphoric acid in the solution (Eq.1) and leads to the formation and deposition of heavy metal tertiary phosphates [11, 12]. In the case of zinc coated steels, hopeith and hureaulith are formed according to the reactions 2 and 3, respectively.



The resulting phosphate coatings provide due to their non-conducting nature, a good protective layer against corrosion. They also form a good base for the deposition of additional painting systems such as cathaphoretic paints [11].

These cathaphoretic paints are deposited in addition to the phosphate layer, and form a first paint layer in order to enhance the corrosion protection of the steel. This first paint layer is deposited by means of cathodic deposition (also called E-coat process). The E-coat process consists in dipping a metallic sample, phosphated, into an aqueous electrolyte containing the paint system [13], composed of pigments, fillers, additives and solvents. The resin, composed of pigments and fillers and usually water-insoluble, is solvated through deprotonation by means of weak organic acids such as acetic acid (Eq.4). The deposition is conducted under direct current with applied potentials ranging from 300 up to 400 V [14]. Due to the applied potential, the electrolysis of water occurs (Eq.5), leading to formation of hydroxyl ions and increase of the pH, allowing coagulation of the solvated resin on the cathode (Eq.6) and formation of the cathaphoretic coating [15]. Once the desired thickness is deposited, the coating is cured in an oven at temperatures around 170 – 180 °C [14, 15].



Additional painting systems are then applied on the visible parts, providing a better surface appearance but also an additional barrier protection against the environment. These systems are generally composed of a primer coat, a base coat and a varnish. The primer offers protection against UV and stone-chipping and prepares the surface for further layers by filling defects. The base coat provides the colour of the painting and the varnish offers protection against scratches and better stability against ageing and chemical attack [10].

1.1.3. Assessment of the corrosion performance in the industry

Due to the high complexity of the corrosion protection in the automotive industry, the prediction of the corrosion behaviour of different materials is of crucial interest for the validation of concepts, materials, construction, assemblies and coating systems. Due to corrosion of structural components, the integrity and the safety of the entire vehicle may be compromised. Furthermore, the appearance and the quality of the vehicle can be severely impaired by the presence of red rust on visible components.

Field testing of automobiles have been used for decades because of their good reliability [16]. However, such tests show high costs and are time-consuming. As a result, accelerated corrosion tests (ACT) have been developed in order to gather knowledge on the corrosion behaviour of materials in different exposures in a shorter time, thus reducing the costs. Two different groups can be distinguished among the accelerated corrosion tests – namely the normalized tests certified by institutions such as the VDA (Verband der Automobilindustrie, German Association of the Automotive Industry) or the DIN / EN / ISO institutions (Deutsche Institut für Normung / European Norm / International Organization for Standardization) or the tests developed internally by the automotive manufacturers.

In the automotive industry, the first normalized accelerated cyclic corrosion test of great importance was the VDA 621-415 [17], developed in 1982. It consists in the repetition of cycles with varying climatic conditions:

- salt spraying
- alternating humidity
- alternating temperature
- drying

The VDA 621-415 permits to obtain a picture of the corrosion processes occurring with a good correlation with the corrosion mechanisms observed during field exposure [17]. The test particularly shows inner-rusting, coating delamination, surface and edge corrosion. Assessment of the perforating corrosion in flanges and gaps is also possible. In most cases, the scribe test is performed during these accelerated tests. It consists in painted metallic sheets with the surface scratched following defined patterns. On the basis of the VDA 621-415, the VDA 233-102 was more recently developed in order to assess the behaviour of new materials and coatings. Compared to the cyclic corrosion tests previously described, the continuous salt spray test DIN EN ISO 9227 [18] only provides information on the corrosion performance in a unique environment. This test is however widely used by industrials and researchers to assess the level of corrosion protection of new materials. In parallel, industrials have developed internal testing processes to assess corrosion protection of the raw materials and assemblies using their own criterion. All car manufacturers have now their own corrosion test such as the Renault ECC1, the Volvo VICT, the Volkswagen PV1210 etc. Daimler AG is using two cyclic corrosion tests depending on the type of products [19] – namely the Mercedes-Benz Static Corrosion Test (MeKo-S) and the Mercedes-Benz Dynamic Corrosion Test (MeKo-D).

The MeKo-S test is carried out on raw materials, single parts or assemblies for duration of eight weeks. It consists of the succession and repetition of different phases.

The MeKo-D corrosion test is carried out on complete vehicles only, with similar conditions to the MeKo-S. The process also includes, apart from various situations of salt and water spraying, various environments and different dynamic programs.

Advantages

The use of accelerated corrosion tests permits to obtain an important amount of information on the corrosion behaviour of a given material in a relatively short time (a few weeks at most) by using relatively simple characterization techniques such as image analysis. Because these tests are normalized, another advantage is the possibility to easily reproduce the tests and compare different materials or solutions. The information obtained is in a first time visual, with assessment of the appearance of the samples during the test. The proportion of red rust covering the surface of the samples at the end of the test is one of the most used parameters when comparing the performance of different materials. It can be determined at the end of the corrosion test or monitored at different time intervals in order to assess the evolution of red rust during the test. Evaluation of the mass loosed is also an important parameter obtained from corrosion tests. It is measured after removal of the corrosion products according to the norm DIN EN ISO 8407 [20] by gravimetric method. This characterization method is often used for

comparison between different materials. Moreover, by using samples at different stages of the corrosion test it is possible to monitor corrosion of the specimens and to obtain the corrosion rate in a given environment. Finally, it is possible to obtain information on the corrosion products formed at different stages of the corrosion test. This could be achieved by using a combination of characterization methods such as Scanning Electron Microscopy (SEM), Energy Dispersive Spectroscopy (EDS), X-Ray Diffraction (XRD), Raman Spectroscopy, X-Ray Photoelectron Spectroscopy (XPS) and / or Glow Discharge Optical Emission Spectroscopy (GDOES). While these characterization methods are more time-consuming and more difficult to interpret, they permit to obtain more detailed knowledge on corrosion products formed at specific stages and thus to better understand corrosion mechanisms in a given environment.

Correlation between corrosion tests and field exposure

The ability to reproduce the corrosion mechanisms observed during real exposure is a complex topic. Fujita et al., for example, reported contradictory results concerning two different corrosion tests [21] and therefore developed a “Perforation Corrosion Index (PCI)”. The PCI is defined as the corrosion rate ratio between the coating and the substrate steel, and permit to determine among various corrosion tests which one is most representative of the field exposure.

The comparison between neutral salt spray test (DIN EN ISO 9227 [18]) and cyclic corrosion test (DIN EN ISO 11997-1 [22]) has been studied by Edavan and Kopinski [23]. They observed a strong difference of corrosion performance between continuous corrosion test, cyclic corrosion test and natural exposure. A proposed explanation for such a difference is the repetition of stresses and relaxation due to climatic cycles. These changes in humidity (water uptake, drying) and temperatures (freezing cycles) for the most, are known to induce strains in the materials due for example to differences in thermal expansion coefficients. The cyclic corrosion test shows as a result a similar behaviour to that of natural exposure. The impact of the test conditions between continuous salt spray ATSM B117, cyclic corrosion test DIN EN ISO 11997-1 and natural exposure during the test was found to induce important variations in the simulated corrosion performance. Such differences were also reported by Bandyopadhyay et al. [24]. In 2008, LeBozec et al. conducted a comparative study between normalized, industrial corrosion tests and field exposure [16]. They performed a complete testing on cold rolled steel and hot-dip galvanized steel using the VDA 621-415 [17], neutral salt spray test (DIN EN ISO 9227 [18]) as well as corrosion tests from automotive manufacturers (Renault, Volvo, Volkswagen, General Motors and Daimler). These accelerated tests were compared to three field environments – namely vehicle in “de-icing salt area”, vehicle in “other area” and “marine stationary site”. They noticed that accelerated corrosion tests carried out with high salt loads and high humidity levels show poor correlation with real exposure and thus do not reflect the situation on vehicles, also reported by Hosking et al. [25]. Besides, tests with a lower salt load provided a good correlation with field results obtained on vehicles in “de-icing salt area” and in “other area”.

According to the literature, it is possible to define a list of corrosion tests showing good performances for life prediction of the materials, like the Daimler Chrysler KWT-DC [16], General Motors GM9540P [16, 26], Renault ECC1 D172028 [16] and Volvo VICT VCS1027,149 [16]. On the basis of these studies, complementary information about other corrosion tests, such as exposure conditions, was added in order to obtain the most thorough overview of accelerated corrosion tests. The overview of the corrosion tests is presented in Table 1. With the help of this work, it could be possible to determine the validity of newly developed corrosion tests. However, the choice of corrosion test cannot be made by only considering its proximity to real exposure. The time required to run the corrosion test is also a very important parameter as time-consuming tests involves higher costs. However, these long-lasting experiments have proven to give results closer to field observations.

Table 1: Overview of the corrosion tests

Test standard	Exposure			Temperature (°C)	Relative humidity (%), duration	Test duration (days)	Ref.
	salt solution, pH, deposition rate in 80cm ²	Frequency	Chloride deposition (mg/cm ²) test				
Renault ECC1 D172028	NaCl 1 wt.%, pH 4, 5 mL/h	30 min/day, 3.5 h/week	8	35	20, 1 h 35 min	42	[16]
				35	55, 2 h 40 min		
				35	90, 1 h 20 min		
Volvo VICT VCS1027, 149	NaCl 1 wt.%, pH 4, 120 mL/h	3 x 15 min, 2 times/week, 1.5 h/week	27	45	50, 4 h	42	[16]
				35	95, 4 h		
VDA 621-415 (old)	NaCl 5 wt.%, pH 6.5-7.2, 1.5 mL/h	24 h/week	136	40	100, 8 h	70	[16, 17]
				18-28	50, 16 h		
				23	50, 48 h		
Volkswagen PV1210	NaCl 5 wt.%, pH 6.5-7.2, 1.5 mL/h	4 h/day (5 days), 20 h/week	68	23	50, 4 h	42	[16]
				40	100, 16 h		
General Motors GM9540P (B)	NaCl 0.9 wt.%, CaCl ₂ 0.1 wt.%, NaHCO ₃ 0.255 wt.%, pH 6-9	4 x 30 min/day, 14 h/week	not determined	50	100, 8 h	40	[16]
				60	30, 8 h		
Daimler Chrysler KWT-DC	NaCl 1 wt.%, pH 6.5-7.2, 2 mL/h	2 h/day (4 days), 8 h/week	7,30	-15 up to 50	50-100	42	[16]
Salt spray ISO 9227	NaCl 5 wt.%, pH 6.5-7.2, 1.5 mL/h	Continuous	383	35	not controlled	28	[18]
Mercedes-Benz MeKo-S	NaCl 2.5 wt.%, CaCl ₂ 0.5 wt.%	/	/	-35 up to 70	15-98	56	[19]
VDA 233-102	NaCl 1 wt.%, pH 6.5-7.2, 3 mL/h	3 h/day (3 days), 9 h/week	12,3	-15 up to 50	50-100	42	[27]
ISO 11997-1 A	NaCl 5 wt.%, pH 6-7, 2 mL/h	2 h/cycle (30 cycles), 60 h	45,6	35 up to 60	20-95	10	[22]
ISO 11997-1 B	NaCl 5 wt.%, pH 6-7, 1.5 mL/h	24 h/cycle (3 cycles), 72 h	41,0	23 up to 40	50-100	35	[22]
ISO 11997-1 C	NaCl 0.031 wt.%, (NH ₄) ₂ SO ₄ 0.41 wt.%, pH 6-7, 3 mL/h	7 h/cycle (21 cycles), 147 h	not determined	25 up to 40	20-100	42	[22]
ISO 11997-1 D	NaCl 5 wt.%, pH 6-7, 1.5 mL/h	0.5 h/cycle (28 cycles), 14 h	8	30 up to 50	20-95	7	[22]
Volvo STD423-0014	NaCl 1 wt.%, pH 4.2, 1.8 mL/h (15 mm/h)	2 x 15 min/day (2 days), 1 h/week	1	35 up to 45	50-95	42	[28]

1.2. Properties of the current Zn-based coatings

This work will be focused on the first metallic layer ensuring barrier and sacrificial protection of the base steel in the case of cold-formed components solely. In the automotive industry, Zn-based coatings are among the most used and most studied. This chapter will cover the anticorrosive and mechanical properties of the commercial Zn-based coatings. A summary of the Zn-based coatings commercially available is presented in Table 2.

Table 2: Overview of Zn-based alloys coatings commercially available

Company	Product	System	Process	Zn	Al	Mg	Fe	Si	Ref.
ArcelorMittal	Electrogalvanized	Zn	Electrogalvanized	100%	/	/	/	/	[29]
ArcelorMittal	Extragal GI	Zn	Hot dip galvanized	100%	/	/	/	/	[29]
ArcelorMittal	Galfan	ZnAl	Hot dip galvanized	95%	5%	/	/	/	[29]
ArcelorMittal	Galvannealed GA	ZnFe	Galvannealed	90%	/	/	10%	/	[29]
ArcelorMittal	Zagnelis	ZnAlMg	Hot dip galvanized	93.30%	3.70%	3.00%	/	/	[29]
Corus	Galvatite Z	Zn	Hot dip galvanized	100%	/	/	/	/	[30]
Corus	Galvatite ZF	ZnFe	Galvannealed	88-92%	/	/	8-12%	/	[30]
Nippon Steel	Durgrip Zn	Zn	Hot dip galvanized	100%	/	/	/	/	[31]
Nippon Steel	DymaZinc	ZnAlMg	Hot dip galvanized	99.30%	0.20%	0.50%	/	/	[32]
Nippon Steel	Galvalume	ZnAl	Hot dip galvanized	45%	55%	/	/	/	[32]
Nippon Steel	SuperDyma	ZnAlMgSi	Hot dip galvanized	85.80%	11%	3%	/	0.20%	[33]
Nippon Steel	SuperZinc	ZnAlMg	Hot dip galvanized	95.4	4.5	0.10%	/	/	[32]
Nippon Steel	Zinkote	Zn	Electrogalvanized	100%	/	/	/	/	[32]
Nisshin Steel	ZAM	ZnAlMg	Hot dip galvanized	91.00%	6.00%	3.00%	/	/	[34]
Posco	EG	Zn	Electrogalvanized	100%	/	/	/	/	[35]
Posco	GI	Zn	Hot dip galvanized	99.80%	0.20%	/	/	/	[36]
Posco	PosMAC	ZnAlMg	Hot dip galvanized	94.50%	2.50%	3.00%	/	/	[36]
Salzgitter	GI	Zn	Hot dip galvanized	99.80%	0.20%	/	/	/	[37]
Salzgitter	Stronsal	ZnAlMg	Hot dip galvanized	96.80%	1.60%	1.60%	/	/	[38]
Salzgitter	ZE	Zn	Electrogalvanized	100%	/	/	/	/	[39]
SSAB	Z	Zn	Hot dip galvanized	100%	/	/	/	/	[40]
SSAB	ZA (Galfan)	ZnFe	Hot dip galvanized	95%	5%	/	/	/	[41]
SSAB	ZF (GA)	ZnAl	Galvannealed	90%	/	/	10%	/	[42]
TATA Steel	MagiZinc	ZnAlMg	Hot dip galvanized	94%	1.50%	1.50%	/	/	[43]
TATA Steel	ZF	ZnFe	Galvannealed	87-91%	/	/	9-13%	/	[44]
ThyssenKrupp	Z/GI	Zn	Hot dip galvanized	99.80%	0.20%	/	/	/	[45]
ThyssenKrupp	ZE/EG	Zn	Electrogalvanized	100%	/	/	/	/	[45]
ThyssenKrupp	ZF/GA	ZnFe	Galvannealed	90%	/	/	10%	/	[45]
ThyssenKrupp	ZM EcoProtect	ZnMg	Hot dip galvanized	99%	/	1%	/	/	[45]
Voestalpine	Corrender	ZnAlMg	Hot dip galvanized	96.0%	2.0wt%	2.0wt%	/	/	[46]
Voestalpine	Z	Zn	Hot dip galvanized	99.80%	0.2wt%	/	/	/	[47]
Voestalpine	ZF	ZnFe	Galvannealed	90%	/	/	10%	/	[47]
Voestalpine	ZE	Zn	Electrogalvanized	100%	/	/	/	/	[48]

Two different industrial processing methods are available for the production of Zn-based coatings: the hot-dipping process and the electrochemical process.

- During hot-dip galvanizing (HDG), a zinc or zinc-alloy coating is deposited on the surface of the substrate by dipping it into a bath of molten metal. The adhesion of the coating to the substrate is realized thanks to development of intermetallic layers at the interface between steel substrate and metallic coating.
- Electroplating is the second method used for the production of zinc-based coatings. About half of the Zn-based coatings are produced through this process. The whole process can be divided into two stages with at first cleaning and preparation of the substrate and in a second time electrodeposition in the plating bath (usually acid or alkaline).

The surface preparation is a highly important step, aiming to obtain a surface as clean as possible, that is degreased and free from dust and other loose particles, prior the deposition. Traditional surface preparation for hot-dip galvanizing or electroplating includes a degreasing step in acid baths or caustic solutions in order to remove dirt, grease and other organic contaminants; a pickling step in hydrochloric or sulfuric acid aiming to remove oxides products from the steel and a fluxing step, into an acidic zinc chloride and ammonium chloride solution, in order to remove oxides formed after pickling and to prevent formation of new oxides before the deposition step [49].

While deposition of pure zinc coatings is achievable through both processes, deposition of zinc-alloys can be more challenging depending on the alloying elements. Electrodeposition of zinc-alloys is limited for example by the hydrogen evolution reaction [50]. Deposition of metals with a potential lower than

the hydrogen evolution potential can be therefore not achievable by using classical plating baths. On the other hand, the hot-dip galvanizing of two alloying elements presenting a huge difference in their melting temperatures can also be extremely challenging.

1.2.1. Anticorrosive properties of Zn-based coatings

Zinc-based coatings are extensively used in the automotive industry for the sacrificial corrosion protection of steel components. However, it appears from the Table 2 that an extremely large variety of zinc alloys were developed over the last years. It has been demonstrated in the literature that each alloying element, and even small variations of the chemical composition could yield to strong changes of the anticorrosive properties of the deposits.

In the next chapters, the detailed anticorrosive properties of some of the most frequently used zinc-based alloys as well as their corrosion mechanisms will be summarized.

Zn coatings

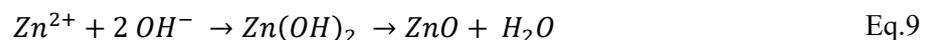
It has been previously stated that Zn coatings can be manufactured using hot-dipping or electrodeposition. In the case of electrodeposited Zn coatings, also called electrogalvanized (EG), the coating is composed of pure zinc. In the case of HDG Zn however, a small aluminium content, about 0.2 wt.%, is present in the deposits. During hot-dip galvanizing, a small amount of Al is added into the bath of molten zinc in order to enhance the adhesion of the deposit by formation of an alloy layer. Due to their corrosion potential lower than that of the substrate steel, Zn coatings offer a sacrificial protection. The corrosion resistance of pure Zn coatings has been widely investigated in the literature, but the understanding of their corrosion mechanisms and the formation of the different corrosion products can be quite challenging because of the strong influence of environmental and atmospheric conditions, explaining the necessity of simulating corrosion processes.

The behaviour of zinc during and after exposure to the neutral salt spray test as well as the corrosion mechanisms involved have been extensively reported in the literature [51-55]. The corrosion products formed were found to depend on the time of exposure and to vary under different experimental conditions. After short exposure to NaCl (sodium chloride) containing environment, zinc oxide (ZnO), zinc hydroxycarbonate (hydrozincite, HZ) and zinc hydroxychloride (simonkolleite, ZHC) are formed on the surface of the coating. These products were also reported during atmospheric corrosion [53]. When increasing the exposure time, the proportion of ZHC increases. At longer exposition times, the main corrosion products are ZnO, SZCH (sodium zinc carbonate hydrate) and HZ, while the amount of ZHC decreases. It has been also demonstrated that Zn coatings electrodeposited from alkaline baths show a lower corrosion rate compared to those obtained from acidic baths [53].

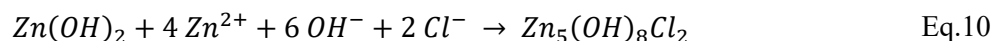
At early stages, anodic Eq.7 and cathodic Eq.8 reactions occur:



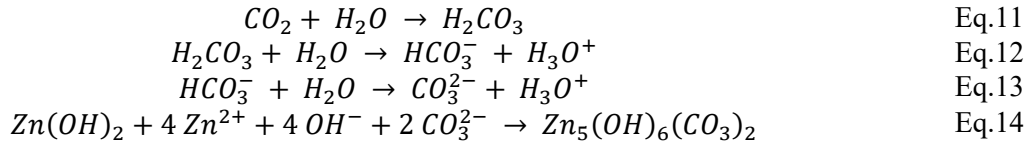
The increase of the pH leads to formation of the following corrosion products. For zinc oxide (ZnO):



for zinc hydroxychloride ($Zn_5(OH)_8Cl_2$), ZHC:



and for hydrozincite ($Zn_5(OH)_6(CO_3)_2$), HZ:



In other environments, the variety of the corrosion products leads to more complex and less studied mechanisms. A summary of the corrosion products formed on pure zinc coatings in various environments is given in Table 3.

Depending on their properties, the corrosion products can form a protective layer due to their compactness, adherence or insolubility. It was found that the protective ability of zinc corrosion products can vary significantly [8]. For instance, the formation of zinc carbonate films inhibits the permeation of O_2 and H_2O , therefore reducing the corrosion rate [8]. Suzuki [56] demonstrated that the formation of hydroxychloride enhances the compactness of the corrosion layer, and therefore increases the barrier protection of the film. It can be seen in the literature that zinc oxide ZnO is a very common corrosion product of zinc and plays an important role in the corrosion process. Its stability is pH dependent, stable only between pH 6 and 12 according to the pH-potential diagram [8].

Table 3: Overview of zinc corrosion products formed in various environments. SST: salt spray test DIN EN ISO 9227, VDA 233-102

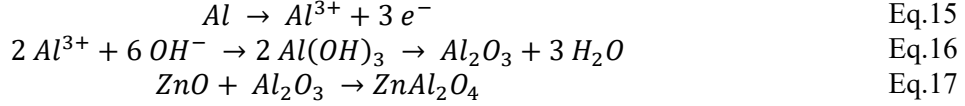
Environment	Corrosion products	Reference(s)
Marine environment	ZHC, HZ, ZHS, ZSC, ZnO	[51]
Urban environment	HZ, ZHS	[51]
Rural environment	HZ, ZHS	[51]
Industrial environment	HZ, $ZnSO_4 \cdot nH_2O$, $Zn_4SO_4(OH)_6 \cdot H_2O$, $Zn_4Cl_2(OH)_4SO_4 \cdot 5H_2O$	[8]
Seawater	ZnO, ZnCl ₂ , ZnCl ₂ ·4Zn(OH) ₂ , $Zn_4(CO_3)(OH)_6 \cdot H_2O$, ZnS	[8]
NaCl 0.1 % (SST)	ZHC, HZ, ZnO	[51]
NaCl 0.4 % (SST)	ZHC, HZ, ZnO	[51]
NaCl 1 % (SST)	ZHC, HZ, ZnO	[51]
NaCl 1 % (VDA)	ZHC, HZ, ZnO	[51]
NaCl 3.5 %	ZnO, NaCl, ZnCl ₂	[57]
NaCl 5 % (SST)	ZHC, HZ, ZnO, SZCH, ZnCO ₃ , ZnCl ₂	[51-53, 58]
Na ₂ SO ₄ 1 % (SST)	HZ, ZHS, ZnO	[51]
Rain water 0.1 % (SST)	HZ, ZHS, ZSC, ZnO	[51]
Rain water 1 % (SST)	HZ, ZHS, ZSC, ZnO	[51]
Rain water 0.1 % (VDA)	ZHC, HZ, ZHS, ZnO	[51]
Modified rain water (SST)	ZHC, HZ, ZSC, ZnO	[51]
7.21 g/L NaCl in methanol (28 days)	ZHC, HZ, ZnO, Na ₂ CO ₃ (H ₂ O), carbonates	[59]
0.1 g/L Ca(OH) ₂	ZnO	[8]
0.8 g/L Ca(OH) ₂	Ca[Zn(OH) ₃] ₂ ·2H ₂ O	[8]
0.1-1.5 M KOH	ZnO, Zn(OH) ₂	[8]

Zn-Al and Zn-Al-Mg alloy coatings

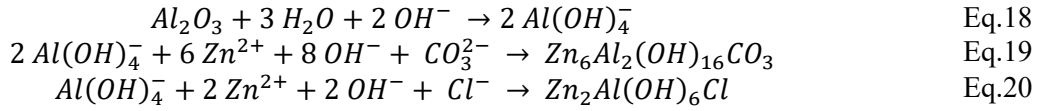
Zn-Al, also called “Galfan”, and Zn-Al-Mg alloy coatings are produced through hot-dipping. The composition of the coatings can vary depending on the manufacturers but ranges for Zn-Al coatings

around 5 wt.% Al and for the Zn-Al-Mg coatings from 2.5 up to 4 wt.% Al and from 1.5 up to 3 wt.% Mg.

According to Zhang [60], the first stage of corrosion for Zn-Al alloys starts with the simultaneous formation of zinc and aluminium oxides ZnO and Al₂O₃ and zinc aluminate ZnAl₂O₄ according to the reactions Eq.9 and Eq.16 and Eq.17, respectively.

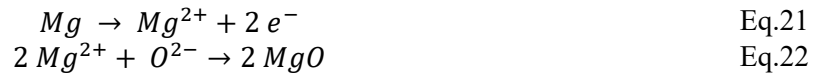


Both zinc and aluminium oxides are present at the early stages of corrosion for pure zinc and pure aluminium. When corrosion progresses, the zinc aluminate products evolve due to the instability of the aluminium oxide and lead to the formation of layered double hydroxides (LDH) as according to Eq.19 and Eq.20. The LDH products are typical corrosion products of alloyed metals and thus not found during corrosion of pure Zn or Al [60].



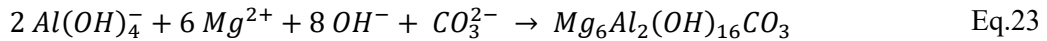
However, traditional corrosion products of pure zinc such as hydrozincite (Zn₅(CO₃)₂(OH)), simonkolleite (Zn₅(OH)₈Cl₂H₂O) and sodium carbonate (Na₂CO₃(H₂O)) were detected in the work of Prosek [59]. It appears from this study that the formation of hydrozincite is preferred to the formation of simonkolleite in Zn-Al alloys. It has also been demonstrated that the corrosion rate is drastically reduced when using Zn-Al coatings, with an almost seven-fold improvement of the mass loss compared to pure Zn coatings. This is supposed to be linked to the increased formation of simonkolleite, forming compact corrosion products and thus enhancing the barrier protection of the corrosion layer.

In order to further improve corrosion resistance of Zn-Al coatings, the addition of magnesium up to 3 wt.% as alloying element was investigated by industrials. During early stages, Zn²⁺, Al³⁺ and Mg²⁺ ions are quickly formed due to reactions Eq.7, Eq.15 and Eq.21.

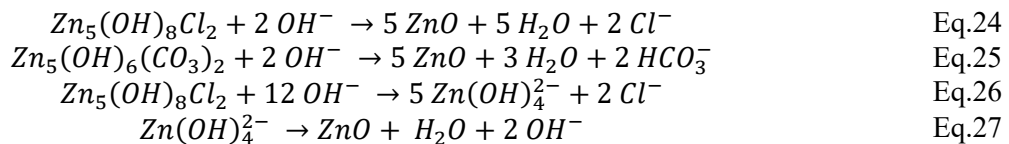


The formation of these metallic ions leads then to the formation of zinc oxide, zinc hydroxychloride, hydrozincite, aluminium oxide and magnesium hydroxide according to equations Eq.9, Eq.10, Eq.14, Eq.16 and Eq.28, respectively. However, the formation of magnesium hydroxide drastically hinders the formation of zinc corrosion products.

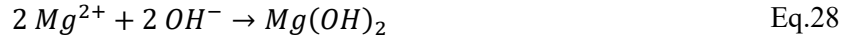
Due to the dissolution of aluminium oxide in Eq.18, LDH are formed according to reactions Eq.19, Eq.20 and Eq.23.



In a recent study, Salgueiro Azevedo et al. [51] suggested that during corrosion of Zn-Al-Mg alloys, zinc oxide was not formed directly because of the preferred formation of ZHC and LDH, but was more likely to be a product of the transformation of zinc salts with further corrosion according to Eq.24 to Eq.27 :



Because of the increased stability of magnesium hydroxide ($Mg(OH)_2$, MH) in water containing environments [61], this product is formed over MgO by the direct precipitation of the Magnesium ions Mg^{2+} according to Eq.28.



A summary of the corrosion products formed on Zn-Al-Mg coatings in various environments is given in Table 4.

Table 4: Zinc-Aluminium-Magnesium corrosion products formed in various environments. SST: salt spray test DIN EN ISO 9227, VDA 233-102

Environment	Corrosion products	Reference(s)
Marine environment	ZHC, HZ, ZHS, LDH	[51]
Urban environment	ZHS	[51]
Rural environment	ZHS	[51]
NaCl 0.1-5 % (SST)	ZHC, HZ, LDH	[51, 52]
NaCl 1 % (VDA)	ZHC, HZ, LDH	[51]
Na ₂ SO ₄ (SST)	HZ, ZHS, LDH	[51]
Rain water 0.1-1 % (SST)	ZHS	[51]
Rain water 0.1 % (VDA)	ZHC, ZHS, LDH	[51]
Modified rain water (SST)	ZHS, LDH, ZSC	[51]
NaCl (OCP, cathodic polarization exposure)	LDH	[62]
Rain water (OCP exposure)	ZHS, HZ	[62]
Rain water (cathodic polarization exposure)	HZ, LDH	[62]
7.21 g/L NaCl in methanol	HZ, Al ₂ O ₃ , Mg(OH) ₂	[59]

Zn-Fe coatings

Zn-Fe coatings, also known as galvanized (GA) coatings, consist of alloys of Zn and Fe. The Zn-Fe coatings are produced into a two-step process consisting at first of hot-dipping the steel substrate into a bath of molten zinc and in a second time heat treating the Zn-coated steel substrate, also called annealing. During this annealing step, the Zn-coated steel coils are heated up to temperatures in the 500 – 600 °C range. Due to thermal diffusion, the zinc coating alloys with the steel substrate and it results in a Zn-Fe alloy coating containing about 10 wt.% iron and composed of three intermetallic phases with various compositions:

- (i) Zeta (ζ) FeZn₁₃, containing about 5 – 6 wt.% Fe
- (ii) Delta (δ) FeZn₁₀, containing about 7 – 12 wt.% Fe
- (iii) Gamma (Γ) Fe₃Zn₁₀, containing about 16 – 28 wt.% Fe

Due to various iron contents the phases present in the layer have different corrosion potentials. Because of this difference of potential between the iron-rich and the zinc-rich phases, these alloys show the preferential dissolution of the less noble zinc-rich FeZn₁₃ phase, and cracks are formed on the surface

of the coating [63]. As a result, GA coatings are more subject to pitting corrosion due to localized corrosion than HDG or EG coatings [63].

The comparison between Zn-Fe and pure zinc coatings (both galvanized and electrogalvanized) was studied by Fujita and Mizuno [21]. They found out that Zn-Fe and electrogalvanized pure Zn coatings show similar results in perforation corrosion after exposure in accelerated corrosion tests. When compared to other Zn-based alloys like Zn-Ni or Zn-Co [55], Zn-Fe coatings show the lowest performance in weight loss in urban, marine and salt spray exposures, also confirmed by Dosdat et al. [64]. GA coatings present signs of red rust at early stages of corrosion which are expected to be due to the presence of iron through the entire thickness of the coating and do not necessarily reflect corrosion of the substrate steel. However, because such products form red rust, considered as critical in terms of visual appearance and quality, Zn-Fe coatings are not extensively used in the automotive industry although their functional properties are not affected.

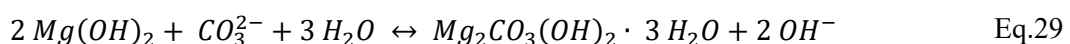
When exposed to a chloride-containing atmosphere, formation of sodium zinc chlorhydrosulfate ($\text{NaZn}_4\text{Cl}(\text{OH})_6\text{SO}_4 \cdot 6\text{H}_2\text{O}$), simonkolleite, hydrozincite and zinc oxide were observed on Zn-Fe deposits at early stages of corrosion [65]. An increase of the exposition time leads to the additional formation of calcium silicate hydroxide hydrate ($\text{Ca}_{4.5}\text{Si}_6\text{O}_{15}(\text{OH})_3 \cdot 2\text{H}_2\text{O}$), zinc sulphate hydroxide hydrate ($\text{ZnSO}_4 \cdot 3\text{Zn}(\text{OH})_2 \cdot 4\text{H}_2\text{O}$) and zinc chlorhydroxysulfate ($\text{Zn}_4\text{Cl}_2(\text{OH})_4\text{SO}_4 \cdot 5\text{H}_2\text{O}$). Corrosion resistance of painted GA-coated steels was recently investigated under long term atmospheric corrosion [66]. The samples were submitted to cyclic corrosion tests, respectively SAE J2334 for 4320 hours and GM 9540P for 3840 hours, and field exposure with intermittent spraying over three years. Compared to electrogalvanized (EG) and hot-dip galvanized coatings, the results show a small improvement for Zn-Fe coatings in the average scribe delamination after exposition to cyclic tests. A significant improvement was however observed after three years of field exposure. The oxidized area was found to be of only 3 % for GA against 22 and 21 % for EG and GI, respectively. The average scribe delamination, characterizing the amount of paint detachment from the substrate along the scribe, was also significantly reduced with 4.6 mm in the case of GA coating against 33 mm for both EG and GI coatings.

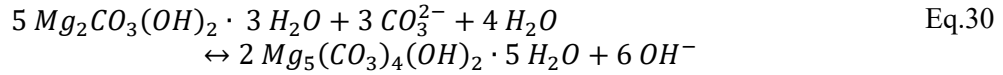
Zn-Mg coatings

Zn-Mg alloy coatings are compared to the Zn-Al-Mg coatings far less used in the automotive industry. They are mainly produced by means of hot-dip galvanizing and contain approximately 1 wt.% Mg. Other processes are available to deposit Zn-Mg alloys, influencing the structure of the alloy. They can be obtained by means of Physical Vapour Deposition (PVD), performed in a single-step [67], or in multiple steps when combined for example with classical galvanizing [68]. Electrochemical processes can also be used, as studied by Morishita et al. [69-71], who produced Zn-Mg alloys in a three-step process: electrodeposition of zinc, electrodeposition of magnesium and finally a thermal treatment to enable magnesium diffusion into zinc.

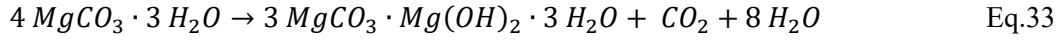
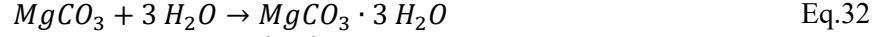
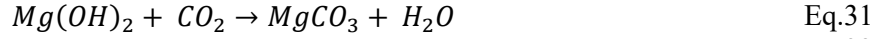
According to the literature [26], corrosion of Zn-Mg alloys is characterized by the formation of simonkolleite at early stages according to Eq.10 and MgO according to Eq.22. The presence of MgO was even detected at the initial state, before corrosion took place, therefore forming a passivation layer. Unlike zinc oxide, the formation of MgO is beneficial to the coating, as MgO is a good insulator and inhibits the corrosion process by limiting the reduction of oxygen [25].

Further corrosion products were detected under other environmental conditions. According to a study carried out by Lindström et al. [72] magnesium hydroxide is transformed into magnesium hydroxycarbonate (MHC) in presence of carbon dioxide into atmospheric environment, according to the reactions 29 and 30. Magnesium hydroxycarbonates are stable corrosion products under alkaline and neutral conditions. However, as reported by Hosking, they are able to be dissolved during wetting, in particular in acidic medium.





Another process proposed by Jönsson in a more recent study [73] is that the transformation of magnesium hydroxide into magnesium carbonate (MC) occurs in presence of carbon dioxide (Eq.31), forming nesquehonite when hydrated (Eq.32) and finally hydromagnesite (HM, Eq.33).



A summary of the corrosion products formed on the Zn-Mg and pure Mg coatings in various environments is given in Table 5.

Table 5: Zinc-Magnesium and Magnesium (*) corrosion products in various environments

Environment	Corrosion products	Reference(s)
NaCl 1 % (Volvo STD 423-0014)	ZHC, MH, MHC	[25]
Atmospheric conditions (with CO ₂)*	MHC	[72]
Atmospheric conditions (without CO ₂)*	MH, traces of MHC	[72]
Atmospheric conditions (with CO ₂)*	MC, Nesquehonite, HM	[73]

It can be concluded from the literature data that the corrosion products of magnesium are much more stable and therefore have a beneficial effect on the corrosion resistance of Zn-Mg alloys in various conditions because of the preferential corrosion of the Mg-rich phases. When submitted to a 5 % NaCl spray test, a 24-fold improvement in the time of red rust appearance was reported by Kawafuku [67] on a 20 g/m² Zn-Mg coating as compared to a 40 g/m² Zn EG. A ten-fold improvement was noticed by Morishita [69, 70] (Zn-Mg vs. Zn EG) during a 5 % salt spray test.

Comparative studies

In order to compare the different Zinc-based coatings available on the market, multiple aspects of the corrosion resistance have to be considered, such as the difference between resistance of bare and painted coatings, the difference between modes of corrosion and the testing method used.

Here, different commercial products available at steel providers were compared based on the literature. For each comparative study analysed, the ranking obtained and the corrosion test used have been noted and summarized in Table 6. For each ranking in the literature, a grade was attributed to the alloy: one point for the best alloy, two for the second one, etc. The average grade of the alloy was finally determined by taking into account all studies realized on this specific alloy, and normalized with the number of rankings, defining an “overall corrosion performance” OCP index (Eq.34). In the case of Zn-Fe and Zn-Ni coatings, the number of comparative studies available in the literature could not be high enough to obtain a representative grade.

$$\text{OCP} = \frac{\text{average grade}}{\text{number of rankings}} \quad \text{Eq.34}$$

Table 6: Summary of comparative studies on the corrosion performance of Zn-based coatings

Corrosion test	Ranking	Source
VDA 621-415	Usibor GA > Usibor GI > Z100 > Usibor AluSi	[64]
VDA 621-415	MZ100, MZ140 > MZ70 > GA90 > GI140, GI100	[74]
VDA 621-415	ZnAlMg-14 > ZnAlMg-10 > Galfan-20 > GI-20, ZnAlMg-7 > GI-10	[75]
Volvo STD423-0014	MZ > GI140 > GA90 > GI100	[74]
VDA 621-415	GA > GI, AluSi > Z100	[64]
Nissan CCT-I	Galvalume > SuperDyma > ZAM > Galfan > GI	[23]
DIN EN ISO 11997-1	Galvalume, ZAM, Galfan > SuperDyma > GI (Cr-free) Galvalume, ZAM, SuperDyma, Galfan > GI (Cr)	[23]
DIN EN ISO 11997-1	ZAM > SuperDyma > GI > Galfan > Galvalume (Cr and Cr-free)	[23]
EIS (ISO 11997-1)	SuperDyma, Galfan > ZAM > GI > Galvalume (Cr) Galfan, ZAM, GI > SuperDyma > Galvalume (Cr-free)	[23]
EIS (CCT-I)	ZAM, SuperDyma, Galvalume, GI > Galfan (Cr) ZAM > SuperDyma, GI, Galvalume > Galfan (Cr-free)	[23]
EIS (natural exposure)	ZAM, SuperDyma, Galvalume, Galfan > GI (Cr) GI > ZAM > Galfan > SuperDyma > Galvalume (Cr-free)	[23]
Field exposure (2 years)	ZM > GI	[51]
DIN EN ISO 9227	ZM > GI	[51]
OCP, EIS, Potentiodynamic polarization	ZnNi > Zn	[76]
DIN EN ISO 9227	ZM > Z	[77]
DIN EN ISO 6270-2	ZM > Z	[77]
VDA 621-415	ZM > Z	[77]
VDA 233-102	ZM > Z	[77]

Table 7: Overall corrosion performance of commercial Zn-based coatings

Alloy system	Overall corrosion performance (normalized)
Zn-Al-Mg	8.44
Zn	13.30
Zn-Al-Mg-Si	18.00
Zn-Mg	18.05
Zn-Al	22.31
Zn-Fe	32
Zn-Ni	/

The ranking obtained in Table 7 concerns only the corrosion performance and does not take into account other requirements of the automotive industry, such as the formability, the ability to be painted, welded, etc. In addition, Zn-Fe coatings for example would have to be discarded because of the early and massive formation of red rust during exposure to corrosive environments due to presence of Fe in the coating, a critical factor in the automotive industry. Another very important consideration to take into account concerns the environmental and/or health regulations. This applies in particular to Zn-Ni coatings, restricted because of health and environmental issues [9].

1.2.2. Mechanical properties

Because Zn-based coatings are available in a large range of alloys and compositions, mechanical and thermo-mechanical properties may show great variations between the different products. These changes of properties have a direct impact on the cold formability, the paintability and more generally on the global processability of the products. The aim of the present section is to provide an overview of

the mechanical properties of Zn-based coatings, as well as the experimental tests and criteria that are applied for the evaluation of the adhesion, paintability and cold formability of coated steel sheets.

In the automotive industry, metallic coatings are deposited on the steel coils prior to forming operations. During these forming operations, the coatings have to withstand the same stresses as the substrate and failure of the deposits may arise. The failure of the coatings may occur through mechanisms of delamination, peeling and flaking and may lead to exposure of the steel substrate. Delamination occurs when the coating adhesion is insufficient and it results in the deposit being locally detached from the substrate but still having its structural integrity. Peeling can be considered as a step further, with partial detachment of the coating. Flaking is considered as the total detachment of small chunks of the coating.

Different mechanisms of adhesion of the coating can be distinguished [78]:

- Interfacial adhesion
- Interdiffusion adhesion
- Intermediate layer adhesion
- Interlocking adhesion

In interfacial adhesion, the forces are dispersed around a thin interface such as in the case of electrodeposited Zn coatings. Interdiffusion adhesion can be represented with hot-dip galvanized or galvanized coatings and substrate forming an alloy layer at the substrate – coating interface with a gradient of the composition due to diffusion processes. Adhesion through intermediate layer is obtained with the use of an additional layer between the substrate and the coating. At last, interlocking is more considered as a mechanical adhesion in presence of a rough interface between the coating and the substrate.

Amongst Zn-based deposits, electrodeposited coatings show the weakest adhesive properties due to the absence of alloying phases with the substrate steel. Improvement of the adhesion strength of electrodeposited coatings is however possible by means of preparation of the substrate's surface. Ye et al. [79] obtained after mechanically polishing a steel substrate prior to electrodeposition of Zn coatings an improvement of the adhesion strength. By polishing the substrate, the surface roughness could be controlled, leading to a shift from interfacial adhesion to interlocking.

A second parameter of importance in the assessment of the cold formability is the mechanical behaviour of the deposit, and more precisely its ductility. The ductility characterizes the ability of the material to withstand deformation. A highly ductile material will be able to deform up to high strains without cracking or fracturing. The ductility depends on various parameters such as the grain size, the phase composition, preferred crystallographic orientations, coating thickness and so on [80]. In the particular case of Zn coatings, the forming behaviour is also perturbed by the removal of chunks from the deposit during forming operations, leading to some changes in the friction parameters and affecting surface appearance.

The assessment of the formability by evaluation of the cracking behaviour is a widespread method in the case of coatings. The density and propagation of the cracks are strongly dependent on the strains applied during the mechanical tests, increased strain results in higher stresses which enhance cracking phenomena. Different coatings will present different compositions, phases and microstructures, thus reacting and behaving differently under a same strain. Depending on these various behaviours, it is possible to conclude on the formability of various coatings. The grain size is probably the most influencing factor on the mechanical properties of a material. The hardness, tensile strength, yield strength are all known to increase with decreasing grain size [81]. While an increase of these properties is known to hinder the ductility of a material, the presence of specific phases or alloys can actually improve the formability and reduce cracking. For example, the grain refinement of Zn-Al alloys was proven to significantly enhance the ductility of the material [82].

The most common technique used to assess the cracking behaviour of a material is the tensile test. In the case of coated steel however, any conclusion based on the values of the applied strain is difficult to obtain due to the much greater thickness of the substrate compared to that of the coating. As a result, the mechanical properties of the substrate, in this case the stiffness, are hiding the properties of the coating,

becoming thus negligible. This is known as the general rule of mixture, traditionally used in the case of laminates [83].

The mechanical behaviour of Zn-Fe alloy coated mild steel was investigated by Panagopoulos et al. [84]. They determined the Ultimate Tensile Strength (UTS) and the ductility of the coated steel and assessed the crack density of the coatings after tensile tests at different strains. The results obtained showed a diminution of the UTS for Zn-Fe coated steel compared to Zn coated. Further investigations showed a decrease of the ductility by increase of the Fe content in the deposit [84]. Similar investigations were carried out by Song et al. [85] on hot-dip galvanized steel, where partial delamination of the coating was observed.

The ductility of hot-dip galvanized low carbon cold-rolled steel was studied by Tzimas and Papadimitriou [86] by means of 3-points bending test according to the ASTM E290-92. The identification of the types of cracks and the cracking modes were realized on cross-sections and the crack density was determined from surface and cross-sectional analyses. The crack density was determined by summation of the through-thickness transverse cracks and the through thickness confined cracks (Fig.7). These analyses permit to determine the cracking behaviour of the coating during deformation.

Any conclusion based on the values of the applied strain is however difficult to obtain. In fact, in the case of metallic coated specimens, the thickness of the substrate is much higher than that of the coating. As a result, the mechanical properties of the substrate (in this case the stiffness) are covering the properties of the coating, the latter becoming thus negligible.

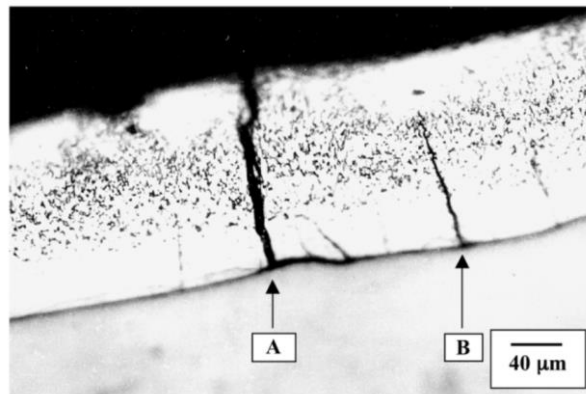


Fig.7: Different type of transverse cracks observed in a hot-dip galvanized Zn coating: (A) through-thickness and (B) confined cracks [86]

The microstructure of the deposits also plays an important role in their mechanical and forming behaviour. In the case of hot-dip galvanized deposits, deformations at low strains (lower than 5%) leads to twinning and to intergranular cracking at higher strains [80, 87]. Zn-Fe coatings, because of their brittle intermetallic phases, are particularly prone to powdering and flaking [80, 84].

1.3. Comparative review of commercial coatings for the automotive industry

When used for automotive applications, metallic coatings have to fulfil high anticorrosive properties – namely a sacrificial corrosion protection and the formation of stable corrosion products. A second essential characteristic consists in a good formability. This particular aspect requires the combination of a high ductility, a low hardness as well as good adhesive properties. Additional features such as the good adhesion and appearance of the cataphoretic paint, good welding properties and low manufacturing costs are also of great importance in such a mass-industry.

Comparative studies of Zn-based coatings have been largely performed in the literature. The corrosion behaviour was extensively investigated by means of accelerated corrosion tests like the salt spray test

or the VDA corrosion tests [23, 51, 64, 74, 75, 77]. Fewer comparative studies are available regarding the mechanical properties [88-90]. A comprehensive review of the anticorrosive, forming, welding and painting properties of Zn-based coatings was reported by Marder [80].

As stated in the previous section 1.2.1, it appears quite clearly from the literature that coatings containing aluminium and magnesium provide overall the best corrosion resistance, followed by Zn-Ni coatings. Concerning pure Zn and Zn-Fe coatings, the majority of the studies outline a better corrosion performance of Zn-Fe over pure Zn [64, 74]. However, because the onset of red rust is in the automotive a critical criteria for the aspect of the vehicle, the use of Zn-Fe coatings is not recommended. Concerning the forming properties, the microstructure of the deposits plays an important role in their mechanical behaviour. In the case of hot-dip galvanized deposits, deformations at low strains (lower than 5%) leads to twinning and to intergranular cracking at higher strains [80, 87]. Due to the presence of numerous intermetallic phases presenting a fragile behaviour, the occurrence of powdering as well as flaking is quite common [80, 84]. Very few studies were carried out on the forming properties of Al and Mg containing deposits. However technical reports and communications from the steel suppliers often states the lower forming properties of the Zn-Mg and Zn-Mg-Al alloy coatings. Additional requirements such as the costs, the weldability and the paintability of the deposits also need to be taken into account. The various key advantages and challenges of the current commercialized coatings are summarized in Table 8.

Table 8: Advantages and challenges of commercialized Zn-based alloy coatings

	Advantages	Challenges
Zn coatings	<ul style="list-style-type: none"> - Cathodic protection - Formability - Wide range of manufacturing processes 	<ul style="list-style-type: none"> - Fumes toxicity during welding - Adhesive properties
Zn-Al coatings	<ul style="list-style-type: none"> - Cathodic protection - Formability 	<ul style="list-style-type: none"> - Weldability - Paintability - Not available through electrodeposition
Zn-Al-Mg coatings	<ul style="list-style-type: none"> - Cathodic protection - Highly stable corrosion products 	<ul style="list-style-type: none"> - Formability - Weldability - Not available through electrodeposition
Zn-Fe coatings	<ul style="list-style-type: none"> - Cathodic protection - Paintability 	<ul style="list-style-type: none"> - High Fe-content - Formability - Manufacturing process in two steps
Zn-Mg coatings	<ul style="list-style-type: none"> - Cathodic protection - Highly stable corrosion products 	<ul style="list-style-type: none"> - Formability - Not available through electrodeposition

Based on this comparative overview of the commercial coatings, it appears that optimal coatings fulfilling all requirements for an application in the automotive industry are still missing. As a result, the search for a more competitive anticorrosive coating system remains a challenging task, which concerns the principal objective of this doctorate thesis.

1.4. Alternative coating systems and promising solutions

In addition to a large range of commercial alloys, the research conducted over the last years lead to the development of alternative Zn-based alloys, new coating systems and solutions in order to further improve the properties of the deposits.

The following chapters will be dedicated to the identification of alternative coating systems presenting advantageous anticorrosive and mechanical properties for an application in the automotive as a

sacrificial coating. Literature data on the deposits as well as on their manufacturing processes will be gathered in order to define a promising research track for this thesis.

1.4.1. Identification of promising coating systems

Within the scope of this thesis, alternative coating systems presenting an improvement of the anticorrosive and/or mechanical properties over the commercial products were identified. Due to the novel character of these various coating systems, numerous patent applications were submitted, as summarized in Table 9. A detailed literature research regarding these promising routes is detailed in appendix 1.

Table 9: Summary of the alternative metallic alloys, coating systems and processes identified in the framework of this work

Publication	Solution	Ref.
DE 102017002385 A1	Zn-Co-Fe alloys	[91]
DE 102017003234 A1	Zn-particles, Zn-Mn-particles, Zn-alloys-particles	[92]
DE 102017011553 A1	High Entropy Alloys (HEA)	[93]
DE 102017010175 A1	Zn-Mo, Zn-Mn-Mo alloys	[94]
DE 102017011557 A1	Zn-Mn with a decrease of the Mn content from the surface towards the substrate-coating interface	[95]
2018ID00340	Pulse electrodeposition of Zn-Mn	Submitted
2018ID02829	Zn-Mn-CeO ₂ composite	Submitted
2018ID02997	Zn-Mn-nanocontainers with active corrosion protection	Submitted

Among the various approaches suggested in Table 9, two coating systems were considered:

(i) The primary solution investigated concerns the electrodeposition of Zn-Mn, more precisely under pulse currents.

(ii) The second approach considered involves the codeposition of particles or nanoparticles into a Zn-Mn metallic matrix in order to obtain metal matrix composite (MMC) coatings reinforced by particles.

The reasons leading to the selection of these two approaches and the current state of the literature on these themes will be detailed in the following sections.

1.4.2. Properties of Zn-Mn-based coatings

Anticorrosive properties

The first motivation for the choice of Zn-Mn alloy coatings is motivated by the anticorrosive properties provided. This aspect was largely investigated in the literature and the alloying of Mn with Zn was reported to improve the corrosion protection in comparison to pure Zn deposits. In most cases, these alloys were developed and investigated for marine, automotive and aeronautic applications.

Due to the lower standard electrode potential of Mn²⁺/Mn compared to that of Zn²⁺/Zn, with -1.18 V vs. SHE (standard hydrogen electrode) and -0.76 V vs. SHE respectively, Zn-Mn alloys show in most cases an increase of the cathodic protection [96-98]. In addition, the corrosion of Zn-Mn alloys leads to the formation of particularly advantageous corrosion products. During corrosion of Zn-Mn, Mn dissolves preferentially due to its lower potential into Mn²⁺ ions, causing an increase of the pH due to the HER [99]. When Mn is totally dissolved, dissolution progresses with Zn and due to the higher pH, ZHC is directly formed [98, 99]. Similar investigations were carried out by Ortiz et al. [53] by means of salt spray test. The authors reported the formation of SZCH, HZ, ZHC and traces of ZnO and MnO at early stages of corrosion. At longer exposures, the traces of MnO disappeared and the corrosion products

observed are composed of zinc carbonates ($\text{NaZn}_3(\text{CO}_3)_4(\text{H}_2\text{O})_3$ and $\text{Zn}_5(\text{OH})_6(\text{CO}_3)_2$), ZHC and various zinc and manganese oxides (ZnO , $\alpha\text{-Mn}_{0.98}\text{O}_2$ and Mn_5O_8). The Zn-Mn coatings performed in salt spray test better than the Zn and Zn-Co alloys with the presence of red corrosion products after 432 hours of exposure compared to 429 hours for Zn-Co and 298 hours for the best Zn deposits. If the exposition times are further increased, only ZHC and carbonates are observed. Additional corrosion products – namely Mn_2O_3 – were reported by Bozzini et al. [100]. In most cases, the good corrosion behaviour of the Zn-Mn deposits was closely related to the presence of ZHC in the layer of corrosion products, thus permitting the formation of a compact layer of low dissolution rate. The high anticorrosive properties of the Zn-Mn alloys were obtained for a wide range of composition, usually reported in the 10 – 30 wt.% Mn domain [96, 99, 101-105]. It was also proven that an increase of the Mn content in the alloys was linked to higher anticorrosive properties [96].

Mechanical properties

Studies of the mechanical properties of Zn-Mn coatings are very scarce in the literature. Bozzini et al. [100] determined the microhardness of electrodeposited low manganese (below 2 %) Zn-Mn deposits and reported values of hardness values comprised between 50 and 65 Hv. Ganesan et al. [97] reported for deposits containing 17 at.% Mn hardness values of 68 Hv against 79 Hv for pure Zn deposits. It should be noted that Zn-Mn deposits obtained by means of pulse plating present an increased hardness, in comparison to deposits obtained by continuous current, caused by a reduction of the grain size [106]. The plastic behaviour of low-Mn coatings was investigated by Bozzini et al. [100] through the determination of the hardness, plasticity and wear resistance. The authors reported high plasticity parameters ($\delta_H > 99\%$) and crystallographic structures favourable to plastic behaviour. The investigation of the plastic flow curves for pure Zn and Zn-Mn coated steels showed lower flow curves in the case of Zn-Mn coated steels suggesting an easier formability as in the case of Zn coated steels [100]. Shivakurama et al. [107] conducted bending tests up to angles of 180° on 5 to 20 μm thick Zn-Mn (of unknown composition) coatings deposited on 1 mm thick steel. The observations showed no traces of peeling, cracking or flaking on the specimens, even at high bending angles. The adhesion behaviour was also qualitatively studied by Ganesan et al. [97]. No evidences of peeling and/or flaking were observed on both pure Zn and Zn-Mn deposits. These few results obtained in the literature tend to indicate that promising adherence and forming properties can be obtained with Zn-Mn coatings.

1.5. Deposition processes of Zn-Mn-based coatings

The knowledge of the main synthesis methods for the manufacturing of Zn-Mn coatings is of critical importance for the definition of the most promising solution. In the case of the automotive industry, the selection of the most stable and efficient process is relevant in order to reach high production rates and strict quality standards. In addition, numerous concerns regarding the environmental impact and the associated costs needs to be taken into account.

1.5.1. Hot-Dip Galvanizing – HDG

Hot-dip galvanizing of Zn-Mn coatings is scarcely reported in the literature. To the knowledge of the author, very few studies concerning this particular process applied to the deposition of Zn-Mn have been reported.

First investigations on the subject were reported by Diaz Ballote et al. [108], who deposited Zn-Mn coatings by addition of 1 wt.% Mn into the molten metal bath. The resulting Zn-Mn deposits were reported to have significantly better corrosion resistance than pure zinc thanks to the formation of various manganese oxides such as Zn_2MnO_4 , Mn_3O_4 and MnO at the surface during hot-dipping. Similar

experimental conditions were later investigated by Pistofidis et al. [109] with molten zinc bath containing 1 wt.% Mn. However, the deposited coatings showed a very low Mn content, according to the authors below EDS sensitivity, and the resulting structure of the deposits was not affected by the addition of Mn into the molten bath. The addition of small amounts of Mn, from 0.01 to 0.1 wt.%, into molten zinc during hot-dip galvanizing was investigated by Bakhtiari [110]. According to the author, addition of Mn into the molten bath did not impact the composition of the intermetallic Zn-Fe layers. However, it appeared that addition and increased amount of Mn improved the uniformity and the compactness of the coating. Additionally, the presence of Mn hindered the diffusion of zinc and iron thus reducing the amount of Fe and Fe-rich phases in the deposit. As a result, the coatings become more sacrificial towards steel and the corrosion current density was proved to decrease contributing to better anticorrosive properties. In a more recent study, Wang and Zeng [111] observed after hot-dipping the formation of a Mn oxide film at the surface of deposits containing up to 0.7 wt.% Mn. The authors also observed some changes in the intermetallic layers, the addition of Mn promoting the development and growth of the Fe-poor phases and hindering the growth of the Fe-rich phases. These observations, combined with the assumptions of Bakhtiari [110], seem to confirm the blocking effect of Mn against diffusion phenomenon.

Despite their interesting properties, particularly in regard to the corrosion resistance, the development of Zn-Mn coatings by hot-dip galvanizing is quite challenging and shows some challenges. At first, the amount of Mn in the deposits is very low with deposits not even reaching 1 wt.% Mn. On a second note, Zn and Mn present a huge difference in terms of melting temperatures with 419.58 °C for Zn and 1245.85 °C for Mn [112]. Considering the phase diagram of Zn and Mn, presented in Fig.8 [112], this requires low amounts of Mn into the molten bath to ensure proper homogeneity of the bath and to avoid evaporation of Zn.

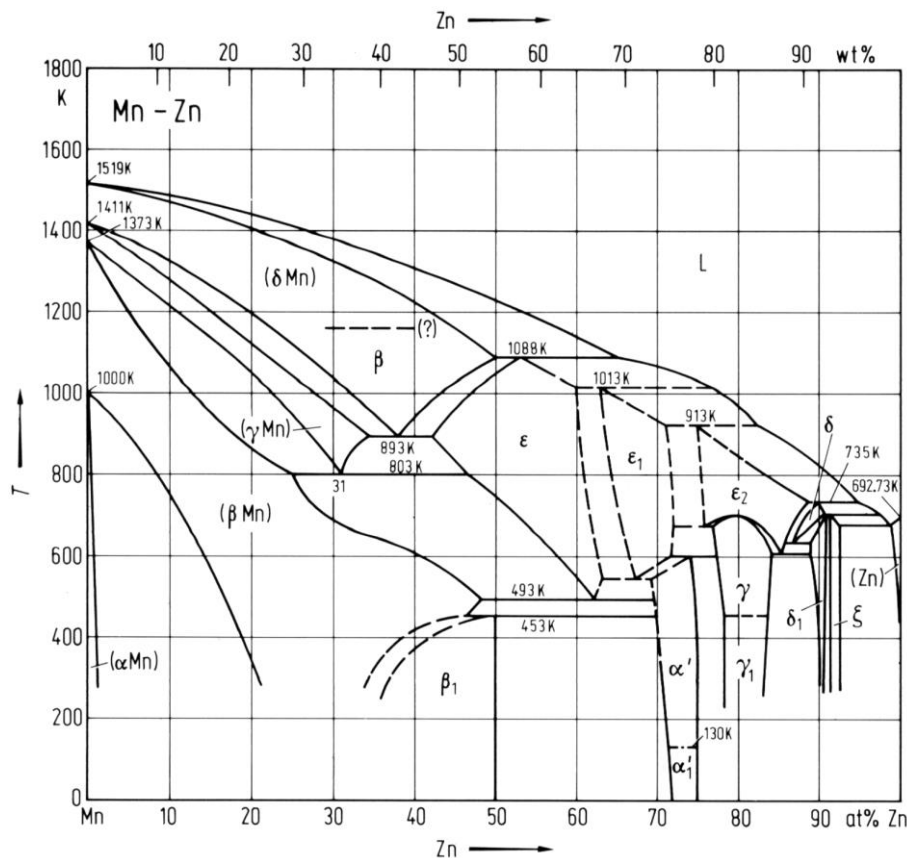


Fig.8: Mn-Zn phase diagram

1.5.2. Physical Vapor Deposition – PVD

The use of physical vapour deposition (PVD) as growth method for Zn-Mn coatings was investigated in the literature. PVD processes, and particularly electron beam evaporation and thermal jet-evaporation provide several advantages. They are perfectly suited for continuous deposition with higher material efficiency, i.e. lower amounts of waste, than electroplating or hot-dipping methods [68].

Münz et al. reported in 2004 the deposition of Zn/Mn multilayers by means of ion beam assisted deposition (IBAD) [113]. Deposits were composed of multiple layers composed of pure Zn, pure Mn or Zn-Mn alloys ranging from 25 to 75 at.% Mn. The thickness of the layers was found to be ranging from 0.5 to 8 μm . As usually reported in the case of Zn-Mn deposits, an improvement of the corrosion resistance and of the time before appearance of red rust were observed by the authors. The analysis of the corrosion products formed on the alloys revealed the formation of simonkolleite and hydrozincite, similar to the corrosion products of pure Zn coatings and known to provide good barrier properties.

As a drawback, the use of PVD techniques implies much higher costs in comparison to other deposition processes, with complex equipment. Therefore, this approach is not competitive enough for a final industrial process and was not retained in this work.

1.5.3. Electrodeposition

The electrodeposition of Zn-Mn alloys coatings is largely reported in the literature, in most cases in aqueous electrolytes. In order to understand the mechanisms of alloy electrodeposition, a few concepts have to be kept in mind. The codeposition of Zn-based alloys requires that both Zn and one or more additional metal ions have to be simultaneously dissolved in the electrolyte [114]. Another key point is the position of the elements in the electromotive force (EMF) series. Elements too far from each other's will be challenging. Lastly, the potential window is also limited by the electrochemical system of the electrolyte. Concerning the water, the limitation on the cathode is the hydrogen evolution reaction, for which the position depends of different factors such as the pH of the electrolyte, the nature and the surface state of the electrode.

In the case of Zn-Mn codeposition and considering the respective standard electrode potentials, namely -0.76 V vs. SHE for Zn and -1.18 V vs. SHE for Mn has a standard potential of -1.18 V, Zn is the nobler element and will be preferentially electrodeposited. From the literature data, the growth mechanism of Zn-Mn is considered as a normal codeposition, meaning that an increase of the applied current density will lead to an increase of the amount of Mn deposited [114, 115]. This solution is, on the downside, a promoter for the hydrogen evolution reaction (HER). The HER can be seen as the deposition of a third element at the cathode with the formation of hydrogen gas [114]. This reaction has a strong impact on the composition and the morphology of the deposited coatings. According to the literature data, HER is significant for Zn-Mn due to the low deposition potentials of Zn and Mn. In addition, further drawbacks arises due to the presence of manganese increasing the catalytic activity of the alloys and thus promoting hydrogen evolution [115]. This assumption is supported by an early study conducted by Tkalenko et al. reporting the lower overvoltage of hydrogen on Mn than Zn [116]. In addition, Mn was reported as an alloying element with Ni in order to enhance its activity for hydrogen evolution [117]. The increase of the HER with increase of the cathodic current density during the deposition of Zn-Mn coatings was also reported by Bucko et al. [115], resulting in porous deposits due to the entrapped H_2 bubbles. Similar conclusions were obtained by Ganesan et al. [97] and Close et al. [118] during potentiostatic deposition of Zn-Mn coatings. For more cathodic potentials, the deposits display mat appearance and heterogeneous surface morphology.

In order to increase the Mn content in the coatings, an increase of its ionic concentration in the electrolyte can be considered. Increase of the Mn^{2+} concentration in the plating bath was specifically investigated by Bucko et al. [115], who observed an increase of the amount of Mn in the coating. However, the intensity of the HER was also significantly increased.

The composition and the nature of the electrolyte are of significant importance during electrodeposition of Zn-Mn deposits. According to the literature data, three types of electrolytes are used to deposit Zn-Mn: the sulphate-, pyrophosphate- and chloride-based electrolytes.

- Sulphate-based plating baths are the most extensively investigated in the literature, leading in higher Mn content in the deposits [96, 119]. On the downside, the literature mention in most cases various drawbacks such as low current efficiencies [119] or poor solution stability due to the precipitation of Mn(III)-citrate complexes [120]. Furthermore, an increased heterogeneity of the deposits at high current densities was reported by Bucko et al. [115].
- The deposition from pyrophosphate electrolytes was investigated, amongst others, by Sylla et al. [101] and Bucko et al. [98]. Deposits containing up to 29 at.% of Mn were obtained by Sylla et al. [101]. They however presented a cauliflower-like morphology with nodules between 1 and 2 μm diameters. The use of additives improved the morphology of the deposits, with compact, homogeneous and semi-bright coatings but with a reduction of the Mn content from about 29 to 24 at.%.
- The deposition from chloride-based electrolytes was often reported as highly efficient, and producing compact and homogeneous deposits [121, 122]. These deposits also appeared to provide better corrosion resistance compared to the one obtained from sulphate-based or pyrophosphate-based electrolytes. The range of current densities to be used for the successful deposition of the coatings is also larger than with other baths [115].

In order to facilitate deposition and inhibit hydrogen evolution the addition of boric acid has been often suggested. Acid boric in the plating bath was reported to act as a pH buffer and to adsorb on the cathode surface, reducing the active surface for proton reduction [121, 123]. In addition, it was suggested in the case of chloride-based electrolytes that the use of boric acid, regulating the pH in a slightly acidic domain, together with the presence of chloride ions, complexing the metallic cations, could prevent the formation of hydroxides [115].

Various additives were used in the literature to facilitate Zn-Mn deposition and to improve the microstructure and the properties of the deposits: sodium gluconate [97], benzylidene acetone [53, 96], benzoic acid [96], polyethylene glycol (PEG) [53, 96, 121], 4-hydroxybenzaldehyde (4-HB) [115, 118], 3-hydroxybenzaldehyde (3-HB) [124], triton X₁₀₀ [124], ammonium thiocyanate (NH₄SCN) [118, 125], ethylenediaminetetraacetic acid (EDTA) [107], cetyl trimethyl ammonium bromide (CTAB) [107] and pyrophosphate ions [98, 101] among others. Their specific modes of action are summarized below:

- The addition of sodium gluconate was investigated by Ganesan et al. [97] on Zn and Zn-Mn coatings. The authors reported a decrease of the overvoltage for Zn deposition, an inhibitive effect for the HER and a diminution of the current when Zn preferentially deposits over Mn.
- PEG, while often used in the literature, does not seem to lead to a significant shift of potentials between Zn and Mn [121, 124]. A reduction of HER was observed by Sylla et al. [121] as well as a diminution of the Mn content.
- Inhibition of HER was observed by using benzaldehydes 4-HB and 3-HB, particularly during deposition at high current densities [115, 118, 124].
- An improvement of the amount of Mn codeposited was observed by Loukil et al. [124] by using of triton X₁₀₀ over PEG.
- The use of ammonium salts NH₄Cl, (NH₄)₂SO₄ and NH₄SCN was reported to increase the amount of Mn codeposited [118, 124, 125]. The use of NH₄SCN was also reported to provide more stable Mn phases and more compact deposits with lower roughness [118].
- Investigations conducted by Shivakurama et al. [107] demonstrated the stabilizing effect of EDTA, particularly at high current densities.
- The use of CTAB as surfactant also proved to form more uniform, bright deposits [107].

The use of additives may however lead to significant challenges such as more complex electrochemical systems and a lower stability of the electrolyte. In addition, the use of additives can lead to the

incorporation of unwanted elements in the deposits, as observed by Ortiz et al. [53] and Close et al. [118] who reported traces of sulphur due to the use of NH_4SCN .

Another interesting approach to overcome the drawbacks of Zn-Mn deposition with a limited use of additives consists in the use of pulse plating instead of continuous plating.

The pulse current (PC) electrodeposition, compared to traditional continuous current (CC) electrodeposition, consists in applying a current or potential alternating between at least two different values. Two categories of waveforms are usually defined – namely unipolar with all pulses either positive or negative and bipolar where the waveform is composed of anodic and cathodic pulses [126]. Various pulses are then available the most known being pulse current (PC), superimposed pulse current (SPC) and reversed pulse current (RPC) [126]. Traditional pulse current electrodeposition is the simplest solution available when carrying out pulse electrodeposition. The waveform is composed of cathodic pulses at a given potential or current for a specific pulse duration t_{on} (ON-time), followed by a relaxation time t_{off} (OFF-time) at zero potential or current. A schematic of the different parameters involved during PC electrodeposition is presented in Fig.9.

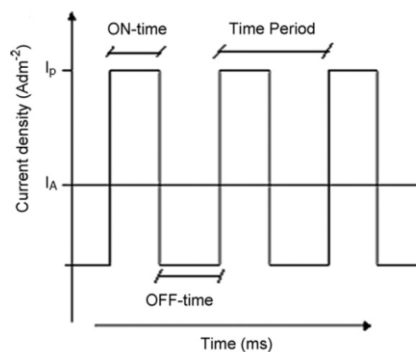


Fig.9: Typical pulse current waveform for electrodeposition [126]

In the case of pulse current, the Nernst layer permits to re-equilibrate the concentrations during the OFF-time. The Nernst diffusion layer δ_N (Fig.10), represents the distance at which the concentration of the metallic ions is considered equal to the bulk concentration [127]. This phenomenon originates from variations of the concentration of ions in the electrolyte. The regions with high current densities are ion-deficient, i.e. depletion occurs more rapidly, compared to regions with low current densities. During OFF-time, ion diffusion occurs leading to the recovery of an homogeneous concentration, with the interfacial concentration equal to the bulk one [126]. It has also been demonstrated that the Nernst diffusion layer was affected during pulse electrodeposition, pulsating together with the pulse current with the same frequency [127]. This results in a duplex Nernst diffusion model (shown in Fig.11) leading to an increased homogeneity of the current distribution and thereby to an increased homogeneity of the deposits.

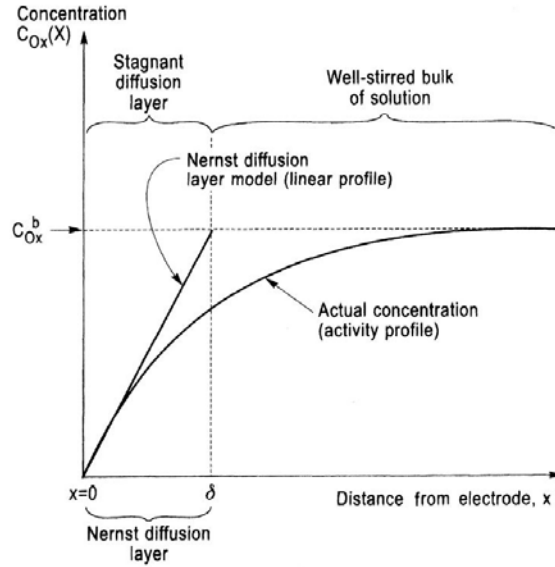


Fig.10: Variation of the concentration of the reactant in the special diffusion-limited case. c_{Ox}^b is the concentration of the bulk; $c_{Ox}(X)$ is the concentration at the surface [127]

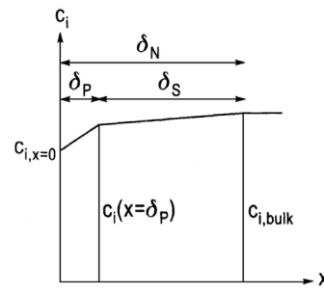


Fig.11: Schematic concentration profile at the cathode for pulse plating conditions: δ_p the thickness of the pulsating diffusion layer, δ_s the thickness of the stationary diffusion layer and δ_N the thickness of the Nernst diffusion layer [127]

While direct current galvanostatic electrodeposition permits to vary only one parameter – namely the current density – the use of pulse plating leads to a three variables system.

These three variables are the average current density j_a , the peak current density j_p and the pulse duration or ON-time t_{on} . On the basis of these three parameters, it is possible to determine the duty cycle γ (eq.35), the frequency F (eq.36) and the OFF-time t_{off} (eq.37) according to the following equations:

$$\gamma = \frac{j_a}{j_p} \quad \text{Eq.35}$$

$$F = \frac{\gamma}{t_{on}} \quad \text{Eq.36}$$

$$t_{off} = \frac{1 - t_{off} \times F}{F} \quad \text{Eq.37}$$

Pulse electrodeposition of Zn-Mn alloys was already reported in the literature [106, 128, 129]. Danilov et al. obtained Zn-Mn deposits with up to 50% Mn from citrate electrolytes [128]. The authors observed an increase of the Mn content with an increase of the current density. Investigations with pulse durations between 0.1 ms up to 1 s show an increase of the Mn content by increasing the ON-time. Studies were conducted by Müller et al. with pulse, reversed and superimposed current [106, 129]. The use of pulse plating led to an improvement of the deposit morphology and of their microstructures while the current

efficiency and the Mn content remained similar to that observed during continuous current deposition [129]. Coatings were found to be monophasic (ϵ -phase) and to have a very good appearance. Similar results were obtained by using reversed and superimposed current [106]. The use of reverse pulse plating showed a poor current efficiency resulting in an uneconomical process, while the superimposed pulse appeared to be slightly more efficient than pulse plating [106].

1.5.4. Conclusion

The different advantages and disadvantages of the three main processes available for the deposition of Zn-Mn-based coatings, namely hot-dip galvanizing, physical vapour deposition and electrodeposition were described in the previous sections.

While each deposition method present advantages as well as disadvantages, it was decided to make use of electrodeposition in the framework of this thesis, and more precisely pulse electrodeposition. The use of hot-dip galvanizing, while largely used in the industry for the production of Zn coatings, is however not suitable for the deposition of Zn-Mn alloys due the large difference of melting temperature between the two metals. While offering some advantages, the use of PVD still present some significant drawbacks with amongst others high processing costs as well as the necessity for complex equipment.

As previously described, the use of electroplating offers numerous advantages in the deposition of Zn-Mn deposits. It provides a large range of experimental parameters, such as the composition of the plating bath and the electrical parameters. More specifically, pulse electroplating enlarges the amount of tunable parameters and it permits to avoid the use of additives in the electrolyte, reducing processing costs and incorporation of unwanted elements.

1.6. Particular case of Zn-based metal matrix coatings reinforced by particles

It was stated in chapter 1.4.1 that the codeposition of particles or nanoparticles into a Zn-Mn metallic matrix was considered in the framework of this thesis for an application as sacrificial coating in the automotive industry. The deposition of metal matrix composites (MMCs) however, is significantly distinguishable from the electrodeposition of metallic alloys. In order to better understand this new system, the mechanisms involved in particle codeposition and the specific properties of such coatings, especially with Zn- and Zn-Mn-based matrices will be described in the following sections.

1.6.1. Interest of Zn-based metal matrix coatings

In numerous cases investigated in the reference literature, particle-reinforced deposits were developed as coatings for internal surfaces (rotor tips, cylinders, pistons, etc.) of engines in the automotive industry [130]. The properties for these deposits were as a result focused on a high hardness, corrosion resistance and a good lubrication. Over the last years, the development of MMC was extended to other fields such as semi-conductors, water treatment, electrodes for fuel cells, etc. However, in a vast majority of the studies carried out until this day, the anticorrosive, hardness and wear properties of the deposits were of primary interest.

The corrosion behaviour of Zn-SiC coatings was investigated by Sajjadnejad et al. [131, 132]. The authors observed similar behaviour between pure Zn and composite coatings after potentiodynamic polarization, suggesting that similar dissolution reactions are taking place in both cases [131]. The incorporation of SiC nanoparticles in the Zn matrix permitted a shift of the corrosion potential to the positive direction, resulting in a lower corrosion rate. This phenomenon is due to the inert behaviour of the particles acting as a physical barrier against initiation and progress of the corrosion defects [131-

133]. Such a behaviour was also reported for Zn-TiO₂ coatings [134-137]. The corrosion behaviour of Zn-TiO₂ and Zn-Ni-TiO₂ coatings was studied in salt spray test by Praveen and Venkatesha [135, 136]. The authors observed an improvement in the time before white rust appearance due to the incorporation of particles. As the particles are inert and are not affected by corrosion mechanisms, they build a stable and compact passive layer improving the protection of the underlying substrate and decreasing the corrosion current density [137-139]. When considering all the electrochemical studies performed on Zn-based metallic coatings with incorporated particles or nanoparticles, the trend shows a clear improvement of the corrosion properties with a positive shift of the corrosion potential and a reduction of the corrosion rate.

The microhardness of Zn-based matrices reinforced with particles was studied many times in the literature. Praveen and Venkatesha observed in the case of Zn-TiO₂ layers a higher hardness than pure Zn coatings, from 70 Hv for the pure Zn coating to 110 Hv for the Zn-TiO₂ deposits [136]. This increase of the hardness is due to grain refinement, coupled to the particles dispersed in the matrix impeding displacement of the dislocations during indentation. Similar observations and conclusions were reported by Sajjadnejad et al. on Zn-SiC coatings [131, 132] and by Malatji et al. [140] on Zn-Al₂O₃, Zn-Cr₂O₃ and Zn-SiO₂. Composite coatings provide interesting friction and wear properties compared to pure metallic coatings. Praveen and Venkatesha performed pin-on-disc experiments on Zn-TiO₂ coatings and observed an increased wear resistance of the composite coating compared to pure Zn coating [136]. Similar results were obtained by Malatji et al. on various composite coatings by means of dry abrasion [140]. This reduction of the wear loss is assumed to be due to the hindering of the movement of the dislocations by the particles and to the reduced grain size [140]. The particularly good input of the Al₂O₃ particles is supposed due to their low coefficient of friction and their self-lubricating properties [141].

In the framework of this work, three MMC coating systems based on Zn and/or Zn-Mn were considered as particularly promising and resulted in patent applications – namely Zn-Mn with Al₂O₃ nanoparticles [92], Zn-Mn with Ce-containing nanoparticles (patent submitted) and Zn-Mn with active nanocontainers (patent submitted).

However, only the first solution, namely the incorporation of Al₂O₃ nanoparticles into a Zn-Mn metallic matrix was investigated in this thesis. Further literature regarding the Ce-containing deposits and the addition of active nanocontainers can be found in appendix 1.

The use of Al₂O₃ nanoparticles offers numerous advantages over some of the other particles usually encountered in the literature. Good chemical stability, high hardness and a good resistance against wear are usually reported [142-145]. Al₂O₃ particles have been widely used in the literature and, such as most of oxide particles, improvement of the anticorrosive and surface properties were generally reported. Alumina nanoparticles however seem to provide high anticorrosive properties with a lower corrosion potential than Zn and particularly promising tribological properties with a four-fold decrease of the mass loss compared to pure Zn, as reported by Malatji et al. [140]. Another motivation for the choice of Al₂O₃ particles originates from their large availability and relative low cost. In fact, Al₂O₃ nanoparticles are amongst the cheapest according to the various manufacturers consulted.

1.6.2. Mechanisms of particle codeposition

Metal matrix composites (MMCs) are composed of a reinforcing material, composed of fibres or particles in most cases, incorporated into a metallic matrix, formed of pure metals or alloys. Because of the high amount of combination regarding the materials, a wide range of physical, electrochemical and mechanical properties can be obtained.

The codeposition mechanisms during cathodic electrodeposition of particles into metallic matrices have already been studied in the literature. Five steps could be identified [130, 146-148]:

- (i) Formation of charged particles in the bulk electrolyte. This is due to the adsorption of ions and surfactants on the surface of the particles;

(ii) Transport by convection of the charged particles towards the cathode, typical length of the convection layer < 1 mm, controlled by hydrodynamics factors such as the stirring rate and/or the geometry of the electrochemical cell;

(iii) Diffusion through the concentration boundary layer, with a typical length of hundreds of μm . Various factors such as the charge, size and concentration of the particles influence the diffusion process;

(iv) Migration driven by the potential gradient across an electrical double layer (typical length of a few nm). In this case again, the charge, size and concentration of the particles but also the HER and the current density can influence this process;

(v) Adsorption of the charged particles on the metal surface; discharging of the particles covered by adsorbed zinc ions and physical entrapment of the particles into the metallic deposit, affected by stirring rate and geometry of the system.

The five processes occurring during the codeposition of particles into metallic matrices is presented in Fig.12.

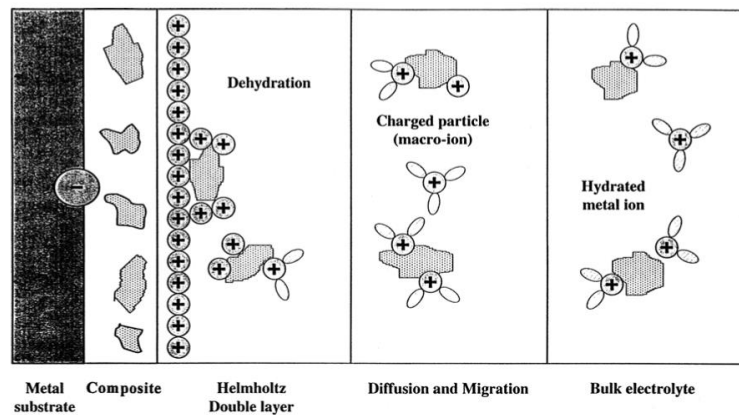


Fig.12: Processes occurring during particle codeposition into a metallic deposit [148]

As introduced previously, the codeposition of particles into metallic deposits is relying on many process parameters:

- Properties and characteristics of the particles: concentration, surface charge, type, shape, size
- Composition of the electrolyte: concentration of species, additives, temperature, pH, surfactants
- Deposition parameters: mode of deposition (direct current, pulse current, pulse reversed current), current density, pulse parameters (pulse time, duty cycle)
- Hydrodynamics: agitation type, flow regime (laminar, mixed, turbulent)
- Geometry of the electrode: rotating disc electrode, rotating cylinder electrode, tank

It was additionally demonstrated that specific texture of the metallic matrix also plays an important role in the deposition mechanism and more specifically in the physical entrapment of particles. As it can be seen on Fig.13, a pyramidal texture will favour the entrapment of the particles and therefore their incorporation [149], while other textures such as basal and prismatic do not offer the features required for the entrapment of the particles.

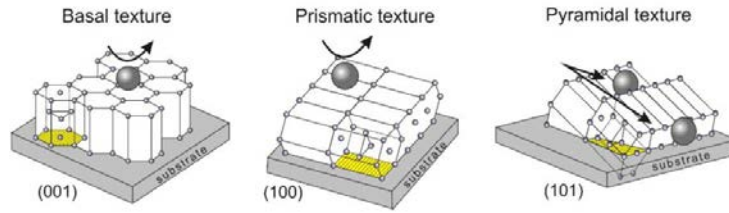


Fig.13: Schematic representation of the growth texture of zinc deposits and entrapment mechanisms of particles [149]

Various mathematical models have been developed in order to better understand the mechanism of electrodeposition with inclusions of particles. A summary of the main mathematical models describing the behaviour of metal electrodeposition with inclusions of particles is presented in appendix 2 and is based on the review of Low et al. [146]. It should be noted that these models remain incomplete and only reflect specific process parameters. There is no general rules as for other cases of electrodeposition and the systems needs to be optimized individually [150].

It should be noted that all mathematical models and mechanisms for particle codeposition have been defined, for the most, on the basis of studies performed on Ni and Cu matrices. Guglielmi's model, despite being the first one to be formulated, was extended to the case of Zn-based matrices and is still extensively reported in recent studies. The model developed by Guglielmi suggests two steps in the codeposition of particles: at first the particles come near the surface of the cathode and are adsorbed, then they lose their ionic cloud, their charge due to surfactants and ions, and become adsorbed with stronger forces [151]. The mathematical model takes into consideration various phenomena [151]:

- Electrophoresis of the particles;
- Charge transfer electrode kinetics;
- Langmuir adsorption of the particles.

However, the model does not take into consideration the phenomenon of mass transport of the particles, the nature and the size of the particles and of the ions of the growing metallic matrix [130] as well as the adhesion forces on the particles [152]. In order to better understand the mechanisms occurring on the particles at the surface of the electrode during deposition, Fransaer proposed a process ruled by force balance [153], represented in Fig.14. In this model, the adhesion force is a combination of electroosmotic, electrophoretic, hydration, friction and removal forces. The electroosmotic force originates from the overlap of the electrical double layers of the particles and electrode. The electrophoretic forces come from the applied electric field on the electrical double layers. Hydration and friction forces are defined by the hydrophobicity/hydrophilicity and by the texture and surface roughness around the particle, respectively. The removal forces finally consist in the hydrodynamics at the electrode surface.

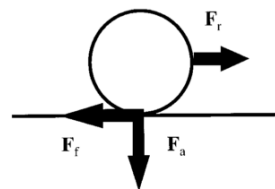


Fig.14: Force balance on a particle adsorbed on the electrode: F_r is the friction force, F_a is the adhesion force and F_r is the removal force [153]

It is important to note that the models described in this section are limited to specific coating systems (i.e. one metallic matrix and one type of particle). It is therefore quite difficult to draw some conclusions for the deposition of other composite systems. However, the general physical and electrochemical principles discussed in these models stay valid.

1.6.3. Effect of the zeta (ζ) – potential

A critical parameter for the successful codeposition of particles into a metallic matrix is the ζ -potential. For particles in suspension, the ζ -potential is the potential difference between the electrolyte and the slipping plane of the particle, which should not be mistaken with the surface charge density referring to the amount of charges on the particle per unit size of area. This slipping plane defines the interfacial layer thickness beyond which the ions present in the solution do not move with the particle (Fig.15). The region where the ions of the solution follow the particles is called the electrical double layer, composed of the Stern layer where the ions are strongly bonded to the particle and the diffusion layer where the ions are loosely bonded.

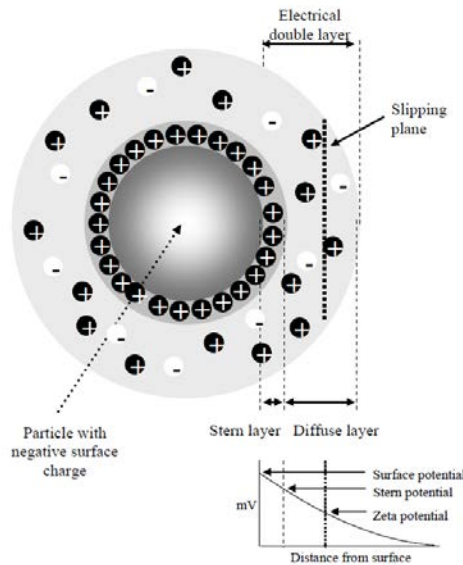


Fig.15: Schematic representation of the charge distribution around a particle in suspension [154]

The knowledge of the ζ -potential permits to evaluate the electrostatic stability of particles in suspension. In order to obtain a stable suspension, i.e. the particles well dispersed, the ζ -potential needs to be high, either positive or negative. On the opposite, the solution will be unstable for low ζ -potential and aggregation, flocculation or sedimentation can occur (Fig.16).

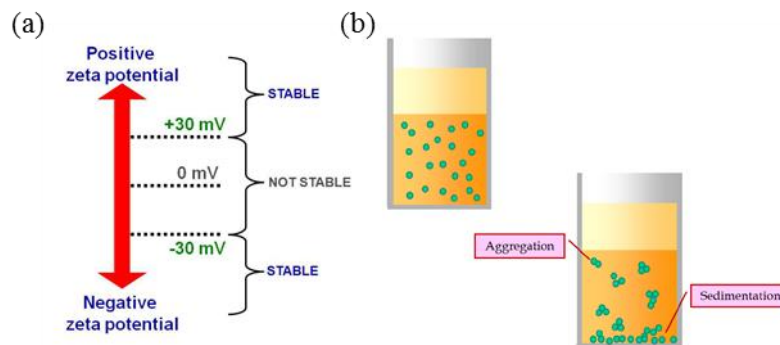


Fig.16: Relation between the ζ -potential and the stability of suspensions [155], (a) representation of the stable and unstable regions according to the value of the ζ -potential and (b) schematic of stable particles in suspension, well dispersed and unstable particles in suspension leading to aggregation and sedimentation

It is also important to note that the ζ -potential depends on the pH of the solution, as demonstrated by Azizi et al. on Zn-SiO₂ deposits [148]. A decrease of the pH leads to an increase of the ζ -potential due to adsorption of H⁺ ions on the surface of the particles [156]. As a result, it is possible to obtain in most cases an isoelectric point for a specific value of the pH where the particles demonstrate a zero charge. Therefore, the suspension is highly unstable and needs to be avoided for a successful codeposition.

1.6.4. Influence of electrolyte composition

Apart from the addition of surfactants, the chemical composition of the electrolytes used for the electrodeposition of metallic matrix composite coatings is the same as the one used during the electrodeposition of the metallic matrix in absence of particles [130]. This means that, in an ideal case, an electrolyte dedicated to a specific metallic coating can be used as it is for the synthesis of a composite coating, presenting the same specific metallic matrix, by simply adding the particles in the plating bath. Concerning the influence of particle concentration, it has already been demonstrated in the case of Ni based matrices that an increase of the particle concentration in the electrolyte leads to an increase of the amount of particles incorporated until a plateau is reached [146]. In the case of Zn-Ni matrices, a similar trend was observed. However, unlike the Ni-based coatings, an optimum concentration can be noted for Zn-based coatings followed by a decrease of the particle content if the concentration is further increased.

The addition of surfactants into the electrolyte allows to modify the ζ -potential of the particles and to prevent particle aggregation and sedimentation. In the case of metal-particle co-deposition, anionic and cationic surfactants can be used. Anionic surfactants are composed of a negatively charged functional group at their head, while cationic surfactants are composed of a positively charged group at their head. One usual anionic surfactant for the co-deposition of particles is the sodium dodecyl sulphate (SDS) [131, 156, 157]. Traditional cationic surfactants are for example cetyl trimethyl ammonium bromide (CTAB) [158-160], cetyl trimethyl ammonium chloride (CTAC), N,N-dimethyl dodecyl amine (NND) [161] or cetyl pyridinium chloride (CPC). It appears that the use of cationic surfactants is preferred in the electrodeposition of composite coatings. In this case, the cationic surfactants are adsorbed on the particle surface, which increases their positive charge. This leads to an enhanced attraction of the particles to the negative cathode [152, 162]. The concentration of surfactants should be selected carefully and be limited to an optimal concentration. Over-concentration of the surfactants leads to the appearance of “free surfactants” that are able to be absorbed and incorporated on the electrode, thereby perturbing the deposit properties by inducing internal stresses [152, 161]. At low concentrations, the amount of surfactants adsorbed on the surface of the particles is too low to permit a proper dispersion in the electrolyte.

1.6.5. Influence of particle size

The influence of the size of the particles is not fully understood yet. Tulio et al. reported an increase of the amount of deposited particles with increased particle size [163] when codepositing 3.4 nm Al₂O₃ and 9.5 nm SiC particles into a Zn-Ni matrix. The authors obtained particle contents of 4 and 7 wt.% for Al₂O₃ and SiC respectively. Similar findings were observed by Malatji et al. with 20 nm SiO₂ and 50 nm Al₂O₃ particles into a Zn matrix, favouring the bigger particles [140]. This behaviour was also observed in the investigations of Vlása et al. [164] and Zheng and An [142]. It may be concluded from these results that an increase of the particle size leads to an increase of the amount of particles in the coating. However, these comparisons have been made with different particles and could also be influenced by the type of the particles. Similar trends were observed by Tulio et al. [163] and Müller et al. [165] on Zn-Ni matrices.

1.6.6. Impact of the stirring conditions

Because of the great influence of the stirring conditions on the dispersion of the particles, this aspect was extensively studied in the literature. However, its effects still appear to be incompletely understood and rather few conclusions can be drawn from the literature. A vast majority of findings show that an increase of the stirring rate permits to obtain higher amounts of incorporated particles up to an optimum and that excessive stirring leads to lower amounts of particles in the deposits. In the latter case, it can be assumed that excessive hydrodynamic forces are able to remove the particles from the

surface of the cathode before proper entrapment [146]. Looking at the results obtained by Tulio et al. and Müller et al. [163, 165], the particle content in the deposits increases with increased stirring rate until it reaches a plateau value upon which an increase of stirring seems counterproductive. The use of ultrasonic stirring was studied by Zheng and An [142] and shows similar response to magnetic stirring.

1.6.7. Effect of the deposition mode and influence of the electrical parameters

Codeposition under direct current was in the case of Zn-based composite coatings widely reported in the literature. The study of the influence of current density on the amount of particles incorporated was largely studied [131, 132, 165, 166] and different models have been formulated in order to explain it:

- (i) A first model suggests that until the optimum current density for which the maximum of particles incorporated is reached, the codeposition is driven by charge transfer. The codeposition evolves then to mass transport beyond this point [147];
- (ii) A second possibility is to consider that the codeposition process is driven by adsorption of the particles up to this optimum current density. Further increase of the current density leads then to an increase of the deposition rate of the metallic matrix, resulting in a lower amount of particles incorporated [167];
- (iii) Fransaer et al. suggested that solvation force is controlling codeposition. The minimum of this solvation force corresponds to the highest incorporation of particles [146, 153].

Deposition under pulse current is largely reported in the literature, but the impact of the pulse parameters on the deposits are complex. A few additional mechanisms concerning the influence of the frequency have to be considered [168]:

- At low frequencies, typically lower than 10 Hz, the reduction rate of the metal matrix is much higher than the adsorption rate of ions on the surface of the particles, resulting in a lower incorporation of particles.
- At low frequencies (< 10 Hz), the duration of the ON-time when the current is applied became too long, which results in the depletion of the electrolyte near the surface of the cathode.
- At low frequencies combined with extended OFF-time, the particles adsorbed on the surface are not entrapped fast enough by the growing matrix and are able to be removed due to the hydrodynamic forces.
- At high frequencies, typically in the 100 Hz range, capacitance effects occur and ions adsorbed on the surface of the particles are only partially discharged, resulting in a virtual direct current and thus a lower amount of particles in the deposit.

The influence of the frequency was confirmed by Sajjadnejad et al. showing an increase of the amount of particles incorporated with an increase of the frequency [131, 134]. The increase of the duty cycle was proven to increase the particle content until an optimum is reached. This behaviour can be explained by the extensive OFF-time at low duty cycles. The particles reduce the concentration gradient between the electrolyte and the surface of the cathode resulting in an increased concentration of particles adsorbed on the surface during the ON-time and thus more particles in the deposit [134].

1.6.8. Conclusion

Based on the reference literature described in this chapter, it seems clear that the codeposition of inert particles inside a metallic matrix is a rather complex process influenced by numerous factors.

However, it is possible to draw some trends and conclusions from the literature in order to better define the optimal research path:

- The use of particle-reinforced deposits leads in all the cases investigated in the literature to an improvement of the anticorrosive properties in comparison to the metallic matrix alone. Similarly, an increase of the hardness as well as better friction and wear properties are generally observed, independently from the system investigated.
- The dispersion and the stabilization of the particles is of particular importance for the successful incorporation of the particles in the matrix. As a result, a preliminary study should be conducted in order to stabilize the particles prior to the deposition experiments.
- It appears that the plating bath used for the deposition MMC does not vary from the standard electrolyte used for the electrodeposition of the matrix alone [130], apart from the addition of particles and surfactants.
- Stirring the plating bath during the deposition seems to facilitate the incorporation of particles, to some extent. Indeed, excessive hydrodynamic forces were reported to remove the particles from the surface and reduce incorporation rate [146].
- Despite being a complex process, the use of pulse plating provides numerous advantages for particle codeposition. The presence of an OFF-time permits to reduce the growth rate of the metallic matrix in comparison to particle incorporation and therefore leads to higher particle contents. However, additional mechanisms need to be taken into account [168].

1.7. Aim of the study and experimental approach (EN) – But de l'étude et approche expérimentale (FR)

Aim of the study and experimental approach (EN)

The problematic of corrosion is, as demonstrated in the first section of this work, of great importance in the automotive industry due to the consequences implied by the corrosion of steel-based components. Numerous solutions and measures are implemented by the automotive manufacturers when designing modern passenger vehicles. These designing steps involve the definition of appropriate constructions and assemblies of the components, proper sealing and waxing and the use of a layering system. This layer system is, as previously stated, composed of a metallic coating providing sacrificial protection towards the steel substrate, a phosphate conversion coating and a cathodic paint. Combining these different actions, the corrosion of steel components can be considerably hindered.

In the framework of this thesis, the specific problematic of the sacrificial metallic layer is of interest. Several metallic alloys and systems are currently available on the market for steel products designed for automotive applications. Among these coating systems, the Zn-Mg and Zn-Al-Mg are reported to provide the best corrosion resistance due to the formation of stable corrosion products, however, they are known to be particularly challenging during welding operations. Zn-Fe coatings offer excellent adhesion to the substrate because of intermetallic layers built during annealing, but they are quite brittle and therefore not well-suited for forming operations. Pure zinc coatings, despite providing a slightly lower corrosion resistance compared to Zn-Al-Mg or Zn-Fe alloys, are predominantly used due to their good formability and suitability for post processes like painting and joining. It therefore appears from this state of the art that the current products have some challenges, more thoroughly summarized in Table 8.

Consequently, the aim of the present work is focused on the study and the development of alternative Zn-based coating systems for cold formed steel body parts with enhanced performance compared to the currently available coating systems.

Based on an in-depth study of the state of the art, various concepts were proposed. Two approaches are considered in this work. The first solution involves the pulse electrodeposition of Zn-Mn alloy coatings. The second approach consists in the codeposition of particles into a Zn-Mn metallic matrix. In the section 1.5 and 1.6, a comprehensive review was conducted on Zn-Mn and Zn-based MMC coatings, respectively. The anticorrosive and mechanical properties of the Zn-Mn alloys were at first reviewed, followed by an overview of the deposition processes available for the manufacturing of Zn-Mn deposits. In this second part, a particular interest was given to the electrodeposition processes. At last, the particular case of the Zn-based MMC coatings was covered.

As a result, the first axis of research covered during this work will be the study and the development of the electrodeposition of Zn-Mn alloy coatings on DC06 IF-steel plates with dimensions of 50 x 50 mm². The transfer from potentiostatic to galvanostatic continuous plating as well as the transfer from galvanostatic continuous to pulse plating will be studied. Deposits will be thoroughly characterized in order to determine their composition, morphology, crystallography and structure. Optimized deposits will be up-scaled on 200 x 200 mm² DC06 steel plates.

In a second axis, the addition of nanoparticles into the metallic Zn-Mn matrix will be considered. The development phase will be carried out on DC06 steel plates with dimensions of 50 x 50 mm². Prior to electrodeposition, the stabilization and the appropriate dispersion of the particles in the plating bath will be studied. The influence of the deposition mode, the applied electrical parameters and the hydrodynamics on the codeposition of particles will be investigated. In order to determine the incorporation rate and the distribution of the particles inside the metallic matrix, deposits will be thoroughly characterized.

The suitability of the deposits for automotive application will be assessed on the basis of their anticorrosive properties, paintability and cold formability. Electrochemical experiments and standardized continuous and cyclic corrosion tests will be conducted in order to determine the corrosion resistance and the corrosion mechanisms of the deposits. Phosphate conversion layer and cathodic paint will be applied on the as-deposited samples on the industrial lines at Sindelfingen plant which quality will be assessed by further corrosion tests. The formability of newly developed coatings will be investigated by means of tensile and bending tests. All alternative coatings will systematically be compared to the commercial deposits.

But de l'étude et approche expérimentale

Comme démontré dans la première partie de ce manuscrit, la problématique de la corrosion est d'importance capitale pour l'industrie automobile de par les potentielles conséquences liées à la corrosion de pièces en acier. De nombreuses solutions et mesures sont implémentées par les constructeurs automobiles lors de la conception de véhicules modernes. Les différentes étapes de développement impliquent la modélisation de concepts et assemblages appropriés pour l'ensemble des composants, l'utilisation de joints et de cires afin d'assurer une étanchéité entre les pièces, ainsi que l'emploi d'un système de revêtements. Ces différentes couches se composent d'un premier dépôt métallique offrant une protection sacrificielle au substrat, un revêtement de phosphate puis une peinture cataphorèse. L'utilisation combinée de ces trois mesures permet de réduire considérablement les phénomènes de corrosion.

Dans le cadre de ce travail de thèse, un intérêt particulier sera porté à la problématique du revêtement métallique sacrificiel. Divers alliages métalliques spécialement conçus pour les aciers utilisés dans l'industrie automobile sont actuellement disponibles sur le marché. Parmi ces revêtements, les alliages de Zn-Mg et Zn-Al-Mg sont reconnus pour offrir la meilleure résistance à la corrosion de par la formation de produits de corrosion particulièrement stables. Cependant, ce type de revêtements sont connus pour être particulièrement contraignant lors d'opérations de soudure. Les revêtements Zn-Fe

offrent une excellente adhésion au substrat grâce à la présence de couches intermétalliques formées durant le recuit. Ces alliages sont en revanche relativement fragiles et cassants et ne sont donc pas bien adaptés aux opérations de mise en forme. Les revêtements de Zinc pur sont, malgré des propriétés anticorrosives moins bonnes que les alliages Zn-Al-Mg ou Zn-Fe, majoritairement employés dans l'industrie grâce à leur bonne aptitude à la mise en forme et aux opérations de peinture et d'assemblage. L'état de l'art conduit sur ces alliages, précédemment résumé dans le tableau Table 9 a cependant révélé certaines limites concernant les performances de ces alliages commerciaux.

L'objectif du travail présenté ici vise à étudier et développer des revêtements alternatifs à base de Zn pour des éléments de carrosserie mis en forme à froid offrant des performances supérieures par rapport aux revêtements actuellement disponibles.

Après une étude approfondie de l'état de l'art, de nombreuses solutions ont été proposées. Deux approches sont considérées dans ce travail. La première solution implique l'électrodéposition impulsioneuse de revêtements Zn-Mn. La seconde approche envisagée consiste en la codéposition de particules dans une matrice métallique de Zn-Mn. Dans les sections 1.5 et 1.6, une revue détaillée a été conduite sur les revêtements Zn-Mn et les dépôts composites à base de Zn, respectivement. Les propriétés anticorrosives et mécaniques des alliages de Zn-Mn ont été dans un premier temps détaillées, ainsi qu'une vue d'ensemble des procédés de déposition des revêtements de Zn-Mn. Sur ce second point, un intérêt particulier a été apporté aux procédés d'électrodéposition. Pour finir, le cas particulier des alliages composites à base de Zn a été abordé.

Le premier axe de travail de cette thèse sera concentré à l'étude et au développement du procédé d'électrodéposition de revêtements de Zn-Mn, qui sera effectué sur des échantillons d'acier DC06 de dimensions 50 x 50 mm². Le transfert du mode potentiostatique vers le mode galvanostatique continu sera étudié ainsi que le transfert du mode galvanostatique continu vers le mode impulsioneuse. Les dépôts obtenus seront minutieusement caractérisés afin de déterminer leur composition, morphologie, cristallographie et structure. Le protocole d'élaboration des revêtements sera appliqué à des dépôts sur des échantillons plus importants de 100 x 200 mm².

Dans un second axe, l'incorporation de nanoparticules dans la matrice métallique Zn-Mn sera considérée sur des échantillons d'acier DC06 de dimensions 50 x 50 mm². En amont des dépôts, la stabilisation et la dispersion correcte des particules dans l'électrolyte sera étudiée. L'influence du mode de déposition, des paramètres électriques ainsi que de l'agitation sera analysée. Afin de déterminer le taux de particules incorporées dans les dépôts ainsi que leur distribution, les échantillons seront caractérisés.

L'aptitude des revêtements pour une application dans l'automobile sera évaluée sur la base de leurs propriétés anticorrosives, leur aptitude à la mise en peinture ainsi qu'à la mise en forme. Diverses mesures électrochimiques couplées à des tests de corrosion continus et cycliques standardisés seront conduits dans le but de déterminer leur résistance à la corrosion et les mécanismes de corrosion des dépôts. L'application de revêtements de phosphate et de peinture cataphorétique sur les lignes de production de l'usine de Sindelfingen sera évaluée pas d'additionnels tests de corrosion. L'aptitude à la mise en forme des nouveaux revêtements sera étudiée grâce à des tests de traction et de flexion. L'ensemble des revêtements développés lors de ce travail sera systématiquement comparé à certains produits actuellement disponibles sur le marché.

2. Materials and experimental methods

In this chapter, the experimental and characterization methods, as well as the characterization procedures used in the framework of this thesis will be defined. At last, the data regarding the commercial materials used during this work will be presented. The processes developed and used for the deposition of alternative Zn-Mn coatings will also be described.

All experimental conditions for the manufacturing and the characterization of the deposits are summarized in this section.

Les méthodes expérimentales et les différents tests de caractérisation ainsi que les protocoles associés seront définis dans ce chapitre. Les données concernant l'ensemble des matériaux commerciaux utilisés dans le cadre de ce travail seront également décrites ici. Pour finir, les divers procédés qui ont été développés et utilisés pour le dépôt des revêtements alternatifs à base de Zn-Mn seront développés. Enfin, l'intégralité des conditions expérimentales pour l'élaboration ainsi que la caractérisation des dépôts sera compilée dans cette partie.

2.1. Procedure

In order to fully characterize the commercial coatings and the newly developed deposits and determine their material, anticorrosive, painting and mechanical properties, various techniques and test methods will be conducted in this work. An overview of these characterization techniques and experimental methods is given in Table 11. The essential techniques used in the framework of this thesis will be described in the following sections.

Table 10: Overview of the characterization techniques and experimental methods used in this work for the characterization of alternative coatings

Electrochemical system	LSV	<i>Electrochemical system</i>
	Potentiostatic mode, galvanostatic mode, pulse mode	<i>Cathodic electrodeposition of Zn-Mn coatings</i>
	DLS	<i>Dispersion of the particles in the plating bath</i>
Material properties	SEM – EDS / FIB – SEM	<i>Surface properties Composition Defects (pores, cracks) Inner microstructure Thickness Crystallite size</i>
	SEM – EBSD	<i>Grain orientation Grain size distribution</i>
	XRD	<i>Crystallographic phases Crystallographic orientation Texture</i>
	Confocal microscopy	<i>Roughness</i>
	Optical microscopy	<i>Thickness</i>

Anticorrosive properties	LSV	<i>Corrosion potential</i> <i>Corrosion current</i> <i>Corrosion rate</i>
	SST / CCT	<i>Formation of red rust</i> <i>Corrosion rate</i> <i>Cathodic protection</i>
	Coulometry	<i>Cathodic protection</i> <i>Thickness</i>
Mechanical properties	Indentation test	<i>Hardness</i>
	Tensile test	<i>Cracking behaviour</i> <i>Adhesion properties</i>
	Bending test	<i>Cracking behaviour</i> <i>Adhesion properties</i>

2.2. Electrochemical setups

2.2.1. Electrolytes

In this work, Zn-Mn deposits were obtained from chloride-based electrolytes, whose composition is shown in Table 11. Chloride-based electrolytes have been widely investigated in the literature [115, 118, 123, 124]. The particular case of the electrolyte used in this work was investigated by Close et al. [118, 169]. The choice to work from chloride-based electrolytes was made on the basis of the literature studies previously discussed in chapter 1.5.3. Chloride-based plating baths are often reported as highly efficient and result in homogeneous and compact deposits [121, 122]. The $[\text{Mn}^{2+}]/[\text{Zn}^{2+}]$ ratio of 8 was optimized by Close et al. [118, 169]. The addition of H_3BO_3 was motivated by the results obtained in the literature and previously discussed in chapter 1.5.3. On the basis of these observations, it was also decided to discard the use of additives in this work.

The same composition of the electrolytic bath was chosen for the electrodeposition of Zn-Mn- Al_2O_3 coatings. The use of surfactant, although reported to be beneficial in the reference literature, was also discarded in this work in order to avoid incorporation of surfactant and pollution of the deposits.

The initial pH of the electrolytes in both cases was of approximately 4.5.

In the case of the electrolytes containing Al_2O_3 nanoparticles, a Qsonica sonicator with probe diameter of 13 mm and a frequency of 20 kHz was used to perform the ultrasonication.

Table 11: Composition of the electrolyte bath used for the deposition of Zn-Mn and Zn-Mn- Al_2O_3 coatings

Coatings	KCl	MnCl_2	ZnCl_2	H_3BO_3	Al_2O_3 particles
Zn-Mn	2.8 M	0.6 M	0.075 M	0.32 M	
Zn-Mn- Al_2O_3	2.8 M	0.6 M	0.075 M	0.32 M	1 g/L

2.2.2. Electrodeposition setups

In order to precisely control the various parameters influencing the electrodeposition process, a dedicated three-electrode deposition cell was designed for this work. The electrodeposition cell, presented in Fig.17, permits to coat substrates up to 200 x 200 mm² with control of the electrolyte temperature, electrolyte stirring and inter-electrode distance. The electrodeposition cell contains an

electrolyte volume of 7 litres. The electrodeposition was conducted using a VersaSTAT 3 potentiostat / galvanostat (Princeton Applied Research) coupled with a current booster (KEPCO). A three electrode configuration was used. An Ag/AgCl/KCl_{sat} reference electrode was used for the deposition. A pure Zn counter electrode (99.95% purity) was used as soluble anode in order to supply the plating bath with Zn²⁺ ions. The anode was systematically etched in a 6 M HCl solution for about 10 s and rinsed with deionized water prior to electrodeposition. The steel substrates (working electrode) were systematically degreased using acetone in order to remove oils and residues. Working and counter electrodes were immersed into the electrolyte parallel to each other and separated of 5 cm.

During the development phases of the investigations, steel substrates of dimension 50 x 50 mm² were used for the deposition. Substrates of area up to 100 x 200 mm² were used for the up-scaling.

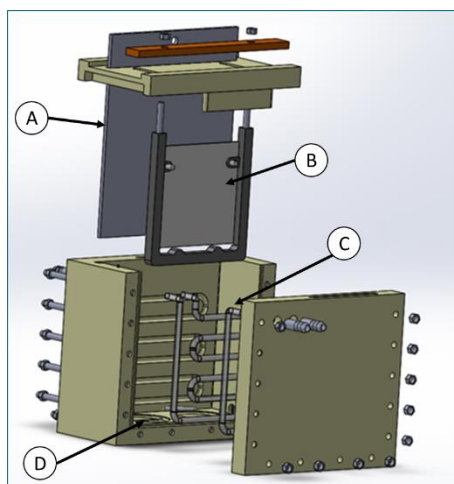


Fig.17: Schematic of the three-electrode cell (electrolyte volume of 7 litres) used in this work with, A the soluble anode (Zn, 99.95% purity), B the cathode (steel substrate), C the heating/cooling system and D the three magnetic stirrers

Changes of the temperature were reported to significantly impact the deposition of Zn-Mn coatings. An increase of the deposition temperature leads to a better appearance of the deposits but more importantly to a decrease of the Mn content [122], as also observed by Müller [119]. In order to avoid any undesired perturbations due to changes of the room temperature, a Huber Minichiller 280 thermostat was used to control the temperature during the deposition and set at 20 °C.

The impact of the stirring conditions on Zn-Mn deposits is also contrasted in the literature. Savall et al. reported an improvement of the surface appearance as well as a decrease in roughness with on the other hand a decrease of the Mn content [122]. The decrease of Mn with use of stirring was also observed by Loukil and Feki [123]. As a result, the plating baths were left unstirred during the deposition of Zn-Mn coatings. In the case of the deposition of Zn-Mn-A₂O₃ coatings however, various stirring speeds were used in order to investigate the impact of stirring conditions on the incorporation of particles.

In order to better understand the impact of the geometrical parameters of the electrodeposition cell, numerical analyses were carried out using the FEM-based software COMSOL Multiphysics. These investigations are described in appendix 3 and discussed in section 3.5.3.

An additional setup was used for the linear scan voltammetry experiments. A VersaSTAT 3 potentiostat/galvanostat in a thermostated three electrode cell. 1 cm² DC06 steel coupons were used as working electrode and oriented parallel to a pure Zn counter electrode (99.95 % purity). The counter electrode was systematically etched in a 6 M HCl solution and rinsed with deionized water prior to the experiment. An Ag/AgCl/KCl_{sat} reference electrode was used.

Hull cell experiments

The Hull cell is a technique commonly used in the literature to determine optimal deposition parameters under various conditions. Ortiz et al. used this method to define the optimal deposition current density for Zn, Zn-Co and Zn-Mn coatings [53]. The optimal bath composition and deposition parameters were similarly determined by Hedge et al. on Zn-Ni, Zn-Fe and Zn-Ni-Fe deposits [170] and by Shivakurama et al. on Zn-Mn [107].

A dedicated Hull cell, as defined in the DIN 50957 standard [171] and represented in the Fig.18, was used for the experiments. DC06 substrate steel plates, of dimensions 100 x 100 mm (active surface 50 x 100 mm) and 1.5 mm thick were used as a cathode while a pure zinc plate, of dimensions 60 x 100 mm was used as soluble anode. The experimental setup used for the electrodeposition is depicted in Fig.19. Prior to electrodeposition, the Zn anode was chemically etched in HCl 6M for 10 s, then rinsed with deionized water. The substrate steel was degreased with acetone and rinsed with deionized water.

A potentiostat/galvanostat Gamry Reference 3000 was used to apply the electrical parameters and was controlled by the Gamry Framework software. The deposition was carried out galvanostatically at current densities of 1 A. The deposition time was ruled by electric charges of 980 and 1950 Coulomb in order to obtain deposits approximately 10 and 20 μm thick, respectively.

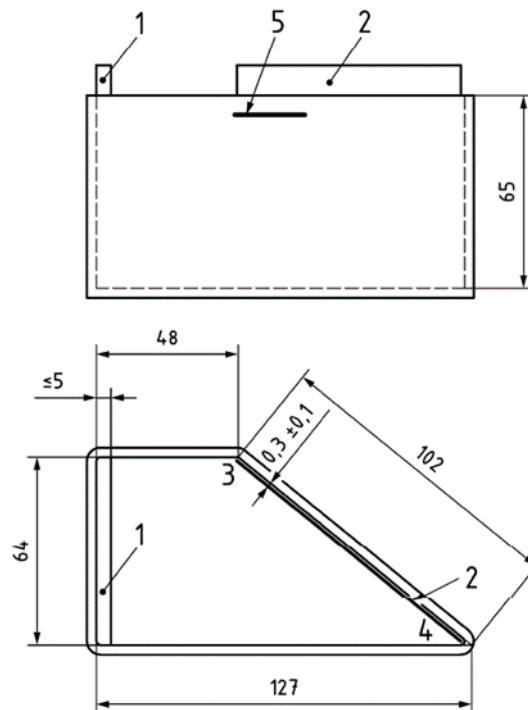


Fig.18: Schematic of the standard Hull cell with a volume of 250 mL. Dimensions in millimetres. 1: Anode, 2: cathode, 3: high current density area, 4: low current density area, 5: filling mark (44 mm) [171]

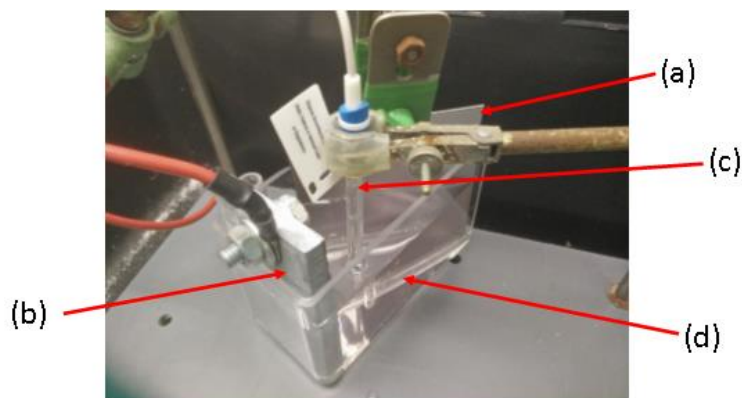


Fig.19: Experimental setup used for the electrodeposition in the Hull cell with (a) steel cathode, (b) Zn anode, (c) reference electrode and (d) standard Hull cell

2.2.3. Characterization of the plating bath

Linear Scan Voltammetry – LSV

During Linear Scan Voltammetry (LSV), the voltage is swept from an upper to a lower limit with a fixed scan rate and the resulting current response is measured. The LSV technique permit to define the electrochemical system by giving the reactions occurring in the potential range investigated [172].

In this work, linear voltammetric studies were systematically conducted prior to the deposition experiments at scan rates of 10 mV/s.

Dynamic Light Scattering – DLS

In order to synthesize MMC coatings, particles have to be dispersed and stabilized in the electrolyte. As stated in the section 1.6, numerous parameters may affect the dispersion of the particles such as the pH, the stirring rate, the presence of additives, etc. As a result, a systematic study was conducted by means of Dynamic Light Scattering (DLS) in order to measure the size of the solubilized particles. The technique relies on the measurement of the Brownian motion, stating that larger particles are slower than small particles, and defined by the translational diffusion coefficient D [173].

The size of the particles is then calculated from the Stokes-Einstein equation (eq.38):

$$d(H) = \frac{kT}{3\pi\eta D} \quad \text{Eq.38}$$

With $d(H)$ the hydrodynamic diameter, D the translational diffusion coefficient, k the Boltzmann's constant, T the absolute temperature and η the viscosity.

Because the particles are in constant and random motion, the intensity of the scattered light fluctuates over time. In order to extract size information, a correlator is used to build a correlation function from which the intensity distribution will be extracted.

However, it is required to pay a particular attention when analysing the intensity distribution from a DLS experiment, due to the crucial differences between intensity, volume and number of the particles. A representation of these differences is found in Fig.20. If it happens that two populations of particles

with 5 and 50 nm sizes are dispersed in equal number in a solution (1:1 distribution), it results in a 1:1000 volume distribution. This is due to the volume of the sphere, equal to $\frac{4}{3}\pi\left(\frac{d}{2}\right)^3$. Further transformed into an intensity distribution, this means a 1:1000000 ratio, due to the scattering intensity proportional to d^6 according to the Rayleighs approximation [173].

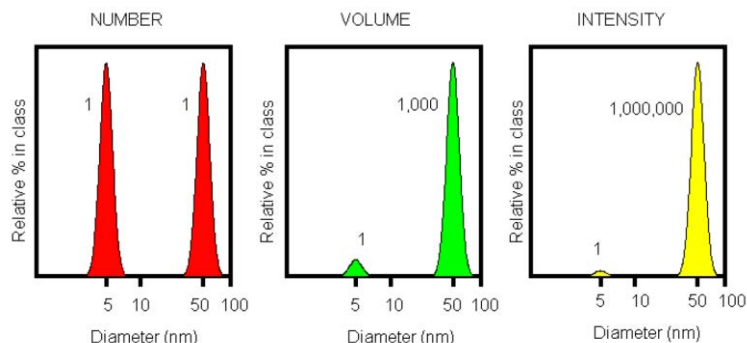


Fig.20: Number, volume and intensity distributions of a bimodal mixture of 5 and 50 nm lattices present in equal numbers, from [173]

In the framework of this thesis, DLS experiments were conducted using a DelsaMax Pro (Beckman Coulter) apparatus on electrolytes submitted to various pre-treatment.

2.3. Preparation of the samples for metallographic analyses

Depending on the characterization methods carried out on the cross-sections, various preparations of the specimens were conducted in this work.

2.3.1. Mechanical polishing

Cross-sections of the electrodeposited samples were prepared for metallographic analyses. The coated plates were cut using a Struers Discotom cut-off apparatus, embedded in EpoMet resin using a Struers CitoPress 20, polished using a Struers TegraPol-31 up to 1200 μm using SiC paper and at last polished with diamond-based suspension of 9, 3 and 1 μm with an alcohol-based solution. The prepared specimens were at last rinsed with ethanol and blow-dried.

2.3.2. Ni-coating

Due to the low adhesion of the deposits on the steel substrate, the deposition of an upper Ni layer on top of the Zn-Mn or Zn-Mn- Al_2O_3 coating was required in order to protect and ensure the integrity of the deposit during cutting and polishing. In addition, the deposition of a Ni layer was also considered on the corroded samples in order to preserve the corrosion products for cross-section analyses.

The Ni coating (about 20 μm thick) was obtained via electrodeposition in a Watts plating bath of the following composition: $\text{NiSO}_4 \cdot 7\text{H}_2\text{O} = 300 \text{ g/L}$, $\text{NiCl}_2 \cdot 6\text{H}_2\text{O} = 60 \text{ g/L}$, $\text{H}_3\text{BO}_3 = 50 \text{ g/L}$, saccharin = 0.5 g/L, coumarin 0.5 g/L and sodium lauryl sulphate (SLS) = 0.5 g/L. The deposition was carried on in a thermostated three electrode cell, at a temperature of 50 $^\circ\text{C}$. An $\text{Ag}/\text{AgCl}/\text{KCl}_{\text{sat}}$ reference electrode and a Ni counter electrode were used. A current density of -0.02 A/cm^2 was used for the deposition.

2.3.3. Focused Ion Beam – FIB

The focused ion beam technique is a nano-machining method. It consists in sputtering an ion beam on the surface of the specimen in order to mill it due to the higher size and mass of the ions. A wide range of geometries are available: the FIB technique offers a 5 nm resolution and geometrical shapes from 1 μm up to 100 – 200 μm . Tilting the specimen allow the preparation of cuts, cross-sections, polishing, etc. [174]. In most cases, the FIB column is couple to a SEM in order to conduct milling and imaging simultaneously. A second possibility offered by this technique is the deposition of a thin films. In this case, a gas of precursor molecules is sputtered on the surface of the specimen where the ion beam is focused. This allows the deposition of a protective mask for example, or the fabrication of nanostructures [174]. In this work, FIB milling was carried out on a Crossbeam FIB-SEM (Zeiss Auriga 40) equipped with a Gemini-type electronic column and an Orsay Physics Cobra ionic column. Gallium ions were used as ion source (Liquid metal ion source – LMIS) for the primary beam. Prior to milling, a thin carbon or platinum layer was deposited on the surface of the specimen in order to reduce surface roughness and defects and to try to improve the quality of the cross-sections.

2.3.4. Ion polishing

Ion polishing was used for the preparation of the samples before EBSD analyses. Due to the low adhesion of the deposits on the substrates, the as-deposited samples were, prior to cutting, coated with a protective Ni layer according to the protocol described previously.

The Ni-coated specimens were then cut using a Struers Labotom and polished with an ion beam in a Gatan PECS-II Model 685. A first two hours step was carried out at 6 kV in order to mill and polish the Ni coating followed by a ten hours step at 4 kV in order to polish the Zn-Mn deposit.

2.4. Microstructural and chemical analyses of the coatings

2.4.1. Optical microscopy

Optical microscopy analyses were carried out on cross-sections using a Leica Leitz DM RM microscope in order to determine the thickness of the deposits. Magnifications up to x 1000 were used. The thickness values further presented in this work were obtained on an average of 40 measurements, distributed on about 10 pictures over 2 cm.

2.4.2. Scanning Electron Microscopy – SEM

Surface and cross-section analyses were performed by SEM throughout this work in order to obtain a better description of the deposits.

During scanning electron microscopy, an incident electron beam (primary electrons, PE) is focused on the surface of a specimen inducing the emission of secondary electrons (SE), backscattered electrons (BSE), Auger electrons, X-rays, absorbed electrons and transmitted electrons from the surface of the sample. The recording and analysis of these emitted signals allow to gain information about the topography, the chemical composition and the crystallography of the specimens. In SEM analysis, the incident beam usually interacts with about 1 μm^3 of the specimen. The secondary electrons (Fig.21) are loosely bound on the outer shell of the atoms and are hence easily ejected from the bulk material due to kinetic energy and inelastic scattering. SE are surface sensitive and give information about the morphology and topography of the specimen [175]. The backscattered electrons (Fig.21) are originating from the incident beam, and backscatter out of the specimen due to elastic scattering with the atoms of

the specimen. BSE are also surface sensitive although less than SE but are mostly used to obtain information on the chemical composition of the materials, due to the phenomena of backscattering increasing with increasing atomic number [175].



Fig.21: Interactions between primary electrons (PE) and the atoms of specimens leading to the formation of secondary electrons (SE) and backscattered electrons (BSE) [175]

In this work, the microstructure of the as-deposited Zn-Mn deposits was investigated by means of SEM (VEGA3, Tescan) with an accelerating voltage between 20 and 30 kV. Characterization of the microstructure of the specimens after electrochemical, corrosion and mechanical experiments was conducted on a FE-SEM (MIRA3, Tescan) with an accelerating voltage of 15 kV.

2.4.3. Energy Dispersive Spectroscopy – EDS

Qualitative and quantitative analysis of the chemical composition was performed on the as-deposited samples as well as on the corroded specimen in order to investigate the composition of their corrosion products.

EDS uses the reflected X-ray beam produced by the incident ion beam during the SEM (described in the previous chapter) to obtain information on the chemical composition locally. These characteristic X-rays (Fig.22) originates from the emission of SE and the vacancy it creates [175]. The emitted X-rays are analysed and lines (K, L, M) of various energies are identified corresponding to specific elements. In theory all elements can be detected and identified, however for lighter elements (usually $Z < 10$) the use of wavelength dispersive X-ray spectroscopy (WDS) can be of interest.

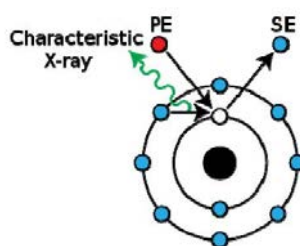


Fig.22: Emission principle of characteristic X-rays [175]

All analyses were performed with an EDS analyser (Nano, Bruker) after Phi-Rho-Z correction. The chemical composition of the as-deposited samples was determined on an average of six punctual measures performed on three different regions of the sample at magnification x 500.

2.4.4. Electron BackScatter Diffraction – EBSD

The microstructure of the coatings was analysed by the EBSD technique. This method, quasi-systematically coupled with a SEM, gives quantitative information on the microstructure of a specimen: grain size, grain orientation, texture, etc. It offers a spatial resolution of the same order of magnitude as

the SEM it is attached to, usually down to 20 nm grains. During EBSD, polished samples have to be placed with a 70° tilt angle in respect to the incident electron beam, and the detector perpendicular to the electron beam (Fig.23) [176].

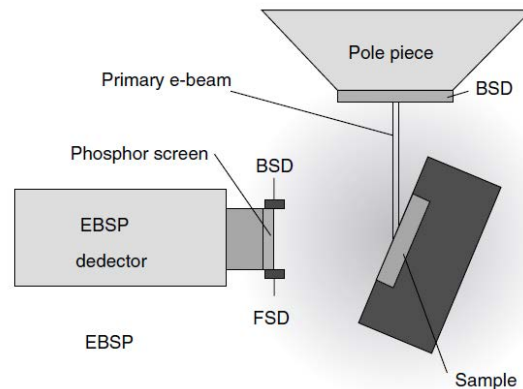


Fig.23: Schematic arrangement of the sample during EBSD [176]

The interaction between the incident electrons and the specimen results in the emission of backscattered electrons, with low energies. These backscattered electrons follow different paths depending on the crystal lattice of the specimen, and are collected on a phosphor screen (Fig.24), creating diffraction patterns also called Kikuchi patterns (Fig.24). Each band on the Kikuchi pattern corresponds to a diffracting plane of the crystal [176]. The width of these bands can then be used to determine the microstructural properties of the material.

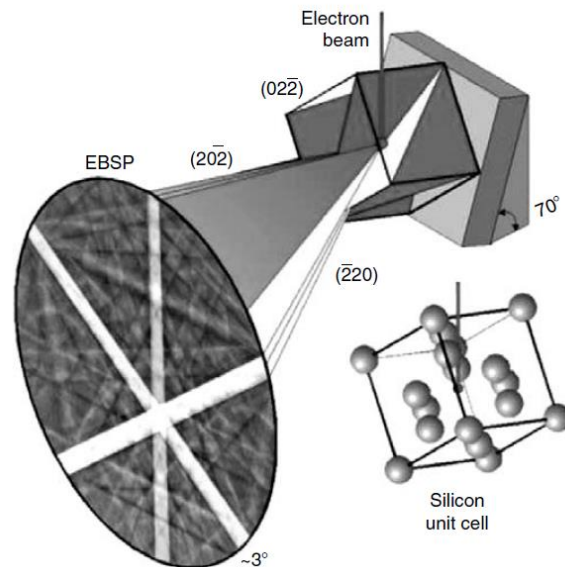


Fig.24: Interaction between the incident electrons and the specimen and resulting diffraction pattern

In this work, EBSD analyses were conducted using a Zeiss Supra 40 SEM equipped with a TKD Optimus EBSD detector (Bruker).

2.4.5. Transmission Electron Microscopy – TEM

In this work, TEM analyses were conducted on the Al_2O_3 particle powder. Prior to analysis, the particles were dispersed into isopropanol at a concentration of 2.5 wt.%/L. A drop of the solution was laid on a TEM grid and let to dry. Analyses were conducted using a Phillips CM200 at 200 kV.

Further details on the TEM technique can be found in appendix 4.

2.4.6. X-Ray Diffraction – XRD

Coatings were systematically analysed by XRD technique, in order to get information about the crystallinity of the studied samples. X-rays are electromagnetic radiations; which wavelengths are of the same order of magnitude as interatomic distances. As a result, X-rays are good candidates for the study of the crystallographic structure of the materials. During XRD, an incident X-ray beam with wavelength λ is focused on the surface of a specimen at an angle θ and scattered by the atoms of the crystal (Fig.25). In the case of Bragg-Brentano diffraction (depicted in Fig.25), incident beams with identical wavelengths are scattered from different atoms situated in planes separated by a distance d_{hkl} , leading to the Bragg's law [177]:

$$2d_{hkl} \sin \theta = n\lambda \quad \text{Eq.39}$$

In this case, the reflected beams are at an angle of 2θ vs. the incident beam.

The following configuration was used for the experiments, with the specimen fixed while the source and detector are rotating at angles of θ and $-\theta$, respectively.

The data collected by the detector are interpreted into intensity vs. angle (in degrees) and form the diffraction patterns. Diffraction peaks on the diffractogram (high intensity at a specific angle) correspond to specific diffraction planes of the specimen. The angle of diffraction and intensity of the peaks give information on the crystallographic properties of the material: phases, preferred orientation, lattice parameters, crystallite size, internal stresses, etc.

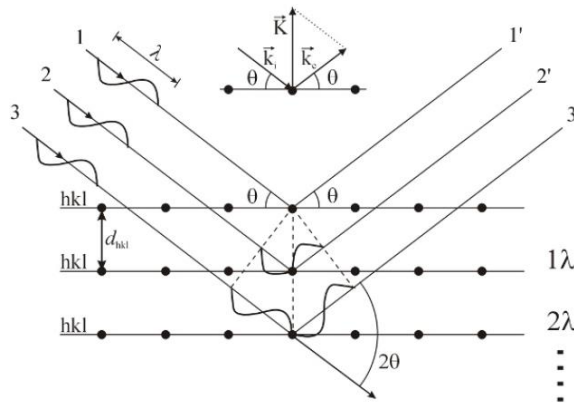


Fig.25: Principle of X-ray diffraction [177]

Crystallographic analyses of the deposits before and after corrosion tests were conducted by XRD measurements using a Bruker D8 Advance diffractometer, with Cu $K\alpha$ radiation at 40 kV and 40 mA in Bragg-Brentano mode. The analysis of the crystallographic phases was performed on the basis of the JCPDS (Joint Committee on Powder Diffraction Standards) and COD (Crystallography Open Database) databases with the EVA 4 software.

2.4.7. Confocal microscopy

The roughness of the substrates as well as of the coatings was assessed by confocal microscopy. An InfiniteFocus (Alicona) apparatus was used for the investigations with a 20x magnification. The

measurements were conducted on 712 x 540 μm² surfaces and permitted to determine the arithmetical mean roughness S_a and the roughness height S_z defined according to the DIN EN ISO 25178-2 [178] standard with the following equations 40 and 41, respectively:

$$S_a = \frac{1}{A} \iint_A |z(x, y)| dx dy \quad \text{Eq.40}$$

$$S_z = \text{sum of the maximum peak height value and the maximum pit height value within a definition area} \quad \text{Eq.41}$$

Based on these two parameters, the S_a/S_z ratio corresponding to the surface roughness homogeneity was calculated.

The use of the arithmetical mean roughness S_a alone is however not sufficient in order to define the roughness profile of the sample as schematized in Fig.26. From this schematization, the consideration of the S_a/S_z ratio makes sense. A higher ratio such as depicted in Fig.26(a) means a smooth surface of the deposit.

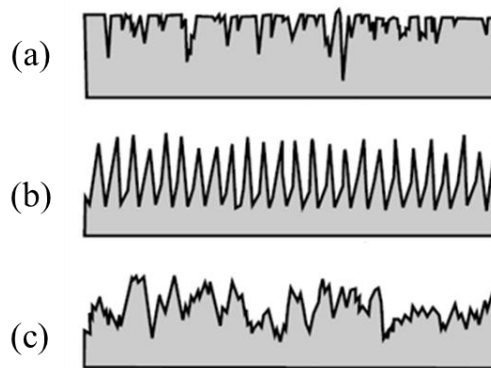


Fig.26: Schematization of various roughness profiles with the same arithmetical mean roughness S_a, the same maximal roughness S_{max} and a low S_z (a), high S_z (b) and medium S_z (c) [179]

2.5. Electrochemical and accelerated corrosion tests

2.5.1. Galvanostatic dissolution – GVA

During galvanostatic dissolution GVA (also called coulometry), a defined area of the sample is immersed into an electrolyte and a constant anodic current density is applied over a given time period in order to dissolve the metallic coating. During GVA, the metallic coating is firstly dissolved at a characteristic potential. Once the coating is dissolved, the process further progress on the substrate steel at a different potential. The potential V is recorded over time and the changes of potential give information such as coating thickness, through thickness homogeneity and galvanic protection. Indeed, from the composition of the coating, the current I and exposed surface S it is possible to transpose the recorded potential vs. time diagram into a good approximation of the potential vs. thickness, considering a 100% faradaic efficiency.

This gives for a pure Zn coating:

$$h = \frac{m_{dissolved}}{S\rho_{Zn}} \quad \text{Eq.42}$$

With h the dissolved thickness of the coating and $m_{\text{dissolved}}$ the mass of the dissolved coating determined based on Faraday's law as followed:

$$m_{\text{dissolved}} = n_{\text{dissolved}}(\text{Zn}) \times M_{\text{Zn}} \quad \text{Eq.43}$$

$$n_{\text{dissolved}}(\text{zn}) = \frac{Q}{2 \times F} = \frac{I \times t}{2 \times F} = \frac{j \times S \times t}{2 \times F} \quad \text{Eq.44}$$

With $n_{\text{dissolved}}$ the amount of dissolved coating in moles, M_{Zn} the molar mass of the coating, Q the electric charge, F the Faraday constant (96500 s.A/mol), I the current in A, j the current density in A/cm² and S the exposed surface in cm².

The above-mentioned formulas were adapted to the Zn-Mn alloys by accounting for their chemical composition, measured systematically via EDS analyses.

The following protocol and setup were used, according to standards of the automotive industry [180].

A Gamry ParaCell electrochemical cell with an active area of 1 cm² was used for the experiments in an electrolyte composed of 100 g/L ZnSO₄.H₂O and 200 g/L NaCl. A platinum counter electrode and a KCl saturated reference electrode (SCE) were used. A current density of 10 mA/cm² was applied by a Gamry Reference 3000 potentiostat/galvanostat controlled by the Gamry Instrument Framework software. The setup is presented in Fig.27.

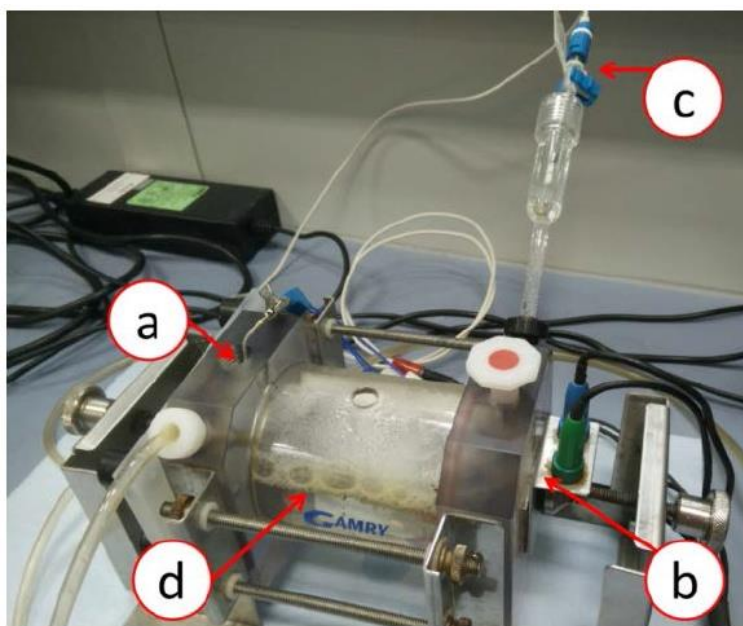


Fig.27: Setup used for galvanostatic dissolution of Zn-based coatings for steel substrates: Platinum counter electrode (a), working electrode (sample) (b), KCl saturated reference electrode (c) and bubbler (d)

2.5.2. Linear Scan Voltammetry – LSV for corrosion experiments

The corrosion behaviour of the deposits was investigated by means of linear scan voltammetry on small-scale coupons (50 x 50 mm²). Measurements were carried out in a 5 wt.% NaCl electrolyte after stabilization of the OCP after 12 hours. The exposed surface was set to 1 cm². An Ag/AgCl/KCl_{sat.} reference electrode and a Pt counter electrode were used for the experiments. The measurements were conducted using a VoltaLAB PGZ 100 apparatus. Cathodic measurements from -0.25 V vs. OCP up to the OCP and anodic measurements from the OCP up to 0 V vs. REF were conducted in two separate experiments in order to avoid during the anodic scan the local basification resulting from the cathodic scan. A scan rate of 0.2 mV/s was used during the experiment. Based on the voltammograms, the value

of the corrosion potential and current density E_{corr} and i_{corr} , respectively, were determined using the Tafel method via the EV-Lab software.

Knowing i_{corr} , the corrosion rate can be calculated using eq.45 :

$$CR = \frac{i_{\text{corr}} \times EW \times K_1}{\rho} \quad \text{Eq.45}$$

with CR the corrosion rate in mm/year, i_{corr} the corrosion current density in $\mu\text{A}/\text{cm}^2$, EW the equivalent weight of the corroding species in g, ρ the density of the corroding species in g/cm^3 , and K_1 a constant equal to $3.27 \times 10^{-3} \text{ mm.g}/\mu\text{A.cm.year}$, according to the ASTM G 102 – 89 [181].

2.5.3. Continuous Salt Spray Test – SST

The assessment of the corrosion resistance by means of the continuous salt spray test DIN EN ISO 9227 [18] is commonly used by industrials and researchers because of its low duration and running costs. Because it is continuous, the salt spray test only provides information in a fixed environment. Three different tests are defined to evaluate corrosion resistance of metallic materials:

- (i) the neutral salt spray (NSS) test,
- (ii) the acetic acid salt spray (AASS) test and
- (iii) the copper-accelerated acetic acid salt spray (CASS) test. In all three cases, the temperature and the relative humidity are held constant, while a solution is constantly sprayed on the samples: a 5 wt.% sodium chloride solution during the NSS test, a 5 wt.% sodium chloride solution with addition of glacial acetic acid during the AASS test and a 5 wt.% sodium chloride solution with addition of glacial acetic acid and copper chloride during the CASS test.

The corrosion behaviour of the coated steel plates was investigated by continuous neutral salt spray test according to the DIN EN ISO 9227 standard [18]. The specimens were cut into 85 x 200 mm coupons, cleaned and degreased using acetone. One side as well as the cut edges were protected using adhesive tape in order to prevent corrosion of bare steel areas and to provide identical exposed areas of $75 \times 175 \text{ mm}^2 \pm 2 \text{ mm}^2$. The samples were then placed in a climatic chamber with an inclination angle of 20° to the vertical (Fig.28) and exposed to a 5% NaCl solution at a temperature of $35 \pm 2^\circ\text{C}$. A one hour break was allowed on a daily basis in order to visually assess the samples. The samples were taken out of the climatic chamber on a daily basis, thoroughly rinsed using deionized water and then dried with ethanol in order to remove the largest and poorly adherent corrosion products, according to the DIN EN ISO 8407 standard [20]. The dried samples were then weighed after the test in order to obtain the mass change due to the corrosion products.

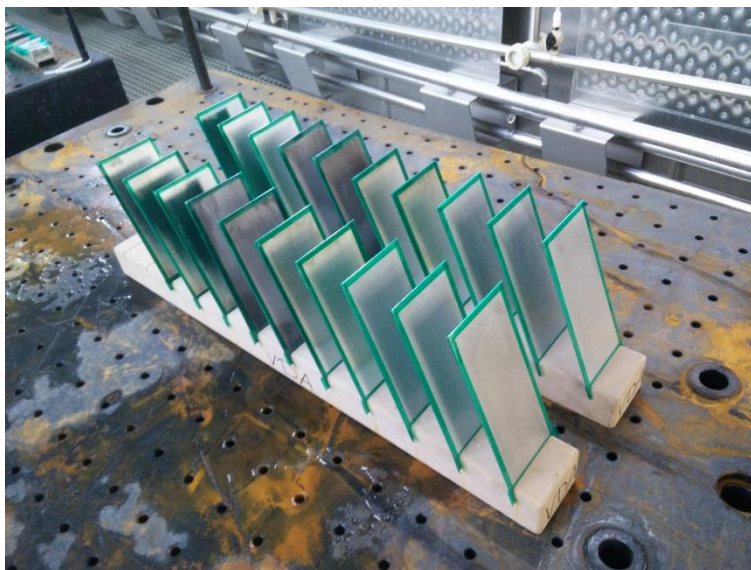


Fig.28: Disposition of the samples during accelerated corrosion tests

2.5.4. Cyclic Corrosion Test – CCT

In addition to the continuous salt spray test previously described, the corrosion resistance of the deposits was also assessed via the cyclic corrosion test VDA 233-102.

The VDA 233-102 is an accelerated corrosion test with varying climatic conditions [27]. The test method consists in six repetitions of seven 24 hours-stages cycles following the sequence B-A-C-A-B-B-A, accounting for total duration of 6 weeks. The temperature and the relative humidity vary during the whole test with during stage A, spraying of a 1 wt.% sodium chloride solution during 3 hours; during cycle B, opening of the climatic chamber during 3 hours for sample evaluation, the salt spray is interrupted during this phase; and during stage C, a phase below 0°C lasting 5 hours. This method is particularly interesting for investigations on the delamination and corrosion creep around defects on coatings, on surface and edge corrosion [27].

The corrosion behaviour of commercial as well as alternative coated steel plates was investigated by means of the VDA 233-102 [27]. Similarly to the salt spray test, the coated plates were cut into 85 x 200 mm coupons, cleaned and degreased using acetone. One side as well as the cut edges were protected using adhesive tape in order to prevent corrosion of bare steel areas and obtain reproducible exposed areas of $75 \times 175 \text{ mm}^2 \pm 2 \text{ mm}^2$. The samples were then placed in the climatic chamber with an inclination angle of 20° to the vertical (Fig.28). The samples were analysed on a weekly basis according to a similar protocol as the one described in the case of the continuous salt spray test.

2.5.5. Image analysis

The image analysis of the surface appearance was realized in order to determine the percentage of red rust formed. The software ImageJ was used. At first, a colour threshold was set to obtain a system of particles corresponding to the red rust areas on the samples according to the HSB (Hue, Saturation, Brightness) parameters of 0:37, 110:255 and 0:255, respectively. The total surface area of these particles was then determined in order to obtain the percentage of red rust, as explained in Fig.29.

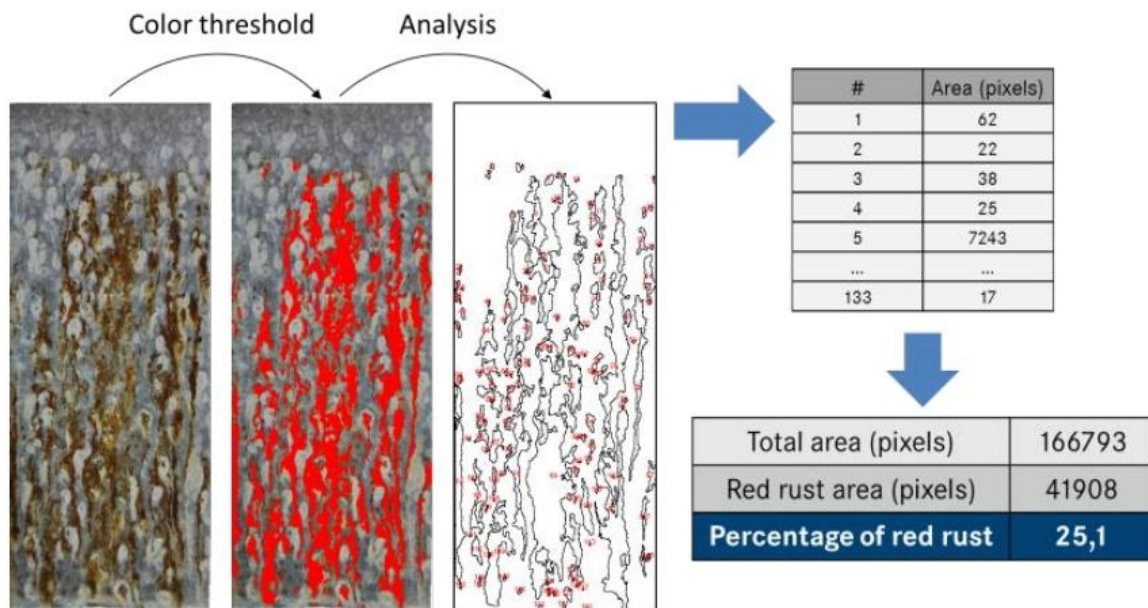


Fig.29: Methodology used for the calculation of the percentage of red rust on surfaces after corrosion test; example of a commercial electrodeposited Zn coating after 96 hours of salt spray test exposure

2.5.6. Removal of the corrosion products

The corrosion products formed on the surface of coated specimens during corrosion tests were removed using a saturated glycine solution (250 g/L) in an ultrasonic bath according to the DIN EN ISO 8407 standard [20]. The samples were immersed in the bath during 10 minutes at 25°C. They were then rinsed with deionized water, dried with ethanol and weighed in order to measure the mass loss induced by the corrosion tests.

2.6. Post-processing: phosphating and electrocoating

In order to obtain insights on the phosphatability and paintability of the developed materials, the coatings were submitted to phosphating and electrophoretic processes. Furthermore, additional corrosion tests on the phosphate and painted coatings were conducted.

2.6.1. Phosphating process

In this work, the phosphating process was conducted directly on the production lines of the Daimler AG plant in Sindelfingen. The entire process consists in ten steps that can be divided into three categories, cleaning, degreasing, and phosphating and that can be described as follow:

- **Sprayed degreasing** with aqueous solution (x2)
- **Immersion degreasing** in aqueous solution
- **Immersion cleaning** in demineralized water (x2)
- **Activation** of the surface using phosphoric and titanatic acid
- **Phosphating** in a tricationic (Zn^{2+} , Ni^{2+} and Mn^{2+}) bath

- **Sprayed cleaning** with demineralized water (x2)
- **Immersion cleaning** in demineralized water

2.6.2. Electrophoretic coating process

Directly following the phosphating process, the samples were electrocoated on the production lines of the Daimler AG plant in Sindelfingen. A thickness of the electrophoretic coating of about 20 μm was deposited at temperatures ranging between 27 and 36 °C.

2.6.3. Corrosion tests with phosphate and electrocoating

Electrocoated Zn-Mn deposits were submitted to the cyclic corrosion test VDA 233-102 for a duration of up to six weeks. Prior to corrosion experiments, the samples were prepared with a scratch, about 1 mm wide along the length of the coupons. The thickness of the scratch was enough so that the steel substrate was reached.

2.7. Mechanical tests

2.7.1. Hardness test

The use of indentation is well-known for determining the hardness of bulk materials. The principle of the indentation test is to apply a hard tip, usually diamond, on the surface of a sample with a given force (load) and to measure the resulting pattern of the tip in the material.

In order to determine the hardness of the samples, Vickers microhardness measurements were carried out using a Struers Duramin apparatus. A load of 50 g was applied during a dwell time of 10 s. The value of the microhardness was determined on the average of 10 measurements.

2.7.2. Tensile test

A widespread technique for the investigation of the forming properties of automotive steels is the tensile test. For the study of the cold forming properties, tensile tests are performed at room temperature using constant strain rates. Samples are usually mounted between two grips. The strain is determined in a defined area using an extensometer and the load applied is recorded in order to obtain the stress-strain curves. From these stress-strain curves, various mechanical properties can be determined (Fig.30) [182].

During tensile testing of ductile materials, a linear elastic deformation is first observed at low strains, until the yield point is reached. Beyond this point, the deformation becomes plastic and thus irreversible. In the plastic region, a specific strain hardening process up to the ultimate tensile point (UTS) can be observed until the maximum stress the material can withstand is reached. Further deformation beyond this point leads to the failure of the probe. The strain at which the failure occurs is then used for the assessment of the ductility of the material. The method for such tests performed at room temperature is known as the DIN EN ISO 6892-1 [182]. Microscopic analyses after tensile tests can permit to determine the crack density with different experimental conditions such as various strains or stresses. These analyses were performed by Panagopoulos and al. [84] on galvanized steel and by Song et al. [85] on hot-dip galvanized steel. The authors were able to determine the coating adhesion strength from the

average crack gap measured directly from the tensile test thanks to an in situ tensile test in a Scanning Electron Microscope (SEM).

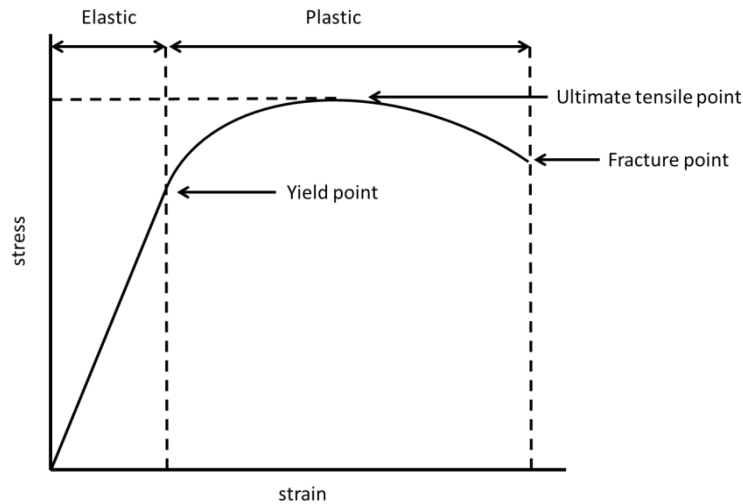


Fig.30: Typical stress-strain diagram obtained from tensile test of a ductile material

In this work, the formability of the coatings was assessed by means of traction tests, according to the standard DIN EN ISO 6892-1 [182]. Commercial coated steel plates were cut in a press to samples size of 250 x 30 mm. All samples were then milled and mounted into a Zwick/Roell Z100, controlled and programmed through the testXpert II software. The tests were carried out at constant strain rates: 0.01, 0.1 and 1 mm/s up to the failure of the samples, and at 0.1 mm/s up to 10, 20 and 30 % strain.

The analysis of the mechanical properties of the samples was performed on the basis of the stress-strain curves. Assessment of the formability through the formation of cracks was performed by means of SEM analyses on surface and cross-sections.

2.7.3. Bending test

Another possibility to assess the formability of coated steel sheets is the bending test. In the case of the study of the cold formability, the test is performed at room temperature. Typical tests are the 3- and 4-points bending tests. Further details on the procedures for the bending test are defined in the DIN EN ISO 7438 standard [183]. The ductility of hot-dip galvanized low carbon cold-rolled steel was studied by Tzimas and Papadimitriou by means of 3-points bending test [86] according to the ASTM E290-92. The identification of the types of cracks and the cracking modes were realized on cross-sections and the crack density was determined from surface and cross-sectional analyses. The crack density was determined by summation of the through-thickness transverse cracks and the through thickness confined cracks. These analyses permit to determine the cracking behaviour of the coating during deformation.

The ability of the coatings to sustain tensile and compressive stresses was assessed by means of a three-point bending test, according to the VDA 238-100 standard [184] (Fig.31). Commercial coated steel plates were cut in a press to the sample size of 60 x 60 mm and mounted into a Zwick 1464 testing device, controlled and programmed through the testXpert II software.

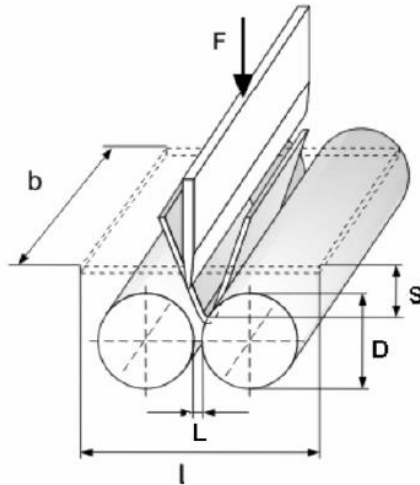


Fig.31: Schematic of the three-point bending device, according to the VDA 238-100 standard [184]. F: punch force in N; S: punch stroke in mm; D: roller diameter in mm; L: roller distance in mm; l: sample length in mm; a: thickness in mm; b: sample width in mm; r: punch radius in mm; α : bending angle in $^{\circ}$

A roller diameter of 300 mm, punch radius of 0.2 mm and roller distance of two times the sample thickness plus 0.5 mm were used. The tests were performed at constant deformation speeds of 0.01, 0.1 and 1 mm/s up to the failure of the samples. Additional tests were performed at 0.1 mm/s up to bending angles of 30, 60, 90 and 120°. Similarly to the tensile tests, analysis of the bending behaviour of the samples was performed on the basis of the stress-strain curves, and through SEM analyses of the surface and cross-sections in order to assess the formation of cracks.

2.8. Materials

2.8.1. Steel substrate

In the framework of this work, interstitial-free (IF) steels of grade DC06 were used as substrate for the electrodeposition of Zn-Mn alloy coatings. This material was selected because of its wide range of application for cold formed components. DC06 grade steel can be found for example in the superstructure (body sides, roof, front wing, outer pillars, etc.) or in linings (doors, hood, trunk) [185]. IF steels such as the DC06 are defined as cold rolled carbon steels [186], showing between 0.05 and 0.25 % of carbon. The precise chemical composition, as defined in the DIN EN ISO 10130 standard [186] and provided by the steel suppliers ArcelorMittal Automotive [185] and Voestalpine Stahl GmbH [187] are summarized in the Table 12 below.

Table 12: Chemical composition of DC06 steel according to the DIN EN ISO 10130 standard and technical data sheet from steel suppliers

max. wt. %	C	Mn	P	S	Ti	Si
DIN EN ISO 10130 [186]	0.020	0.250	0.020	0.020	0.300	/
ArcelorMittal Automotive [185]	0.010	0.250	/	/	/	0.030
Voestalpine Stahl GmbH [187]	0.020	0.250	0.020	0.020	0.300	/

Alloying elements serve a specific purpose in steels. The presence of carbon eases for example the formation of austenite, leading to an increase of the mechanical strength but a lower toughness. DC06 steels present a low amount of carbon offering the advantage of better ductility [188]. Manganese is

added to improve the ductility and to stabilize the austenitic and ferritic microstructures at low and high temperatures, respectively [188]. The presence of phosphorus in steel permits to increase the corrosion resistance and the yield strength [189]. The addition of low amounts of sulphur leads to an improved weldability and formability. However this element slightly reduces the corrosion resistance [188]. Small amounts of Ti in steel permit to form carbides and to avoid the formation of interstitial solutes in the liquid iron [190]. Silicon leads to increased corrosion resistance at low and high temperature. Besides, the incorporation of Si favours the formation of a ferritic microstructure and leads to an improved strength [188].

IF steels, due to their low amounts of carbon, present a body centered cubic (BCC) ferritic matrix, confirmed by XRD analyses (Fig.32) that revealed the presence of a single Fe-phase BCC (JCPDS n° 00-006-0696) with no preferential orientation of the planes in respect to the surface. The ferritic structure forms polyhedral grains, with well-defined darker grain boundaries that can be seen on the micrograph in Fig.33. Analyses of the grain size distribution were conducted on cross-sections and on the surface of DC06 steel. In order to calculate the grain size, the intercept method was conducted on the SEM-micrographs (Fig.33). The micrographs clearly show that the grains are stretched in one preferential direction corresponding to the vertical direction in Fig.33. This direction can be associated to the rolling direction, used for the manufacturing of the steel coils and deforming the grains [191]. On cross-sections (Fig.33b), grains size is calculated at $26.44 \pm 0.66 \mu\text{m}$ and $15.87 \pm 0.49 \mu\text{m}$ in the vertical and horizontal directions, respectively. Similarly, values of $25.39 \pm 0.69 \mu\text{m}$ and $16.61 \pm 0.65 \mu\text{m}$ were measured on the surface of the samples (Fig.33a).

SEM analysis of larger cross-sections of the substrate prepared via FIB technique is presented in Fig.34. The micrograph reveals an upper layer of the substrate, of about $2.6 \mu\text{m}$ thickness, with significantly finer grains. This observation confirms the grain refinement due to cold rolling, and may have an impact on the first stages of electrodeposition and ultimately on the adhesion of the deposited layers.

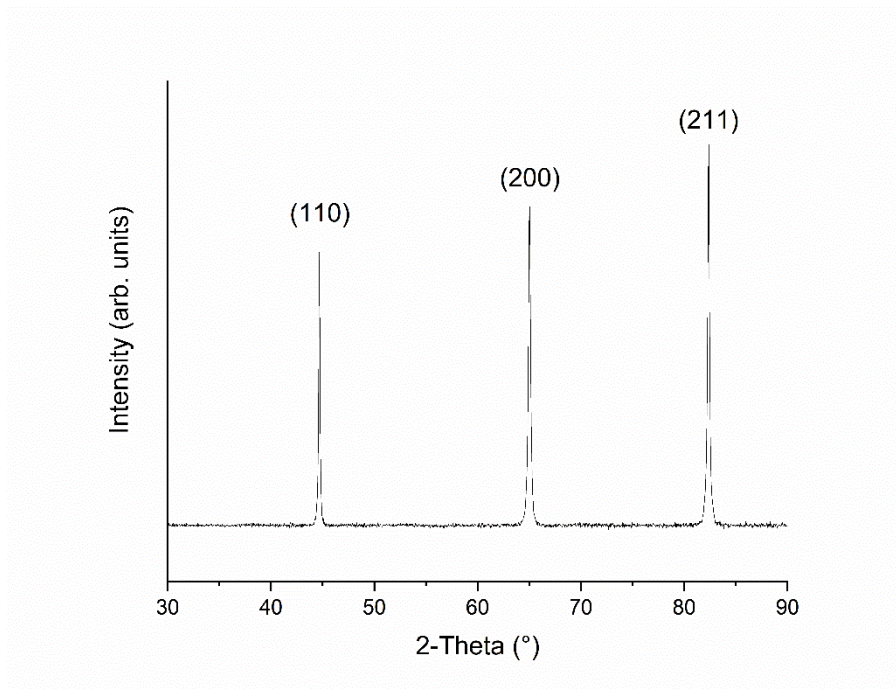


Fig.32: XRD pattern of the substrate DC06 steel (JCPDS n° 06-0696)

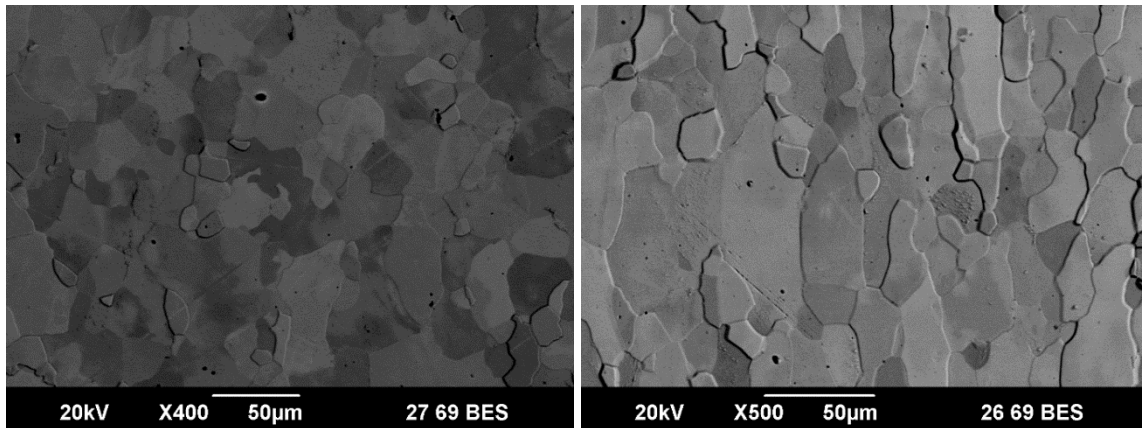


Fig.33: SEM-micrograph of the surface (a) and cross-section (b) of the DC06 substrate steel, obtained in BSE mode

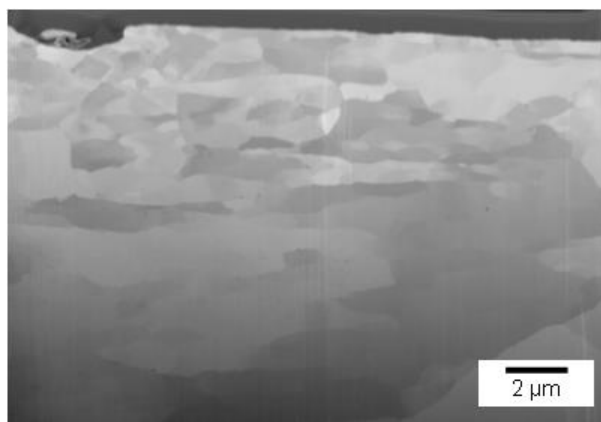


Fig.34: SEM-micrograph of the cross-section of the DC06 substrate steel, prepared via FIB

In the IPF performed on the surface of the substrate, presented in Fig.35a, the grains are clearly preferentially oriented with the (111) plane perpendicular to the surface, according to the orientation triangle in Fig.35b. This information is required to fully understand the orientation mechanism of the deposits as the texture of the substrate greatly influence the texture of the coating [114].

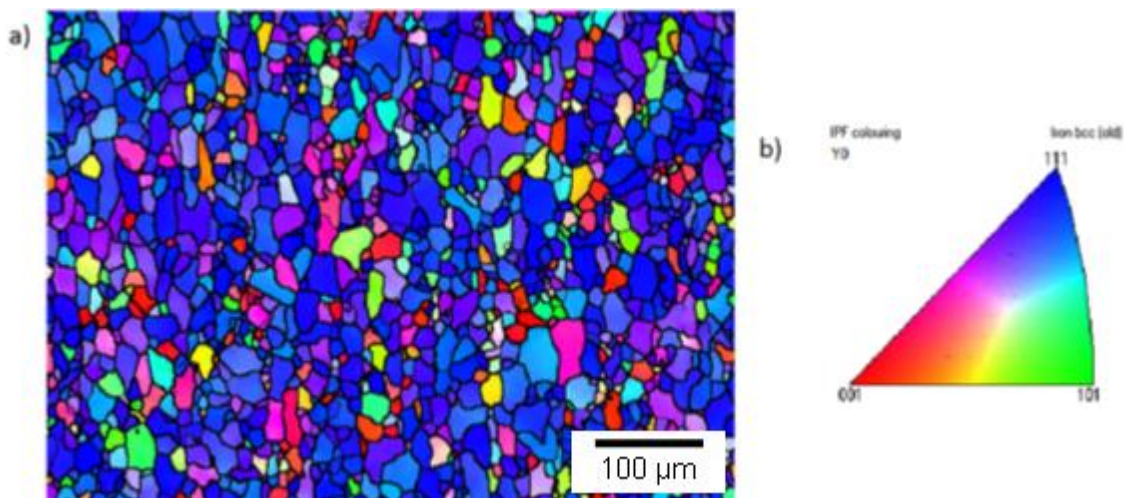


Fig.35: Electron Backscatter Diffraction (EBSD) mapping of the surface of the substrate with (a) Inverse Figure Pole (IPF) showing grain orientation of DC06 on cross-section and (b) orientation triangle corresponding to the mapping

Confocal microscopy analyses were performed on as-delivered DC06 steel in order to define the surface topography of the substrate. A mean surface roughness value S_a of 685.4 ± 15.5 nm was measured on a

surface of $712 \times 540 \mu\text{m}^2$. The measure was repeated on five areas and revealed a homogeneous average roughness.

DC06 steels provide a low yield strength, comprised between 120 and 180 MPa [185, 187] and a high ductility with an elongation at fracture above 40 % strain [185, 187]. A summary of the mechanical properties of DC06 steel are given in the Table 13 below. As it can be seen, DC06 steel offers a relatively high plastic strain ratio. This plastic strain ratio characterizes the ability of a material to limit thinning when submitted to tensile forces, indicating therefore its capacities for drawing. The higher the plastic strain ratio of a material is, the higher its drawing capacities are. Another characteristic of the formability is given by the strain hardening exponent. The strain hardening exponent qualifies the response of the material during plastic deformation and is measured as the slope of the stress-strain curve between the yield and ultimate tensile strengths. A low strain hardening exponent like for DC06 steel means that the material is able to achieve high strains at low strength, facilitating the drawability.

Table 13: Mechanical properties of DC06 steel, as specified in the DIN EN ISO 10130 standard [186]

Yield strength (MPa)	Ultimate Tensile Strength (MPa)	Elongation at fracture (min.%)	Plastic strain ratio, r (min)	Strain hardening exponent, n (min)
170	270 – 330	41	2.1	0.220

2.8.2. Commercial coatings

Various commercial coated steel products were used in this work:

- hot-dip galvanized Z 100 deposited on DX56 D steel,
- galvanized ZF 100 deposited on DX56 D steel,
- electrogalvanized ZE 75/75 deposited on DC06 B steel and
- hot-dip galvanized ZM 90 deposited on S220 GD steel.

All products were supplied from the steel manufacturer Voestalpine GmbH and were used as reference materials for the determination of the anticorrosive properties, phosphatability, paintability and cold forming properties. The properties and the composition of these products are listed in Table 14 and Table 15, respectively and are based on data from supplier.

Table 14: Properties of the coatings and substrate steels. Data provided by Voestalpine GmbH

Substrate	Coating	Coating properties		Substrate properties		
		Weight on both sides (g/m ²)	Coating thickness (μm)	0.2% Yield point (MPa)	Tensile strength (MPa)	Fracture elongation (%)
DX56 D	Z 100	100	7	120-180	260-350	39
	ZF 100	100	7			
DC06 B	ZE 75/75	54	7.5	130-180	270-350	41
S220 GD	ZM 90	90	6.5	220	300	20

Table 15: Composition of the substrate steels. Data provided by Voestalpine GmbH

Substrate	Substrate composition						
	C (wt.%)	Si (wt.%)	Mn (wt.%)	P (wt.%)	S (wt.%)	Ti (wt.%)	Al (wt.%)
DX56 D	0.12	0.5	0.6	0.1	0.045	0.3	/
DC06 B	0.02	/	0.25	0.02	0.02	0.3	/
S220 GD	0.2	0.6	1.7	0.1	0.045	/	/

Delivered materials were thoroughly characterized. The thickness of the coatings was measured on cross-sections by optical microscopy and confirmed by coulometry (Fig.36), the results obtained are summarized in Table 16. The results obtained either by coulometry or by optical microscopy on cross-sections are in good agreement with the data provided by the supplier. All coatings present similar thicknesses, approximately 7.5 μm according to the coulometric analysis (Table 16). The potential vs. thickness curves presented in Fig.36 reveal differences in the corrosion potential between the coatings. ZE 75/75, ZF 100 and ZM 90 coatings contain larger amounts of Zn and therefore present a lower potential than ZF 100 which contains 10 wt.% of iron. In addition, it is possible to distinguish on this diagram the presence of various phases in the coatings, presenting various corrosion potentials. In the case of ZE 75/75 and ZM 90 only one phase is visible. For the Z 100 coating, a very thin plateau about 0.1 – 0.2 μm thick is noticeable at potential of -0.8 V. This thin layer is a supposed diffusion layer formed between Zn and the steel substrate during the hot-dipping process. On ZF 100 coated samples, the presence of multiple intermetallic phases is observed (Fig.36) with 4 successive plateau between -0.85 V and -0.74 V.

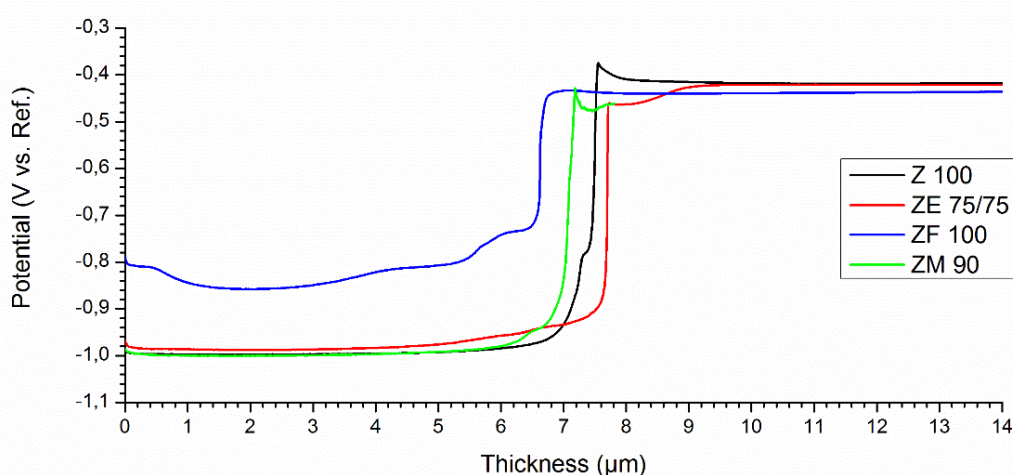


Fig.36: Evolution of the electrochemical potential of coating and substrate materials during coulometry of commercial products Z 100, ZE 75/75, ZF 100 and ZM 90

Table 16: Thickness of the coatings: provided by the steel supplier and measured by means of coulometry and optical microscopy

Coatings	Z 100	ZE 75/75	ZF 100	ZM 90
Data provided by the steel supplier (μm)	7.0	7.5	7.0	6.5
Measured by coulometry (μm)	7.8 ± 0.2	8.0 ± 0.1	6.9 ± 0.2	7.6 ± 1.5
Measured by optical microscopy (μm)	8.0 ± 1.8	8.8 ± 1.3	8.8 ± 1.2	7.2 ± 0.2

The composition and the morphology of the commercial deposits were determined by means of SEM-EDS (Table 17). XRD (Fig.37) was also carried out on the surface of the samples in order to determine their crystallographic structure (Table 17).

- In the case of the Z 100 coatings, the chemical analysis show small concentrations of Fe and Al with 2.8 wt.% and 1.3 wt.%, respectively (Table 17). The presence of Fe is due to the diffusion phenomenon occurring at the relatively high temperatures during hot-dipping. Al also originates from the hot-dipping process, more precisely from the molten bath where it is added in order to improve the adhesion of the coating on the substrate. The XRD analysis (Fig.37(a)) show predominantly the zinc phase (JCPDS n° 04-0831) and weak signals for iron (JCPDS n° 06-0696) that could originate either from the small amount of Fe observed in the coating during EDS analyses or from the higher penetration of the X-rays at high angles. This monophasic

crystallography correlates well with the coulometric analysis (Fig.36) during which one homogeneous phase could be observe together with a thin interphase.

- Similar results were obtained on ZE 75/75 (Table 17), with an even lower concentration of Fe detected with 1.8 wt.%, the rest is Zn. A single Zn phase (JCPDS n° 04-0831) was therefore detected during XRD analyses (Fig.37(b)). Again, a good correlation is observed with the galvanostatic dissolution (Fig.36) with one single phase observed in both cases.
- On ZF 100 coated samples, 10.9 wt.% of iron were detected together with 1.6 wt.% of aluminium (Table 17). Similarly to the Z 100 samples, the presence of Al originates from the bath of molten metal used during hot-dip galvanizing. The high amount of Fe results from the annealing step permitting the diffusion of iron into the Zn deposit. Multiple crystallographic phases are observed after the XRD analyses (Fig.37(c)) with various iron-zinc phases Fe-Zn₇ (JCPDS n° 02-1184), Fe-Zn₁₃ (COD n° 2010723) and Fe-Zn_{10.98} (JCPDS n° 45-1184) as well as the iron phase (JCPDS n° 06-0696). The Fe-Zn₁₃ corresponding to the ζ-phase with 6 to 6.5 wt.% Fe and the Fe-Zn₁₁ corresponding to the δ-phase with 7 to 10 wt.% Fe have also been reported elsewhere [192]. The presence of these multiple phases was expected from the galvanostatic experiments (Fig.36) with the presence of three plateau, presenting different potential, that likely correspond to three phases of slightly different composition.
- ZM 90 samples present three distinct phases during SEM analyses, with different compositions (Table 17). What seems to be the main phase is composed of 90.5 wt.% Zn, 5.4 wt.% Al and 4.1 wt.% Mg. Inside this “matrix”, inserts composed of 93.1 wt.% Zn, 4.8 wt.% Al and 2.1 wt.% Mg are visible. The last minority phase is composed of 79.3 wt.% Zn, 11.6 wt.% Al and 9.1 wt.% Mg. XRD analyses revealed a predominant phase of Zn (JCPDS n° 04-0831). A second phase corresponding to magnesium-zinc Mn-Zn₂ (JCPDS n° 01-1211) was also detected as well as traces of the iron Fe phase (JCPDS n° 06-0696) (Fig.37(d)). Interestingly, the presence of these two phases presenting different chemical compositions could not be observed during coulometric experiments (Fig.36).

Table 17: Chemical composition (SEM-EDS) and crystallographic phases identified during XRD analyses

	Composition	Crystallographic phases
Z 100	95.9 wt.% Zn - 2.8 wt.% Fe - 1.3 wt.% Al	Zn (JCPDS n° 04-0831) Fe (JCPDS n° 06-0696)
ZE 75/75	98.2 wt.% Zn - 1.8 wt.% Fe	Zn (JCPDS n° 04-0831)
ZF 100	87.4 wt.% Zn - 10.9 wt.% Fe - 1.6 wt.% Al	Fe-Zn ₇ (JCPDS n° 02-1184) Fe-Zn _{10.98} (JCPDS n° 45-1184) Fe-Zn ₁₃ (COD n° 2010723) Fe (JCPDS n° 06-0696)
ZM 90	93.1 wt.% Zn – 4.8 wt.% Al – 2.1 wt.% Mg 90.5 wt.% Zn – 5.4 wt.% Al – 4.1 wt.% Mg 79.3 wt.% Zn – 11.6 wt.% Al – 9.1 wt.% Al	Zn (JCPDS n° 04-0831) Mg-Zn ₂ (JCPDS n° 01-1211) Fe (JCPDS n° 06-0696)

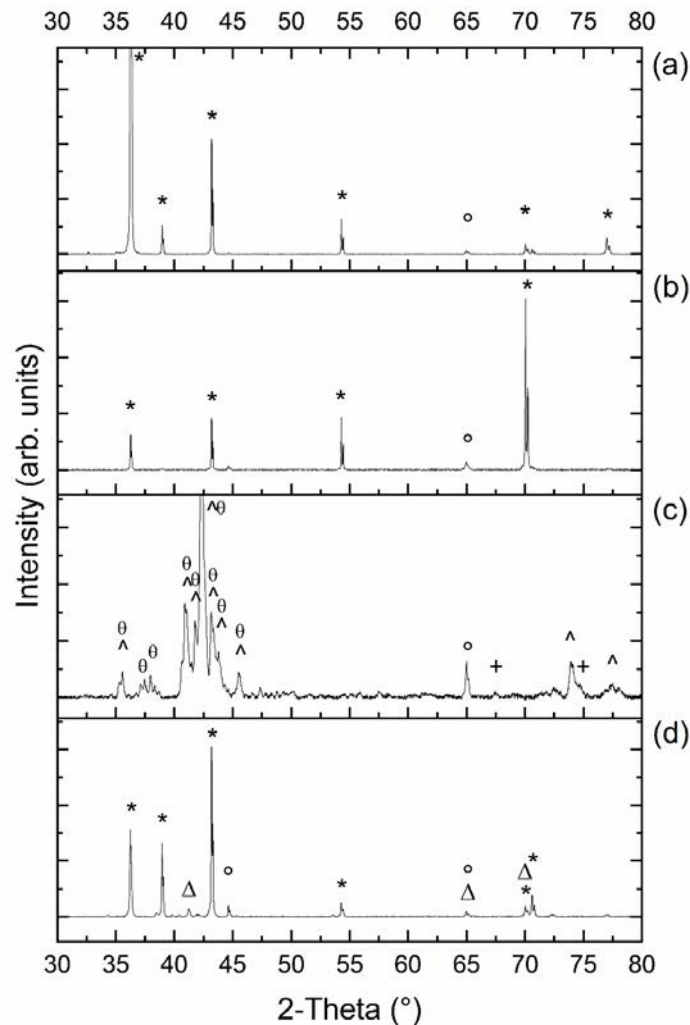


Fig.37: XRD patterns of the commercial coatings Z 100 (a), ZE 75/75 (b), ZF 100 (c) and ZM 90. Diffraction peaks corresponding to the Zn-phase * (JCPDS n° 04-0831), Fe-phase ° (JCPDS n° 06-0696), Fe-Zn₇ + (JCPDS n° 02-1184), Fe-Zn₁₃ ^ (COD n° 2010723), Fe-Zn_{10.98} Θ (JCPDS n° 45-1184) and Mg-Zn₂ Δ (JCPDS n° 01-1211)

2.8.3. Al₂O₃ particles

Al₂O₃ particles were selected for the investigations on the Zn-Mn composite coatings. More precisely, the choice was focused on Al₂O₃ nanoparticles with a particle size ranging inferior to 50 nm according to the supplier Sigma Aldrich (ref. 544833). The choice of Al₂O₃ was made based on the literature review conducted in chapter 1.6 as well as on the material costs and availability.

The size, the shape and the crystallography of the particles were characterized via TEM and XRD analyses. The TEM micrograph presented in Fig.38 clearly shows the shape of the particles, in the form of rods. The diameter of the rods can be estimated to be around 5 to 10 nm with a length of up to 80 nm.

XRD analysis (Fig.39) performed on the alumina powder revealed a cubic structure corresponding to the COD 1101168 diffraction pattern of the cubic γ-Al₂O₃. From the XRD patterns, the particle size was determined thanks to the Scherrer equation

$$\tau = \frac{K \times \lambda}{\beta \times \cos \theta} \quad \text{Eq.46}$$

With τ the mean size of the ordered crystalline domain (corresponding to the grain size), K a dimensionless shape factor, λ the wavelength (1.52×10^{-10} m), β the line broadening at half the maximum intensity (1.440) and θ the Bragg angle equal to 33.3° .

This results to a crystallite size around 6.3 nm. Additional TEM observations (Fig.38) show that particles have a rod-like shape with a wide range of lengths, between 20 to 100 nm. However, the particles width is inferior to 20 nm and can therefore be compared with the crystallite size determined via XRD.

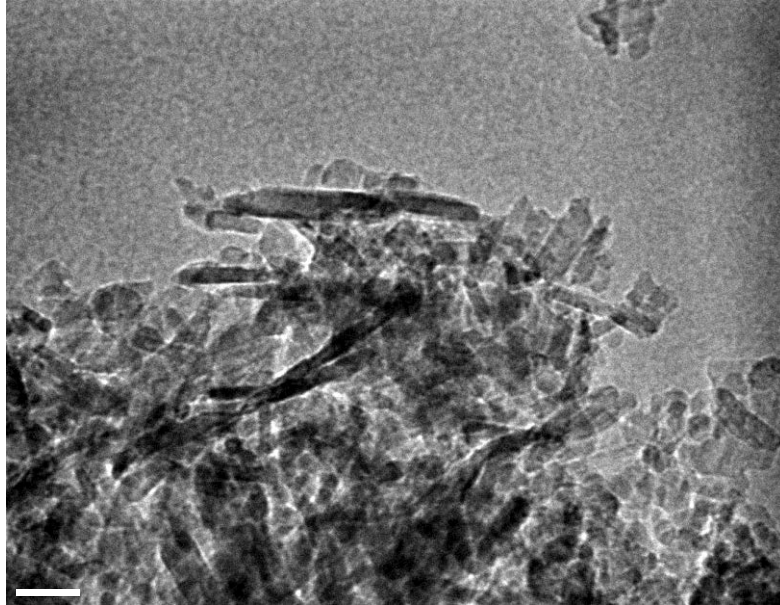


Fig.38: TEM micrograph of the alumina nanoparticles

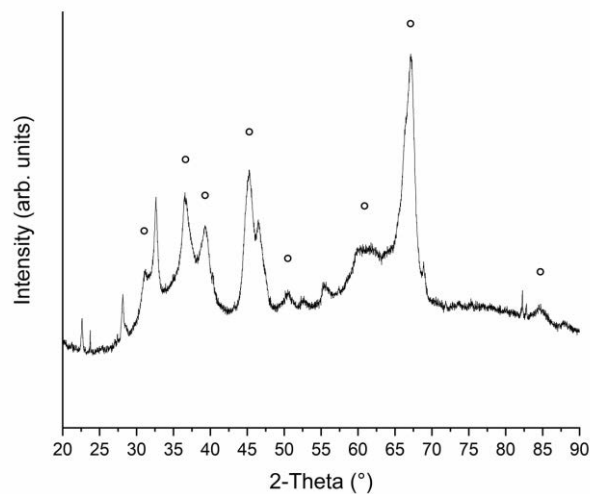


Fig.39: XRD pattern of the alumina powder, as delivered. Diffraction peaks corresponding to the Al₂O₃ phase (COD 1101168)

2.9. Experimental approach and deposition parameters

The aim of this work is to develop alternative Zn-based alloy coatings for automotive cold formed steel body parts with enhanced anticorrosive and mechanical properties compared to the currently available coating systems. As previously stated, two approaches were considered on the basis of the literature. In the first one, the use of galvanostatic pulse plating was investigated in order to improve the properties of Zn-Mn deposits. In the second one, the deposition of Zn-Mn composite coatings was studied. The experimental approach leading to the deposition of the pulse Zn-Mn and the composite coatings is described in Fig.40.

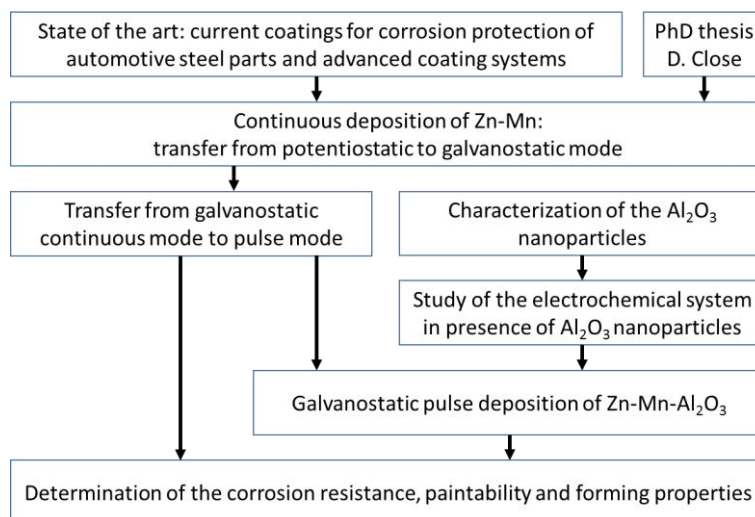


Fig.40: Overview of the experimental approach considered in this work

The potentiostatic continuous deposition of Zn-Mn coatings was comprehensively investigated in the PhD thesis of Close [169], and forms the basis of the present work together with the results of the literature.

- The first step of this work consists in the **pulse electrodeposition of Zn-Mn**.
 - To do so, the transfer from potentiostatic to galvanostatic continuous plating was investigated with the help of linear scan voltammetry (LSV) and deposits carried out at potentials from -1.2 to -1.8 V and current densities of -0.015 A/cm².
 - The transfer from galvanostatic continuous to pulse plating was then studied in order to further improve the deposits. The influence of the electrical parameters – namely the average current density ranging from -0.01 to -0.02 A/cm² and peak current density ranging from -0.025 to -0.1 A/cm² – as well as the influence of the time parameters – namely pulse duration between 1 and 50 ms – were investigated.
 - The optimal deposition parameters were determined on the basis of the chemical composition, morphology and microstructure of the deposits.
 - The anticorrosive properties of the as-deposited coatings were assessed by means of electrochemical and industrial ageing tests. Coated samples were additionally phosphated, painted and submitted to tensile and bending tests in order to determine their paintability and formability.
- In the second part of this work, the **development of ZnMn-Al₂O₃ coatings** was studied.
 - Prior to the investigation of the electrodeposition process, the Al₂O₃ nanoparticles were comprehensively characterized.
 - In addition, the proper dispersion of the particles at concentrations ranging 0.25 to 10 g/L into the plating bath and the behaviour of the new electrochemical system were studied.
 - ZnMn-Al₂O₃ deposits were obtained by means of galvanostatic pulse plating. The influence of the electrolyte composition, average and peak current densities in the -0.01

to -0.02 A/cm^2 and -0.025 to -0.1 A/cm^2 ranges, respectively, and pulse duration from 1 to 50 ms were investigated.

- Materials properties as well as anticorrosive, painting and forming properties were systematically evaluated, as previously described.

3. Study, deposition and characterization of advanced Zn-Mn coatings

Disclaimer: A part of the results presented and discussed in this chapter were gathered into a scientific article published in the Journal of Applied Electrochemistry [193]. Some of these results were also presented in the form of oral contributions at the 13th International Workshop on Electrodeposited Nanostructures – EDNANO XIII in Bristol (United Kingdom) and at the Matériaux 2018 conference in Strasbourg (France) as well as in the form of a poster at the 2019 colloquium “La Métallurgie, quel avenir!” in Nancy (France).

3.1. Aim and procedure (EN) – But et procédure (FR)

It was reported in section 1.4 that the Zn-Mn alloy coatings could provide very promising properties, especially regarding their corrosion behaviour. In this case, the specific mechanism of corrosion of Zn-Mn is expected to lead to the rapid formation of highly stable corrosion product known as zinc hydroxychloride (ZHC). [96, 98, 105]. Literature data suggests that optimal corrosion properties are obtained in the 10 – 30 wt.% range [96, 99, 101-105]. In addition to the composition of the alloys, the crystallographic texture and the surface morphology of the deposits usually plays an important role in the corrosion behaviour.

A specific review on Zn-Mn-based alloys presented in section 1.5 outlined the benefits of manufacturing Zn-Mn deposits through aqueous electrodeposition. In addition to the advantageous properties of these deposits, the use of aqueous electrodeposition brings additional advantages such as a better finishing, more uniform deposits, a more precise control of the parameters and lower running costs. It however appears that the electrodeposition of Zn-Mn from aqueous electrolytes has some challenges. The codeposition of Zn-Mn is, according to the classification of Brenner, a normal codeposition mechanism [194], which means that high Mn contents are obtained at high cathodic current densities or potentials. This requirement is particularly problematic given that deposition at high cathodic current densities or potentials leads to low current efficiencies and poor appearance of the deposits due to hydrogen evolution reaction (HER), previously described in the section 1.5.3.

One way to overcome the drawbacks of Zn-Mn electrodeposition consists in using additives in order to enhance Mn deposition and to improve the microstructure and the properties of the deposits [115, 118]. However, the use of additives reduces the stability of the electrolyte and may induce the incorporation of unwanted elements affecting the properties of the deposits. Another competitive approach consists in the use of pulse plating instead of the continuous mode. The pulse plating permits to significantly inhibit the intensity of the HER, even at high current densities, and to improve the appearance and the morphology of the deposits.

From these statements, developments have been realized in order to synthesize Zn-Mn coatings that meet the following requirements:

- Growth method: galvanostatic pulse electrodeposition
- Electrolyte: aqueous medium without additives
- Chemical composition of the coatings: between 10 and 30 wt.% Mn

Consequently, a specific study of the deposition parameters under continuous current will be firstly conducted by means of linear scan voltammetry (LSV) experiments. The impact of the current density on the properties of the deposits under continuous mode will be discussed in section 3.2. In the second section 3.3, the transfer to the pulse plating will be studied in order to try to enhance the Mn content and to improve the compactness of the deposits. Various phenomena involved during pulse plating will be taken into account in order to define the process window for the electrical and time parameters. The composition, morphology, texture and microstructure of the pulse deposits will be thoroughly

characterized. The last sections 3.4 and 3.5 will correspond to a summary of the optimal deposition parameters selected and a brief study of the up-scaling and reproducibility, respectively.

Il est apparu dans le chapitre 1.4 que les alliages de Zn-Mn pouvaient apporter des propriétés très prometteuses, en particulier concernant leur comportement en corrosion. Plus particulièrement, le mécanisme de corrosion du Zn-Mn conduit à la formation rapide d'un produit de corrosion extrêmement stable, le zinc hydroxychlorure (ZHC) [96, 98, 105]. La littérature suggère que les meilleures propriétés anticorrosives sont obtenues pour des alliages contenant entre 10 et 30 m.% de Mn [96, 99, 101-105]. Outre la composition des alliages, il a été démontré que la texture cristallographique et la morphologie des dépôts jouaient un rôle important dans le comportement en corrosion.

Une analyse de la bibliographie sur les alliages à base de Zn-Mn présentée dans le chapitre 1.5 a permis de souligner les avantages de l'électrodéposition en phase aqueuse pour l'élaboration de dépôts de Zn-Mn. Cette technique offre, outre de meilleures propriétés des dépôts, de nombreux avantages tels qu'un meilleur état de surface, des revêtements plus uniformes, un contrôle plus précis des paramètres et des coûts de fabrication moins élevés. Il apparaît cependant que l'électrodéposition de Zn-Mn en phase aqueuse présente certaines complications. La codéposition de Zn-Mn correspond, selon la classification de Brenner, à un mécanisme de codéposition dit normal [194]. Cela signifie que les quantités importantes de Mn sont obtenues à des densités de courants cathodiques ou potentiels élevés. Cette condition est particulièrement problématique du fait que la déposition à fortes densités de courants cathodiques ou forts potentiels provoque des rendements faradiques très faibles ainsi qu'une mauvaise apparence des dépôts causés par l'évolution d'hydrogène (HER) précédemment décrite dans la section 1.5.3.

Afin de résoudre les problèmes liés à l'électrodéposition du Zn-Mn, l'utilisation d'additifs permettant de favoriser la déposition du Mn par rapport au Zn et d'améliorer la microstructure et les propriétés des dépôts peut être envisagée [115, 118]. Cependant, l'utilisation d'additifs diminue la stabilité de l'électrolyte et peut conduire à l'incorporation d'éléments indésirables pouvant affecter les propriétés des revêtements. Une seconde approche consiste à utiliser des courants impulsionnels au lieu des courants continus traditionnellement utilisés. La déposition par courants impulsionnels permet de réduire de manière significative l'intensité de l'évolution d'hydrogène, même à très fortes densités de courants, ainsi que d'améliorer l'apparence et la morphologie des dépôts.

Sur la base de ces énoncés, différents développements ont été effectués dans le but de synthétiser des revêtements de Zn-Mn en suivant les exigences suivantes :

- *Méthode de croissance : électrodéposition galvanostatique impulsionnelle*
- *Électrolyte : milieu aqueux en absence d'additifs*
- *Composition chimique des revêtements : entre 10 et 30 m.% de Mn*

En conséquence, une étude spécifique des paramètres de déposition sous courants continus sera tout d'abord effectuée via voltamétrie linéaire (LSV). L'impact de la densité de courant sur les propriétés des dépôts sera discuté dans le chapitre 3.2. Dans un second chapitre 3.3, le transfert vers l'électrodéposition impulsionnelle sera étudié dans le but d'augmenter la quantité de Mn codéposée et d'améliorer la compacité des dépôts. Les divers phénomènes impliqués au cours de l'électrodéposition impulsionnelle seront pris en considération afin de définir la fenêtre du procédé pour les paramètres électriques et temporels. La composition, la morphologie, la texture et la microstructure des dépôts pulsés seront rigoureusement caractérisées. Les dernières sections 3.4 et 3.5 seront respectivement consacrées à un résumé des paramètres optimaux pour l'électrodéposition et à une brève étude de reproductibilité et de mise à l'échelle.

3.2. Preliminary study of the deposition under continuous currents

This section is dedicated to the galvanostatic synthesis of Zn-Mn. Various deposits will be obtained from an additive-free chloride electrolyte described in Table 11, page 64 and using the experimental setup described in section 2.2.2.

A thorough characterization of the deposits will be carried out in order to determine their chemical composition and morphology. In addition, a particular attention will be given to the microstructure and the crystallographic texture of those deposits.

3.2.1. Study of the electrodeposition system

In order to define the electrodeposition system of Zn-Mn and to better understand the plating bath used in the framework of this thesis, linear voltammetric studies were conducted in various electrolytes containing:

- i. 2.8 M KCl
- ii. 2.8 M KCl and 0.32 M H₃BO₃
- iii. 2.8 M KCl, 0.32 M H₃BO₃ and 0.075 M ZnCl₂
- iv. 2.8 M KCl, 0.32 M H₃BO₃ and 0.6 M MnCl₂
- v. 2.8 M KCl, 0.32 M H₃BO₃, 0.075 M ZnCl₂ and 0.6 M MnCl₂

The resulting voltammograms are presented in Fig.41.

The scans obtained in the electrolytes (iii) and (iv) containing ZnCl₂ and MnCl₂, respectively, clearly depict the positions of the cathodic peaks corresponding to the reduction of Zn²⁺ and Mn²⁺ into Zn and Mn, respectively. These peaks are observed at about -1.2 V for Zn and -1.8 V for Mn. In comparison to the voltammograms obtained in the electrolytes (i) and (ii) without the metallic salts, these results confirm that the cathodic peaks observed can be effectively attributed to Zn and Mn.

When both Zn and Mn salts are present in the electrolyte (electrolyte (v)), a slight shift of the reduction potential for Mn can be observed while the large cathodic peak corresponding to the reduction of Zn into Zn²⁺ is still observed around -1.2 V. This observation is in good accordance with the values reported in the literature by Gomes et al. at -1.08 V [160], Bucko et al. at -1.12 V [115] and Close et al. at -1.1 V [118]. The cathodic peak corresponding to the reduction of Mn into Mn²⁺ can be observed at approximately -1.6 V. This constitutes a shift of about 0.2 V, but is in good agreement with previous reports of the literature on Zn-Mn electrolytes [115, 118, 121]. Although this difference is usually related to the presence of additives, usually bringing the reduction potentials of Zn and Mn closer to each other's [118], the combined use of Zn and Mn salts can also lead to such effects.

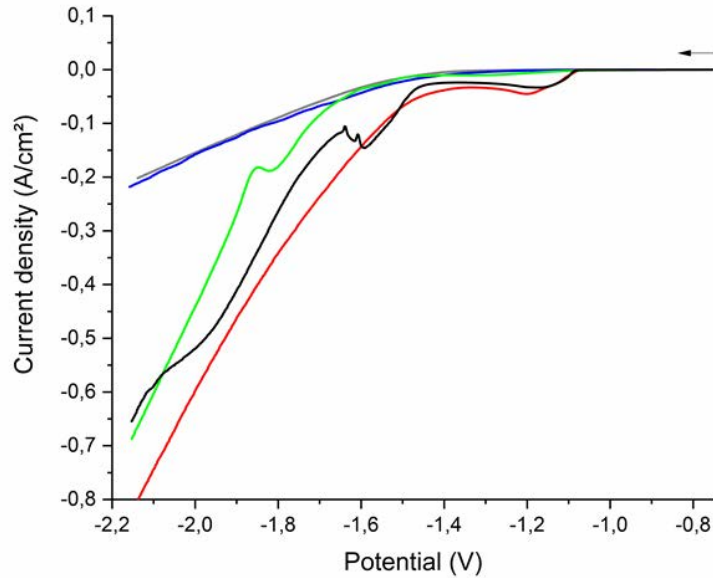


Fig.41: Linear voltammograms obtained during cathodic scan between potentials of -0.6 and -2.2 V on DC06 steel at a scan rate of 10 mV/s; voltammograms obtained in electrolytes containing 2.8 M KCl (grey), 2.8 M KCl and 0.32 M H₃BO₃ (blue), 2.8 M KCl, 0.32 M H₃BO₃ and 0.075 M ZnCl₂ (red), 2.8 M KCl, 0.32 M H₃BO₃ and 0.6 M MnCl₂ (green) and 2.8 M KCl, 0.32 M H₃BO₃, 0.075 M ZnCl₂ and 0.6 M MnCl₂ (black)

3.2.2. Transfer from potentiostatic to galvanostatic mode

The influence of the current density on the composition, morphology and surface roughness of Zn-Mn deposits was firstly investigated by means of electrodeposition experiments in the Hull cell. The Zn-Mn deposits will be obtained galvanostatically with a current of 1 A. The deposition was ruled by electric charges of 1950 Coulomb, corresponding to deposition times of 30 minutes.

The experimental protocol and electrolyte used for these experiments are previously described in section 2.2.

The appearance of the deposits obtained after deposition in the Hull cell with an electric charge set to 980 Coulomb is presented in Fig.42, with the calculated current density distribution along the sample.

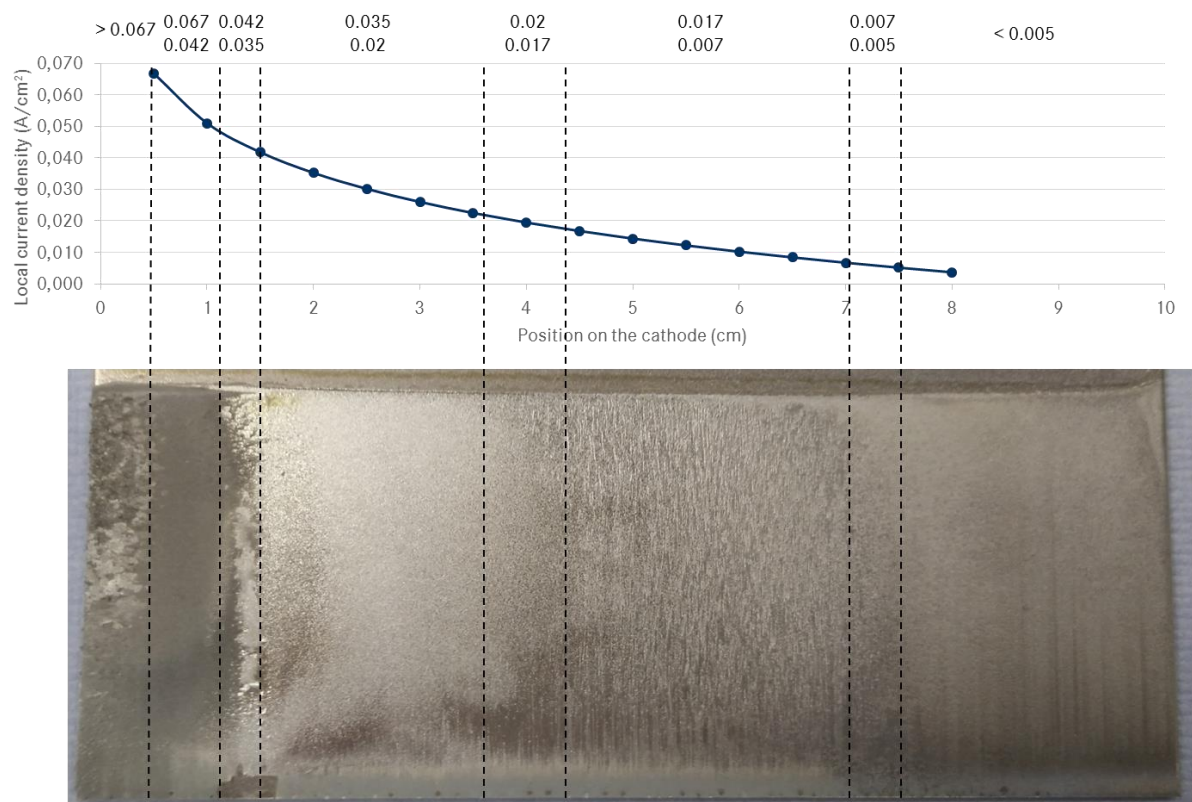


Fig.42: Visual appearance of the deposited Zn-Mn coating (1950 Coulombs) and respective distribution of the current density along the cathode

It appears that the current density has a significant impact on the appearance of the deposits. At high current densities, higher than 0.067 A/cm², the coating is powdery and presents almost no adherence to the substrate. Between 0.067 and 0.042 A/cm², the deposit presents a grey-mat “burnt” appearance. A thin blistered and cracked area presenting a very poor adhesion is observed between 0.042 and 0.035 A/cm². The poor appearance and adhesion of the deposits at high current densities can be explained by the high contribution and high intensity of the HER in this domain. The formation of hydrogen gas leads to the formation of bubbles on the surface of the cathode in parallel to the growth of the coating. These bubbles then escape towards the surface of the electrolyte and form some channels and bridges inside the deposit, leading to a poor cohesion and adhesion of the coating. In addition, the entrapment and accumulation of hydrogen bubbles growing below the surface of the deposit leads to the rupture of the coating and to the formation of craters.

For current densities below 0.035 A/cm², the deposits present an adequate adherence to the steel substrate. Between 0.035 and 0.02 A/cm², the coating presents a dull aspect, with a transition to semi-bright between 0.02 and 0.017 A/cm². From 0.017 to 0.007 A/cm², the surface is to be bright and streaky. At low current densities below 0.007 A/cm², the surface tends towards a duller or matter appearance, especially below 0.005 A/cm². It can also be noticed that the bottom of the sample appears burnt over a thickness of about 5 mm.

The increase of the current density leads to significant changes of the morphology of the deposits. The SEM micrographs presented in Fig.43 depicts the changes observed in the Hull cell. At low current densities, below 0.007 A/cm² (Fig.43, (a) to (c)), a relatively compact deposit presenting fine crystallites can be observed. In addition, numerous pores are observed on the surface revealing an improper covering of the steel substrate. At 0.01 A/cm² (Fig.43d), large “tooth-like” crystallites are formed on the surface of the deposit. At current densities of 0.013 and 0.015 A/cm² (Fig.43(e) and Fig.43(f), respectively), the deposit is quite compact and present fine crystallites. Very few pores and defects can be observed on the surface suggesting the good covering of the substrate. Further increase of the current

density up to 0.019, 0.022 and 0.026 A/cm² leads to the formation of dendritic deposits as depicted in Fig.43(g), (h) and (i), respectively. The use of very current density of 0.03 A/cm² leads to the formation of blistered and powdery deposits (Fig.43(j)). The surface is mostly formed of oxygen-rich craters as well as few dendritic aggregates. This is mostly due to the high intensity of the hydrogen evolution reaction at those currents.

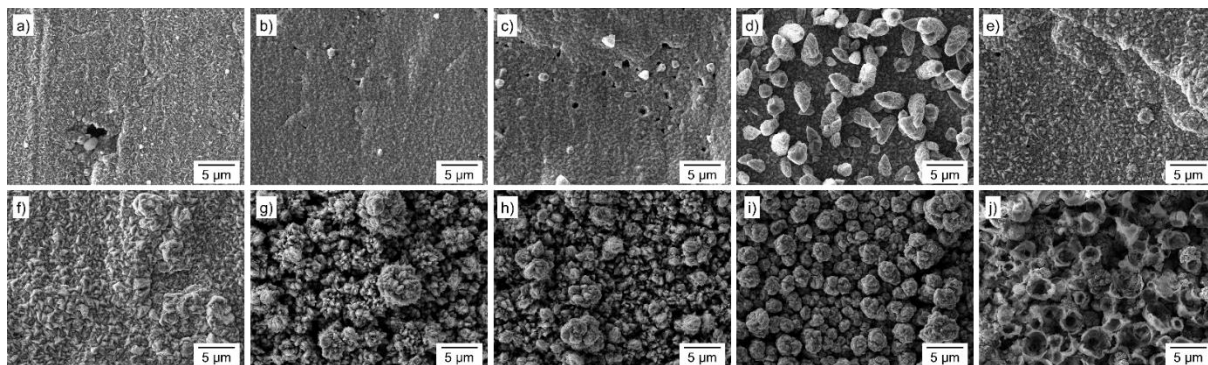


Fig.43: SEM micrographs of the Zn-Mn coatings deposited in the Hull cell at a current of 1 A and an electric charge of 1950 Coulomb; micrographs obtained at 0.001 A/cm² (a), 0.004 A/cm² (b), 0.007 A/cm² (c), 0.01 A/cm² (d), 0.013 A/cm² (e), 0.015 A/cm² (f), 0.019 A/cm² (g), 0.022 A/cm² (h), 0.026 A/cm² (i) and 0.03 A/cm² (j)

The evolution of the Mn content in function of the current density was determined by means of SEM-EDS analyses conducted on the surface of the Zn-Mn deposits. The results are presented in Fig.44. A first increase of the Mn content is observed when the current density increases up to 0.01 A/cm². This behavior is expected due to the normal codeposition character of the Zn-Mn alloys [194] and was largely reported in the literature [96, 115, 122]. A plateau seems to be reached for current densities between 0.007 and 0.013 A/cm², with the highest Mn content measured at 0.01 A/cm² with 16.8 wt.%. Above 0.01 A/cm², a decrease of the Mn content is measured, especially above 0.013 A/cm². This observation is quite surprising and does not correlate with the results of the reference literature nor with the normal codeposition mechanisms known for Zn-Mn alloys. One possible explanation could originate from the intensity of the HER in those regions and to the preferential oxidation of the Mn as deposition occurs.

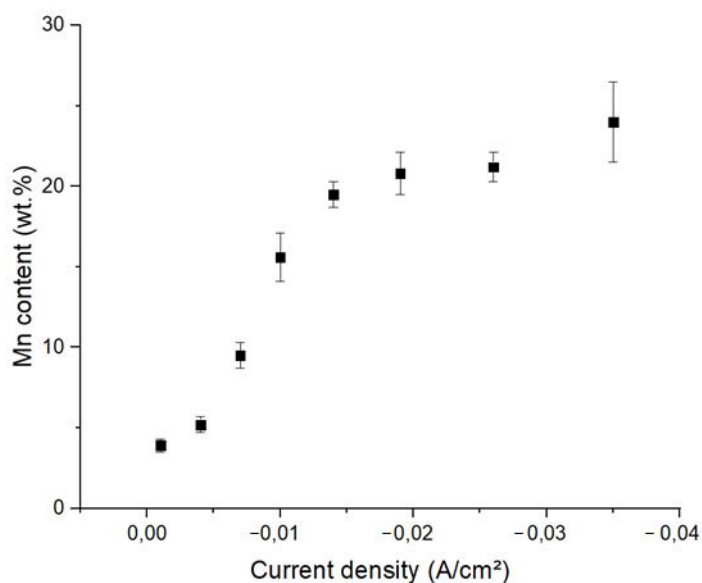


Fig.44: Evolution of the chemical composition (Mn content) depending on the current density on the surface of Zn-Mn coatings deposited in the Hull cell at 1 A and 1950 Coulomb

The thickness of the deposits was measured by means of coulometry on various areas corresponding to various current densities. On the basis of these results and considering the theoretical thicknesses

calculated according to the equations 43 and 44 (page 74), the faradaic efficiency could be determined along the samples. An increase of the faradaic efficiency is observed up to 0.019 A/cm² where a maximum is reached at 70%. Further increase of the current density however resulted in a drastic decrease of the efficiency, down to about 45% at 0.03 A/cm². The increased intensity of the HER at high current densities previously postulated is supported by these observations. This behavior was also observed by Bucko et al. [115] and Bozzini et al. [100].

Electrodeposition attempts were performed for various fixed potentials and current densities. Semi-quantitative chemical analyses carried out on the surface of the deposits via EDS are summarized in Table 18. They reveal an increase of the Mn content with increase of the deposition potential or current density. This behaviour is expected due to the normal codeposition mode of the Zn-Mn [194]. Indeed the coatings obtained at -1.25 V appeared almost purely composed of Zn. At -1.6 V, a Mn content of 12.6 wt.% was measured, whereas the further increase of the potential up to -1.8 V permitted to obtain up to 16.7 wt.% Mn. It should be noted that a Mn content of 11 wt.% was reported by Close et al. using the same plating bath under potentiostatic mode at -1.62 V [118]. These results are in good agreement with the literature and correspond to the normal codeposition mode of Zn-Mn [194].

In order to define a suitable electrochemical setup for industrial processes, galvanostatic deposition was tested for different fixed applied current densities. The deposits obtained at -0.015 A/cm² have led to coatings containing 13.1 wt.% Mn, demonstrated a relationship between potentiostatic and galvanostatic modes (Table 18). In the literature data, the same trend was observed by Bucko et al. who reported 11.6 and 18.8 wt.% Mn at current densities of -0.2 and -0.3 A/cm², respectively [115].

Table 18: Summary of the deposition modes, applied values and measured average values of the current density and potential investigated

Applied deposition parameters	Resulting average current density / potential	Mn content (wt.%)	Reference
Potentiostatic, E = -1.2 V	$i_{av} = -0.009$ A/cm ²	0.2 ± 0.2	Fig.45(a)
Potentiostatic, E = -1.6 V	$i_{av} = -0.016$ A/cm ²	12.6 ± 1.2	Fig.45(b)
Potentiostatic, E = -1.8 V	$i_{av} = -0.027$ A/cm ²	16.7 ± 0.5	Fig.45(c)
Galvanostatic, i = -0.015 A/cm ²	$E_{av} = -1.56$ V	13.1 ± 1.7	Fig.45(d)
Hull cell, i = -0.001 A/cm ²	/	3.9 ± 0.4	Fig.44
Hull cell, i = -0.004 A/cm ²	/	5.2 ± 0.5	Fig.44
Hull cell, i = -0.007 A/cm ²	/	9.5 ± 0.8	Fig.44
Hull cell, i = -0.01 A/cm ²	/	15.6 ± 1.5	Fig.44
Hull cell, i = -0.014 A/cm ²	/	19.5 ± 0.8	Fig.44
Hull cell, i = -0.019 A/cm ²	/	20.8 ± 1.3	Fig.44
Hull cell, i = -0.026 A/cm ²	/	21.2 ± 0.9	Fig.44
Hull cell, i = -0.035 A/cm ²	/	24.0 ± 2.5	Fig.44

SEM micrographs of the deposits obtained under potentiostatic and galvanostatic modes are presented in Fig.45. The deposits obtained under potentiostatic mode at a deposition potential of -1.2 V appear quite rough and present a well-defined pyramidal morphology with relative coarse crystallites (Fig.45(a)). At -1.6 V (Fig.45(b)), the deposits show a morphology similar to the one observed under galvanostatic mode at -0.015 A/cm² (Fig.45(d)). Both deposits present a relatively smooth surface without well-defined structures or distinguishable crystallites. Numerous crevices can be observed on the surface of the two coatings. A further increase of the deposition potential to -1.8 V leads to a second change of the morphology with the formation of groups of hexagonal platelets parallel to the surface and stacked on top of each other (Fig.45(c)). In the latter case, the coating surface is rough and numerous crevices can be observed. Bucko et al. reported a similar morphology on Zn-Mn deposits obtained from chloride electrolytes at -0.03 A/cm² [115].

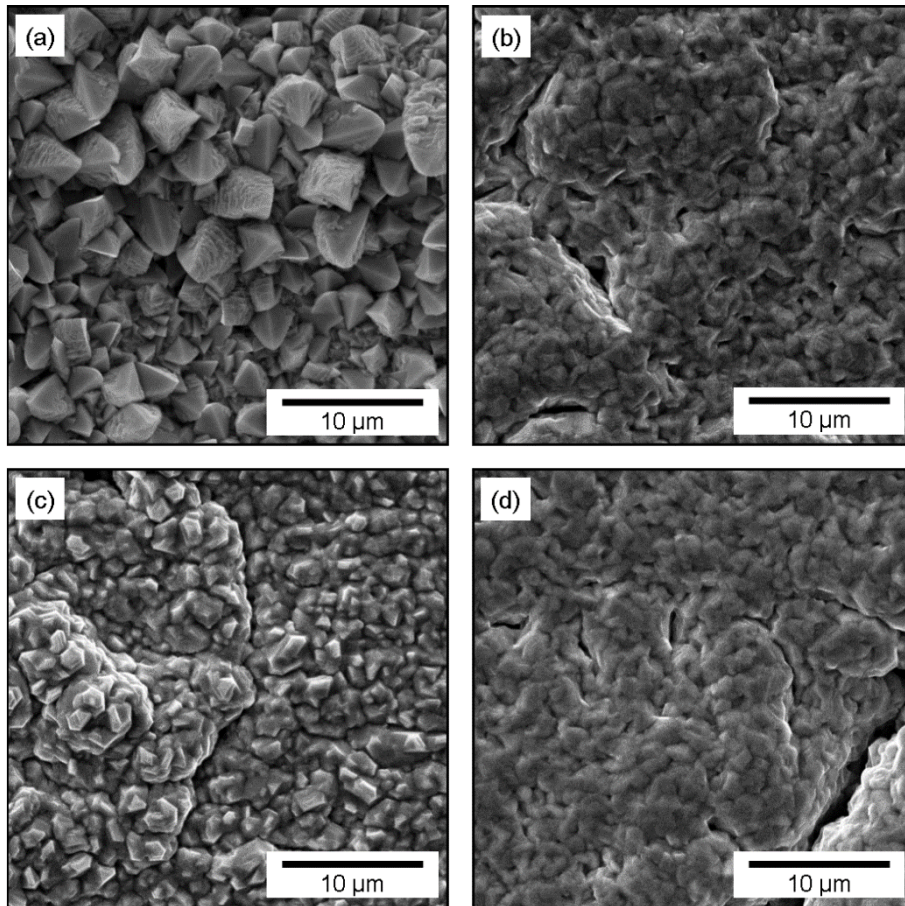


Fig.45: SEM micrographs of the surface of Zn-Mn layers deposited on DC06 steel at potentials of -1.25 V (a), -1.6 V (b), -1.8 V (c) and at a current density of -0.015 A/cm² (d)

Closer observation of the surface morphology (Fig.46) reveals for the deposits obtained at 0.015 A/cm² a very fine stacking of hexagonal platelets, all oriented parallel to the surface. This could suggest a hexagonal structure of the coatings and the preferential crystallographic orientation of this structure.

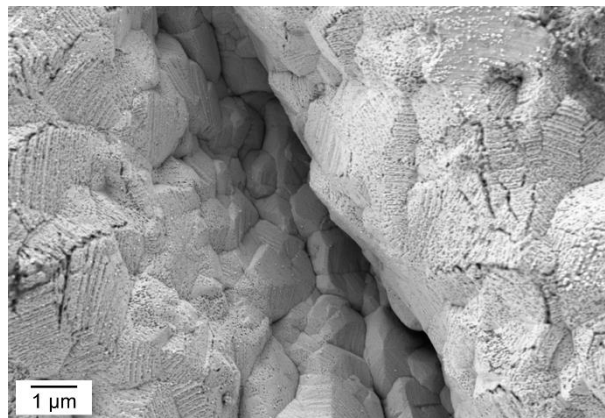


Fig.46: SEM micrograph of the surface of Zn-Mn layers deposited on DC06 steel at a current density of -0.015 A/cm²

Whatever the deposition mode, either potentiostatic or galvanostatic, the Mn content in the deposits seems to be directly governed by the cathodic conditions. However, the crystallinity of the deposits also appears to depend on the growth parameters. Therefore, systematic studies were performed in order to have better understandings of the electro-crystallization processes.

3.2.3. Crystallography and texture of the deposits

XRD analyses were conducted on the coatings deposited potentiostatically at -1.6 V and galvanostatically at -0.015 A/cm². The resulting diffraction patterns are presented in Fig.47(a) and (b), respectively. It should be noted that the intensity scales on the XRD patterns presented in the zooms of the Fig.47 were restricted in order to better depict the diffraction peaks otherwise masked by the peak at 41°.

Both potentiostatic and galvanostatic deposits present patterns corresponding to the hexagonal close-packed (HCP) ϵ -ZnMn phase (JCPDS n° 04-003-4358) represented in Fig.47(c). It should be noted that the patterns observed in Fig.47(a) and (b) could correspond either to the ϵ_1 -ZnMn phase, or to the similar ϵ_2 -ZnMn phase. The former phase corresponds to the stoichiometry Zn_{0.73}Mn_{0.27} observed for alloys containing between 29 and 37 wt.% Mn according to Okamoto and Tanner [195]. The later ϵ_2 -ZnMn phase however should provide a better fit for the deposits investigated here. Indeed, this phase correspond to the stoichiometry Zn₄Mn observed for Mn contents between 12 – 25 wt.% [195], matching the compositions measured in the deposits (Table 18). However these two phases present only some minor shifts of the diffracting peaks due to the changes in the lattice parameters. Due to the large range of composition of the ϵ phases, this crystallography is largely observed in the literature. A summary of the phases reported and the associated preferred orientations for Zn-Mn deposits obtained without additives is given in Table 19.

Considering the literature data reported in Table 19, Zn-Mn deposits obtained without additives present in most cases a preferential orientation with the high angle planes (that is, a plane with an angle close to 90° in respect to the basal plane, e.g. (11.0) or (10.0) planes) oriented perpendicular to the growth direction with in particular the (10.1) [98, 121, 123] or in some cases the (11.0) [118]. In the present work however, a preferred crystallographic orientation was observed on both deposits with the basal plane (00.2) oriented parallel to the surface (Fig.47).

Table 19: Phases and preferred crystallographic orientations of additive-free Zn-Mn deposits reported in the literature.

Electrolyte	Mn content (wt.%)	Phases	Preferred orientation	Reference
Chloride	12.8	ϵ -ZnMn	(10.1)	Sylla et al. [121]
Pyrophosphate	3.98	ϵ -ZnMn	(10.1)	Bucko et al. [98]
Pyrophosphate	9.93	η -ZnMn ϵ -ZnMn	(10.1)	Bucko et al. [98]
Chloride	5.5	η -ZnMn ϵ -ZnMn ζ -ZnMn	(10.1)	Loukil and Feki [123]
Chloride	11	Zn ϵ -ZnMn	(11.1)	Close et al. [118]

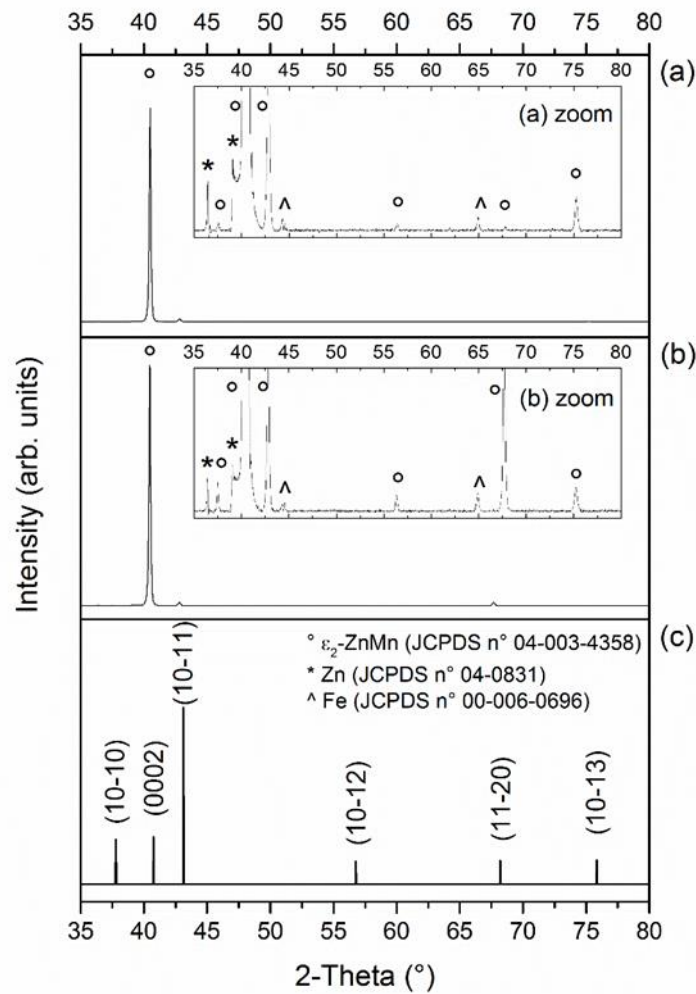


Fig.47: XRD patterns of Zn-Mn deposits obtained under potentiostatic mode at -1.6 V (a) and under galvanostatic mode at -0.015 A/cm² (b) and diffraction lines of the ϵ_2 -ZnMn (JCPDS n° 04-003-4358) phase (c); patterns obtained in the Bragg-Brentano mode without tilting

The (00.2) orientation of the ϵ -phase was observed in combination with the α -phase by Diaz-Arista et al. [125] but using ammonium thiocyanate as an additive. The formation of low-angle planes (planes close to the basal plane) such as the basal (00.2) plane during continuous current electrodeposition in absence of additives was already reported on pure Zn deposits by Nayana and Venkatesha [196, 197]. In the case of Zn-Mn, an opposite behaviour was reported by Close et al. with a shift from (10.1) and (11.0) texture towards a strong (00.2) texture with the addition of additives [118].

Complementary EBSD analyses conducted on cross-sections of the samples are presented in Fig.48 with the corresponding inverse pole figure (IPF) colouring in Fig.49. The results show clearly the formation of long columnar grains with a preferred orientation of the grains with the (10.1) and (12.0) planes oriented parallel to the cross-section. These two orientations on the EBSD mappings both correlates with the observations of the Fig.47 suggesting the basal plane perpendicular to the growth direction. A trend is also observed between the columnar grains following mostly the preferred orientation previously mentioned and the smaller grains near the substrate – coating interface being more randomly oriented. Given the fact that the DC06 steel substrate presents a combination of the (211), (200) and (110) planes parallel to the surface and the Zn-Mn deposits the basal (00.2) plane parallel to the surface, this leaves the possibility for a Burger's orientation relationship $\{110\}_{Fe} \parallel \{00.2\}_{Zn}$ between the substrate and the deposit. The growth of Zn deposits following Burger's orientation relationship was previously

observed in the literature but in the case of electropolished substrates [198] [199]. In the case investigated here however, this orientation relationship was observed on unprepared substrates.

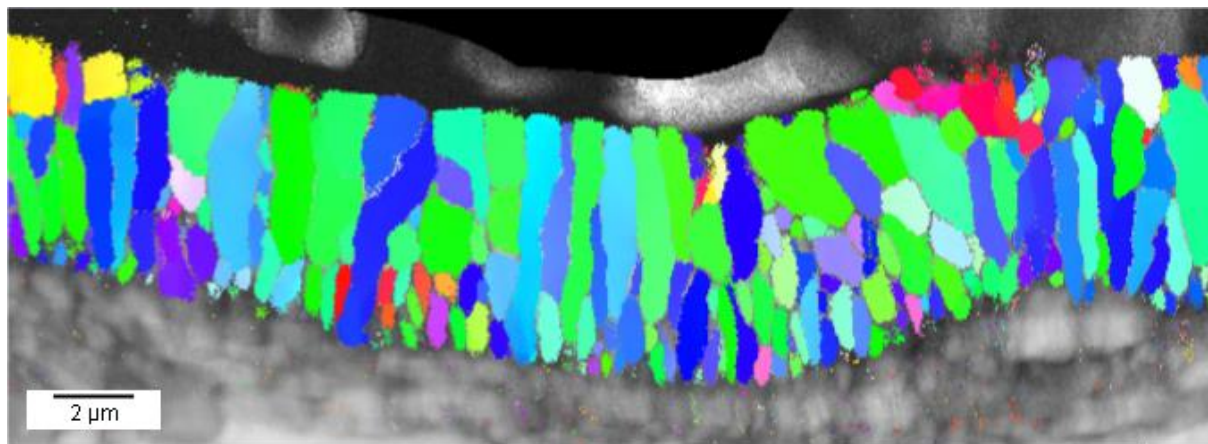


Fig.48: Orientation mapping of the cross-section of a Zn-Mn coating deposited under continuous current at 0.015 A/cm² after ion polishing; measurement steps of 0.05 μm and corresponding inverse pole figure (IPF) in Fig.49

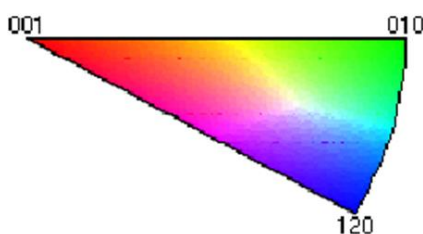


Fig.49: Inverse pole figure (IPF) corresponding to the mapping in Fig.48

3.2.4. Microstructure of the deposits

General microstructure

Analyses of the microstructure of the deposits obtained galvanostatically at -0.015 A/cm² were carried out by means of FIB-SEM. The micrograph obtained on the cross-section of the specimens is presented in Fig.50.

The microstructure and the shape of the grains is well-distinguishable on the cross-sections and confirms the previously discussed conclusions based on EBSD analyses. The deposits present a large population of long columnar grains growing in most cases uninterrupted from the substrate steel Fig.50. It appears that these columnar grains present a somewhat conical shape with a rather small contact area with the substrate and expanding towards the surface of the deposit. This means that a higher population of smaller grains will be located near the substrate – deposit interface (about 2 – 3 μm thickness) and entrapped, confirming the observations of Fig.48.

The presence of a similar columnar microstructure was also observed by Close on deposits obtained potentiostatically in presence of additives [169]. Such a pronounced conical shape of the grains was however not observed. This observation may be related to the absence of additives, and especially to the absence of NH₄SCN. NH₄SCN was previously reported to considerably reduce the size of the grains and lead to more uniform deposits [125, 169]. In the absence of additives, such as in this work, grain growth is not inhibited and preferential growth of some grains or crystallites can occur.

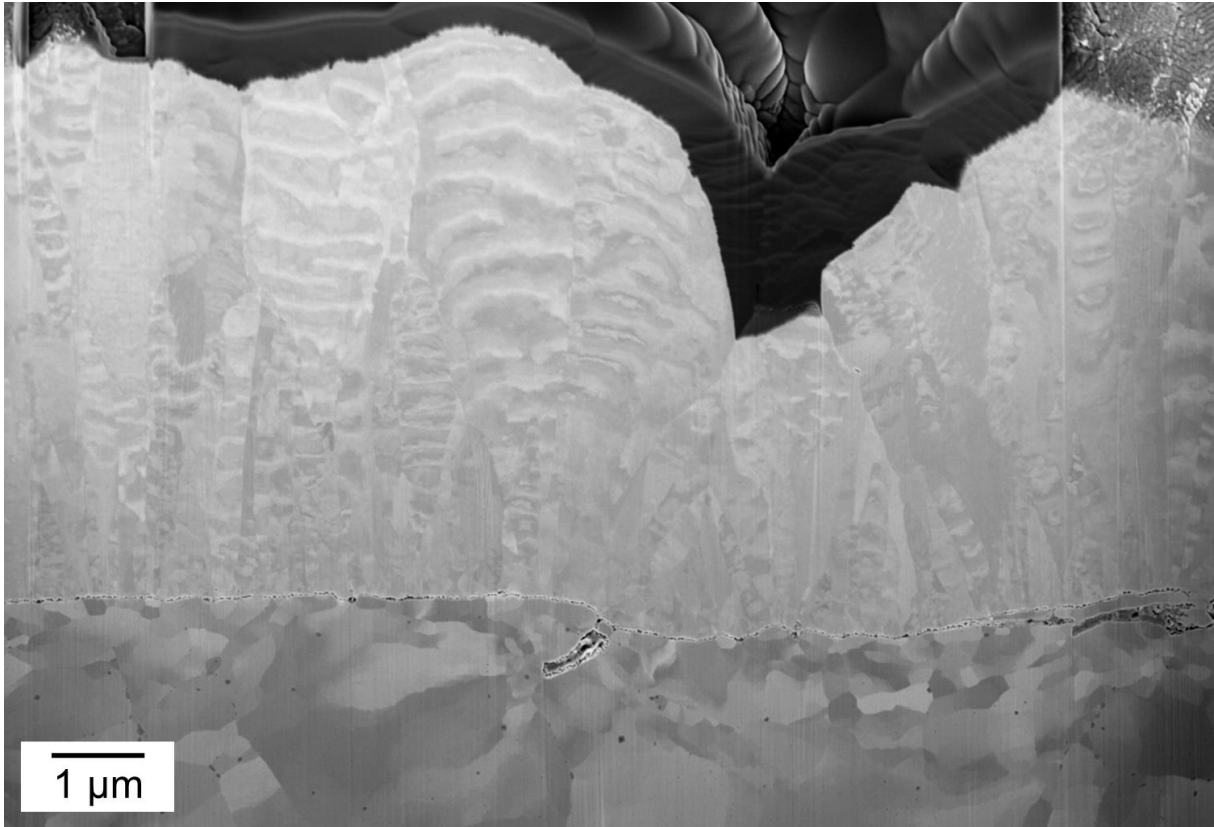


Fig.50: Cross-sectional micrograph of Zn-Mn deposited under continuous current at 0.015 A/cm^2 after FIB-SEM milling and polishing

An average grain size of $0.9 \mu\text{m}^2$ was measured on the basis of the EBSD mappings (Fig.48). The statistical analyses carried out in order to obtain the distribution of the grain size show two grain populations. A majority of the grains, mostly located near the substrate – coating interface appears almost equiaxed with an aspect ratio of about 1.3 and rather small with an average size of $0.05 \mu\text{m}^2$ (Fig.51). The second grain population corresponds to the long columnar grains, with an aspect ratio of 3.8, significantly larger with an average size around $2.6 \mu\text{m}^2$.

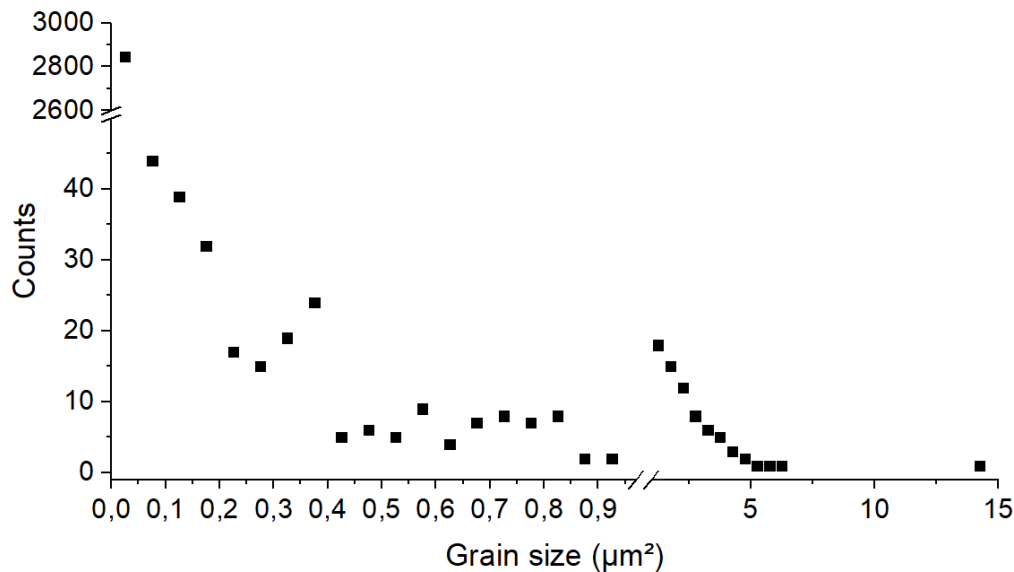


Fig.51: Grain size distribution of Zn-Mn deposited under continuous current at 0.015 A/cm², from orientation mapping presented in Fig.48

Strata

In addition, some strata, about 250 nm thick and oriented perpendicular to the growth front of the grains are also observed inside the columnar grains (Fig.50 and Fig.52b). Based on those observations, it seems that these strata form a somewhat repeating cycle, and are specific to each grain. Therefore, the following hypotheses can be formulated:

- One first possibility could originate from some changes of the ionic composition (i.e. the Mn^{2+}/Zn^{2+} ratio) locally in the vicinity of the cathode, leading to some small changes of the chemical composition. Similarly, some variations or perturbations of the applied current density and/or potential locally could also result in some changes of the chemical composition inside the grains. Such hypotheses would correspond well to the observations of Saltykova, who reported the presence of similar strata perpendicular to the growth front in the case of electrodeposited Ru-Ir alloys [200]. These strata were only observed in cases where the limiting current density was exceeded and were reported to be the result of periodic changes of the alloy composition.
- The origin of these strata could also be related to some fluctuations of the pH during the electrodeposition process. In cases such as the one investigated in this work where the composition of the alloy is known to be pH-dependent, the local fluctuation of the hydrogen evolution reaction may lead to such strata in the deposit, perpendicular to the substrate.
- Another explanation could be related to some fine disorientations of the lattices inside those grains or crystallites. This could originate from variations of the overpotential locally. Indeed, the influence of the current density and the overpotential on the orientation of electrodeposits was largely reported in the literature [201-203].
- Finally, the local adsorption of hydrogen at the surface of the deposit could be responsible for the formation of these strata. It is known that hydrogen bubbles form on the surface of the deposit during the deposition and grow until they detach and escape through the electrolyte. One can easily imagine that hydrogen simultaneously adsorbs inside the deposit during the formation

and growth of the bubbles, which may perturb the microstructure of the deposit locally, resulting to the formation of strata.

Further characterization of those deposits were attempted in order to further understand the origin of these strata and to confirm or refute the above-mentioned hypotheses. EBSD analyses conducted on those specimens and presented in Fig.48 does not revealed any disorientations that could match the patterns formed by the strata. Similarly, the EDS analyses carried out on cross-sections could not support some changes of the chemical composition. However, this is mostly due to the fine scale of the strata, about 250 nm thick, significantly below the $1 \mu\text{m}^3$ interaction volume of the EDS.

Substrate – coating interface

At the substrate – coating interface, thin and discontinuous layer is observed with numerous bridges ensuring a connection between the substrate and the deposit (Fig.52 (b) and Fig.53). Large cavities and porosity are also observed inside the deposits (Fig.52 (a)). These bigger cavities, mostly located at the substrate – coating interface are supposedly caused by the hydrogen evolution reaction generating hydrogen bubbles channelling towards the surface of the deposits and opening through crevices and holes as observed in Fig.52. Pores are also observed inside the steel substrate, as in Fig.50 and Fig.52.

The formation of these blisters is supposed to originate from hydrogen evolution and permeation into the steel substrate. This phenomenon was reported to be particularly intense when high cathodic current densities were applied and when no additives were used [204]. During hydrogen evolution, a large fraction of the adsorbed hydrogen reacts and form gaseous dihydrogen that is released directly in the solution, thus the formation of bubbles at the cathode. Simultaneously, a small fraction of the adsorbed hydrogen diffuses into the steel substrate. Hydrogen adsorption in the steel substrate may lead to an increase of the internal pressure, decohesion of the grains and formation of hydride compounds [205]. This results in some losses of the mechanical properties and to the formation of blisters [206]. This effect was reported to be particularly important during the early stages of the deposition, at times where the substrate is not fully covered and where hydrogen evolves directly on the surface of the substrate [207, 208].

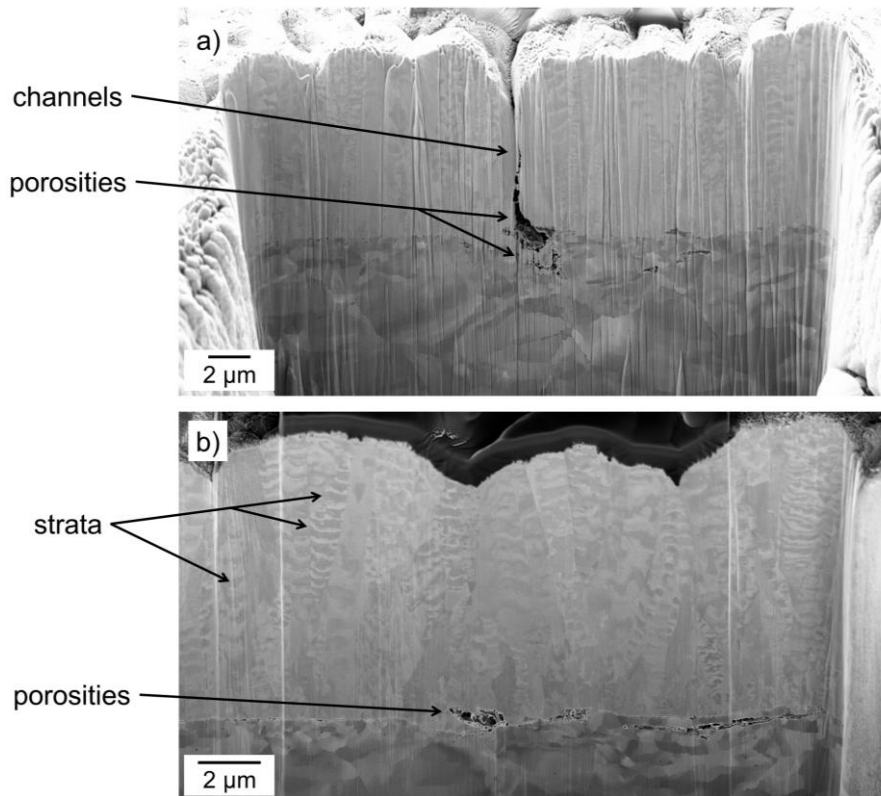


Fig.52: Cross-sectional micrographs of Zn-Mn deposited under continuous current at 0.015 A/cm² after FIB-SEM milling and polishing; presence of large porosity and channels (a) and details of the microstructure (b)

Numerous connections between the grain boundaries of the substrate and the deposit can be observed with in some cases one steel grain leading to one Zn-Mn grain (Fig.53). Overall, it appears that numerous Zn-Mn grains are formed on each steel grain. Such observations were also made by Greul et al. on Zn deposits obtained on deformed (skin pass rolled) steel substrates [198]. In those cases, the authors did not observe any orientation relation between the grains of the substrate and the coating.

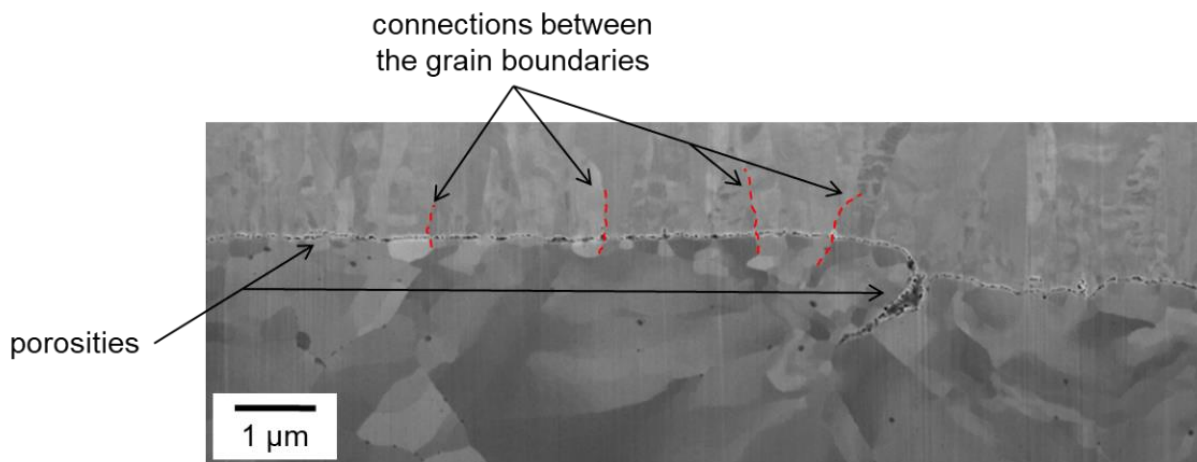


Fig.53: Cross-sectional micrograph of Zn-Mn deposited under continuous current at 0.015 A/cm² after FIB-SEM milling and polishing, focus of the substrate-coating interface

3.2.5. Discussion and conclusion

In this first part, the electrodeposition of Zn-Mn coatings under continuous currents and from additive-free chloride electrolytes was investigated.

The results obtained show a good correlation between the potentiostatic and galvanostatic modes, with an increase of the Mn content with increase of the applied potential or current density, according to the model of Brenner [194]. The deposition of coatings containing high Mn-contents and presenting a satisfactory appearance and homogeneity was however challenging. On the basis of the Mn content and the deposit morphology, the optimal deposition conditions under continuous current were defined with an applied current density of -0.015 A/cm^2 permitting to obtain relatively homogeneous deposits containing about 13 wt.% Mn.

Further analyses of these deposits revealed a monophasic crystallography and a strong preferential orientation with the basal planes (00.2) oriented parallel to the surface of the deposits. It appeared that the deposits form an interesting microstructure composed of large columnar grains presenting a conical shape. The presence of strata was observed in those grains, whose origin remains unknown. These strata are however most likely attributed to some local chemical variations or due to some artefacts from the FIB preparation.

Porosity was observed at the interface between the deposit and the substrate, ascribed to hydrogen evolution leading to the formation of bubbles at the interface. In numerous cases, these pores channel towards the surface and form some defects inside the deposits. In addition, the high intensity of the HER, in particular during the early stages of the process, was leading to possible hydrogen embrittlement in the steel substrate.

Although the deposits obtained under continuous current presented relatively high Mn-contents and a satisfactory appearance, numerous aspects and properties of these coatings can be improved. A refinement of the microstructure would be beneficial, especially towards the anticorrosive properties of the deposits. In addition, the high intensity of the HER during continuous electrodeposition leads to numerous problems such as porosity and inhomogeneous growth.

3.3. Towards new properties: study of the electrodeposition under pulse current

As previously discussed, the literature data on Zn-Mn alloys suggests that optimal anticorrosive properties are obtained for deposits containing between 10 and 30 wt.% Mn [96, 99, 101-105]. In addition to the composition of the alloys, the crystallography, the texture and the surface morphology of the deposits also play an important role in their corrosion behaviour. In the case of Zn deposits, it was demonstrated that close packed planes were more prone to resist corrosion and dissolution due to the high binding energy of the atoms in this configuration [209, 210]. This means that deposits presenting a preferential basal (00.2) fiber texture have higher corrosion resistance than deposits presenting a pyramidal or a prismatic texture. Furthermore, it is well known that the texture of metallic deposits has an impact on the mechanical properties.

It was demonstrated in the previous section that the electrodeposition of Zn-Mn coatings under continuous current leads to various issues. The deposition of high Mn-containing deposits is quite challenging, in particular due to the HER leading to inhomogeneous deposits, inclusion of porosity and potential hydrogen embrittlement in the steel substrate.

The use of the pulse plating instead of the traditional continuous plating for the electrodeposition of Zn-Mn alloy coatings is expected to solve the above-mentioned issues and to significantly improve the properties of the deposits. According to the literature, the use of pulse plating permits to obtain higher Mn contents and monophasic deposits, both leading to advantageous anticorrosive properties. Due to the high number of process parameters involved, proper tuning of the deposit properties is also possible.

In this section, the pulse electrodeposition of Zn-Mn alloy coatings will be considered. The influence of the electrical and time parameters on the composition, morphology, microstructure, crystallography and texture of the deposits will be investigated. The deposits will be obtained from an additive-free chloride electrolyte described in Table 11, page 64 and using the experimental setup described in 2.2.2. A preliminary study of the electrolytic system under pulse current will be conducted prior to electrodeposition experiments in order to identify the optimal range of deposition parameters.

3.3.1. Preliminary modelling of the pulse electrodeposition

Pulse electrodeposition is affected by various processes such as the charge and discharge of the electrical double layer (EDL) and the depletion rate of the species near the electrode surface, also called maximum plating rate. In this section, the various phenomena involved during the pulse electrodeposition will be considered in order to define appropriate domains of investigation.

Charging and discharging time

When a peak cathodic current density is applied, a capacitive current first charges the double layer and is followed by a faradaic current during which metal deposition occurs [211, 212]. A similar process takes place when the current is switched off. As a result, these charging and discharging times, t_{ch} and t_{disch} respectively, are depending solely on the peak current density for a defined electrochemical interface, namely for a given electrolyte and working electrode.

In order to determine the values of t_{ch} and t_{disch} , the potential transients versus time were measured for a range of peak current densities (Fig.54). It appears from these measurements that a higher charging time is required at low peak current densities (Fig.54(a)), as already suggested by the models of Puipe and Ibl [212]. On the discharging time (Fig.54(b)), a minimum is observed at j_p of 0.03 A/cm² and an increase of the discharging time is noted with the increase and decrease of the peak current density. Additionally, the value of the discharging time measured at a peak current density of 0.02 A/cm² is quite close to the value of the off-time, calculated for these conditions according to the Eq.37. This particularity suggests that for pulse on-time below 20 ms and peak current densities below 0.02 A/cm², the off-time might be insufficient for a full capacitive discharge. To conclude, these experimental values of t_{ch} and t_{disch} correspond to the lower limits of the on- and off-time, respectively.

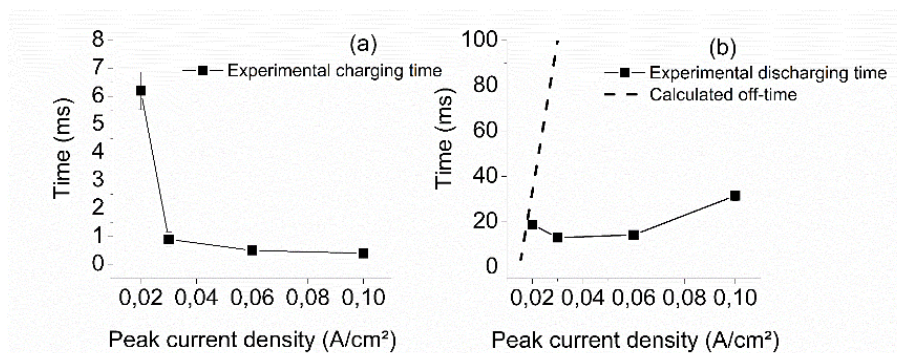


Fig.54: Values of the charging (a) and discharging (b) times measured from the potential transients vs. time at various peak current densities at a pulse on-time t_{on} of 100 ms and an average current density of 0.015 A/cm²; corresponding evolution of the calculated off-time t_{off} (dashed line, (b))

Maximum plating rate

The maximum plating rate usually corresponds to the current at which the concentration of the deposited species at the surface of the electrode reaches zero, thus called limiting current density j_{LIM} during continuous plating and $j_{p,LIM}$ for pulse plating. In the case of pulse plating, this current is related to the peak current density j_p applied for a pulse on-time t_{on} [211].

One way to determine the limiting current density during pulse plating $j_{p,LIM}$ is based on the dual diffusion layer concept. This model was proposed by Ibl on the basis of approximations of the limiting current density integrated over the pulse period [211, 213], and was corrected by Datta and Landolt [214] resulting in the following equation:

$$\frac{j_{p,LIM}}{j_{LIM}} = \frac{1}{\sqrt{\left(\frac{4}{\pi} \cdot \frac{D t_{on}}{\delta_s^2}\right) (1 - \gamma)^{3/2} + \gamma}} \quad \text{Eq.4}$$

With $j_{p,LIM}$ and j_{LIM} the pulse and continuous limiting current densities, respectively, with:

$$j_{LIM} = -\frac{DzFC_{\infty}}{\delta_s} \quad \text{Eq.5}$$

with the duty cycle γ defined by Eq.1, D the diffusion coefficient, δ_s the thickness of the diffusion layer.

During continuous current electrodeposition, the applied current density is usually chosen below 0.4 times the limiting current density. This is due to the fact that the use of higher currents leads to the unstable growth of the deposit and to the formation of protrusions and dendrites [215]. For an applied current density higher than 0.5 times the limiting current density, the formation of dendrites is strongly enhanced [215]. Studies performed by Chène and Landolt on pulse electrodeposited copper seem to reinforce these challenges with compact deposits obtained at high current efficiencies with $j_p/j_{p,LIM}$ ratios up to 1 [216].

The phenomenon of pulse limiting current can be illustrated by the measurement of the transition time during the monitoring of the deposition potential, as presented in Fig.55 where two reactions are taking place. The first reaction occurring at a potential around -1.8 V corresponds to the metal deposition and lasts about 16 ms. When the metal ions are depleted in the vicinity of the cathode, the reaction switches to the next available reaction, in this case the hydrogen evolution at a potential more cathodic, here around -2.1 V.

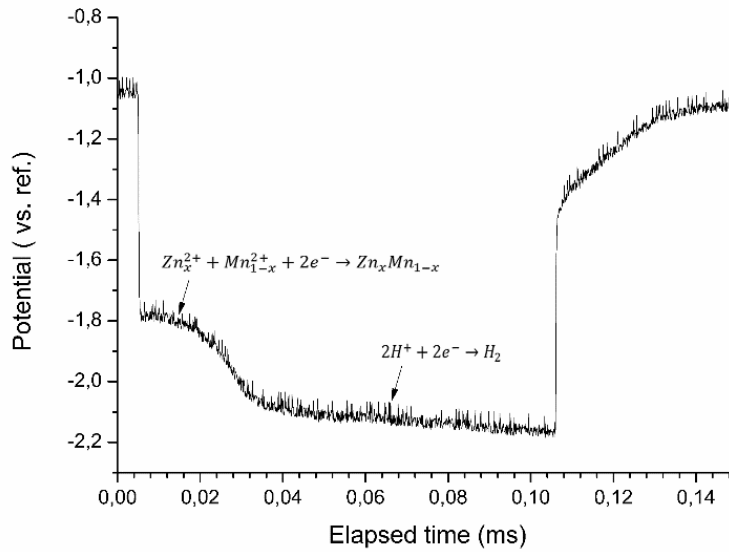


Fig.55: Typical potential transient during pulse electrodeposition at a t_{on} of 100 ms, an average current density of 0.015 A/cm² and a peak current density of 0.1 A/cm²; evolution from Zn-Mn electrodeposition to hydrogen evolution

Available range of parameters

The phenomena of charge/discharge and maximum plating rate described previously are illustrated in Fig.56 depending on the on-time and peak current density, for an average current density of 0.015 A/cm².

- The measurements of the charging and discharging times based on the potential transients define two regions, namely **region 2** in which the off-time t_{off} is insufficient for the full capacitive discharge, and **region 3** in which the pulse on-time is too low, associated to pure capacitive current with no faradaic part (i.e. deposition does not occur).
- **Region 4** corresponds to the experimental pulse limiting current density where the metal ions are depleted and the HER takes place.

The theoretical plating rate was also determined using eq.4 and considering the Zn²⁺ ions as the limiting specie, with a diffusion coefficient $D = 7.03 \times 10^{-6}$ cm²/s [217] and a thickness of the diffusion layer determined as $\delta_s = \sqrt{D \times t_{on}}$. The limiting $j_{p,LIM}/j_{LIM}$ ratios of 0.4, 0.5 and 1 were used to determine the regions 5, 6 and 7, respectively.

- **Region 5** is defined by $0.4 < j_{p,LIM}/j_{LIM} < 0.5$ and represents the domain where protrusions are supposed to occur during continuous plating (CP).
- **Region 6** is defined by $0.5 < j_{p,LIM}/j_{LIM} < 1$ and corresponds to the expected rapid formation of dendrites under CP mode.
- **Region 7** is defined by $j_{p,LIM}/j_{LIM} > 1$ and represents the limit fixed by Chène and Landolt under pulse currents [216].

This plot highlights the **region 1**, where the time and electrical parameters should be optimal.

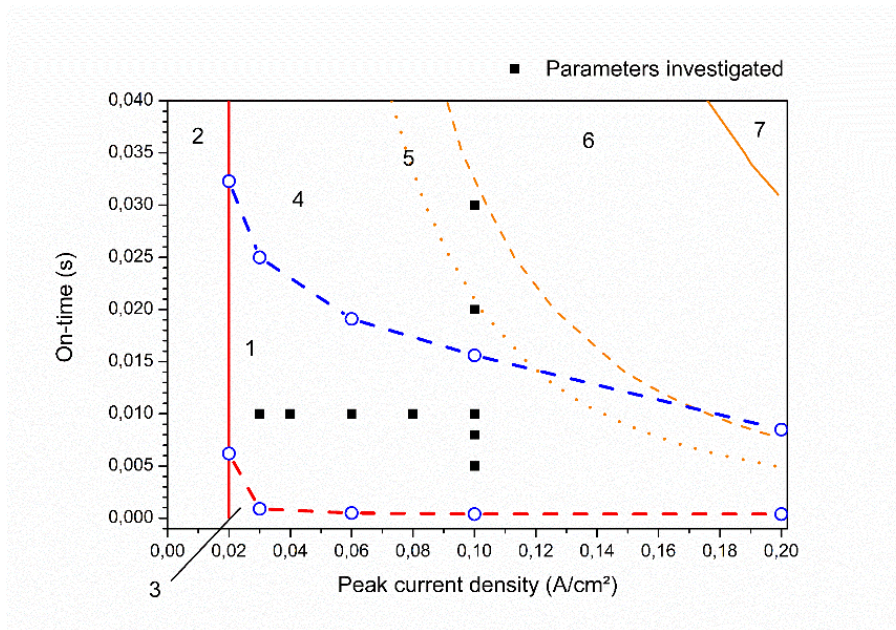


Fig.56: Illustration of the phenomena of charge/discharge and maximum plating rate from experimental monitoring of the potential vs. time (circles) and theoretical calculations. Range of optimal parameters (1); domain of $t_{\text{disch}} > t_{\text{off}}$ (2); domain of $t_{\text{ch}} > t_{\text{on}}$ (3); pulse limiting current density and transition time where depletion of metal ions occurs, as determined experimentally (4); domain where protrusions are expected during continuous plating with $0.4 < j_{p,LIM}/j_{LIM} < 0.5$ (5); domain where dendrites are expected during continuous plating with $0.5 < j_{p,LIM}/j_{LIM} < 1$ (6); and theoretical limit of the pulse plating $j_{p,LIM}/j_{LIM} > 1$ (7)

Conclusion

On the basis of this preliminary study and the information displayed on the Fig.56, the optimal set of parameters could be defined within the following limits:

- Peak current density ranging from 0.03 up to 0.1 A/cm²
- On-time ranging from 5 up to 30 ms

In the upcoming sections, the influence of these parameters on the material properties of the deposits will be thoroughly investigated and discussed.

3.3.2. Influence on the composition

Effect of the electrical parameters

The influence of the electrical parameters, namely the average and peak current densities, on the Mn content of the deposits was investigated by means of SEM-EDS, with the Fig.57 showing the influence of the alloys composition depending on the peak and average current densities. All deposits were obtained with a pulse duration t_{on} of 10 ms.

The results show an increase of the Mn content with the increase of the peak current density from 0.025 to 0.06 A/cm², where a plateau seems to be reached. This increase of the Mn content at higher peak current densities was previously observed by Danilov et al. [128]. As previously stated, the electrodeposition of Zn-Mn alloys follows a normal codeposition mechanism [194], corresponding to the behaviour observed here. On the other hand, it is important to note that for a decreasing peak vs. average current density ratio, the resulting duty cycle increases. For duty cycles above 0.5, i.e. $j_p < 0.03$

A/cm^2 and $j_p < 0.04 A/cm^2$ for j_a of $0.015 A/cm^2$ and $0.02 A/cm^2$ respectively, the off-time becomes shorter than the on-time which means that the deposition behaviour becomes closer to that observed in continuous plating. Two phenomena may take place in this case:

- the extended on-time leads to an increase of the hydrogen evolution hindering Mn codeposition [194]
- the electrolyte is not able to be fully replenished in the vicinity of the cathode due to the reduced off-time, leading to the faster depletion of the metallic ions and a higher intensity of the HER.

A further increase of the peak current density above $0.06 A/cm^2$ and up to $0.1 A/cm^2$ does not seem to significantly affect the amount of Mn codeposited. For this range of high current densities, the stagnation of the Mn content can be explained by two competing mechanisms:

- the amount of Mn is increasing due to the mechanism of normal codeposition discussed previously
- the resulting decrease of the duty cycle (due to the increased peak current density) leads to an increase of the off-time (by considering j_a and t_{on} constant). In the case of Zn-Mn alloys, the use of extensive off-time was stated to initiate surface corrosion and preferential dissolution of Mn thus reducing the amount of Mn incorporated [211].

The investigations carried out at various average current densities did not result in significant variations of the Mn content (Fig.57). This observation is supported by the results reported by Müller et al. [106, 129] where stable Mn contents of about 15wt.% were observed in the $0.01 - 0.02 A/cm^2$ range of j_a . Further increase of the average current density above $0.02 A/cm^2$ would result in an increase of the duty cycle and as a result in a decrease of the off-time. It has been observed that the required discharging time at high current densities can become quite significant (Fig.54). Therefore, the deposition at high duty cycle and high peak current densities would only result in the depletion of the electrolyte and lower Mn contents.

As a result, it seems that the deposition of coatings with Mn content higher than 15 wt.% is not possible by further increasing the average and/or peak current densities in the conditions investigated here. The highest Mn content measured in this study was of 15.2 wt.% obtained at an average current density of $0.015 A/cm^2$, a peak current density of $0.1 A/cm^2$ and a pulse duration of 10 ms.

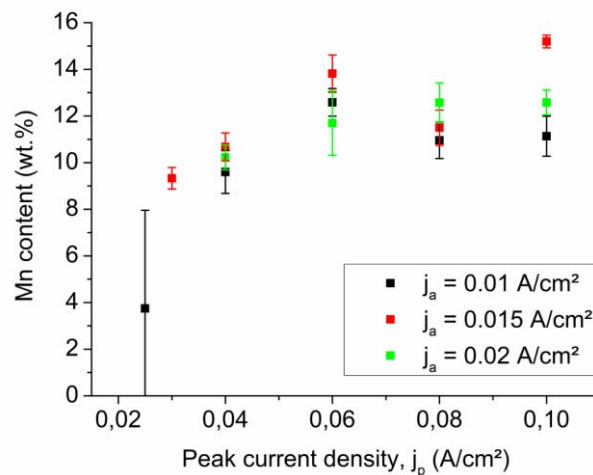


Fig.57: Dependency of the Mn content on the peak current density j_p for average current densities of 0.01, 0.015 and $0.02 A/cm^2$. In all cases, the pulse duration t_{on} is of 10 ms

Effect of the time parameters

The influence of the on- and off-time on the composition of the deposits was investigated by means of SEM-EDS analyses with the resulting Mn contents presented in Fig.58. A clear trend can be observed with the decrease of the Mn content with an increase of the time parameters, namely for t_{on} and t_{off} above 10 and 57 ms, respectively. Below these values, it seems that a plateau is reached with a Mn content of approximately 15 wt.%. It should be noticed that the average and peak current densities are kept constant during those experiments, which means that the duty cycle is also constant and equal in this case to 0.15. The decrease of the Mn content with the increase of the on- and off-time was already observed by Müller et al. [106]. This phenomenon can be explained by two hypotheses. As previously stated, surface corrosion is likely to occur during the relaxation time, leading to the preferential dissolution of Mn [211]. A second hypothesis in this case is related to the extended on-time, above the transition time according to the study of the process window (Fig.56). This may lead to the depletion of the metallic ions in the vicinity of the cathode and to a higher intensity of the HER.

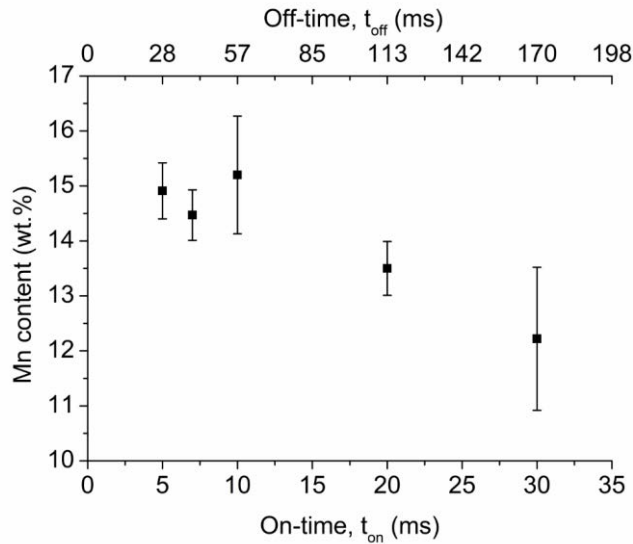


Fig.58: Dependency of the Mn content on the pulse on-time t_{on} and off-time t_{off} for an average current density $j_a = 0.015$ A/cm² and a peak current density $j_p = 0.1$ A/cm²

3.3.3. Efficiency

The faradaic efficiency of the deposits was evaluated by means of gravimetric method, based on the ratio between the theoretical and experimental mass of coating deposited. The theoretical thickness is calculated from the following equation:

$$thickness = \frac{m_{deposited}}{S\rho_{Zn-Mn}} \quad \text{Eq.47}$$

With $m_{deposited}$ determined from the equations 43 and 44 detailed in the section 2.5.1 and ρ_{Zn-Mn} the density of the deposited alloy, accounting for the Mn content measured on the sample via EDS.

The values obtained on the pulse coatings deposited at an average current density of 0.015 A/cm² and various peak current densities and pulse durations are summarized in the three-dimensional scatter plot presented in Fig.59.

The results show a clear increase of the faradaic efficiency with decrease of the pulse duration, with up to 90% efficiency achieved for an on-time of 5 ms. The use of a pulse on-time of 10 ms results in a faradaic efficiency around 75%, similar to the 73% obtained under continuous current with a current density of 0.015 A/cm². For longer on-times of 20 and 30 ms, a strong decrease of the efficiency is observed, down to 66 and 47%, respectively. These low efficiencies observed for longer pulses can be explained by two factors. The increase of the contribution of the HER on one hand, above the transition time is very likely to explain these results. On the other hand, an increase of the pulse duration means an increase of the off-time, during which dissolution phenomenon are likely to occur. This behaviour is observed for peak current densities of 0.06 and 0.1 A/cm².

By comparison with the reference literature, Müller et al. [106] observed in the presence of EDTA an increase in the current efficiency with increase of the off-time. However, the faradaic efficiencies measured by the authors were quite low, systematically below 45%.

Variations of the peak current density, with average current density and pulse duration constant, does not result in a clear influence on the faradaic efficiency. The highest efficiencies are obtained with peak current densities of -0.04 and -0.1 A/cm² resulting in 83 and 76%, respectively.

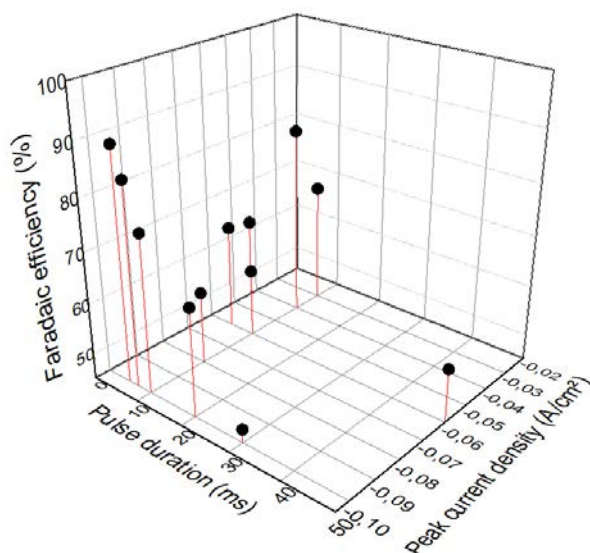


Fig.59: Faradaic efficiencies of the pulse deposits determined on the basis of the ratio between theoretical and experimental mass of coating deposited

3.3.4. Influence on the morphology

Effect of the electrical parameters

The influence of the electrical parameters, namely the average and peak current densities, on the morphology of the deposits was investigated by means of SEM. The micrographs obtained on the surface of the alloys deposited at an average cathodic current density of 0.015 A/cm² and a pulse duration of 10 ms are presented in Fig.60.

A first notable change of the surface morphology can be observed in comparison to the deposits obtained under continuous current (Fig.45). Under pulse plating conditions (Fig.60), the deposits are homogeneous with uniformly distributed crystallites and almost defects free. This improvement of the surface homogeneity brought by the pulse plating was already largely reported in the literature, as well as the improvement of the surface appearance and the formation of smaller crystallites [106, 129, 218].

A refinement of the crystallite size can be observed with the increase of the peak current density. Up to $j_p = 0.04 \text{ A/cm}^2$ (Fig.60(a)) the crystallites appears quite large while above 0.06 A/cm^2 they are significantly smaller. This refinement of the crystallites is usually associated to the increase of the overpotential [202, 219, 220], here caused by the increased of the cathodic peak current density, and the higher concentration of adatoms favouring nucleation over crystallite growth at high current densities [126].

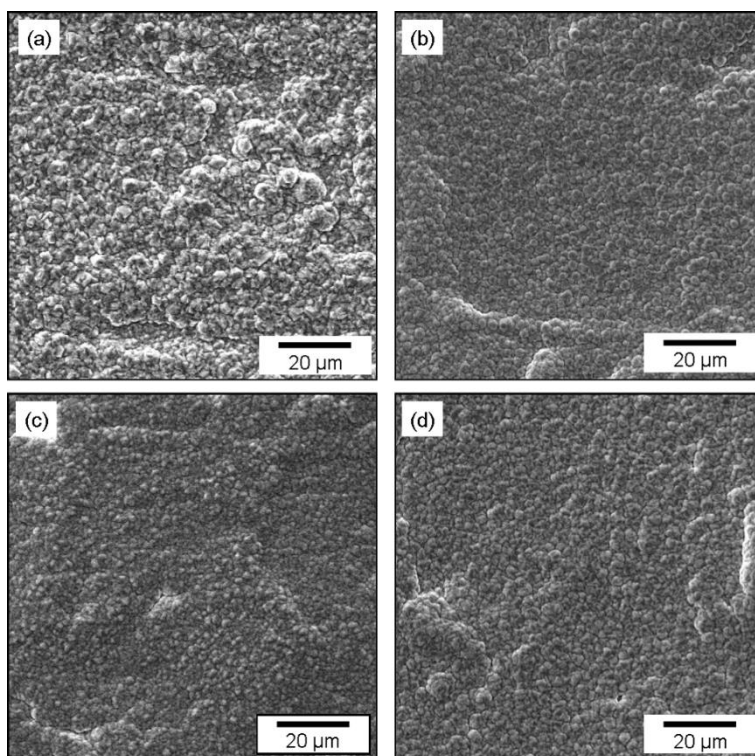


Fig.60: SEM micrographs of the surface of Zn-Mn deposits obtained on DC06 with $j_a = 0.015 \text{ A/cm}^2$ and $t_{on} = 10 \text{ ms}$, $j_p = 0.04 \text{ A/cm}^2$, $t_{off} = 10 \text{ ms}$ and containing 9.6 wt.% Mn (a); $j_p = 0.06 \text{ A/cm}^2$, $t_{off} = 30 \text{ ms}$ and containing 13.8 wt.% Mn (b); $j_p = 0.08 \text{ A/cm}^2$, $t_{off} = 43.3 \text{ ms}$ and containing 11.5 wt.% Mn (c); $j_p = 0.1 \text{ A/cm}^2$, $t_{off} = 56.7 \text{ ms}$ and containing 15.2 wt.% Mn (d)

Effect of the time parameters

The influence of the time parameters, namely the on- and off-time, on the morphology of the deposits was investigated by means of SEM. The micrographs obtained on the surface of the alloys deposited at an average cathodic current density of 0.015 A/cm^2 and a peak current density of 0.1 A/cm^2 are presented in Fig.61.

The variation of the on- and off-time leads to significant changes in the morphology of the deposits. At a long on-time of 30 ms, the deposits show a well-defined chevron-type morphology which is typical of electrodeposited Zn (Fig.61(a)). This morphology was also observed by Savall et al. [122] on Zn-Mn deposits obtained by continuous plating and by Müller et al. on pulse Zn-Mn deposits [129]. By decreasing the pulse on-time down to 20 ms, this chevron-type morphology can still be distinguished but the edges seem to smoothen (Fig.61(b)). With a t_{on} of 10 ms, the proportion of finer crystallites between the chevrons seems to increase and the surface roughness seems to decrease (Fig.61(c)). Using short pulses of 5 ms, the deposits appear to be significantly smoother and more homogeneous than using longer time parameters (Fig.61(d)). No specific geometries could be distinguished from the surface of those samples. While the impact of j_p on the crystallite size is well documented in the literature, the contribution of the pulse on-time is still unclear. The formation of smaller crystallites when using short

pulses, as observed in this work, can be expected. The use of short pulses does not permit the growth of the crystallites and the repeated interruptions of the deposition process promote nucleation and formation of new crystallites over growth. These hypotheses are in good agreement with some of the reference literature [211]. However, these observations are in apparent contradiction with Youssef et al. [202], reporting a decrease of the crystallite size with increase of the on-time on Zn electrodeposits. Nevertheless, their results were obtained at varying duty cycles with increasing average current density that could involve additional phenomena.

The surface roughness was measured by means of confocal microscopy and the arithmetical mean roughness S_a and maximum height S_z were determined (Fig.62). The measurements show firstly that the arithmetic mean surface roughness is not clearly impacted by the time parameters. For on-time from 7 to 30 ms, the measured S_a was either almost identical or lower than the one measured on the steel substrate at about $0.85 \mu\text{m}$. Besides, the S_a/S_z ratio corresponding to the surface roughness homogeneity is also not significantly impacted. The best homogenizing effect was obtained with a pulse on-time of 5 ms presenting the highest ratio.

This levelling effect can be explained by the following mechanism:

- Due to the use of short pulses, the growth of the crystallites is repeatedly interrupted which inhibits the formation of columns and dendrites and leads to a more homogeneous crystallite size distribution. The use of shorter pulses further enhances the formation of homogeneous crystallites and results in the formation of evenly levelled deposits. This also correlates very well with the reduction of the crystallite size previously discussed.

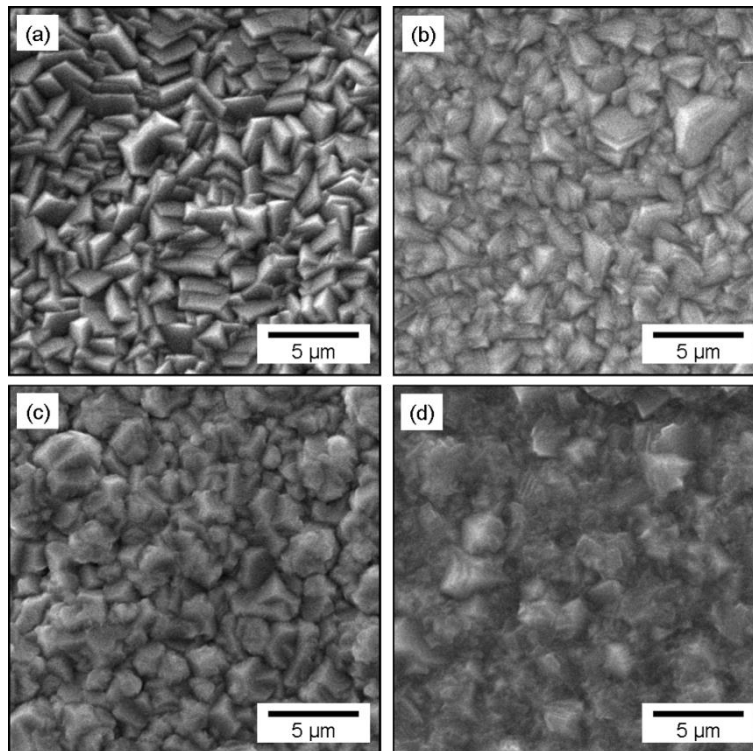


Fig.61: SEM micrographs of the surface of Zn-Mn deposits obtained on DC06 steel with $j_a = 0.015 \text{ A/cm}^2$ and $j_p = 0.1 \text{ A/cm}^2$ and different time parameters: $t_{\text{on}} = 30 \text{ ms}$ and $t_{\text{off}} = 170 \text{ ms}$ (12.2 wt.% Mn) (a), $t_{\text{on}} = 20 \text{ ms}$ and $t_{\text{off}} = 113 \text{ ms}$ (13.5 wt.% Mn) (b), $t_{\text{on}} = 10 \text{ ms}$ and $t_{\text{off}} = 56.7 \text{ ms}$ (15.2 wt.% Mn) (c) and $t_{\text{on}} = 5 \text{ ms}$ and $t_{\text{off}} = 28.3 \text{ ms}$ (14.9 wt.% Mn) (d)

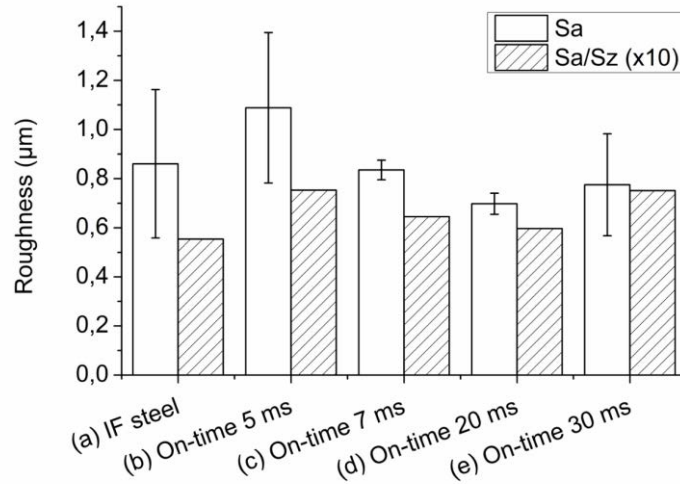


Fig.62: Evolution of the arithmetical mean roughness S_a (μm) and the S_a/S_z ratio for the as-delivered steel substrate (a) and deposits obtained at pulse on-time t_{on} from 5 to 30 ms (b – e)

3.3.5. Influence on the microstructure

General microstructure

The microstructure of the pulse Zn-Mn deposits was analysed by SEM on cross-sections prepared via the FIB technique. Due to the important time required to prepare a FIB cross-section, only a selection of pulse deposits were analysed. Two deposits, obtained under pulse current at an average current density of 0.015 A/cm^2 , a peak current density of 0.1 A/cm^2 and on-time of 30 and 5 ms were investigated, with micrographs presented in figures Fig.63 and Fig.64, respectively.

The inner microstructure as well as the shape of the grains is well distinguishable on the micrograph of the deposits obtained with a t_{on} of 30 ms (Fig.63). The deposits present a mixture of large and sort of columnar grains and smaller equiaxed grains. It can be observed that those small grains appear mostly near the substrate – coating interface, in the first 2 – 3 μm of the deposit. This organization inside the deposit seems similar to the one observed under continuous current (Fig.50). Considering the deposits obtained with a pulse duration of 5 ms (Fig.64), the microstructure is hardly recognizable and appears to be significantly finer in comparison to the pulse deposits obtained at t_{on} of 30 ms (Fig.63). Also, it seems that the inner microstructure of the deposits is much more homogeneous.

Overall, it seems that the grain size in the pulse deposits obtained with an on-time of 30 ms is reduced in comparison to the deposits obtained under continuous current. When considering the micrograph of the deposits obtained with a t_{on} of 5 ms, it can be supposed that the use of pulse plating, especially with short pulse durations t_{on} , permits to significantly reduce the grain size and refine the microstructure. This observation confirms the statements of the previous chapter 3.3.4. Indeed, the use of pulses, in particularly short pulses, permits to promote the nucleation of new grains over the extensive growth of already existing ones [211].

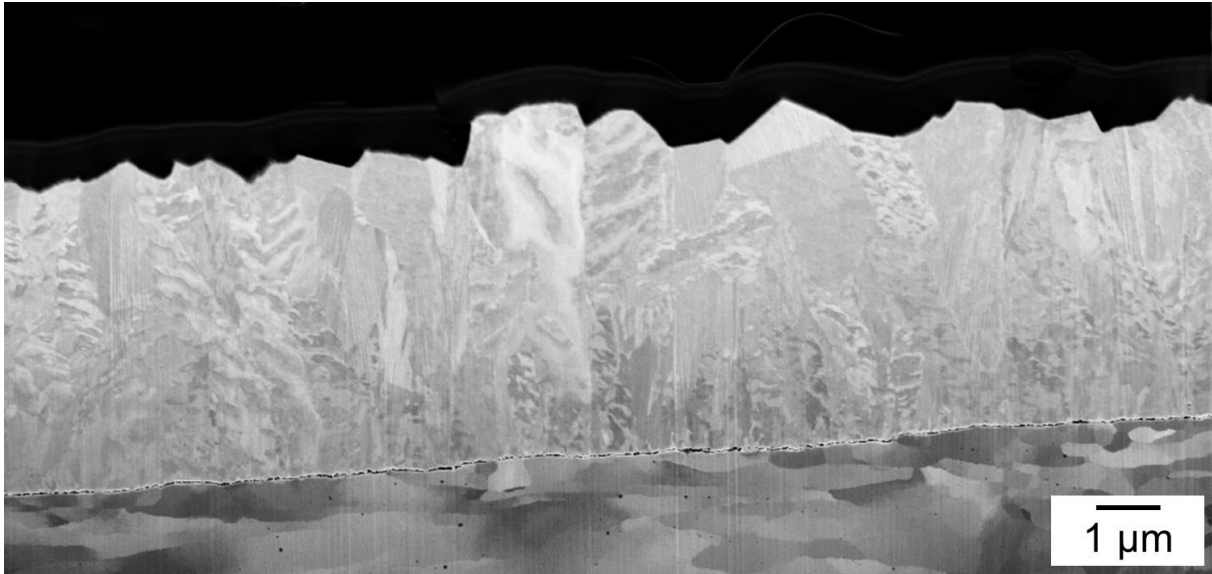


Fig.63: Cross-sectional micrograph of Zn-Mn deposited under pulse current at an average current density of 0.015 A/cm², a peak current density of 0.1 A/cm² and an on-time of 30 ms, after FIB-SEM milling and polishing

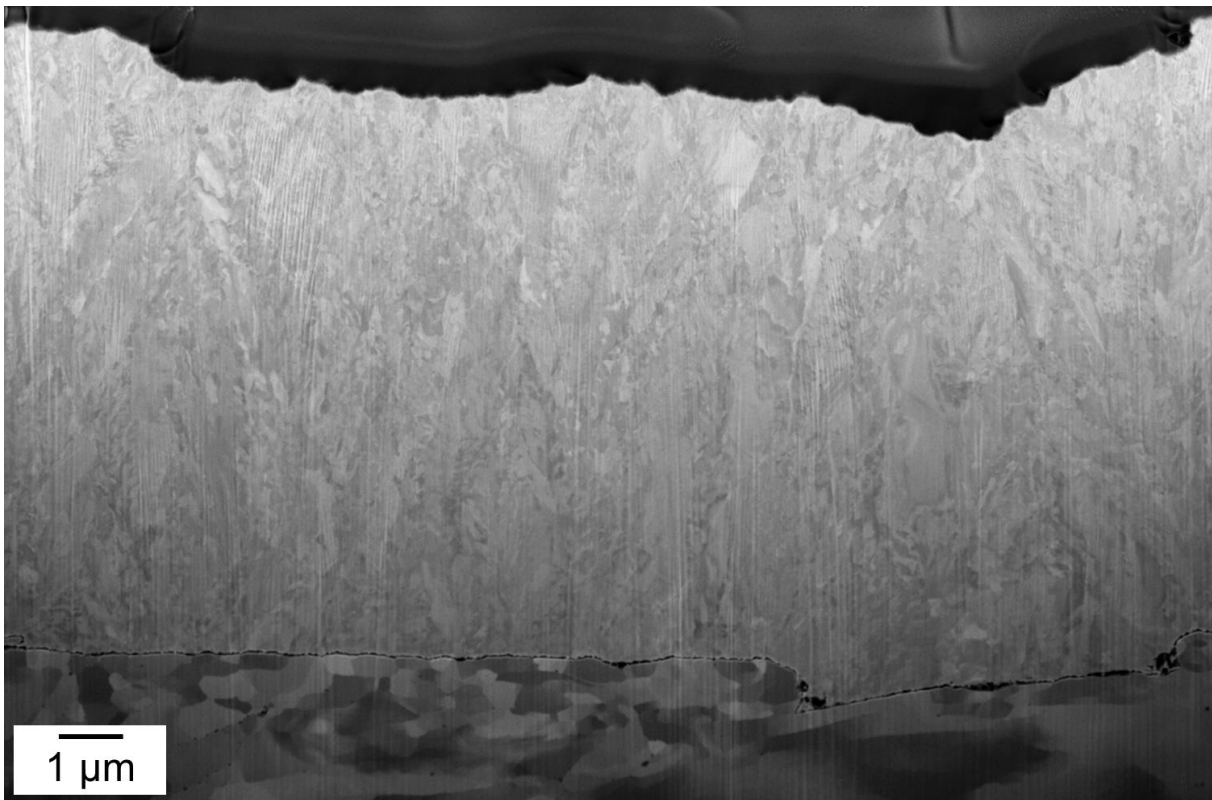


Fig.64: Cross-sectional micrograph of Zn-Mn deposited under pulse current at an average current density of 0.015 A/cm², a peak current density of 0.1 A/cm² and an on-time of 5 ms, after FIB-SEM milling and polishing

The previously-mentioned levelling effect can also be observed when comparing the figures Fig.63 and Fig.64, although being much more pronounced than with the surface roughness measurements described previously (Fig.62). It appears clearly that the deposits obtained with a 5 ms pulse duration (Fig.64) present a much more homogeneous thickness distribution in comparison to the deposits obtained with a 30 ms on-time (Fig.63) as well as a much lower roughness. Such a difference with the roughness measurements can however be explained from the local roughness of the substrate steel. Indeed, it can be observed that the pulse deposits tend to reproduce the roughness of the steel substrate.

Strata

The presence of strata could still be observed under pulse current. However, it appears that these strata are much more distinguishable on the deposits obtained at t_{on} of 30 ms (Fig.63). They present similar shapes and sizes as those observed under continuous current (Fig.50) and are mostly oriented parallel to the growth front as well. On the deposits obtained with short pulse durations however, no distinction between the fine grains and the strata could be made (Fig.64).

On the basis of these observations on the deposits obtained under pulse current, the hypotheses previously formulated in chapter 3.2.4 can be discussed as follows:

- As previously stated, the first possibility could be due to some local variations of the Mn^{2+}/Zn^{2+} ratio or some perturbations of the applied current, leading to some changes of the composition. In the case of pulse plating, this hypothesis would still be valid independently from the pulse parameters applied.
- Similarly, the second hypothesis stating that strata could be due to some disorientations inside the grains due to variations of the overpotential also stay valid under pulse currents.
- The last hypothesis, suggesting that adsorption of hydrogen due to the HER is responsible for the formation of strata also stays plausible under pulse currents. According to the process window for Zn-Mn, the limiting current is exceeded for pulse duration above 17 ms (Fig.56). This means that HER occurs for on-time above 17 ms, with an increased intensity as the pulse duration increases. Accordingly, the strata observed on the deposits obtained with a t_{on} of 30 ms are much more pronounced and distinguishable than on the deposits obtained with t_{on} of 5 ms. This hypothesis seems therefore much more likely than the other two.

In conclusion, the transfer from continuous to pulse plating and the variations of some of the pulse parameters seem to influence the formation of the strata. However, understandings on their origin are still very scarce and further characterization would be required to better comprehend their formation.

Substrate – coating interface

Closer examination of the substrate – coating interface revealed, similarly as for deposits obtained under continuous current, a thin layer of porosity along the interface. In comparison to the continuous coatings however, the pores observed in the figures Fig.65 and Fig.66 are much smaller in size. In this case again, numerous bridges ensure the connection between the substrate and the deposit. In addition, no pores were detected inside the substrate, which suggests that the use of pulse currents helps to decrease the hydrogen evolution.

The relation between the pulse parameters and hydrogen embrittlement was studied by Paatsch [221]. It was reported that a significantly lower amount of hydrogen was able to diffuse during pulse plating in comparison to continuous plating. In addition, the use of short pulses seemed to enhance this phenomenon. One suggested explanation is related to the formation of smaller grains when short pulses are used, which lead to more compact layers hindering hydrogen diffusion [221]. In any cases, it appears that the observations of this work are in good agreement with the early reports from Paatsch.

Some connections between the grain boundaries of the substrate and deposit can be observed, especially on the deposits obtained with pulse duration of 5 ms (Fig.66). Similar occurrences were already reported under continuous plating and by Greul et al. on Zn deposits [198]. In this case, it seems that the use of pulse plating over continuous plating does not significantly impact the orientation relations between the substrate and the deposit, as variations of the pulse parameters. Instead, the texture and the surface state

of the substrate steel, known to be a deciding factor for the first layers of the deposits [198, 199, 222], should be considered.

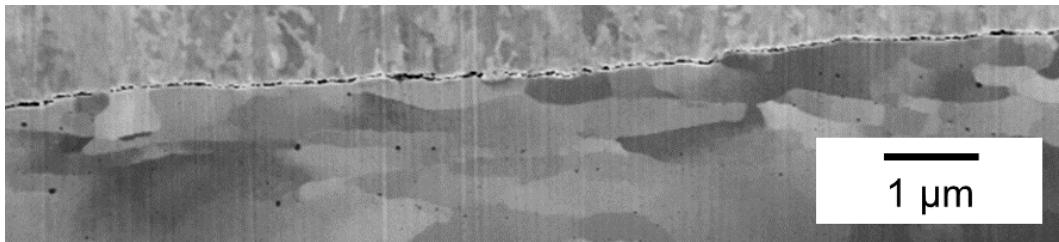


Fig.65: Cross-sectional micrograph of Zn-Mn deposited under pulse current at an average current density of 0.015 A/cm², a peak current density of 0.1 A/cm² and an on-time of 30 ms, after FIB-SEM milling and polishing; focus on the substrate – deposit interface

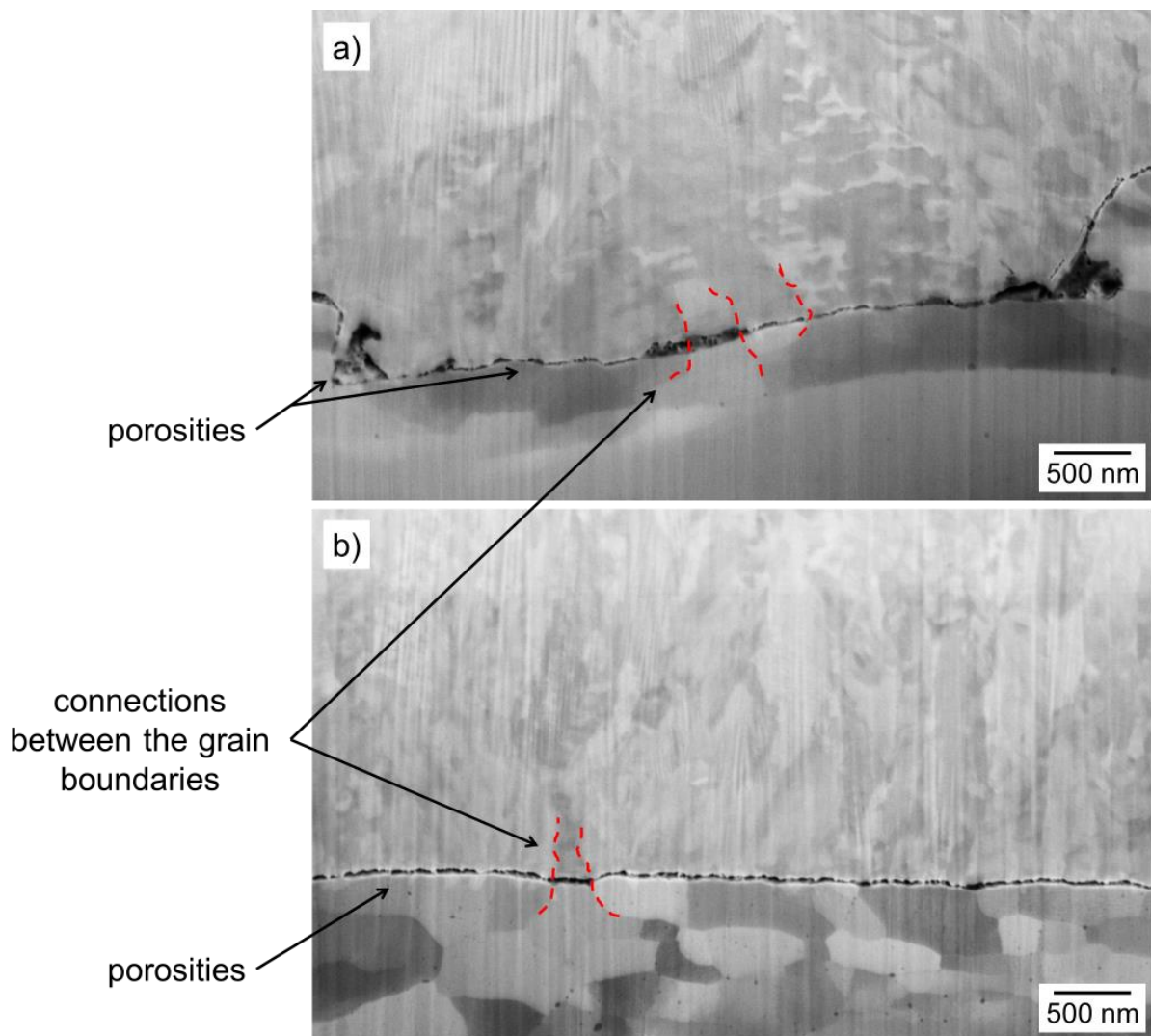


Fig.66: Cross-sectional micrographs of Zn-Mn deposited under pulse current at an average current density of 0.015 A/cm², a peak current density of 0.1 A/cm² and an on-time of 5 ms, after FIB-SEM milling and polishing; focus on the substrate – deposit interface (a) and (b)

3.3.6. Influence on the crystallography and texture

Effect of the electrical parameters

The de-textured diffraction patterns obtained with rotation and tilt of the samples on the pulse Zn-Mn deposits at an average current density of 0.015 A/cm^2 , a t_{on} of 10 ms and peak current densities ranging from 0.03 up to 0.1 A/cm^2 are presented in Fig.67 from (b) to (f). As comparative purposes, the XRD pattern corresponding to the Zn-Mn deposit obtained under continuous current at 0.015 A/cm^2 was also represented in Fig.67a. In order to better define and further understand the textures formed on the deposits, additional analyses were conducted on a few selected samples. The pole figures obtained from the XRD measurements presented in Fig.67c, e and f are presented in the Fig.68, Fig.69 and Fig.70, respectively. These figures were obtained by using a fitting procedure for all XRD patterns, only the recalculated figures will be presented.

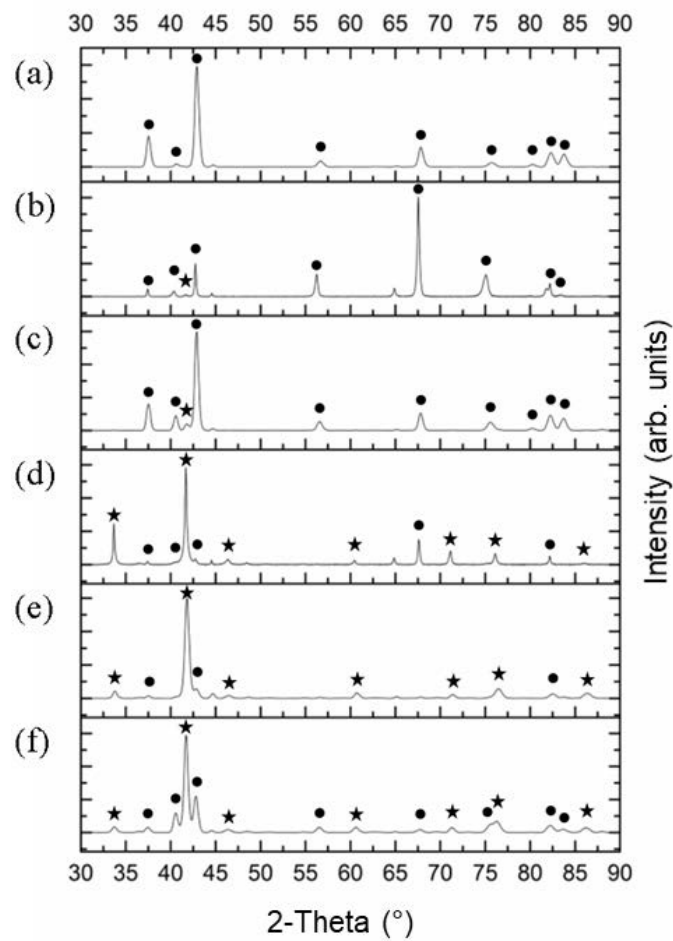


Fig.67: XRD patterns of Zn-Mn deposits obtained under continuous current at 0.015 A/cm^2 (a) and under pulse current at an average current density of 0.015 A/cm^2 , an on-time of 10 ms and a peak current density of 0.03 A/cm^2 (b), 0.04 A/cm^2 (c), 0.06 A/cm^2 (d), 0.08 A/cm^2 (e) and 0.1 A/cm^2 (f); diffraction peaks corresponding to the ϵ_2 -ZnMn (JCPDS n° 04-003-4358) phase ●, and to the γ -ZnMn (JCPDS n° 04-019-6455) phase ★; de-textured patterns obtained with rotation and tilt of the sample

At a low peak current density $j_p = 0.03 \text{ A/cm}^2$ (Fig.67b), the diffraction pattern corresponds to the hexagonal ϵ_2 -ZnMn phase (JCPDS n° 04-003-4358). A shift of the preferential orientation is observed from the (10.1) planes parallel to the surface under continuous current (Fig.67a) to the (11.0) planes toward the surface under pulse plating at 0.03 A/cm^2 . The (11.0) orientation means that the basal planes of the crystal are oriented perpendicularly to the surface of the deposit and corresponds to a prismatic

(type 2) texture, as already observed by Savall et al. [122], Close et al. [118], and Müller et al. [119] in the continuous modes. In addition, a weak signal corresponding to the cubic γ -ZnMn phase (JCPDS n° 04-019-6455) could be detected with a single peak at 41.8° .

An increase of the peak current density up to 0.04 A/cm^2 (Fig.67c) does not yield to significant changes of the phase composition. A biphasic alloy is obtained with the combination of the ϵ_2 -ZnMn and γ -ZnMn phase. Interestingly, it appears that the intensity of the diffraction peak (41.8°) corresponding to the cubic γ -ZnMn phase increases, suggesting an increased amount of this phase. It can also be noted that the preferential orientation of the hexagonal ϵ_2 -ZnMn phase significantly shifts from 0.03 to 0.04 A/cm^2 with in the latter case an apparent preferential orientation of the (10.1) planes toward the surface, as observed under continuous current and corresponding to the pyramidal (type 1) texture. On the other hand, it seems that the orientation of the cubic γ -phase does not evolve in this case with the (330) planes parallel to the surface.

The analysis of the pole figures (Fig.68) exposed the uncertainty of the X-ray diffractograms and the lack of information from this technique. Using the pole figures, two fibre textures could be defined for the predominant ϵ_2 -phase (Fig.68). The first one corresponds to a plane close to (11.0) which means that the basal plane is perpendicular to the growth direction. A second fibre texture of lower intensity could also be observed, corresponding to the plane (11.5) parallel to the surface which means that the basal plane is slightly tilted, with the c axis of the hexagon at an angle of 29° with the growth direction of the deposit. Analyses on the γ -phase also reveal a fibre texture close to the [100] axis tilted with an angle of about 10° (Fig.68), which means that the (330) plane present an angle of about 45° to the surface.

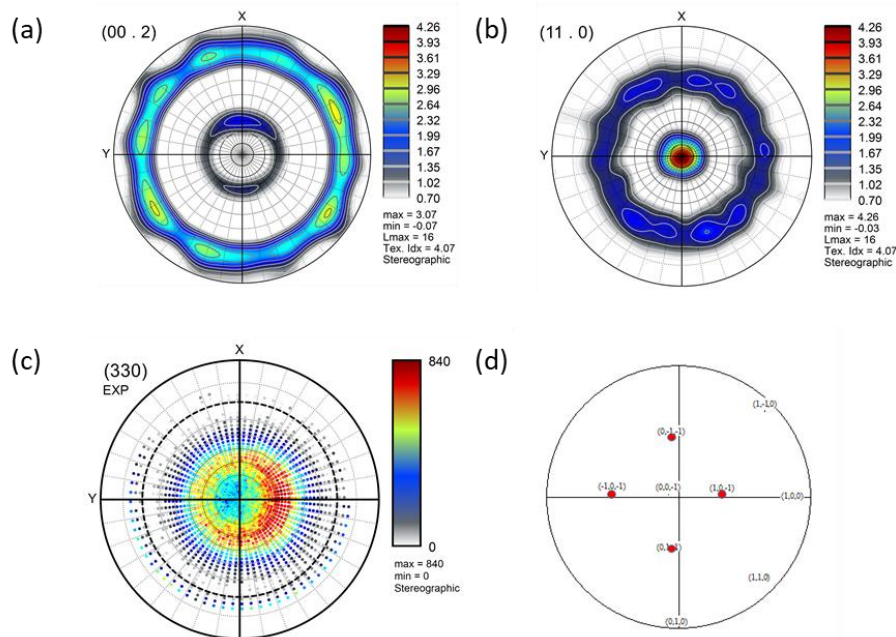


Fig.68: (00.2) (a), (11.0) (b) and (330) (c)(d) pole figures of Zn-Mn deposits obtained under pulse current at an average current density of 0.015 A/cm^2 , an on-time of 10 ms and a peak current density of 0.04 A/cm^2 ; pole figures corresponding to the hexagonal ϵ_2 -phase (a)(b) and to the cubic γ -phase (c)(d) and obtained from the XRD measurement presented in Fig.67c

For deposits obtained at a current density of 0.06 A/cm^2 (Fig.67d), the XRD pattern suggest the predominant presence of the cubic γ -ZnMn phase as well as the diffraction peaks corresponding to the ϵ_2 -ZnMn phase. The intensity of the diffraction peaks for both phases suggests a preferred orientation of the (330) and the (10.1) planes parallel to the surface.

For peak current densities above 0.06 A/cm^2 , the XRD patterns still show the presence of both hexagonal ϵ_2 -ZnMn and cubic γ -ZnMn phases, with a strong majority of the later phase. The signals corresponding to the ϵ_2 phase even almost disappear at a peak current density of 0.08 A/cm^2 (Fig.67e). Nevertheless, a decrease of the intensity for the γ phase is observed when the peak current density is pushed to 0.1 A/cm^2 (Fig.67f) which suggests a “come back” from the hexagonal phase.

However, further analyses of the pole figures on the deposits obtained at a peak current density of 0.08 A/cm^2 show some significant changes of the texture in comparison to the diffractogram analysis. A clear fibre texture along the $[111]$ axis (Fig.69) is observed, which means that the dense direction of the cubic phase follows the growth direction of the deposit. As a result, the (330) plane present an angle of about 35° to the surface that differs from the observations of the XRD patterns. A second weak $[110]$ fibre texture is also observed. Due to the low intensity of the hexagonal phase on the diffractogram, the pole figures corresponding to the ϵ -phase could not be obtained.

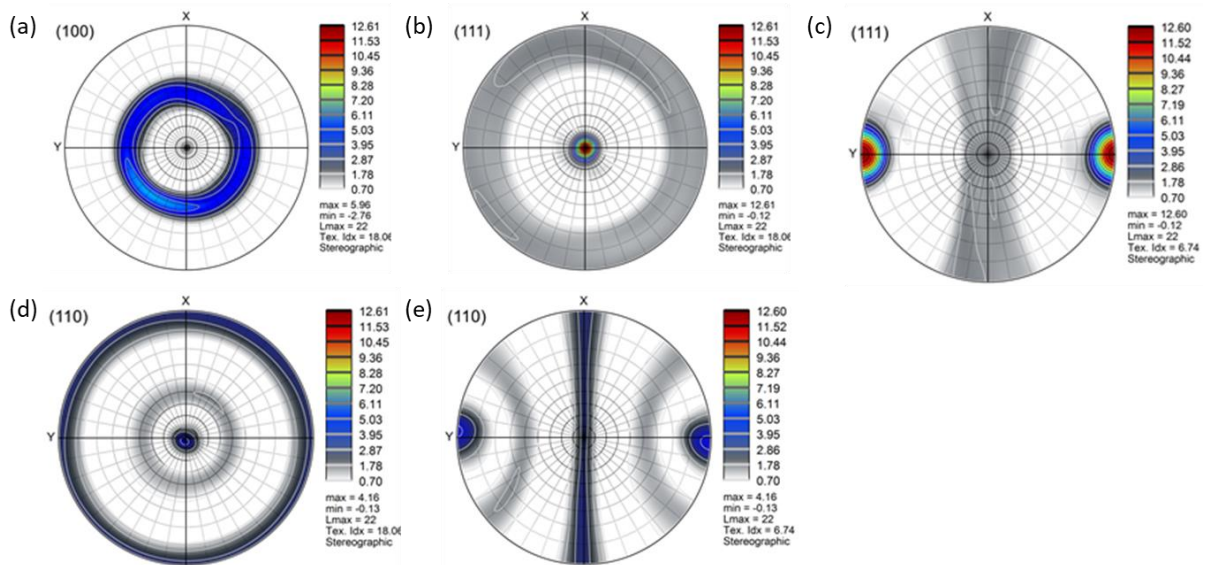


Fig.69: (100) (a), (111) (b) and (110) (d) pole figures of Zn-Mn deposits obtained under pulse current at an average current density of 0.015 A/cm^2 , an on-time of 10 ms and a peak current density of 0.08 A/cm^2 ; pole figures corresponding to the cubic γ -phase and obtained from the XRD measurements presented in Fig.67e; figures (c) and (e) obtained after a $\Pi/2$ rotation of the figures (b) and (d), respectively

In the case of the deposits obtained at a peak current density of 0.1 A/cm^2 , two fibres orientations were observed for the cubic γ -phase (Fig.70).

A first fibre is observed close to the $[110]$ axis while a second partial fibre of lower intensity is observed along the $[100]$ axis (Fig.70). Concerning the hexagonal ϵ -ZnMn phase (Fig.70), two fibres could also be identified as well with a first fibre oriented with the (11.5) plane parallel to the surface and a second one with the basal (00.2) plane parallel to the surface. On the basis of these analyses, a Burgers orientation relationship could be expected between the $[110]$ fiber of the cubic γ -phase and the $[00.2]$ fiber of the hexagonal ϵ -phase.

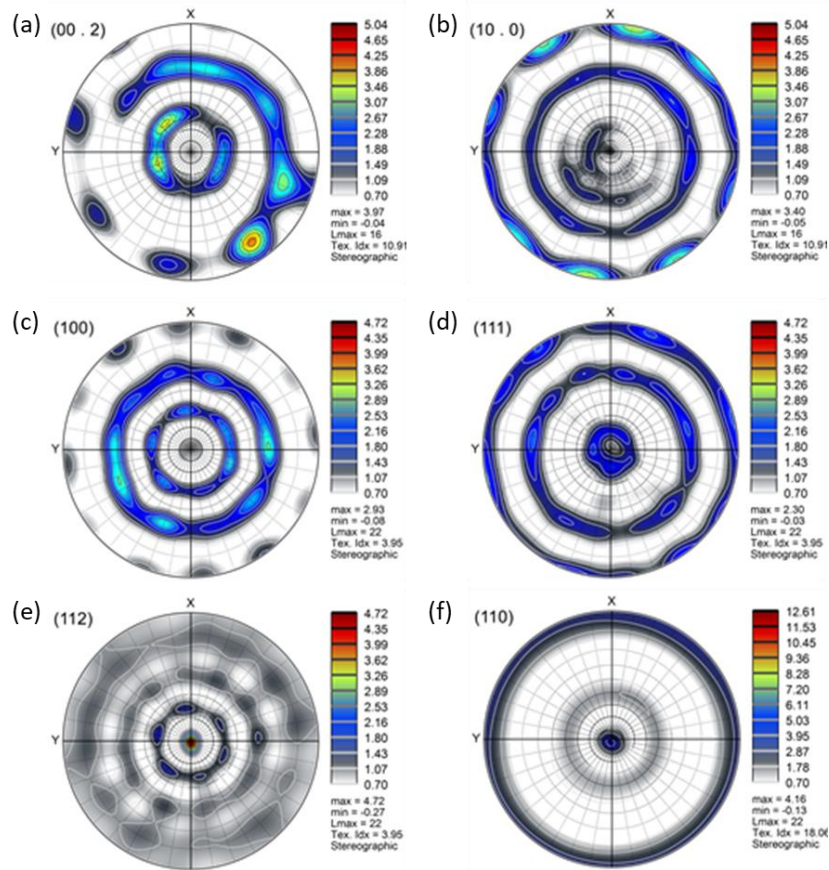


Fig.70: (00.2) (a), (10.0) (b) and (100) (c), (111) (d), (112) (e), and (110) (f) pole figures of Zn-Mn deposits obtained under pulse current at an average current density of 0.015 A/cm², an on-time of 10 ms and a peak current density of 0.1 A/cm²; pole figures corresponding to the hexagonal ϵ -phase (a)(b) and to the cubic γ -phase (c)(d)(e)(f) and obtained from the XRD measurement presented in Fig.67f

Effect of the time parameters

The XRD patterns obtained on the pulse Zn-Mn deposits at an average current density of 0.015 A/cm², a peak current density of 0.1 A/cm² and pulse durations ranging from 100 to 5 ms are presented in Fig.71 from (b) to (g). The diffractogram corresponding to the deposit obtained under continuous current at -0.015 A/cm² was also represented in Fig.71 (a) for comparative purposes.

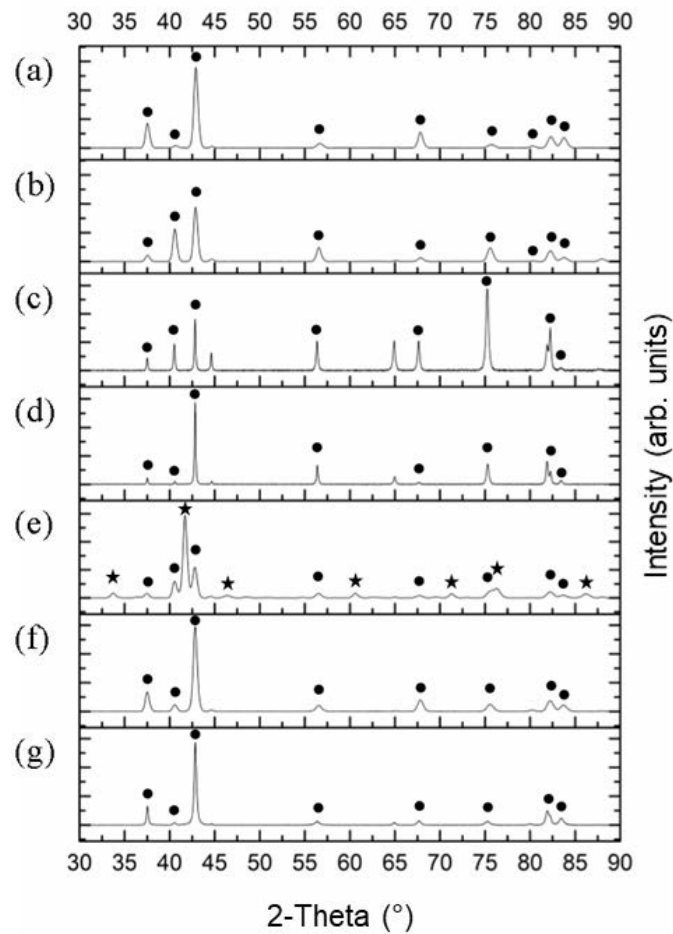


Fig.71: XRD patterns of Zn-Mn deposits obtained under continuous current at 0.015 A/cm^2 (a) and under pulse current at an average current density of 0.015 A/cm^2 , a peak current density of 0.1 A/cm^2 and on-time of 100 ms (b), 30 ms (c), 20 ms (d), 10 ms (e), 7 ms (f) and 5 ms (g); diffraction peaks corresponding to the ϵ_2 -ZnMn (JCPDS n° 04-003-4358) phase ●, and to the γ -ZnMn (JCPDS n° 04-019-6455) phase ★; de-textured patterns obtained with rotation and tilt of the samples

Pulse electrodeposition with a long on-time of 100 ms (Fig.71b) leads to a similar crystallography as the one obtained under continuous current (Fig.71a). The deposits are monophasic and composed of the hexagonal ϵ_2 -ZnMn phase and present a weak preferred orientation with the (10.1) and (00.2) planes towards the surface.

Further analyses of the pole figures, depicted in Fig.72, revealed a fibre texture with the $(2\bar{1}.5)$ planes oriented parallel to the surface, which translates with the basal plane tilted with an angle of about 35° to the surface of the deposit.

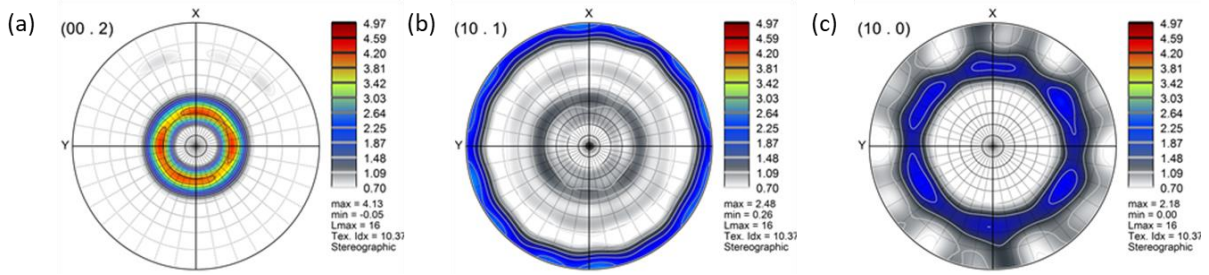


Fig.72: (00.2) (a), (10.1) (b) and (10.0) (c) pole figures of Zn-Mn deposits obtained under pulse current at an average current density of 0.015 A/cm², an on-time of 100 ms and a peak current density of 0.1 A/cm²; pole figures corresponding to the hexagonal ϵ -phase and obtained from the XRD measurement presented in

Decrease of the on-time to 30 ms seems to lead to randomly oriented deposits (Fig.71c). Interestingly, the further decrease of the t_{on} to 20 ms yields to a strong preferred orientation of the deposits with the (10.1) planes parallel to the surface (Fig.71d). With a pulse duration of 10 ms (Fig.71e), both hexagonal ϵ_2 -ZnMn and cubic γ -ZnMn phases are observed, as previously stated in Fig.67f. Remarkably, at $j_p = 0.1$ A/cm² the γ -ZnMn phase could only be observed with a pulse duration of 10 ms. The deposits obtained with short on-times of 7 and 5 ms present the similar crystallography with the ϵ_2 -ZnMn phase and a preferred orientation of the (10.1) planes oriented towards the surface.

Discussion

It was observed in the previous paragraphs that the pulse parameters, namely the peak current density and the pulse duration, had a significant impact on the crystallography of the coatings. A summary of the crystallographic phases observed on the deposits depending on the peak current density and the pulse duration is presented in Fig.73.

It was observed in the range of conditions investigated that both hexagonal ϵ as well as cubic γ phases could be formed over a range of composition varying between 9 and 15 wt.% Mn. As previously discussed, the ϵ_2 phase was reported to form for Mn contents between 12 and 25 wt.% [195]. The second γ phase observed here presents a smaller domain, corresponding to a Mn content from about 13 to 20 wt.% Mn [223], but nonetheless corresponding to the compositions measured in this work. However, these two phases present a significant difference in their thermodynamic stability. Indeed, the ϵ_2 phase is reportedly thermodynamically stable between 640 and 330 °C while the γ phase is thermodynamically stable from 420 °C to room temperature. The formation of the hexagonal ϵ_2 phase would therefore appear to be metastable while the formation of the γ phase would be stable. The formation of the metastable ϵ_2 -ZnMn phase via electrochemical techniques was however reported to be particularly stable in the literature [97, 98, 118, 122, 224-226].

It is nonetheless possible to draw some hypotheses regarding the formation of these bi-phasic alloys:

- Both γ -ZnMn and steel phases present a cubic structure. As a result, the formation of the cubic γ -ZnMn phase could form preferentially at the substrate. This means that on those deposits, a sub-layer of the γ phase should be observed during EBSD analyses. However, this additional cubic phase was not observed on EBSD analyses on the deposits obtained at pulse on-time of 5 and 30 ms.
- As illustrated in the Fig.73, it looks like the second γ -ZnMn phase is only formed when the relaxation time is the 30 – 60 ms region. The formation of the γ phase, of lower energy, could therefore originate from the metastable ϵ phase during the relaxation time via a slip mechanism. Indeed, pole figures obtained on the samples deposited at 0.1 A/cm² revealed the presence of a Burgers orientation relationship that could confirm this behaviour.

As a result, it seems that short relaxation times, below 30 – 40 ms, are not sufficient for this transformation to occur. On the other hand, the deposition at longer on-time above the pulse limiting duration could be too energetic to permit the transformation of the ϵ phase into γ , even if longer relaxation times are used.

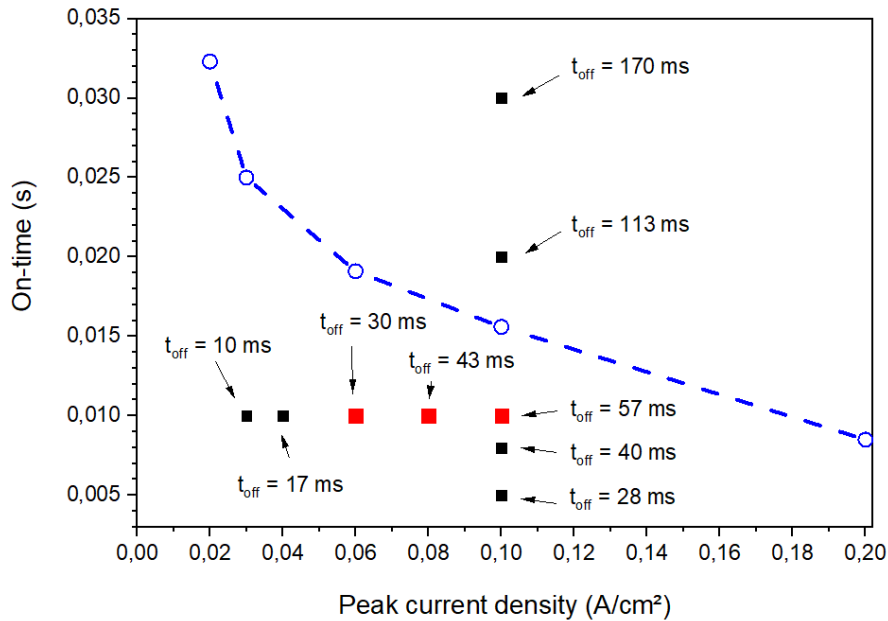


Fig.73: Crystallographic phases observed on pulse Zn-Mn deposits obtained at various peak current densities and pulse durations; crystallographic phases corresponding to the monophasic ϵ_2 -ZnMn deposits (black) and to the biphasic ϵ_2 - and γ -ZnMn deposits (red); respective values of the relaxation time and pulse limiting current density or duration (blue)

Further investigations of the crystallography via EBSD on cross-sections of bi-phasic deposits obtained at a peak current density of 0.1 A/cm² (Fig.74) also tends to confirm this phase transformation hypothesis. Indeed, it can be observed that the cubic phase is principally formed in small amounts between the larger hexagonal grains. In addition, some small grains of the γ phase could also be observed near the substrate – deposit interface.

Additional analyses of grain orientations at the interface between the two phases also showed a Burgers orientation relationship. Indeed, the projection on pole figures presented in Fig.75 show an orientation relationship between one (00.2) plane of the hexagonal phase (Fig.75a) and one (110) plane of the cubic phase (Fig.75b). Similarly, one [111] direction of the γ -ZnMn phase (Fig.75b) can be superposed with one [11.0] direction of the ϵ_2 -ZnMn phase (Fig.75a).

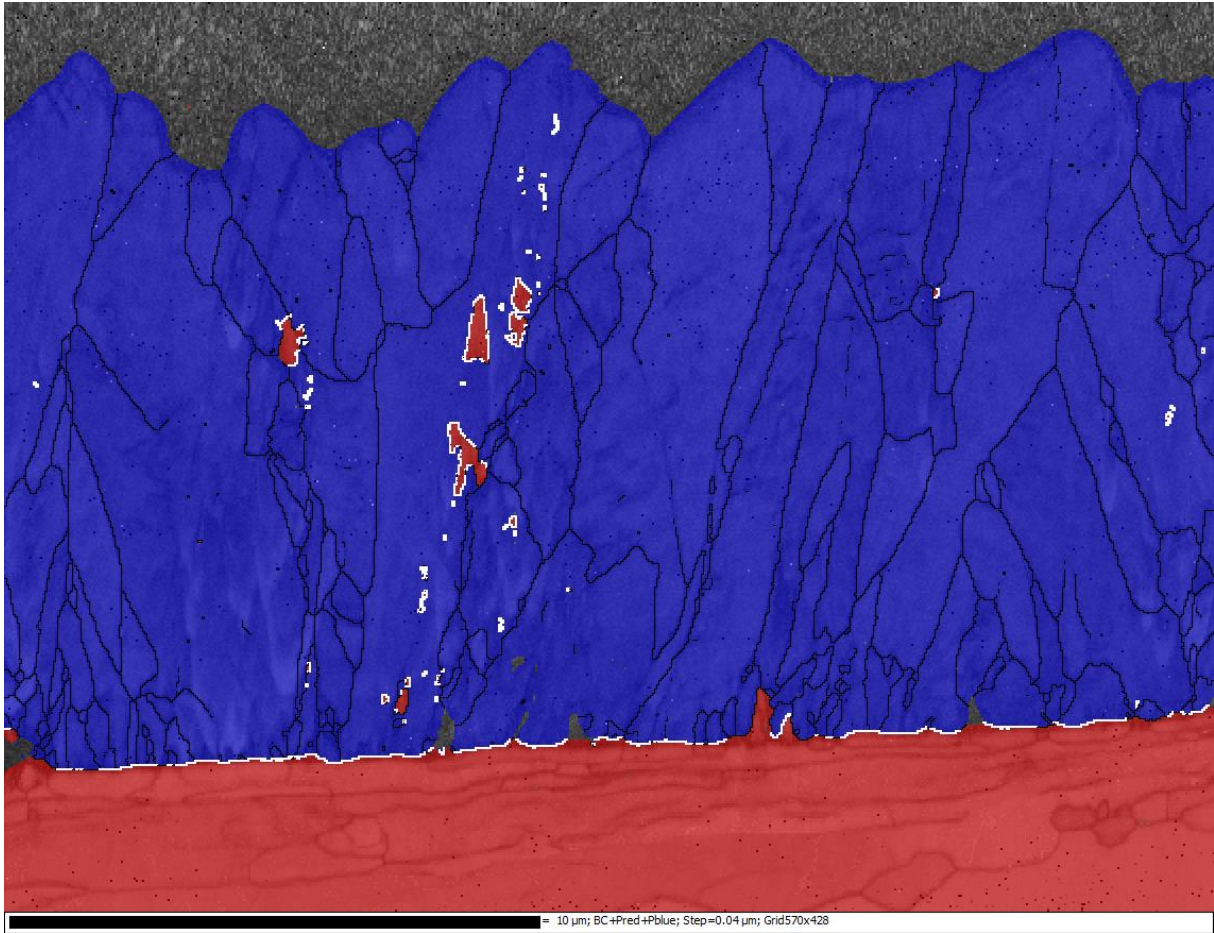


Fig.74: EBSD mapping of a bi-phasic Zn-Mn deposit obtained at a pulse current density of 0.1 A/cm², phases corresponding to the hexagonal ϵ_2 -ZnMn (blue) and cubic γ -ZnMn (red); in white the grain boundaries satisfying a maximal disorientation of 5° in respect to the $\{110\} // \{00.1\}$ and $\langle 111 \rangle // \langle 11.0 \rangle$ relationship

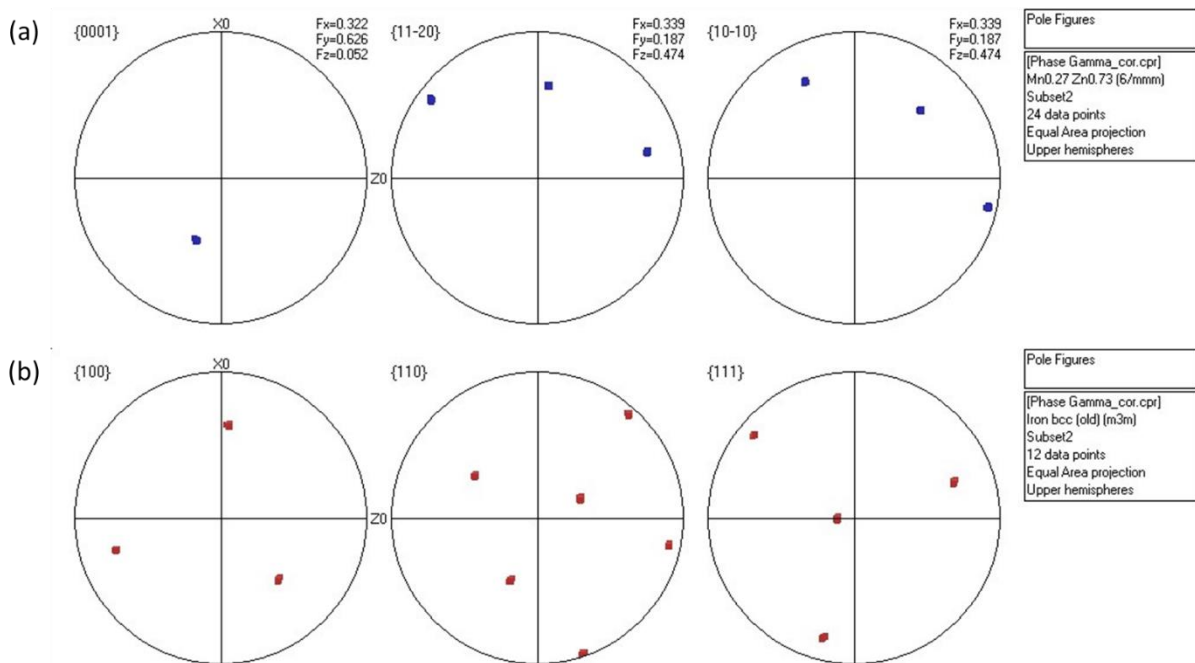


Fig.75: Projection of an interface in pole figures for the hexagonal ϵ_2 -ZnMn phase (a) and for the cubic γ -ZnMn (b); Y0 corresponding to the growth direction and X0 corresponding to the horizontal of the EBSD mapping presented in Fig.74

3.3.7. Discussion and conclusion

In this second part, Zn-Mn deposits were obtained through pulse electrodeposition from additive-free chloride electrolytes. In a preliminary study, the optimal range of deposition parameters was successfully defined on the basis of theoretical considerations and voltage measurements.

The results presented and discussed show an important impact of the pulse parameters, namely the peak current density and the pulse duration on the properties of the deposits. With a proper tuning of the pulse parameters, monophasic Zn-Mn deposits presenting a good surface appearance, and containing up to 15 wt.% Mn were obtained at high faradaic efficiencies. On this basis, the optimal pulse deposition parameters were defined with an average current density of 0.015 A/cm², a peak current density of 0.1 A/cm² and a pulse duration of 5 ms.

Overall, the deposits obtained under pulse currents presented a significant improvement over those obtained under continuous current. An increase of the Mn content was achieved, the morphology and the microstructure of the deposits were drastically refined and the efficiency of the deposition process was considerably enhanced. Although the HER was mostly hindered, the presence of porosity at the coating – substrate interface could still be observed in large amounts.

The use of pulse currents permitted, under certain conditions to enhance significantly the faradaic efficiency of the deposition process. However, the exaggerated use of long pulses leads to a higher contribution of the HER and as a result to a strong decrease of the efficiency.

It was observed that the pulse parameters had a great influence on the crystallography of the deposits. Depending on the parameters applied, coatings presenting various phase composition and crystallographic orientations were observed. It appeared that reorganization could occur during the relaxation time leading to the transformation of the metastable ϵ phase into a more stable γ phase.

3.4. Definition of the optimal parameters

The optimal deposition parameters for the manufacturing of the most promising Zn-Mn deposits can be defined based on the investigations carried out in the previous sections. In order to meet the requirements previously defined in chapter 1.3 and to be competitive in regards to the commercial Zn-based coatings, the deposits developed in the framework of this work have to meet these requirements.

First of all, the anticorrosive properties are of primary interest in this work. It was previously stated that the optimal anticorrosive properties of the Zn-Mn alloys are obtained for Mn contents between 10 and 30 wt.%. In addition, uniform deposits, free of cracks and porosity are also indispensable. Besides advantageous anticorrosive properties, the deposits have to withstand a wide range of mechanical stresses during forming operations. As a result, a good adhesion of the coating to the substrate steel is required. These deposits also need to be suited for numerous post processes such as painting and require a uniform and refined surface morphology.

Using pulse currents, uniform, pore-free and compact Zn-Mn deposits containing 15.2 wt.% Mn could be obtained with high faradaic efficiencies on unprepared IF-steel substrates using the following deposition parameters:

Average current density, j_a	0.015 A/cm ²
Peak current density, j_p	0.1 A/cm ²
Pulse on-time, t_{on}	5 ms
Duty cycle, γ	0.15
Pulse on-time, t_{off}	28 ms
Frequency, F	30 Hz

These deposition parameters will be used to manufacture the pulse Zn-Mn deposits used for the electrochemical, corrosion and mechanical tests and compared to the commercial coatings in chapter 4.

3.5. Up-scaling and reproducibility

In this section, the pulse electrodeposition of Zn-Mn coatings on large scale samples will be investigated. The composition of the electrolyte was identical to the one described in Table 11, page 64, while the setup used is the one described in chapter 2.2.2.

In a first step described in the section 3.5.1, the deposition on larger samples will be studied from 50 x 50 mm² coupons up to surfaces of 100 x 200 mm². The composition, morphology and crystallography of the deposits will be investigated in order to assess the stability of the up-scaling.

In a second section (3.5.2), the reproducibility of the deposition process will be investigated, as well as the stability of the plating bath.

Finally, the stability and the evolution of the already observed edge effect will be discussed and evaluated on samples of various sizes in section 3.5.3. In addition, the use of numerical models will be investigated in order to better understand the origin and the possible solutions for this edge effect.

3.5.1. Up-scaling

In order to assess the stability of the electrodeposition process on larger samples, up to 100 x 200 mm², the chemical composition as well as the morphology and crystallography of the deposits was characterized. Three substrate sizes were used for these investigations, 50 x 50 mm², 100 x 100 mm² and 100 x 200 mm². The samples were after deposition divided into smaller coupons as presented in Fig.76.

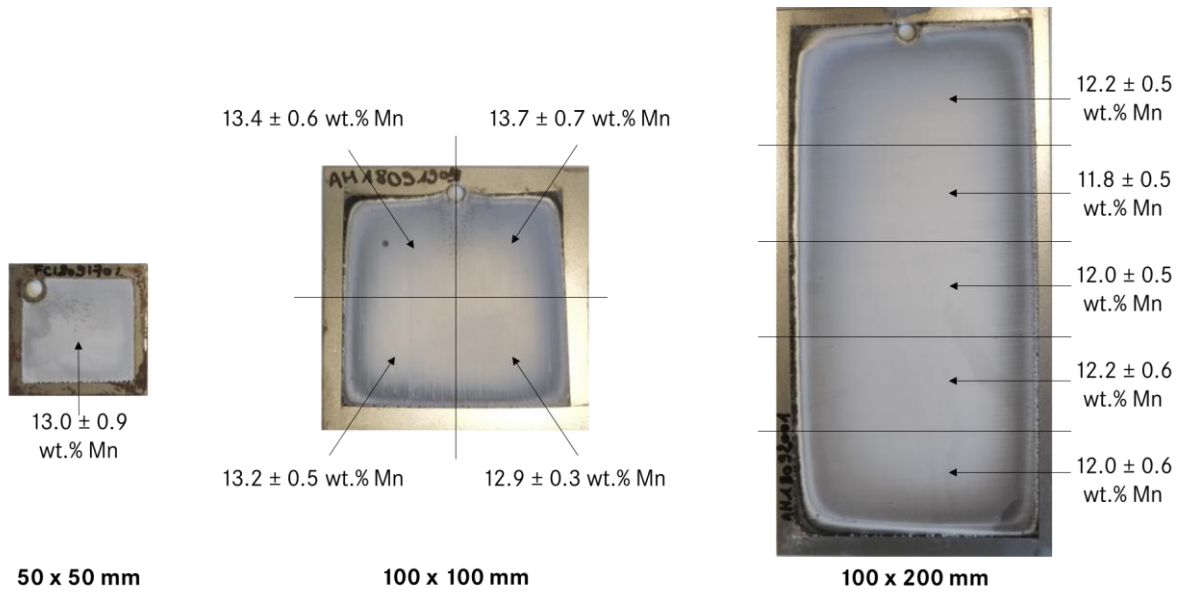


Fig.76: 100 x 100 mm² (a) and 100 x 200 mm² (b) samples coated with approximately 9 μm Zn-Mn via pulse electrodeposition; position of the investigated areas and chemical composition

Independently from the size of the substrate, the deposits present a homogeneous surface appearance, excepted from a small edge effect about 5 mm wide observed similarly on all samples. The deposits present a light-grey mat appearance in all cases. The morphological analyses presented in Fig.77 show the same morphology in the three cases. It can also be observed that the deposits obtained on the large 100 x 100 and 100 x 200 mm² coupons present a homogeneous morphology without differences from left to right or from top to bottom.

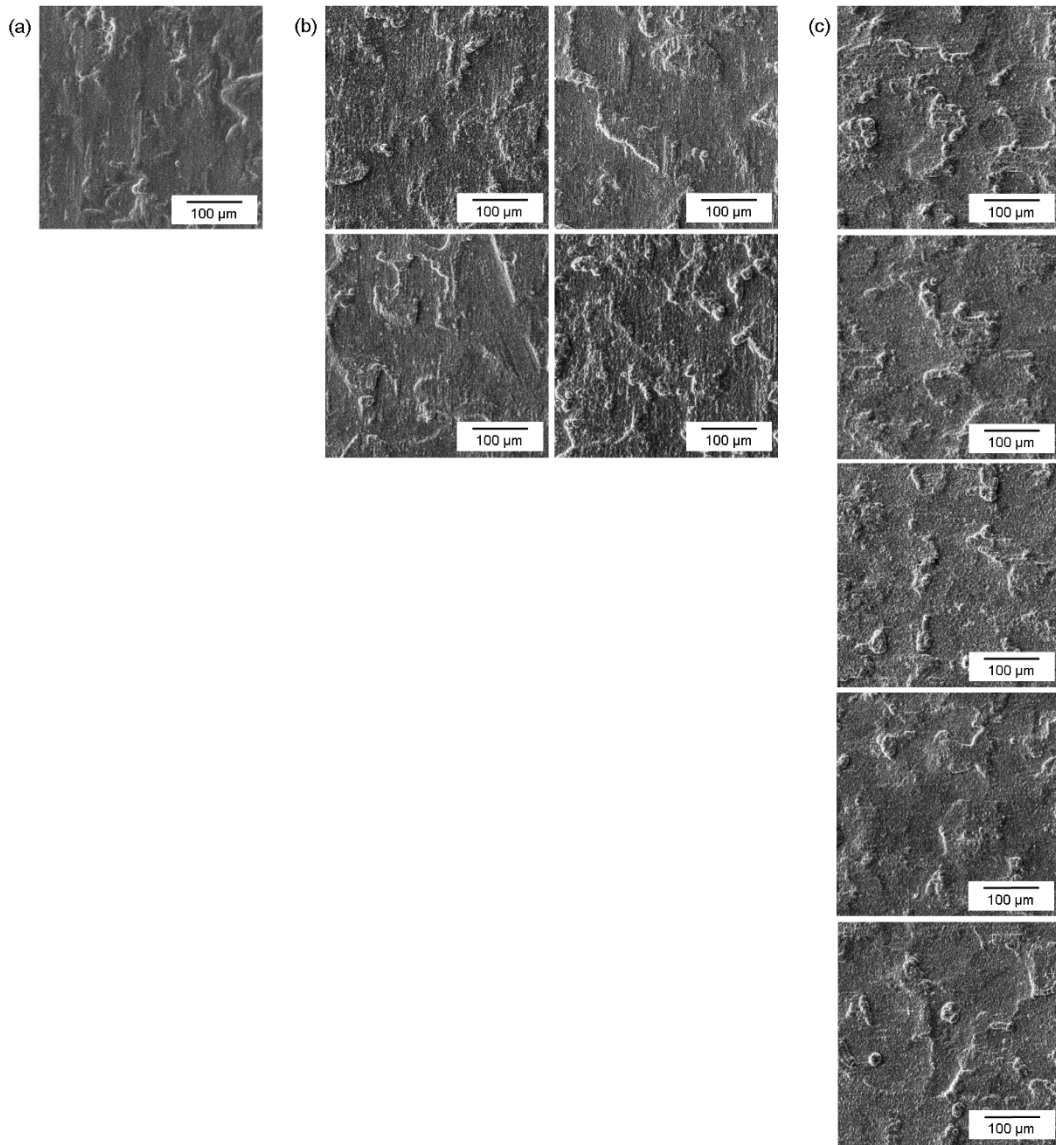


Fig.77: SEM micrographs of the surface of pulse Zn-Mn deposits (thickness of about 9 μm) obtained on DC06 of surface 50 x 50 mm² (a), 100 x 100 mm² (b) and 100 x 200 mm² (c) with an average current density of 0.015 A/cm², a peak current density of 0.1 A/cm² and a pulse duration of 5 ms; position of the micrographs in respect to the areas analysed in Fig.76

The average compositions measured on the different regions of the deposits are summarized in the Fig.76. Similarly, no significant variation of the chemical composition are observed when increasing the size of the substrate. The deposits also presented a homogeneous distribution of the Mn content with no variations observed from the left to the right side of the samples nor from the top to the bottom. On average, a variation of ± 0.6 wt.% Mn from the average Mn content was measured on the samples, independently from the area analysed.

XRD analyses were carried out on the Zn-Mn deposits obtained on 50 x 50, 100 x 100 and 100 x 200 mm² substrates. The resulting patterns obtained systematically in the central region of the samples are presented in Fig.78. It appears that the up-scaling does not significantly impact the crystallography of the deposits. In all cases, a monophasic composition of the hexagonal ε₂ phase was observed. In addition, minimal fluctuations of the peak intensities were observed, which suggest that the process parameters chosen are quite stable on a large range of substrate sizes.

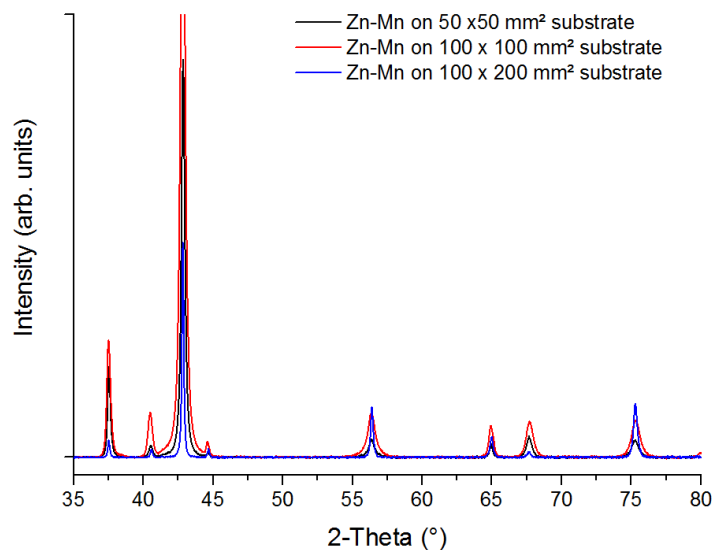


Fig.78: XRD patterns of pulse Zn-Mn deposits (thickness of about 9 μm) obtained on DC06 of surface 50 x 50 mm² (black), 100 x 100 mm² (red) and 100 x 200 mm² (blue) with an average current density of 0.015 A/cm², a peak current density of 0.1 A/cm² and a pulse duration of 5 ms; XRD patterns obtained in the central region of the samples.

The deposits obtained in this work present a remarkable homogeneity of their properties, namely chemical composition, morphology and crystallography, independently from the surface coated. Up-scaling of the electrodeposition process of Zn-Mn coatings was never investigated in the literature. However, it was largely reported that Zn-Mn electrodeposits mostly presented heterogeneous properties when high current densities or potentials were used [227, 228]. The narrow deposition range for Zn-Mn combined with instabilities of the applied electrical parameters could result in strong heterogeneities, in particular regarding the Mn content [228]. In the work of Close [169], similar heterogeneities were observed on deposits obtained under continuous currents. Various aspects of the electrodeposition process likely to be responsible for these heterogeneities, such as the potential distribution and the stirring were investigated without success.

In comparison to this precedent work [169], numerous aspects of the deposition process were modified in this thesis, such as the geometry of the plating cell, the electrical mode used for the deposition and the composition of the plating bath. The absence of additives in this work is actually expected to worsen the homogeneity of the deposits, as largely reported in the literature and already discussed in this work (see section 1.5.3). The use of pulse plating in the other hand is likely to be the deciding aspect in the significant improvement of the deposit homogeneity in comparison to the literature.

3.5.2. Reproducibility

The stability and the reproducibility of the deposition process was evaluated by preparing series of up to 12 deposits of dimensions 100 x 200 mm under pulse plating using the optimal parameters summarized in the previous sections.

An average Mn content of 13.11 ± 1.02 wt.% was obtained on the pulse deposits, while a lower Mn content of about 11.01 ± 0.67 wt.% was measured on the deposits obtained under continuous plating, showing the relatively good reproducibility of the deposition process. In addition, the evolution of the Mn content over a range of 12 deposits on large-scale substrates obtained in the same electrolyte (7 litres) was monitored with the results presented in Fig.79(a). A decrease of the Mn content, from about 14 wt.% down to 12 wt.%, was observed over the period investigated.

In order to try to explain this change in the composition, the variation of the ionic concentrations was determined using the Faraday law and accounting for 100% efficiency. The resulting changes are plotted in Fig.79(b). A slight decrease of the Mn^{2+} concentration can be observed, as well as an increase of the concentration of Zn^{2+} caused by the dissolution of the pure Zn counter-electrode. As a result, the $\text{Mn}^{2+}/\text{Zn}^{2+}$ ratio shows a significant decrease, from 8 to about 7.5 at a charge of 40000 Coulombs. This evolution of the ionic species was previously observed under fixed applied potential via Atomic Absorption Spectroscopy (AAS) with a decrease of the $\text{Mn}^{2+}/\text{Zn}^{2+}$ ratio from 8 to about 6.5 at a charge of 80000 Coulombs [169]. As already demonstrated in the literature, the ionic concentration ratio has a strong influence on the deposits and particularly on the Mn content [97, 115, 118]. A lower $\text{Mn}^{2+}/\text{Zn}^{2+}$ ratio in the electrolyte resulting in a lower Mn content in the deposits.

Additionally, no significant fluctuations of the pH were measured during the deposition process and up to 40000 Coulombs. In contrast with previous work [169], it is supposed that the absence or at least the low intensity of the HER due to the use of properly tuned pulse parameters significantly helps in stabilizing the pH and as a result stabilizes the plating bath.

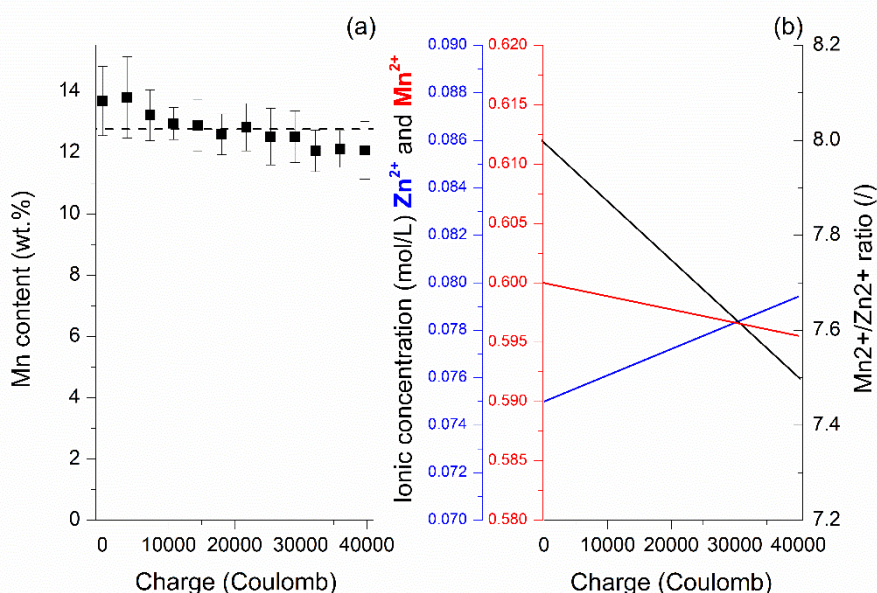


Fig.79: (a) Evolution of the composition of the deposits in a same plating bath and (b) evolution (calculated) of the ionic concentration in Zn^{2+} (blue) and Mn^{2+} (red) as well as the $\text{Mn}^{2+}/\text{Zn}^{2+}$ ratio (black)

3.5.3. Edge effect

As previously mentioned, some edge effect was observed on all the samples coated in this work. SEM-EDS analyses of the morphology and chemical composition in these regions revealed some significant heterogeneities when compared to the middle of the samples. In average, it was observed that this edge effect was about 5 mm wide, presenting a dark-grey mat appearance and independent of the sample size.

The evolution of the Mn along the width of the samples and SEM micrograph of the surface near the edge of 100 x 100 mm² samples are presented in Fig.80 and Fig.81, respectively.

The deposits present a stable composition over about 75 % (up to 35 mm from the centre) of the samples, with in the case depicted in Fig.80 a Mn content around 12.3 ± 0.5 wt.%. Approaching the edges of the sample, a rapid decrease of the Mn content is observed, down to about 6.5 wt.% at 44 mm from the centre.

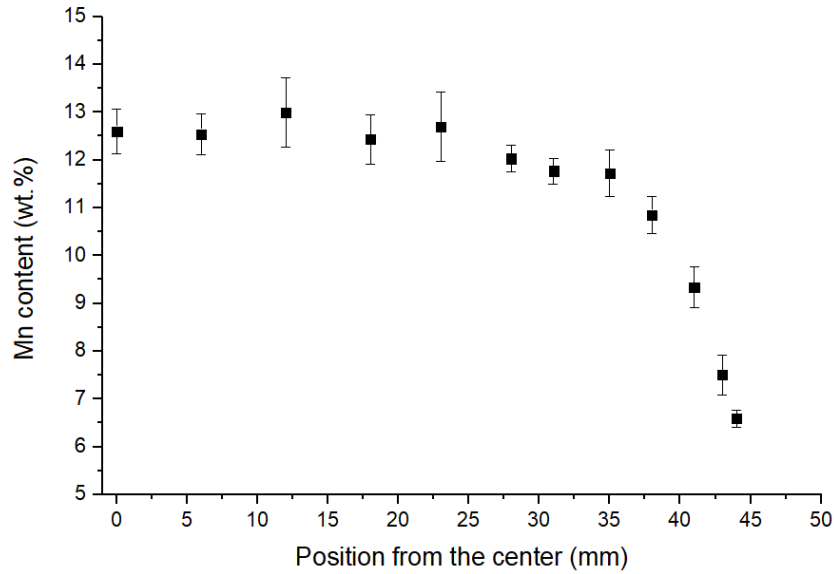


Fig.80: Evolution of the Mn content along the width of the samples (size 100 x 100 mm²); position 0 mm corresponding to the centre of the sample

SEM micrographs of the surface of the deposit at different positions from the centre of the sample are presented in Fig.81. The position of the micrographs corresponds to the position of the EDS analyses presented in Fig.80.

The samples exhibit a homogeneous morphology on about 90 % of the surface, up to 41 mm from the centre (Fig.81j). The last two acquisitions near the edges at 43 and 44 mm (Fig.81(k) and (i), respectively) show a rapid transition towards a cauliflower-like dendritic growth of the deposit. This type of morphology was previously observed in the literature, especially in the research work of Close et al. [118].

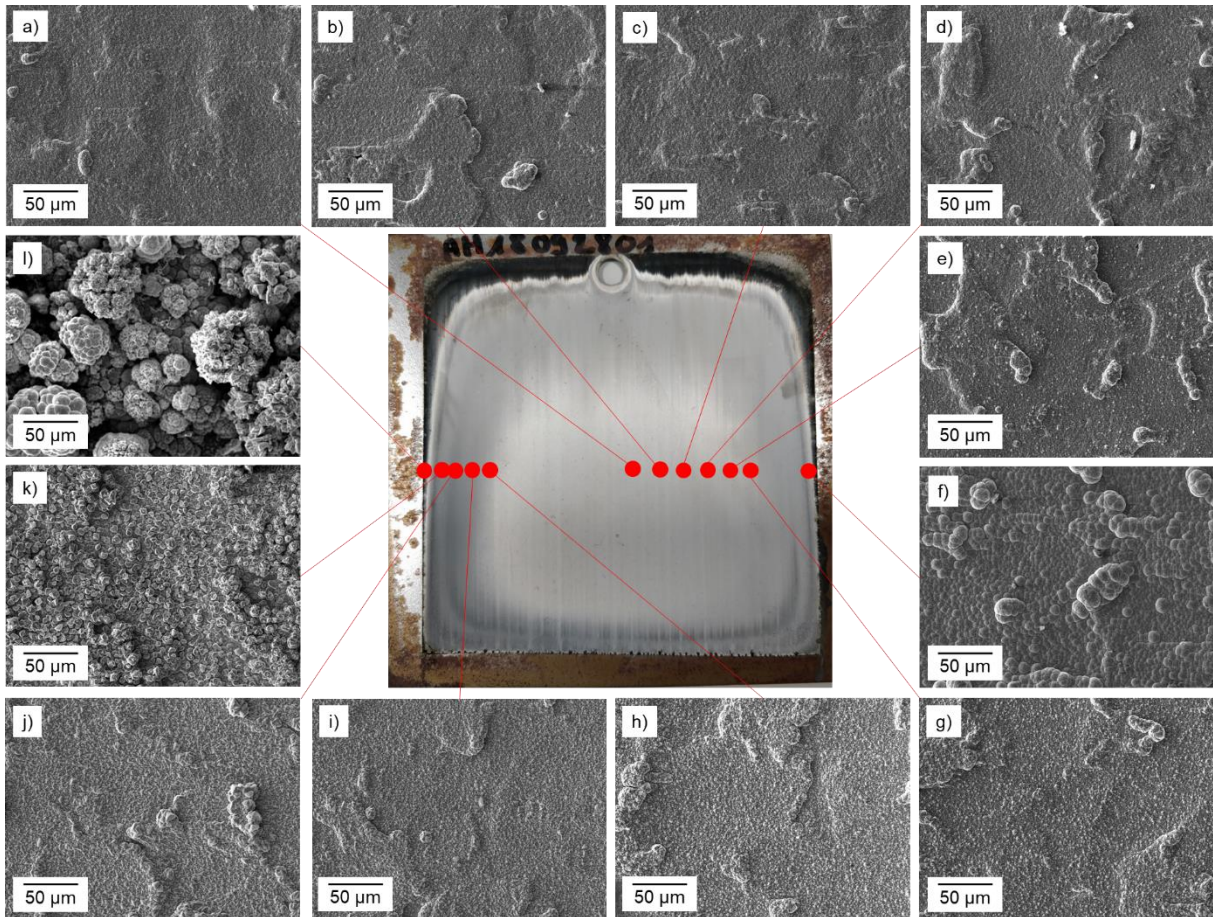


Fig.81: SEM micrograph of the edges on the 100 x 100 mm² samples; micrographs acquired at a distance from the centre of 0 mm (a), 6 mm (b), 12 mm (c), 18 mm (d), 23 mm (e), 28 mm (f), 31 mm (g), 35 mm (h), 38 mm (i), 41 mm (j), 43 mm (k) and 44 mm (l)

In order to better understand the origin of these effects, the electrodeposition process was numerically simulated. The methodology used for the numerical simulation is detailed in appendix 3.

Fig.82 depicts the evolution of the current density on the surface of 50 x 50 mm² samples. An increase of the current density can be observed when approaching the edges of the sample. It is also important to note here that the strong increase of the current density is only observed at about 5 – 6 mm from the edges, correlating with visual observations as well as SEM-EDS analyses of the samples. This variation is due to the inhomogeneous distribution of the current density inside the electrolyte, resulting in the accumulation of the “stream lines” at the edges as depicted in Fig.83 and to the exponential increase of the current density.

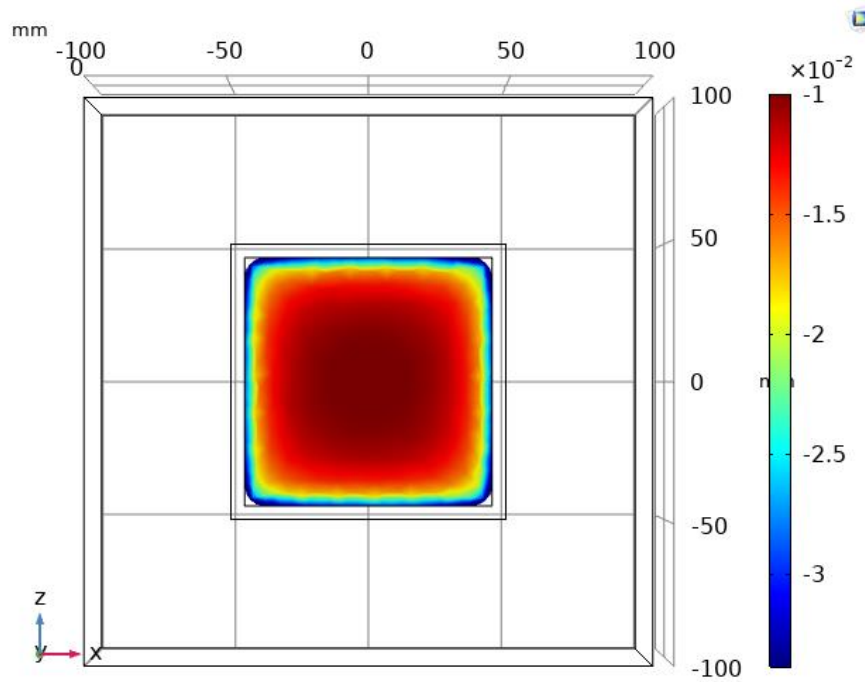


Fig.82: Two-dimensional distribution of the current density (A/cm^2) from numerical simulation on 100 x 100 mm² sample

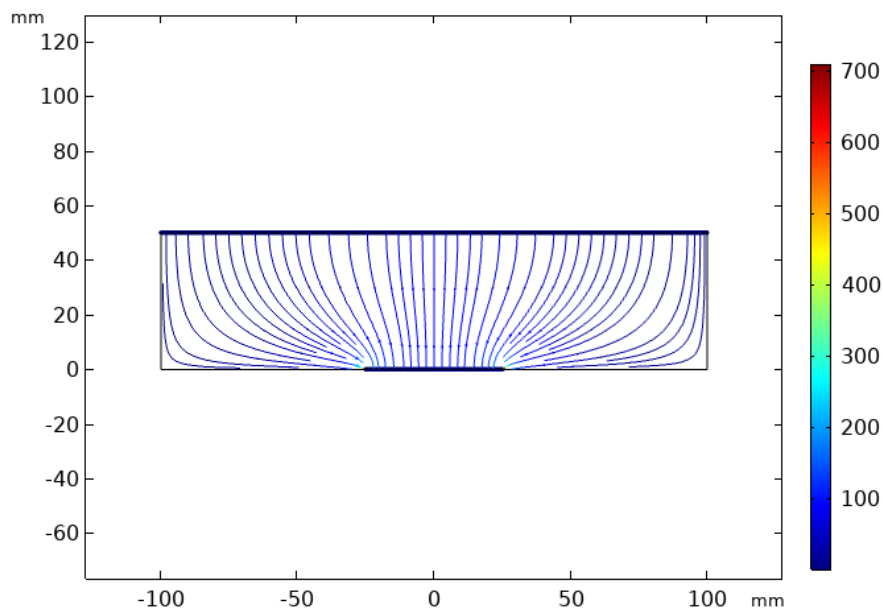


Fig.83: Distribution of the current density between cathode (at position 50 mm) and anode (at position 0 mm)

This increase of the current density results in an increased thickness of the deposit toward the edges and gives a good explanation to the morphologies observed in Fig.81. The evolution of the deposit thickness with increasing deposition time is depicted in the Fig.84.

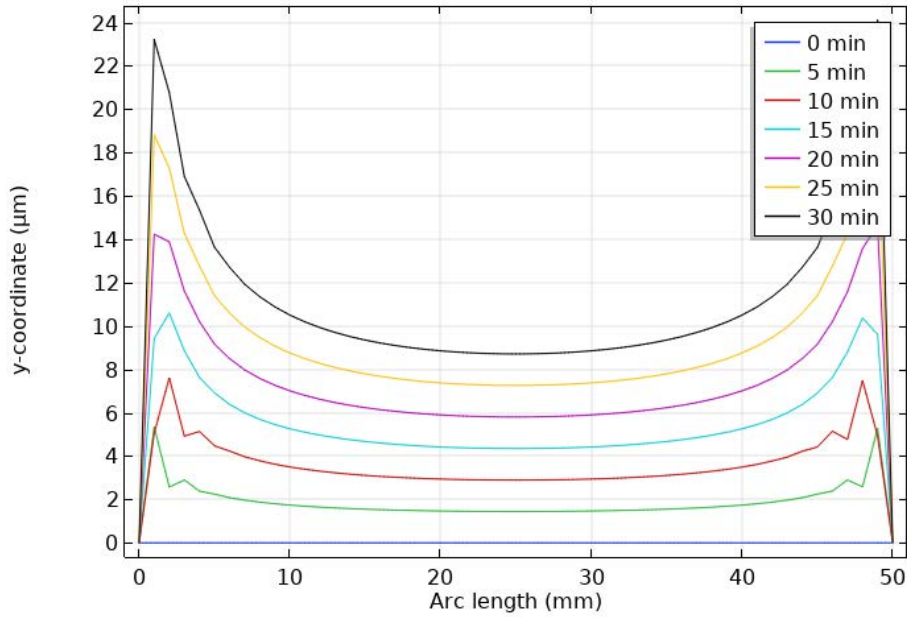


Fig.84: Evolution of the deposit thickness along deposition time on 50 x 50 mm² samples from numerical simulation

When compared to the numerical predictions of the current density (Fig.84), it appears that the current density in the 5 mm near the edge varies between 0.018 and 0.025 A/cm². This is of course in very good agreement with the morphologies observed at the edges of the samples. However, due to the decrease of the Mn content at the edges (expected to increase with increased current density), the increment of thickness is here related to a larger Zn²⁺ supply and therefore higher concentrations of Zn in the alloy.

The two-dimensional distribution of the current density on the surface of the samples (Fig.85) correlates quite well with the appearance of the deposits as displayed in Fig.76. No significant effect of the sample size on the edge effect could be observed between the 50 x 50 mm² and the 100 x 100 mm² samples, Fig.85(a) and (b), respectively. However, a change of the sample geometry towards a rectangular geometry seems to result in a reduce edge effect along the shorter edges of the sample (Fig.85(c)). This effect can be attributed to the shorter distance between the edge of the sample and the side of the simulated electrodeposition cell.

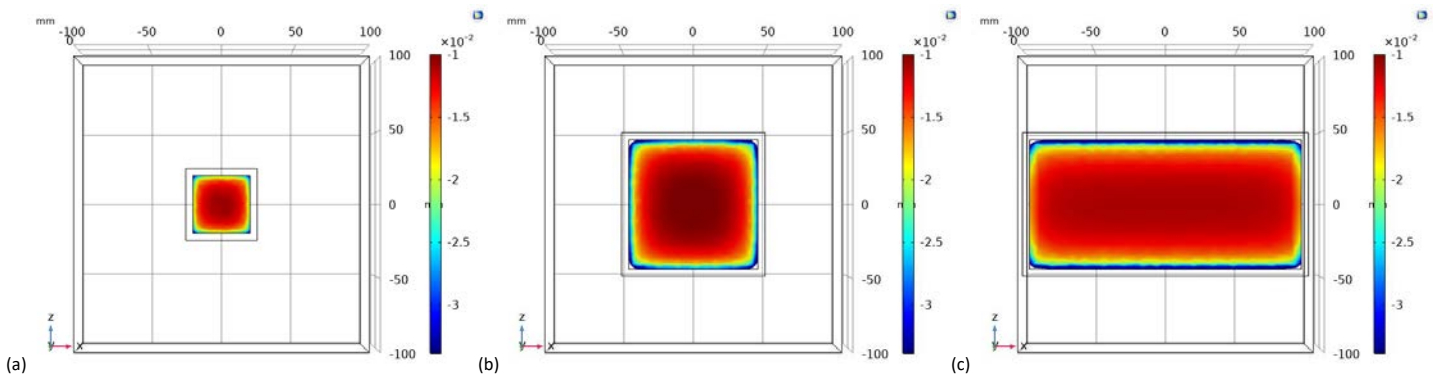


Fig.85: two-dimensional distribution of the current density on 50 x 50 mm² (a), 100 x 100 mm² (b) and 200 x 200 mm² samples (c) from numerical simulation

Further simulations of various sample configurations, with namely electrodeposition on the entire front surface of the sample and electrodeposition on the entire front surface as well as on the edges of the samples are depicted in the Fig.86. It appears that the absence of insulating tape on the front surface of the samples (Fig.86(a)) results in a decrease of the edge effect in comparison to the samples with insulating tape overlying on about 5 mm (Fig.82). The absence of insulating tape on the edges of the

samples leads to further improvement of the distribution of the current density, as depicted in (Fig.86(b) and (c)). This improvement is explained by the more homogeneous distribution of the current density streamlines in the electrolyte.

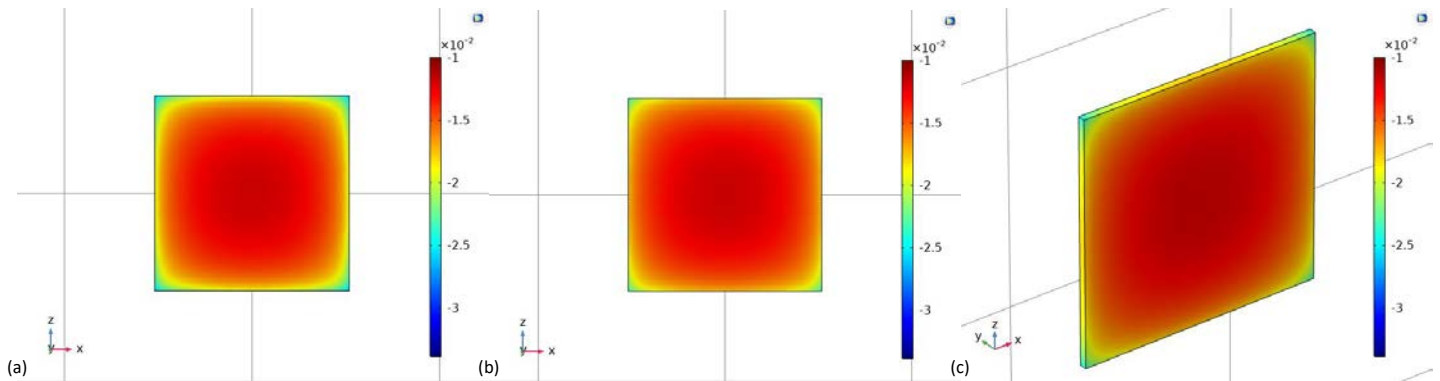


Fig.86: two-dimensional distribution of the current density on $100 \times 100 \text{ mm}^2$ samples from numerical simulation; deposition on the entire front surface (a) and deposition on the entire front surface as well as on the edges (b) and (c)

3.5.4. Conclusion

In this section, the up-scaling of the pulse electrodeposition process was considered. In addition, important process factors such as the reproducibility and the stability of the deposition process were investigated.

The transfer from small scale samples of size $50 \times 50 \text{ mm}^2$ to larger surfaces up to $100 \times 200 \text{ mm}^2$ proved the good stability of the deposition process on samples of various sizes. Indeed, similar morphology, composition and crystallography were observed, independently of the sample size. Furthermore, no variations of the deposit properties could be observed on the samples, excepted from an edge effect. This edge effect was observed on a about 5 mm wide strip, and presented a darker appearance compared to the rest of the deposit. Advanced analyses including Hull cell experiments and numerical simulations exposed a strong increase of the current density at the edges of the samples, due to accumulation phenomena, and leading to dendritic morphologies.

Studies of the reproducibility proved the good stability of the deposition process and of the electrolyte. Deposits presented a loss of about 2 wt.% Mn up to an electric charge of 40000 Coulomb, corresponding to 12 deposits of $10 \mu\text{m}$ thickness on large scale substrates. Calculations of the ionic concentrations depending on the electric charge permitted to explain this gradual decrease in the Mn content. It was observed that while Mn^{2+} ions are slowly consumed during electrodeposition, Zn^{2+} enrichment occurs rapidly due to Zn dissolution at the anode. The combination of these two effects leads to a decrease of the $\text{Mn}^{2+}/\text{Zn}^{2+}$ ratio and a decrease of the Mn content in the deposits.

3.6. Conclusion and outlook on the deposition of Zn-Mn (EN) – Conclusion et perspectives sur la déposition du Zn-Mn (FR)

In this chapter, the use of pulse plating was investigated for the electrodeposition of Zn-Mn coatings from additive-free chloride electrolytes. The influence of the pulse parameters on the composition, morphology, texture and microstructure of the deposits was investigated and compared to the coatings obtained under continuous current. The impact of the chemistry, the texture and the preparation of the substrate on the properties, and especially on the texture and microstructure of the

deposits was also studied. Based on the results obtained, the optimal deposition parameters were proposed and a study of the up-scaling was carried out in order to assess the stability and the ability to industrialize the process.

The alloys obtained under pulse currents show a significant improvement of the coating morphology in comparison to those obtained under continuous currents, even when peak current densities above the pulse limiting current density were used. Compared to deposits obtained under continuous current, higher Mn contents were observed under pulse currents, with up to 15 wt.% Mn versus 13 wt.% Mn under continuous plating.

Analyses of the pulse electrodeposition revealed some complex processes, strongly related to the applied electrical parameters. An increase of the peak current density was reported to enhance Mn codeposition due to normal codeposition mechanism. Investigations carried out with various time parameters revealed a decrease of the Mn content at long off-time. This suggests either a preferential dissolution of Mn occurring during the off-time or the depletion of metallic ions near the cathode due to prolonged on-time above the transition time. This ionic depletion leads to an increased intensity of the hydrogen evolution reaction. This later hypothesis is supported by the decrease of the faradaic efficiency observed with increase of the pulse duration. The use of well-chosen parameters however, leads to a significant increase of the faradaic efficiency, from 65% under continuous plating up to 90% under pulse currents.

Significant changes of the microstructure were observed between the continuous and pulse currents. Deposits obtained under continuous plating conditions present large columnar grains while deposits obtained under pulse current present much finer microstructures. Amongst pulse deposits, those deposited with short pulses present the finest microstructure and the smallest grains, almost equiaxed. Some transitions could be observed with the mixture of large columnar and small equiaxed grains on deposits obtained at longer pulse durations. Overall an increase of the grain size and the amount of columnar grains was observed when increasing the pulse duration.

While the deposits obtained under continuous currents systematically presented a monophasic crystallographic composition of the hexagonal ϵ_2 -ZnMn phase, the pulse deposits presented various crystallographies. Independently of the Mn content, the pulse deposits presented various mixtures of monophasic and biphasic alloys, varying between the hexagonal ϵ_2 and the cubic γ phase.

It was suggested that while the hexagonal ϵ_2 phase was formed automatically during the electrodeposition, the use of a relaxation time could allow the reorganization and the transformation of the metastable ϵ phase into a stable γ phase. On the basis of various pole figures as well as EBSD mappings, it appeared that a Burgers orientation relationship could be identified on the biphasic coatings. It was also observed that the second γ phase could be formed at the boundaries between the hexagonal grains as well as near the substrate – deposit interface.

On the basis of these investigations, it was determined that the Zn-Mn deposits presenting the most promising characteristics were obtained at average peak current density j_a of 0.015 A/cm², peak current density j_p of 0.1 A/cm² and pulse duration t_{on} of 5 ms. Using these parameters, homogeneous, pore-free and compact Zn-Mn deposits containing 15.2 wt.% Mn were obtained at high faradaic efficiencies of 90% from additive-free chloride electrolytes.

Using these deposition parameters, the electrodeposition process was carried out on various substrate sizes up to 100 x 200 mm². Studies of the up-scaling revealed the good stability and the good reproducibility of the deposition process. Deposits presented homogeneous composition, morphology and crystallography independently of their size. However, a thin strip about 5 mm wide and presenting a dendritic morphology was systematically observed and attributed to an edge effect. Numerical simulations and investigations in the Hull cell exposed a strong increase of the current density in those areas, responsible for these changes of morphology.

For the electrodeposition of Zn-Mn- Al_2O_3 composite coatings, the use of pulse plating is crucial for the successful incorporation of particles inside the metallic matrix. The studies conducted in this chapter permitted to understand the mechanisms and phenomena involved during pulse plating and helped to define the optimal deposition parameters for the Zn-Mn metal matrix. However, the investigations conducted in this chapter were contained to rather straightforward rectangular pulses with on- and off-time only. In order to further investigate the electrodeposition of Zn-Mn alloys and to try to further enhance the Mn content of the deposits, more intricate pulse processes such as the superimposed or reverse pulse plating with various waveforms may be of interest. Besides, the combined effect of the pulse plating in presence of additives, also discarded in the framework of this study may help improve the properties of the deposits.

Dans ce chapitre, l'utilisation de courants impulsionnels a été étudiée pour l'électrodéposition de revêtements Zn-Mn obtenus à partir d'électrolytes chlorés en l'absence d'additifs. L'influence des paramètres du courant impulsionnel sur la composition, la morphologie, la texture et la microstructure des dépôts a été analysée et comparée aux dépôts obtenus via le mode courant continu. L'impact de la composition chimique, de la texture et de la préparation du substrat sur les propriétés et plus particulièrement sur la texture et la microstructure des dépôts a également été examiné. Sur la base des résultats obtenus, les paramètres de déposition optimaux ont été proposés et une étude sur des échantillons de tailles variables (up-scaling) a été conduite afin d'évaluer la stabilité et le potentiel d'industrialisation du procédé.

Les alliages obtenus sous courants impulsionnels montrent une amélioration significative de la morphologie en comparaison avec les dépôts obtenus sous courants continus, même lorsque des densités de courants maximale supérieures à la densité de courant impulsionnelle limite sont utilisées. Comparés aux revêtements obtenus sous courants continus, des teneurs en Mn plus élevées ont été obtenues par mode impulsionnel, avec jusque 15 %m Mn par rapport à 13 %m Mn sous courant continu.

Les différentes analyses conduites sur les revêtements impulsionnels ont montré des procédés complexes, fortement reliés aux paramètres électriques appliqués. Une augmentation de la densité de courant maximale a prouvé entraîner une augmentation de la teneur en Mn codéposée. Les études effectuées avec différents paramètres temporels ont révélé une diminution de la teneur en Mn lorsque des impulsions longues sont utilisées. Ceci suggère soit une dissolution préférentielle du Mn durant le temps de pause, soit une déplétion des ions métalliques à proximité de la cathode et due à une déposition prolongée au-delà du temps de transition. Cette déplétion des ions métalliques entraîne une plus grande intensité de l'évolution d'hydrogène. Cette dernière hypothèse est supportée par la diminution du rendement faradique observée avec une augmentation de la durée des impulsions. L'utilisation de paramètres appropriés en revanche, permet d'atteindre des rendements faradiques particulièrement élevés, de 65% sous courants continus jusque 90% sous courants impulsionnels.

Des changements importants de la microstructure ont également été observés lors du passage du courant continu au courant impulsionnel. Les dépôts obtenus en courant continu présentent de grains colonnaires importants alors que les dépôts obtenus sous courants impulsionnels présentent des microstructures significativement plus fines. L'utilisation d'impulsions courtes conduit à la plus fine microstructure avec de petits grains, majoritairement équiaxes. Lorsque des impulsions plus longues sont employées, des transitions sont observées avec une combinaison de grains colonnaires et de plus petit grains equiaxes. De manière générale, une diminution de la taille de grain et une plus faible population de grains colonnaires a été observée lorsque la durée des impulsions augmente.

Alors que les revêtements obtenus sous courants continus présentaient systématiquement une cristallographie monophasique composée de la phase hexagonale ϵ_2 -ZnMn, les revêtements impulsionnels présentent des cristallographies variées. Indépendamment de la teneur en Mn, les dépôts

se composent d'alliages monophasiques et biphasiques, variant entre les phases hexagonales ϵ_2 et cubique γ .

Alors que la phase hexagonale ϵ_2 semble être systématiquement formée lors de l'électrodéposition, il a été suggéré que l'utilisation d'un temps de relaxation suffisamment long permettait une réorganisation et la transformation de la phase métastable ϵ en la phase stable γ . Sur la base de figures de pôles ainsi que de cartographies EBSD, il est apparu qu'une relation d'orientation de Burgers pouvait être identifiée sur les revêtements biphasiques. Il a également été observé que la seconde phase γ pouvait être formée à l'interface entre les grains hexagonaux ainsi qu'à proximité de l'interface entre le substrat et le revêtement.

Sur la base de ces expérimentations, il a été déterminé que les revêtements de Zn-Mn présentant les caractéristiques les plus prometteuses étaient obtenus avec une densité de courant moyenne j_a de 0.015 A/cm^2 , une densité de courant maximale j_p de 0.1 A/cm^2 et une durée de l'impulsion t_{on} de 5 ms. En utilisant ces paramètres, des dépôts Zn-Mn homogènes, sans porosités et compacts contenant environ 15 m.% de Mn ont été obtenus avec des rendements faradiques élevés de 90% à partir d'électrolytes chlorés en l'absence d'additifs.

En utilisant ces paramètres de déposition, le procédé d'électrodéposition a été conduit sur des substrats de différentes tailles jusqu'à des surfaces de $100 \times 200 \text{ mm}^2$. Ces études ont révélé la bonne stabilité et la bonne reproductibilité du procédé d'électrodéposition. Les dépôts obtenus présentent des compositions, morphologies et cristallographies homogènes, indépendamment de leur taille. Cependant, une fine bande de 5 mm de largeur environ et présentant une morphologie dendritique a pu être observée systématiquement et a été attribuée à un effet de bord. À l'aide de simulations numériques et d'études supplémentaires en cellule de Hull, une forte augmentation de la densité de courant a pu être observée dans ces régions, responsable pour ces changements de morphologie.

Afin de permettre la meilleure incorporation de particules possible dans la matrice métallique, l'utilisation de courants impulsionnels semble cruciale lors de l'électrodéposition de revêtements composites Zn-Mn- Al_2O_3 . Les études effectuées dans ce chapitre ont permis de comprendre les mécanismes et les phénomènes impliqués lors de l'électrodéposition sous courants impulsionnels. Ces analyses ont également permis de définir les paramètres de déposition optimaux pour la matrice métallique Zn-Mn. Cependant, les recherches conduites dans ce chapitre ont été limitées à des impulsions de forme rectangulaire. Dans le but de poursuivre les analyses sur l'électrodéposition du Zn-Mn et d'encre accroître la teneur en Mn dans les revêtements, des impulsions plus complexes tels que des impulsions superposées ou renversées de forme variées peut être d'intérêt.

4. Suitability of the pulse Zn-Mn deposits for automotive application

4.1. Aim and procedure (EN) – But et procédure (FR)

In the previous chapter 3, new Zn-Mn alloy coatings were successfully obtained from additive-free chloride electrolytes via pulse electrodeposition. The deposition parameters leading to the most promising deposits were identified and the reproducibility and stability on large-scale samples were confirmed.

A summary of the deposit properties as well as the deposition parameters is presented in the Table 20.

Table 20: properties of the optimal pulse Zn-Mn deposits and associated deposition parameters

Deposit properties	
Mn content (wt.%)	15.2
Crystallography	Monophasic, ϵ_2 -ZnMn
Faradaic efficiency (%)	90
Deposition parameters	
Average current density (A/cm ²)	0.015
Peak current density (A/cm ²)	0.1
Pulse on-time (ms)	5
Duty cycle	0.15
Pulse off-time (ms)	28
Frequency (Hz)	30

In this chapter, the suitability and the performance of the alternative Zn-Mn deposits obtained via pulse electrodeposition will be assessed on the basis of various experimental techniques performed from the laboratory to the industrial scale, and compared with a selection of commercial products described in 2.8.2.

The anticorrosive properties of the deposits will be determined in section 4.2. The electrochemical properties such as the corrosion potential and corrosion current densities will be extrapolated from potentiodynamic scans using the Tafel method. Accelerated corrosion tests both continuous and cyclic will be conducted according to the DIN EN ISO 9227 and VDA 233-102 standards, respectively. Through these corrosion tests, the formation and development of red rust and the evolution of the deposit thickness will be thoroughly characterized. In addition, the nature of the corrosion products will be determined by XRD and SEM-EDS analyses and a mechanism for the formation of the corrosion products for Zn-Mn coatings will be proposed.

In the section 4.3, the forming behaviour of the deposits will be assessed through hardness measurements as well as mechanical tests. Information on the adhesion of the coatings will be obtained via metallographic analyses.

The phosphatability and the paintability of the deposits will be evaluated in section 4.4. The deposits will be first treated with a phosphate conversion coating, which quality and covering will be assessed via SEM-EDS analyses. In a second step, phosphated samples will be coated with an electrolytic paint. The quality of the electrolytic paint will be characterized through various adhesion and scratch tests.

Dans le chapitre 3 précédent, de nouveaux revêtements d'alliages Zn-Mn ont été obtenus avec succès par électrodeposition impulsionsnelle à partir d'électrolytes chlorés en l'absence d'additifs. Les

paramètres de déposition conduisant aux dépôts les plus prometteurs ont été identifiés et la reproductibilité et la stabilité ont été confirmées sur des échantillons à grande échelle.

Un résumé des propriétés des revêtements ainsi que leurs paramètres de déposition est présenté dans le tableau Table 21.

Table 21: propriétés des revêtements optimaux de Zn-Mn et paramètres de déposition associés

Propriétés des revêtements	
Teneur en Mn (%m)	15.2
Cristallographie	Monophasique, ϵ_2 -ZnMn
Rendement faradique (%)	90
Paramètres de déposition	
Densité de courant moyenne (A/cm^2)	0.015
Densité de courant maximale (A/cm^2)	0.1
Temps d'impulsion on (ms)	5
Rapport cyclique	0.15
Temps de relaxation off (ms)	28
Fréquence (Hz)	30

Dans ce chapitre, l'aptitude et la performance des revêtements alternatifs de Zn-Mn obtenus par électrodéposition impulsionnelle seront évalués sur la base de techniques expérimentales variées, de l'échelle de laboratoire à l'échelle industrielle, puis comparées à une sélection de produits commerciaux décrits dans la section 2.8.2.

Les propriétés anticorrosives des revêtements seront déterminées dans la section 4.2. Les propriétés électrochimiques telles que les potentiels et densités de courant de corrosion seront extrapolées à partir de balayages potentiodynamiques par la méthode de Tafel. Des tests de corrosion accélérés continus et cycliques seront conduits sur la base des normes DIN EN ISO 9227 et VDA 233-102, respectivement. À travers ces tests de corrosion, la formation et le développement de la rouille rouge ainsi que l'évolution des revêtements seront méticuleusement caractérisés. En addition, la nature des produits de corrosion sera déterminée par des analyses DRX et MEB-EDS et un mécanisme pour la formation des produits de corrosion dans le cas d'alliages Zn-Mn sera proposé.

Dans le chapitre 4.3, la formabilité des revêtements sera évaluée via des mesures de dureté ainsi que des tests mécaniques. Les informations sur l'adhésion des dépôts seront basées sur des analyses métallographiques.

L'accroche de la couche de phosphate et la recouvrabilité des échantillons revêtus seront examinés dans la section 4.4. Les dépôts seront dans un premier temps traités avec une couche de conversion à base de phosphate, dont la qualité et le recouvrement seront évalués par des analyses MED-EDS. Dans un second temps, les échantillons phosphatés seront recouverts d'une peinture électrophorèse. La qualité de cette couche de peinture sera caractérisée par divers tests d'adhésion et de résistance à la rayure.

4.2. Corrosion resistance

The aspects of primary concern in the framework of this thesis are the anticorrosive properties of the newly developed deposits. As a result, the electrochemical properties and the corrosion behaviour of the Zn-Mn deposits und continuous and cyclic corrosion tests will be investigated in this first section.

To do so, the corrosion parameters, namely the corrosion potential E_{corr} and the corrosion current density i_{corr} will be determined by means of potentiodynamic polarization experiments. The corrosion resistance of the deposits will also be assessed through accelerated corrosion tests, namely continuous salt spray

test and cyclic corrosion test. In order to determine the mechanisms involved during the corrosion of Zn-Mn alloys, a comprehensive characterization of the corrosion products by means of XRD and SEM-EDS on the surface as well as on cross-sections of the samples will be carried out.

4.2.1. Electrochemical properties

The corrosion behaviour of the Zn-Mn coatings deposited under continuous and pulse currents was investigated by means of linear scan voltammetry in a 5 wt.% NaCl electrolyte. In order to compare the effect of the addition of Mn, the experiments were also performed on pure Zn deposits obtained from the same plating bath under potentiostatic mode at a potential of -1.2 V. The Fig.87 shows the typical anodic and cathodic scans recorded. As previously stated, anodic and cathodic measurements were carried out separately in order to avoid during the anodic scan the local increase of the pH resulting from the cathodic scan.

All three deposits present scans of similar forms, in both cathodic and anodic domains. In all three cases, the cathodic and anodic parts of the voltammograms lead to identical corrosion potential. A misfit of about 10 mV is observed for the Zn-Mn and Zn coatings.

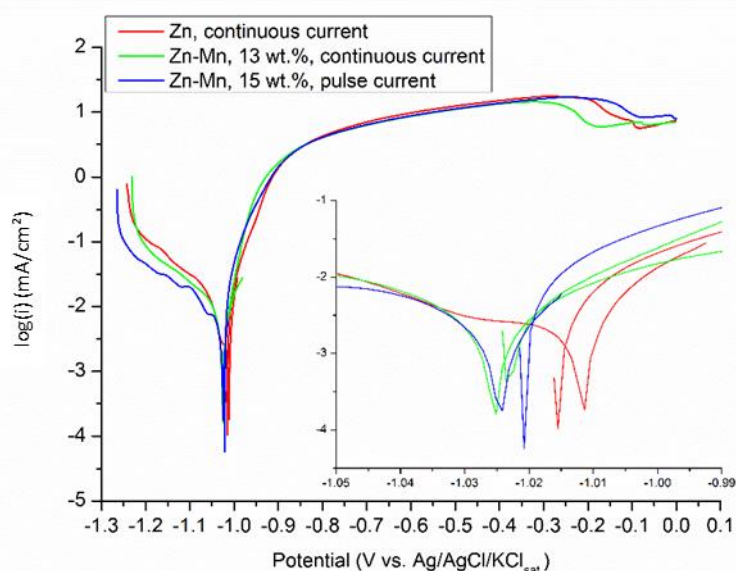


Fig.87: Linear scan voltammograms of pure Zn deposited potentiostatically under continuous current at a potential of -1.2 V (red) and Zn-Mn alloys deposited galvanostatically under continuous (green) and pulse currents (blue); cathodic and anodic scans were recorded in two separate experiments

The determination of the corrosion potential E_{corr} and the corrosion current density i_{corr} was carried out according to the Tafel method on the basis of the scans presented in Fig.87. The average values for the deposits, as well as the calculated corrosion rates are summarized in Table 22. As expected, a decrease of the corrosion potential with increase of the Mn content is observed. Deposits containing 13 wt.% Mn presented a corrosion potential about 10 mV lower than that of Zn while 15 wt.% Mn-containing deposits presented 30 mV decrease versus Zn. Such observations were reported previously in the reference literature and associated to the presence of Mn, of potential lower than Zn [97, 98, 125]. Similar values of the corrosion current density were measured on both Zn-Mn deposits, with about 106 and 108 $\mu\text{A}/\text{cm}^2$ for the pulse and continuous deposits, respectively. This result is not surprising and most likely due to the numerous similarities between the two deposits, namely only a 2 wt.% variation of the Mn content and identical phase composition.

In comparison to the pure Zn deposits, the Zn-Mn alloys permit a two-fold decrease of the corrosion current density. Similar results between Zn and Zn-Mn deposits were previously reported by Ortiz et al. [53].

On the anodic part of the linear voltammograms (Fig.87), a drop of the current density is systematically observed on the three deposits at potential of -0.15 V for the pulse Zn-Mn and continuous Zn deposits and -0.3 V for the continuous Zn-Mn deposit. Such observations were already reported in the literature and related to pseudo-passive behaviours associated to the formation of a compact layer of corrosion products [97, 118, 226]. However, in the case observed here the current densities involved are too important to correspond to a pseudo-passivation. The formation of insoluble corrosion products, in particularly Mn oxides, induces some changes of the catalytic activity of the oxygen reduction [226]. In the case reported here however, the current density drops are observed at a much higher potential, about -0.2 V compared to -0.4 V in the literature and with a significantly lower current density [97, 118]. The presence of a current density drop was nonetheless observed when the cathodic and anodic scans were recorded in a single-step measurement. In this case, a layer of corrosion products could be formed during the cathodic scan, resulting in a drop of the current density, observed at a potential of about -0.45 V and corresponding to a current density of 0.6 mA/cm². Nevertheless, a detailed analysis of the surface of the deposits in both conditions should be carried out in order to better understand the mechanisms involved and the origin of the drop observed at -0.2 V (Fig.87).

Table 22: Corrosion parameters E_{corr} j_{corr} of Zn and Zn-Mn alloys deposited under continuous and pulse currents. Results obtained from linear scan voltammograms using the Tafel extrapolation method

	E_{corr} (mV)	I_{corr} ($\mu\text{A}/\text{cm}^2$)	Corrosion rate (mm/year)
Zn-Mn, 15 wt.% pulse current	-1040 \pm 23	105.8 \pm 6.4	1.55
Zn-Mn, 13 wt.% continuous current	-1020 \pm 21	107.8 \pm 3.8	1.57
Zn, continuous current	-1012 \pm 17	216.7 \pm 10.3	3.23

4.2.2. Anticorrosive behaviour under accelerated corrosion tests

Formation, appearance and development of red rust

The ability of the deposits to resist against the appearance and the development of red rust was assessed through continuous salt spray test and cyclic corrosion tests according to the DIN EN ISO 9227 and VDA 233-102 standards, respectively. During these tests, only large samples coated with Zn-Mn via pulsed electrodeposition were investigated. The surface of the samples was examined after various exposition times during both corrosion tests and the amount of red rust on the surface was determined via image analysis, according to the protocol previously described in section (2.5.5). The appearance of the deposits during the continuous salt spray test and cyclic corrosion test are presented in figures Fig.88 and Fig.89, respectively.

During both corrosion tests, the surface of the deposits is rapidly covered with some white, grey and brownish corrosion products (Fig.88b and Fig.89b). The white corrosion products, or white rust, is well-known during the corrosion of Zn-based coatings and is associated to the formation of Zn corrosion products such as oxides and hydroxides [8]. The brown corrosion products on the other side have also been observed in the literature [96] and were usually associated to Mn oxides [113, 115] while grey areas could either correspond to Mn oxides or remains of the initial Zn-Mn coating. After 48 hours in the salt spray test, the surface is mostly covered by grey and brown corrosion products in addition to white patches (Fig.88c). From 72 hours and up to 96 hours, it seems that the amount of white and brown products decreases and the surface is mostly covered by a compact layer of dark-grey corrosion products

(Fig.88e). The first signs of red rust can be observed after 168 hours of exposure, with about 10 % of the surface covered according to the image analysis (Fig.88f). No significant evolution of the surface appearance is observed during the cyclic corrosion test VDA 233-102. This is due to the significantly reduced corrosiveness of the cyclic corrosion test in comparison to the continuous salt spray test, as previously reported [16, 51] and previously discussed in the section (1.1.3).

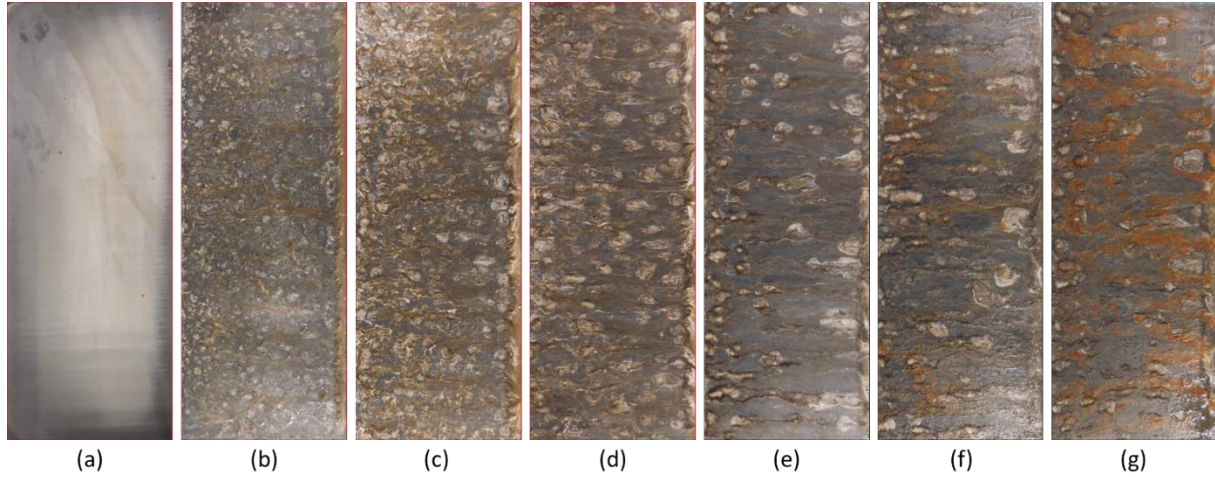


Fig.88: Appearance of pulse Zn-Mn alloy coatings (9.1 μm thickness) at initial stage (a) and after 24 hours (b), 48 hours (c), 72 hours (d), 96 hours (e), 168 hours (f) and 192 hours (g) of exposure in the neutral salt spray test (DIN EN ISO 9227)

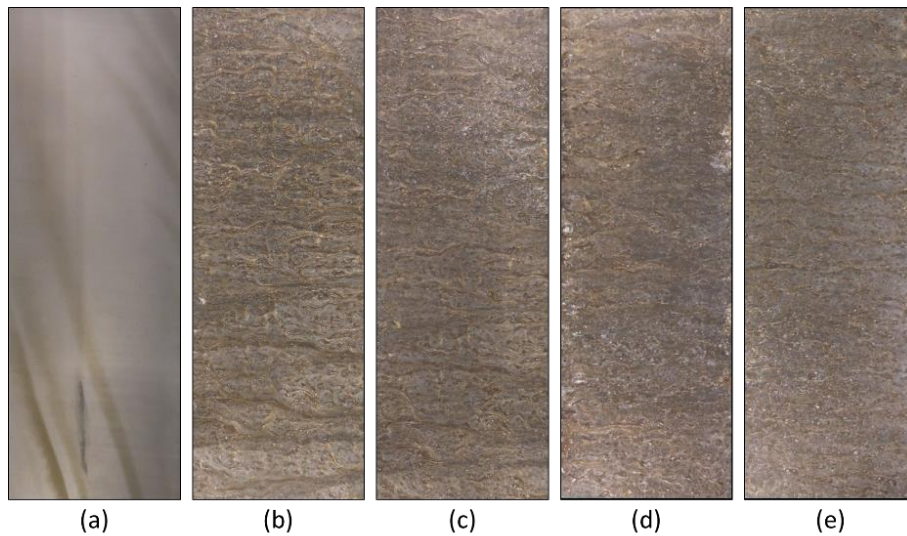


Fig.89: Appearance of pulse Zn-Mn alloy coatings (9.1 μm thickness) at initial stage (a) and after 1 week (b), 2 weeks (c), 3 weeks (d) and 4 weeks (e) of exposure in the cyclic corrosion test VDA 233-102

Image analyses confirm the observations of the Fig.88 and Fig.89. The evolution of the percentage of red rust on the surface of the samples after continuous salt spray test is summarized in Fig.90. It has to be noted that absolutely no signs of red corrosion products could be detected on the surface of the deposits during the entire duration of the cyclic corrosion test VDA 233-102.

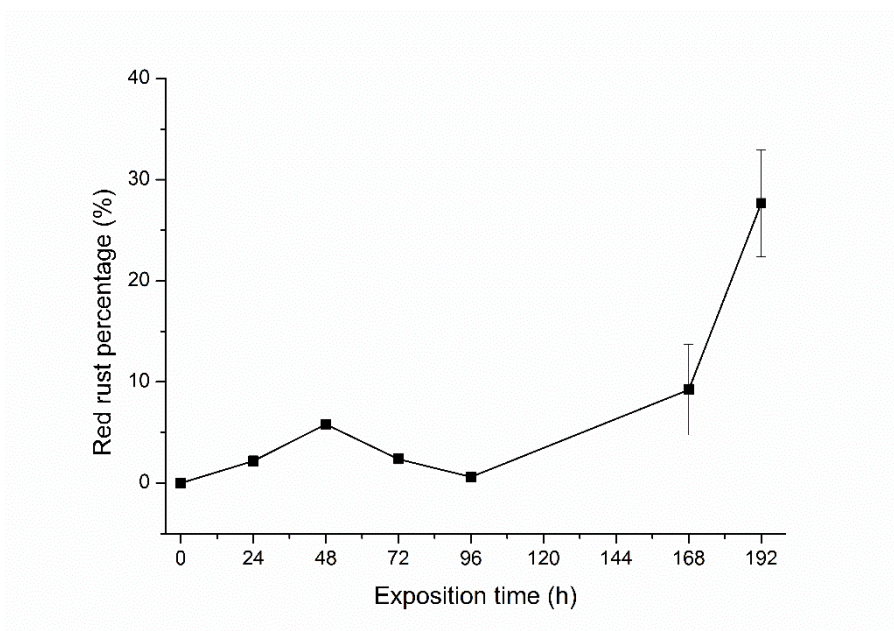


Fig.90: Surface of pulse deposited Zn-Mn (9.1 μm thickness) covered by red rust during neutral salt spray test (DIN EN ISO 9227) up to 192 hours of exposure; the measurement up to 96 hours present a low error not visible on the figure

It is important to mention that image analysis reveals about 5 % of red corrosion products on the pulse Zn-Mn after only 48 hours of exposure in the salt spray test (Fig.90). Interestingly, this “peak” coincides with an increase of the amount of brownish corrosion products observed in Fig.88c, but does not correspond to red rust and to the corrosion of the steel substrate, as this red rust could not be observed on the samples at this stage. This result underlines the limits of the image analysis for the quantification of the red rust, especially in the case of Zn-Mn coatings where brown and red corrosion products associated to Mn and Fe oxides, respectively, are quite likely to be simultaneously present on the surface. The results show a relatively stable behaviour of the samples up to 96 hours of exposure, with close to no red corrosion products detected on the surface of the deposits. A slow increase of the amount of red rust is then observed up to 168 hours of exposure with about 9 % of the surface covered. It can be noted that the first spots of red corrosion products are observed at the edges of the samples, where the deposits present heterogeneous properties such as a reduced Mn content, and a rougher and more porous morphology, as previously discussed in section 3.5.3. After 192 hours, about a quarter of the surface is covered.

The corrosion behaviour of Zn-Mn coatings was previously investigated by means of the salt spray test (ASTM B-117-07a) in the literature [53]. The authors observed the first signs of red rust after 432 hours of exposure. However, these values were obtained on deposits thicker (about 15 – 16 μm) than those investigated in this work (about 9 μm) containing about 6 wt.% Mn and are therefore hardly comparable to the results of this work. A proper analysis of the anticorrosive properties of the Zn-Mn deposits in comparison with commercial coatings will be conducted later in this work.

Corrosion rate

The presence of a remaining cathodic protection of the steel substrate after continuous salt spray test and cyclic corrosion test was measured via coulometry. The experiments were performed after removal of the corrosion products and the results are presented in Fig.91a and b, respectively. A remaining coating thickness of about 4 μm in average was measured after 96 hours of exposure in the continuous salt spray test (Fig.91a) and after 4 weeks of exposure in the cyclic corrosion test (Fig.91b).

Although the results observed after salt spray test seem to contradict the observations of the Fig.88, it does not exclude the possibility for the substrate to be corroded. Indeed, the presence of some defects such as porosity on the Zn-Mn deposits can lead to the local failure of the coating via cracking and delamination, resulting locally in the corrosion of the steel substrate and the appearance of red rust.

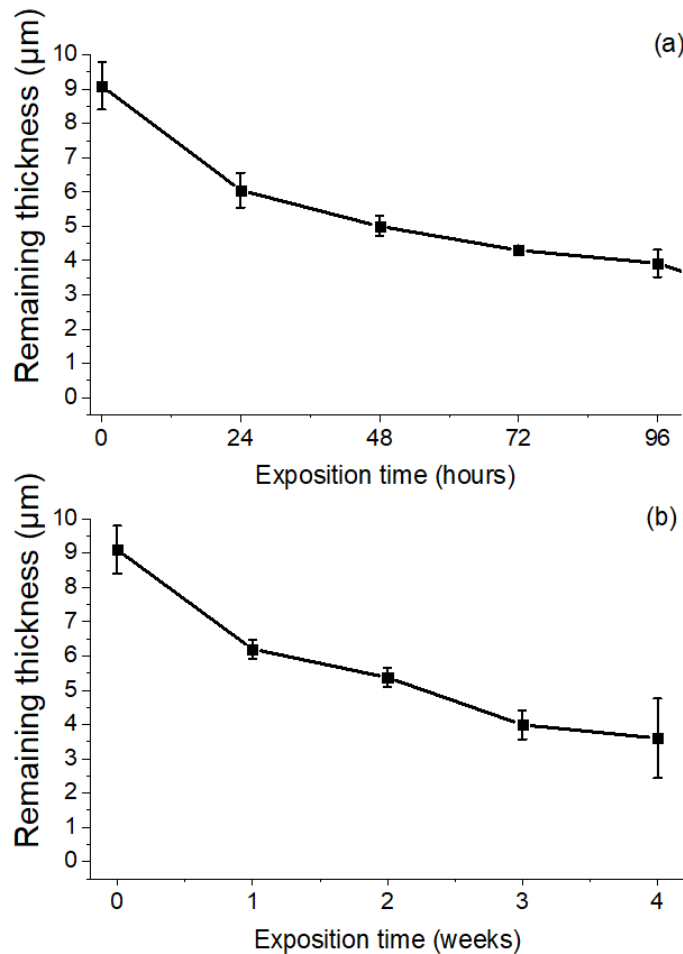


Fig.91: Initial and remaining coating thickness of pulse deposited Zn-Mn (9.1 μm thickness) during continuous salt spray test DIN EN ISO 9227 up to 168 hours of exposure (a) and cyclic corrosion test VDA 233-102 up to 4 weeks of exposure (b)

From these data, an “effective” corrosion rate can be determined for the pulse Zn-Mn deposits, with about 1.295 $\mu\text{m}/\text{day}$ in the continuous salt spray test and 0.049 $\mu\text{m}/\text{day}$ in the cyclic corrosion test. If those results are to be compared with the calculations of the corrosion rate from the Tafel experiments, it appears that the “effective” corrosion rate of the pulse Zn-Mn alloys is significantly lower, with corrosion rates of 0.473 and 0.018 mm/year during salt spray test and cyclic corrosion test, respectively compared to 1.55 mm/year during potentiodynamic polarization. These results also depict the complex relations existing between electrochemical experiments and accelerated corrosion tests. Indeed, each method corresponds to different corrosive media (immersion, continuous salt spray, alternating climate, etc.) and an assessment of the reactivity on various time scales (from a few minutes up to several weeks). As already discussed in section 1.1.3 of this work, the amount of chloride deposited is a major criterion characterizing the corrosiveness of an accelerated test [16]. Tests leading to the deposition of high amounts of chloride, such as the continuous salt spray test DIN EN ISO 9227 (383 mg/cm^2 Cl), leads to corrosion rates significantly higher than tests where low amounts of chloride are deposited, such as the cyclic corrosion test VDA 233-102 (12.3 mg/cm^2 Cl).

4.2.3. Corrosion mechanisms and corrosion products analysis

XRD analyses

The XRD diffractograms obtained for the pulse Zn-Mn alloy coatings after 24, 48, 72, 96 and 168 hours of exposure in the continuous salt spray test DIN EN ISO 9227 are presented in Fig.92 from (a) to (e), respectively.

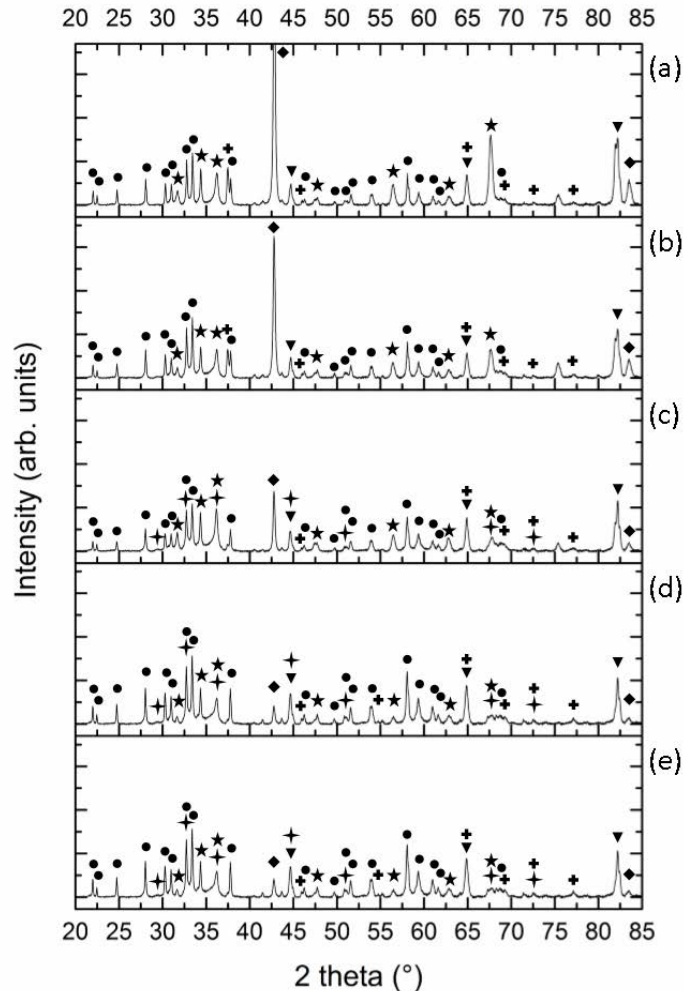


Fig.92: XRD pattern of the pulse Zn-Mn alloy coatings (9.1 μm thickness) after 24 hours (a), 48 hours (b), 72 hours (c), 96 hours (d) and 168 hours (e) of exposure in the continuous salt spray test (DIN EN ISO 9227). Diffraction peaks corresponding to ϵ_2 -ZnMn (JCPDS n° 04-003-4358 ◆), manganese oxide $\text{Mn}_{0.98}\text{O}_2$ (JCPDS n° 81-1947 ✦), Mn_3O_4 (JCPDS n° 01-1127 +), simonkolleite $\text{Zn}_5(\text{OH})_8\text{Cl}_2 \cdot \text{H}_2\text{O}$ (JCPDS n° 07-0155 ●), zinc oxide ZnO (JCPDS n° 05-0664 ★) and Fe (JCPDS n° 06-0696 ▼)

Up to 48 hours of exposure (Fig.92a), the first signals corresponding to corrosion products are already detected with the presence of manganese oxide $\text{Mn}_{0.98}\text{O}_2$, zinc oxide ZnO and simonkolleite $\text{Zn}_5(\text{OH})_8\text{Cl}_2 \cdot \text{H}_2\text{O}$. Although an increased intensity of the peaks corresponding to the steel substrate could be observed, the highest intensity peaks were still recorded for the ϵ_2 -ZnMn phase, confirming the significant thickness of the remaining deposit. After 72 hours (Fig.92c), the appearance of some traces of an additional manganese oxide could be detected, corresponding to Mn_3O_4 . For longer exposures, no significant changes in the composition of the corrosion products could be observed. It is interesting to note the continuous decrease of the peak intensity corresponding to the zinc oxide ZnO with increase of the exposure time, which suggests that this product is not preferentially formed throughout the corrosion process and thus covered by other corrosion products. In addition, the intensity of the ϵ_2 -ZnMn phase

significantly decreases after 48 hours of exposure (Fig.92b) but interestingly, no significant changes in the peak intensity for the steel substrate could be observed. Considering the penetration depth of the X-rays in the order of magnitude of 1 to 10 μm , this suggests the formation of a thick layer of corrosion products. This assumption is supported by continuous increase of the mass gained during exposure to the salt spray test (Fig.93).

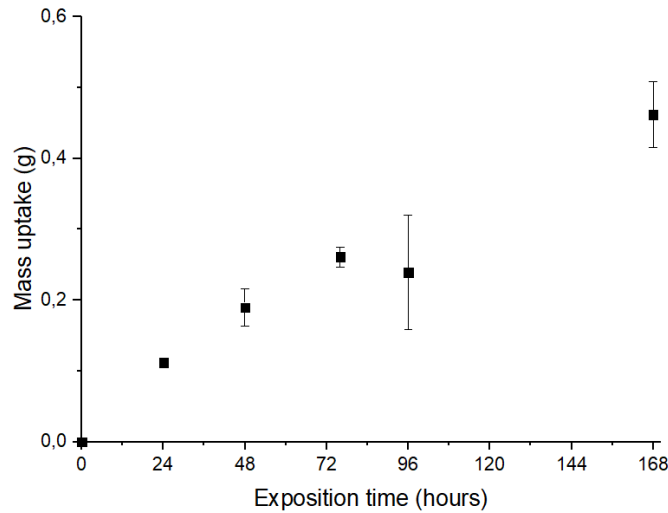


Fig.93: Mass uptake due to the formation of corrosion products on the surface of the pulse Zn-Mn samples ($75 \times 175 \text{ mm}^2 \pm 2 \text{ mm}^2$, $9.1 \mu\text{m}$ thickness) during exposition to the neutral salt spray test (DIN EN ISO 9227)

Chemical analyses

In order to better understand the formation and the distribution of the corrosion products on the surface of the samples, a thorough elemental analysis was carried out on different regions of the deposits after various exposures in the salt spray test. These regions correspond to corrosion products of various colours, as previously identified. A closer look at the surface of the deposits (Fig.94) reveals the presence of light grey (LG), dark grey (DG), brown (B), white (W) and red (R) corrosion products. The results of the EDS analyses conducted on those corrosion products have been gathered in the Fig.95.

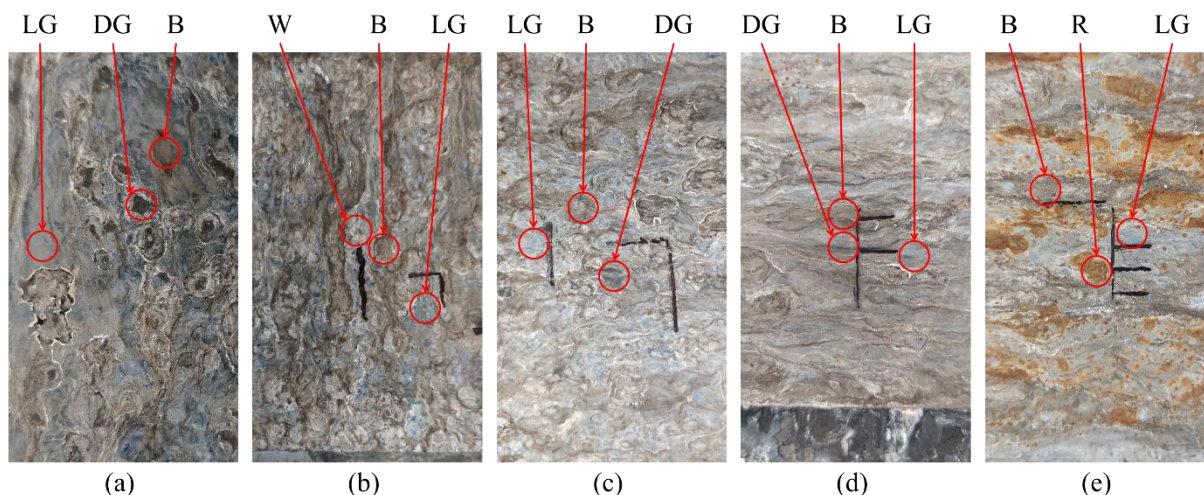


Fig.94: Appearance (close-up) of pulse Zn-Mn alloy coatings (9.1 μm thickness) after 24 hours (a), 48 hours (b), 72 hours (c), 96 hours (d) and 168 hours (e) of exposure in the neutral salt spray test (DIN EN ISO 9227); regions considered for chemical analyses by means of SEM-EDS circled in red and corresponding to LG – light grey, DG – dark grey, B – brown, W – white and R – red corrosion products

The probable phases corresponding to each of the regions investigated were assumed from the chemical composition the analysis of X-ray diffractograms as well as the appearance of the corrosion products.

It can be supposed that the light-grey corrosion products are likely to be composed of a mixture between simonkolleite and zinc oxide. This is supported by the presence of chlorine (between 5 and 7 at.%, Fig.95) and the direct observation of simonkolleite crystals in those regions [229], already forming after 48 hours of exposure (Fig.96f) and particularly well distinguishable after 72, 96 and 168 hours of exposure (Fig.96g, h and i). In addition, EDS mappings performed in those regions after 24 hours of exposure also reveal the presence of Mn oxides on the upper surface (Fig.96e).

A similar composition was measured in the white spots of corrosion products, suggesting also a mixture between ZHC and ZnO (Fig.95). However, due to the presence of white corrosion products in large amounts such as on the pure Zn deposits, this may suggest a higher amount of ZnO compared to ZHC. The presence of simonkolleite crystals can still be distinguished on the Fig.96a, covered by some additional powder-like needles.

Analyses of the darker regions of the samples reveal the absence or very low amounts of chlorine (Fig.95). In addition, the micrographs show a very compact morphology quite similar to the one observed on the deposits prior to corrosion experiments. As a result, it may be supposed that these regions were barely affected by corrosion during the salt spray test, especially during the early stages (Fig.96b after 24 hours). After 72 hours of exposure (Fig.96c), no significant changes of the elemental composition could be observed (Fig.95). However, the micrograph presented in Fig.96c show the formation of some nodules slowly covering the surface and presenting high Mn contents suggesting the presence of Mn oxides. After 96 hours, it appears that the entire surface is covered by Mn oxides as suggested by the high amount of Mn (26 at.%) measured (Fig.95). In addition, the formation of simonkolleite could be observed with some particularly well defined crystals (Fig.96d).

Chemical analyses and EDS mappings on the brown corrosion products after 24 hours of exposure suggest the presence of a layer of Mn oxides covered, or partially covered by a dense network of simonkolleite crystals (Fig.96j). After 48 hours, no traces of simonkolleite could be observed on the micrographs (Fig.96k), as supported by the absence of chlorine (Fig.95) and the increase of Mn (19 at.%) which suggest the presence of only Mn oxides. After 72 hours however, well-defined crystals of simonkolleite could be observed (Fig.96l), in good correlation with an increased amount of chlorine (7 at.%, Fig.95). After 96 and 168 hours of exposure, almost no chlorine could be measured (Fig.95) in

relation with the absence of ZHC crystals (Fig.96m and n). The changes of microstructure as well as the important variation of the Mn content, from 17 to 8 at.% between 96 and 168 hours could suggest the appearance of additional Mn oxides such as Mn_3O_4 as observed on the XRD diffractograms (Fig.92).

The evolution of the Fe content in the different regions of the samples through the corrosion test was also monitored (Fig.95). Some small Fe-amounts could be measured during the early stages, in the dark-grey, light-grey and brown corrosion products. These amounts of Fe are most likely due to the interaction volume of the EDS measurements, resulting in some signals originating from the substrate steel in some cases where the remaining thickness of the deposit may be quite low. This does not depicts the corrosion of the substrate that was also investigated after 168 hours of exposure and recognized with the presence of red corrosion products (Fig.95).

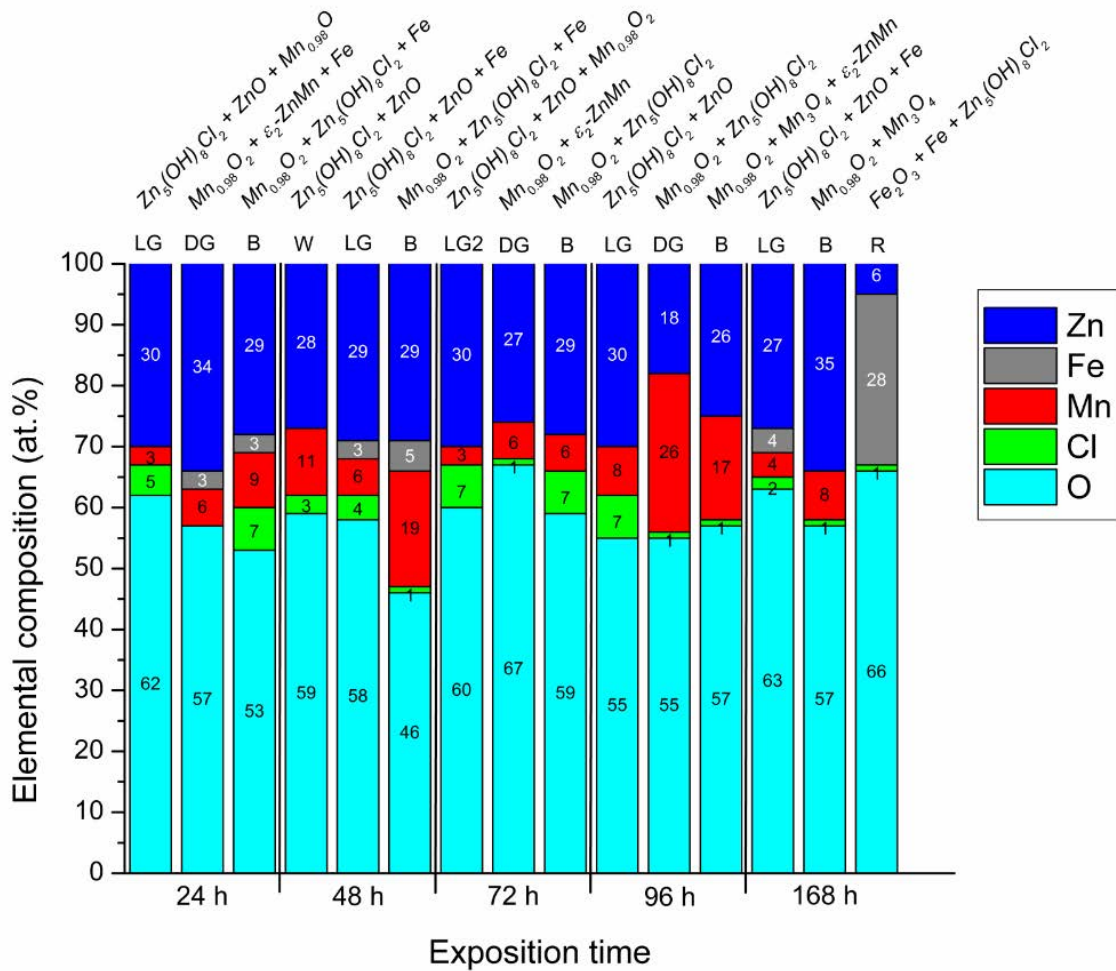


Fig.95: Evolution of the chemical composition on the surface of pulse Zn-Mn deposits (9.1 μm thickness) over exposition time in the neutral salt spray test (DIN EN ISO 9227); measurements performed on various regions depicted in Fig.94; most probable phases included based on the chemical composition, XRD analyses and aspect of the corrosion products

Suitability of the pulse Zn-Mn deposits for automotive application

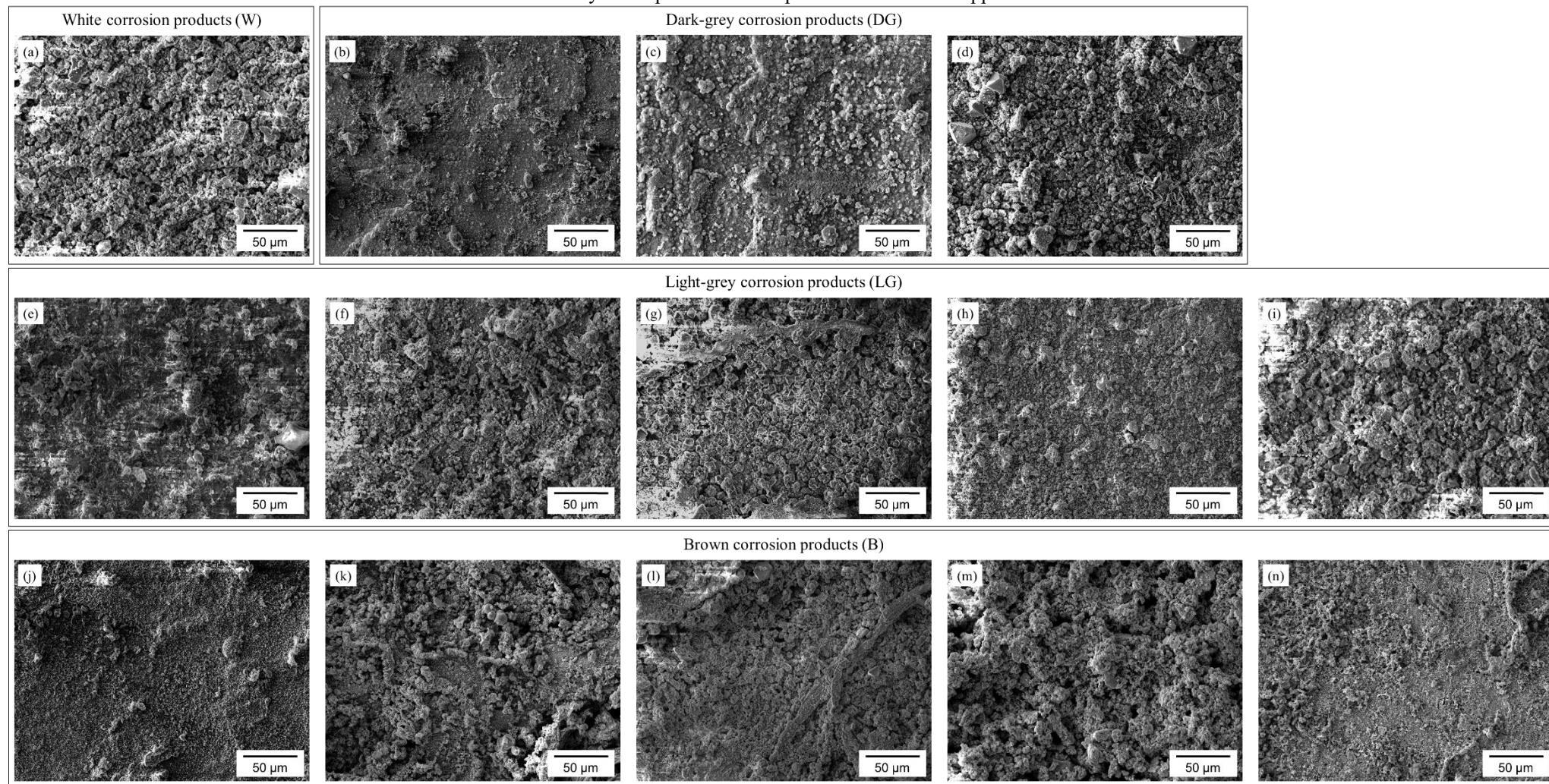


Fig.96: SEM micrographs of the regions investigated on the corroded Zn-Mn samples (9.1 µm thickness) after neutral salt spray test (DIN EN ISO 9227); white corrosion products after 48 h (a); dark-grey corrosion products after 24 h (b), 72 h (c) and 96 h (d); light-grey corrosion products after 24 h (e), 48 h (f), 72 h (g), 96 h (h) and 168 h (i); brown corrosion products after 24 h (j), 48 h (k), 72 h (l), 96 h (m) and 168 h (n)

Similarly, analyses on cross-sections of the corroded samples were conducted with some of the results depicted in the figures Fig.97 and Fig.98 after 24 and 72 hours in the neutral salt spray test, respectively. After 24 hours (Fig.97), a remaining layer of Zn-Mn can be observed on the micrographs, with a thickness between 6 and 8 μm , confirming the measurements displayed in Fig.91a. Chemical analyses reveal in addition to Zn and Mn some “islands” with high concentrations of chlorine and oxygen, mostly located near the surface and likely due to the presence of ZHC and oxides as previously observed. It is also worth to mention that corrosion of the deposit appears to be fairly homogeneous. These observations are, depending on the regions concerned for the cross-section analyses, in good agreement with the observations and measurements carried out on the surface of the deposits. The absence of corrosion products and the relatively high thickness of the remaining coating could well correspond to the dark-grey regions (Fig.96b).

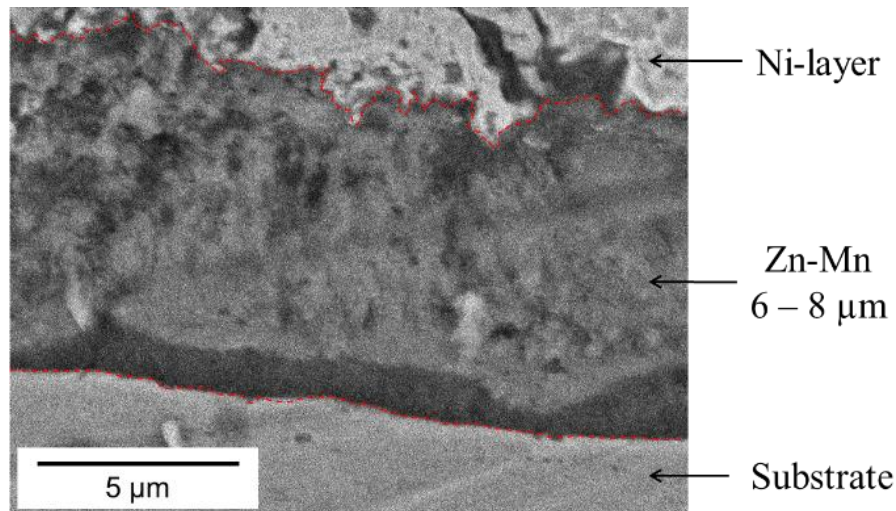


Fig.97: BSE micrograph of the cross-section of a Zn-Mn coated (9.1 μm thickness) steel sample after 24 hours exposition in the neutral salt spray test (DIN EN ISO 9227); sample covered with corrosion products and coated with a Ni-layer; delamination of the Zn-Mn layer from the substrate can also be observed

After 48 and 72 hours, no significant decrease of the remaining coating could be observed. However, the differentiation between the various layers becomes quite complex at this stage. From the BSE micrograph and EDS mappings presented in the Fig.98(a) and (b) after 72 hours of exposition, three layers (in addition to the substrate and the upper Ni-layer) can be observed. A first layer, about 5 to 6 μm thick appears to be composed of a mixture of the initial Zn-Mn coating with ZHC as well as Zn and Mn oxides due to relatively high amounts of chlorine together with Zn, Mn and O. The second layer presents high amounts of chlorine, zinc and oxygen as well as some traces of manganese. This suggests a large amount of ZHC mixed with some Mn oxides. The last upper layer of corrosion products shows no chlorine, low amounts of Zn and high Mn and O contents which suggests the presence of Zn and Mn oxides on the surface. This could well correspond to the brown or light-grey regions observed previously (Fig.96). This also seems to confirm the corrosion mechanisms previously mentioned.

It appears that the formation of a thick and compact layer of corrosion products, mostly composed of ZHC takes place rapidly and provide a complete cover of the Zn-Mn deposit. However, it seems that this first layer of corrosion products acts as a membrane, permitting diffusion and further corrosion of the underlying deposit. According to these observations, it also appears that the outer layer of the corrosion products, in direct contact with the environment, is able to further react and only form oxides. This effect may be related to changes of the pH, not affected by Mn dissolution in those areas.

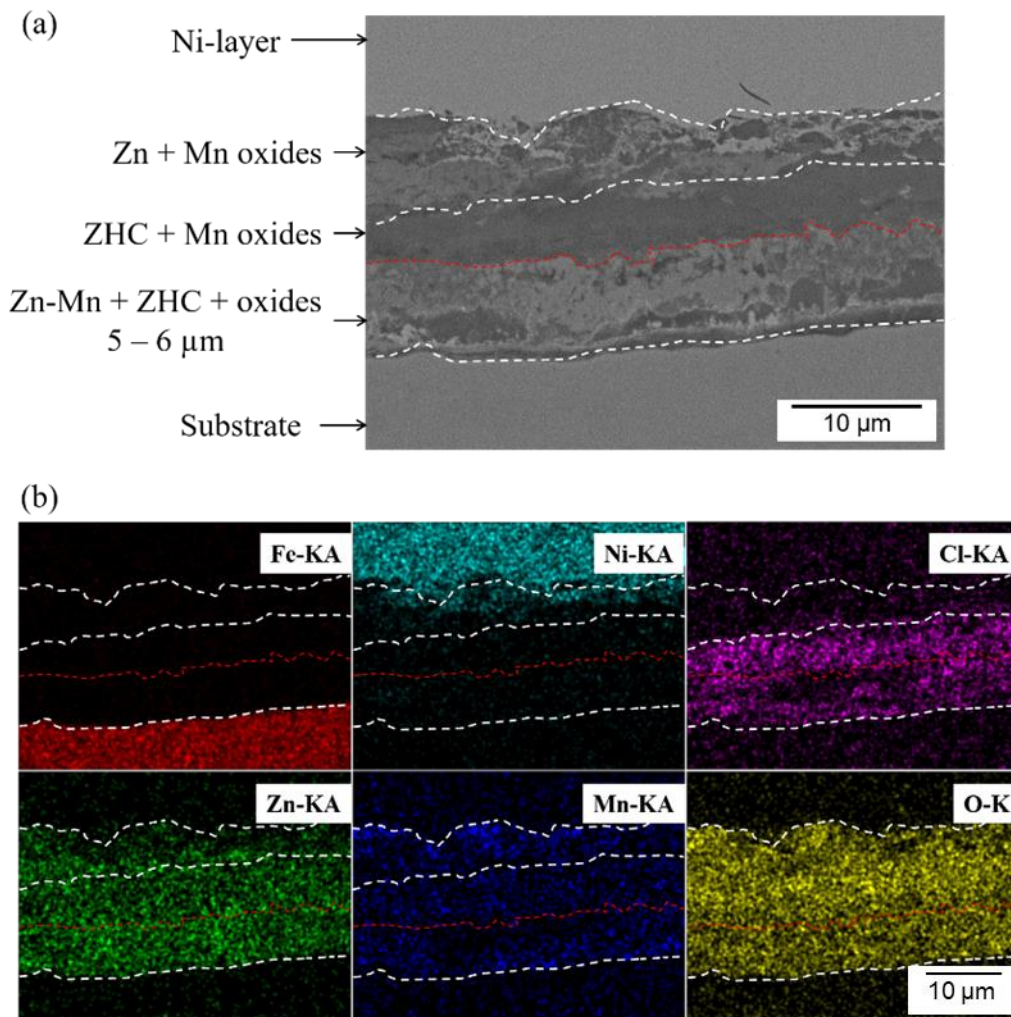


Fig.98: BSE micrograph (a) and EDS mappings (b) of the cross-section of a Zn-Mn coated (9.1 μm thickness) steel sample after 72 hours exposition in the neutral salt spray test (DIN EN ISO 9227); sample covered with corrosion products and coated with a Ni-layer

The analysis of the corrosion products on cross-sections becomes quite challenging after 96 and 168 hours of exposure in the salt spray test. Due to the important thickness of the layer of corrosion products, the deposition of a compact Ni-layer is difficult to achieve and the quality of the prepared cross-sections decreases, so that observations are not possible. Still, some micrographs could be obtained after 168 hours of exposure with the BSE micrograph and EDS mapping presented in Fig.99(a) and (b), respectively. The presence of a corrosion pit inside the steel substrate can be observed, with Fe oxide on top of it. It seems that a porous layer of corrosion products was originally formed in this region, as the Ni coating appeared to fill those pores.

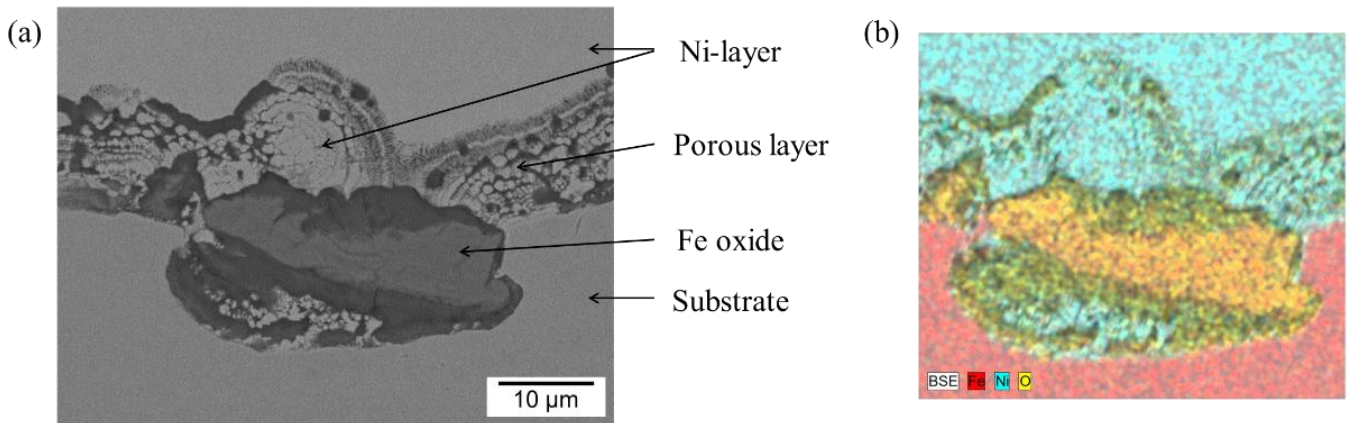


Fig.99: BSE micrograph (a) and EDS mapping (b) of the cross-section of a Zn-Mn coated (9.1 μm thickness) steel sample after 168 hours exposure in the neutral salt spray test (DIN EN ISO 9227); sample covered with corrosion products and coated with a Ni-layer

The composition of the remaining Zn-Mn coating after removal of the corrosion products was also measured via EDS (Fig.100). After 24 and 48 hours of exposure, Mn contents of 13.8 and 13.9 wt.%, respectively, were measured on the surface of the deposits, considered to be identical to the Mn content prior to the corrosion test (13.7 ± 1 wt.% Mn). With increase of the exposure in the corrosion test, it appears that a decrease of the Mn-content is measured with a loss of about 1 wt.% Mn per 24 hours, with 12.6 and 11.5 wt.% Mn measured on the surface of the deposits after 72 and 96 hours of exposure, respectively. This decrease of the Mn content supports the hypothesis of preferential Mn dissolution reported in the literature [99].

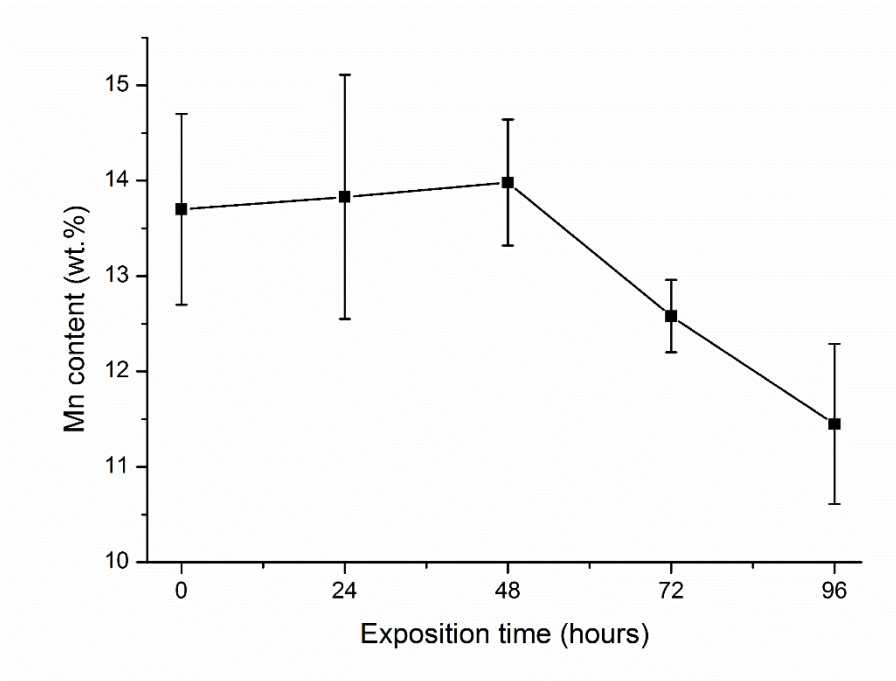


Fig.100: Evolution of the Mn content on the surface of the Zn-Mn deposits (9.1 μm thickness) after exposition in the neutral salt spray test (DIN EN ISO 9227) and removal of the corrosion products

SEM micrographs of the surface of the remaining Zn-Mn coating, presented in Fig.101, suggest an interesting dissolution characteristics. Indeed, it appears that the crystallites are dissolved from the inside. After 24 hours already (Fig.101a), it seems that the largest crystallites are preferentially corroded. After 72 and 96 hours exposition, this phenomenon becomes more evident as depicted in Fig.101(c) and (d), respectively. In these longer exposition cases, it seems that only the outer shell of the crystallites stays undamaged.

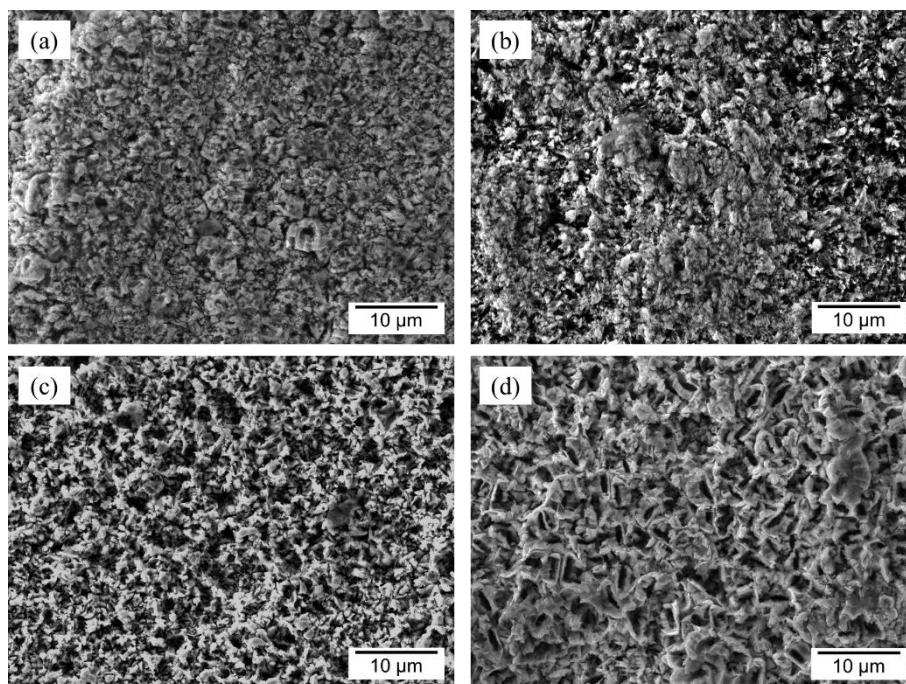


Fig.101: SEM micrographs of the surface of the remaining Zn-Mn coating (initial thickness of 9.1 µm) after 24 hours (a), 48 hours (b), 72 hours (c) and 96 hours (d) exposition in the neutral salt spray test and removal of the corrosion products

Discussion

The corrosion of Zn in chloride containing environments was largely reported in the literature and occurs with the simultaneous formation of zinc oxide, simonkolleite and hydrozincite [51, 53, 230], resulting in a porous layer of corrosion products that does not permit the passivation of the underlying Zn deposit [8, 231, 232]. However, it was largely reported that simonkolleite alone, as main product formed during the corrosion of Zn-Mn alloys, was responsible for the particularly good anticorrosive properties of these alloys, due to a high compactness and a low solubility [56].

Based on the identification of the corrosion products via XRD (Fig.92) as well as SEM-EDS (Fig.95) as discussed in the previous sections and based on the literature [98, 99], the mechanism of preferential formation of ZHC can be detailed. Mn, due to its lower potential is preferentially dissolved into Mn^{2+} ions (eq.48) over Zn, which results according to the literature to cathodic reaction of oxygen (eq.49) and an increase of the pH value according to a preferred “path 1”. However, for deposits with high Zn contents such as those investigated in this study, it could be envisaged that the dissolution of Zn into Zn^{2+} (eq.50) still occurs simultaneously in a secondary “path 2” together with the cathodic reduction of

oxygen (eq.51). Although the mechanism of preferential dissolution of Mn was widely discussed in the literature, the presence of two simultaneous corrosion paths was never considered.

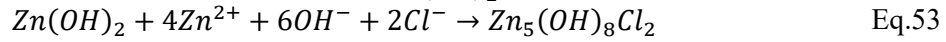
Path 1



Path 2



This leads during the early stages of the corrosion, based on the XRD analyses (Fig.92) as well as on the cross-sectional analyses (Fig.97, Fig.98 and Fig.99), to the parallel formation of manganese and zinc oxides $Mn_{0.98}O_2$ and ZnO, respectively. However, due to the marginal Mn content in the deposits, the amount of manganese oxides formed is expected to stay rather low. Due to the increase of the pH, the Zn^{2+} ions are then preferentially transformed into simonkolleite ZHC (eq.53) over ZnO (eq.54).



Similarly, it seemed based on the observations on the Fig.92 that Mn oxide Mn_3O_4 was first formed after 72 hours of exposure in the salt spray test while $Mn_{0.98}O_2$ was formed during the early stages of corrosion. Considering the Pourbaix diagram of manganese from Charlot [233], it appears that the Mn_3O_4 oxide is stable at higher pH compared to other Mn oxides. Its formation is therefore likely to be related to the hydrogen evolution and the increase of pH throughout the corrosion process. Similar observations were made by Ortiz et al. [53] with the formation of MnO during the early stages of corrosion followed by the formation of more complex oxides at prolonged exposures.

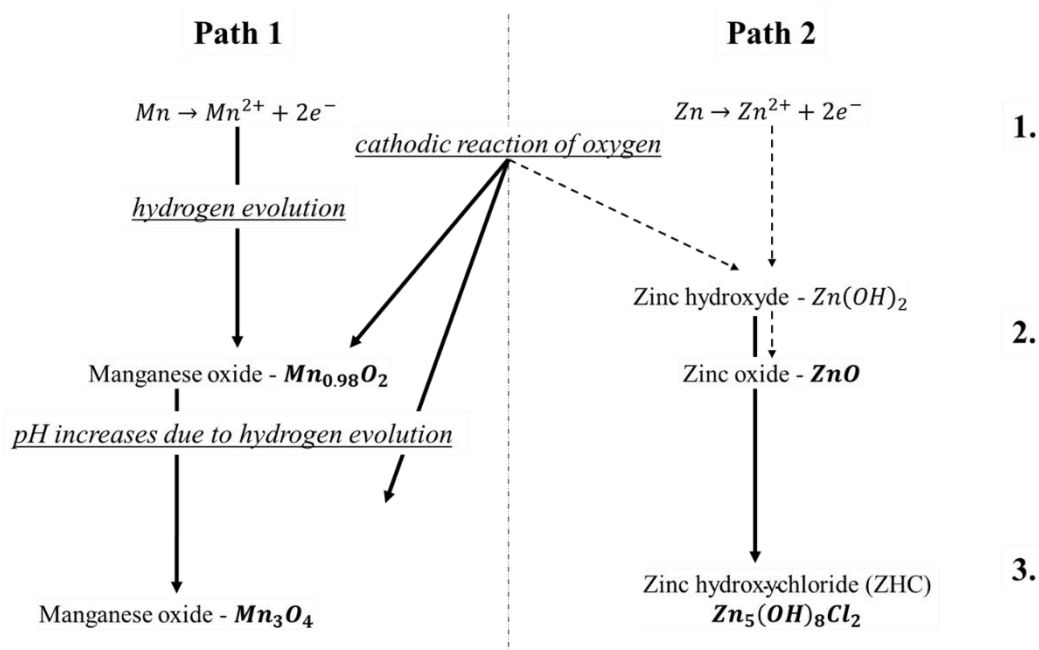


Fig.102: Schematic illustration of the proposed corrosion mechanisms leading to the formation of the corrosion products observed on pulse Zn-Mn deposits. The preferred corrosion paths are illustrated by the large plain arrows while the secondary corrosion paths are illustrated by the thin dashed arrows. Steps by numbers: 1. Reactions at neutral pH, dissolution of Mn into Mn^{2+} , simultaneous dissolution of Zn into Zn^{2+} and cathodic reduction of oxygen; 2. hydrogen evolution and formation of manganese oxide $Mn_{0.98}O_2$ and zinc oxide ZnO via zinc hydroxyde $Zn(OH)_2$; 3. Formation of simonkolleite (ZHC) and formation of manganese oxide Mn_3O_4 at higher pH

4.2.4. Comparison with commercial coatings

Electrochemical analyses

In order to assess the anticorrosive performance of the newly developed Zn-Mn deposits, the corrosion behaviour of the commercial coatings was investigated by means of LSV following the protocol already used for the Zn-Mn deposits (section 2.5.2). The Fig.103 compares the typical anodic and cathodic scans recorded for the pulse Zn-Mn deposits (already displayed and discussed previously) and for the commercial deposits.

All coatings present similar anodic and cathodic scans. As previously observed, a good agreement between the anodic and cathodic sections was also obtained on the commercial deposits, leading to coherent corrosion potential. A maximal misfit of 40 mV was obtained for the electrogalvanized ZE75/75 deposits.

The average values for the corrosion potential E_{corr} and the current density i_{corr} , determined according to the Tafel method are summarized in Table 23, as well as the calculated corrosion rates. Unsurprisingly, the Zn-Fe coatings present the highest corrosion potential, due the presence of about 10 wt.% Fe in the deposit (see section 2.8.2, table 18). On the other hand, the ZM90 coating show the lowest corrosion potential due to the presence aluminium and magnesium (see section 2.8.2, table 18). Interestingly, a rather significant difference in the corrosion potential, about 20 mV, was measured between the Zn deposits ZE75/75 and Z100. Although some low amounts of Al were detected in the Z100 deposits (see

section 2.8.2, table 18), such an impact on the corrosion potential is surprising. Similarly, a 30 mV difference in the corrosion potential between the Zn electrodeposits obtained in this work (Table 22) and the commercial ZE75/75 electrodeposits was measured. Another explanation may originate from surface effects. Indeed, it was previously observed that changes of the crystallographic orientation could lead to variations of the corrosion potential, up to 20 mV [8]. In the same manner, variations of the roughness and of the effective surface area could result in such changes of the corrosion potential [8]. These hypotheses could also explain the apparent “non-impact” of Mn addition on the corrosion potential of Zn alloys, when compared here to the commercial products.

Table 23: Corrosion parameters E_{corr} i_{corr} of Zn-Mn alloys deposited pulse current; comparison with the commercial products Z100 (Zn, hot-dip galvanized), ZE75/75 (Zn, electrogalvanized), ZF100 (Zn-Fe, galvanized) and ZM90 (Zn-Al-Mg, hot-dip galvanized); results obtained from linear scan voltammograms using the Tafel extrapolation method

	E_{corr} (mV)	i_{corr} ($\mu\text{A}/\text{cm}^2$)	Corrosion rate (mm/year)
Zn-Mn, 15 wt.% pulse current	-1040 ± 23	106 ± 6	1.55
commercial Zn (Z100) hot-dip galvanized	-1041 ± 23	80 ± 20	1.20
commercial Zn (ZE75/75) electrogalvanized	-1058 ± 11	58 ± 18	0.86
commercial Zn-Fe (ZF100) galvanized	-954 ± 11	70 ± 6	1.02
commercial Zn-Al-Mg (ZM90) hot-dip galvanized	-1082 ± 9	45 ± 5	0.67

Similar conclusions can be made when considering the values of the corrosion current density. While the Zn-Al-Mg deposits present the lowest corrosion current, the Zn-Mn deposits show surprisingly the “worst” results with a twofold increase in comparison to electrogalvanized ZE75/75 deposits. This last results are quite surprising, especially when considering the difference observed in comparison to the Zn electrodeposits of this work (Table 22). Therefore, it appears that the relation between the addition of Mn and the corrosion current density is more complex than suggested in the literature data. The resulting increase of the corrosion rate for the Zn-Mn deposits over the commercial products needs to be considered as an increase of the reactivity for the Zn-Mn alloys in a specific environment. This result does not necessarily imply lower anticorrosive properties, as demonstrated in the upcoming paragraphs.

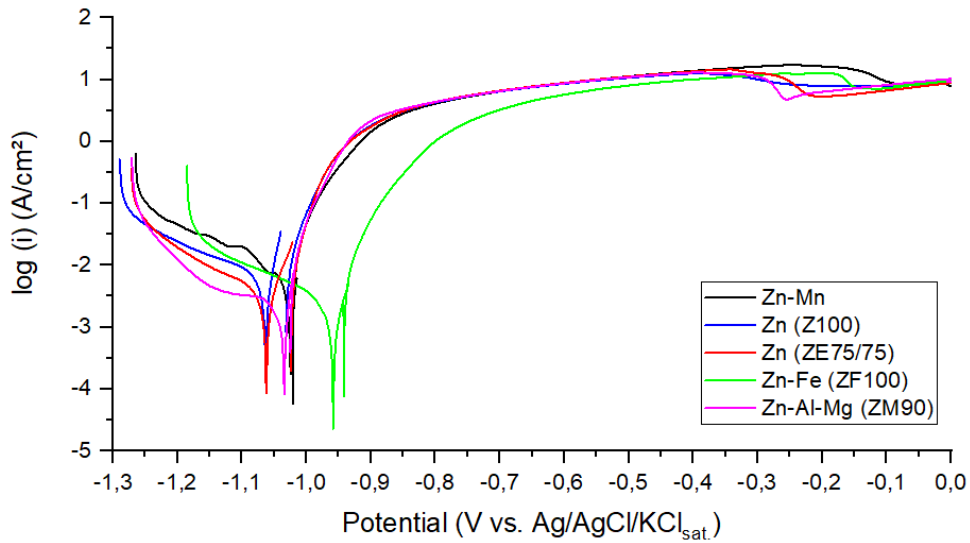


Fig.103: Linear scan voltammograms of pulse Zn-Mn alloys (black); comparison with the commercial products Z100 (Zn, hot-dip galvanized, blue), ZE75/75 (Zn, electrogalvanized, red), ZF100 (Zn-Fe, galvanized, green) and ZM90 (Zn-Al-Mg, hot-dip galvanized, magenta); cathodic and anodic scans were recorded in two separate experiments

Accelerated corrosion tests

The analysis on the formation and covering of red rust during continuous salt spray test (DIN EN ISO 9227) and cyclic corrosion test (VDA 233-102) for the commercial products in comparison to the pulse Zn-Mn deposits is summarized in the Fig.104.

The results show an interesting anticorrosive behaviour of the Zn-Mn deposits in comparison to the commercial products. After salt spray test (Fig.104a), the ZM90 deposits show the best behaviour against the appearance of red rust, with no traces observed up to 192 hours of exposure. The pulse Zn-Mn deposits show here the second-best results with the first signs of red rust observed after 168 hours, versus 72 hours for the ZE75/75 and Z100 and 24 hours for the ZF100 deposits. Similarly, the surface covered by red corrosion products after 1 week (168 hours) is significantly lower for the Zn-Mn deposits, with 9.2 ± 4.5 % covering, in comparison to the ZE75/75 and Z100 deposits, with about 25 ± 10 % covering. After cyclic corrosion test (VDA 233-102), no signs of red rust could be observed on the Zn-Mn and ZM90 deposits, for test duration up to four weeks. In comparison, about 60 % of the surface of the ZE75/75 and Z100 coatings was covered by red rust after the fourth week of exposure.

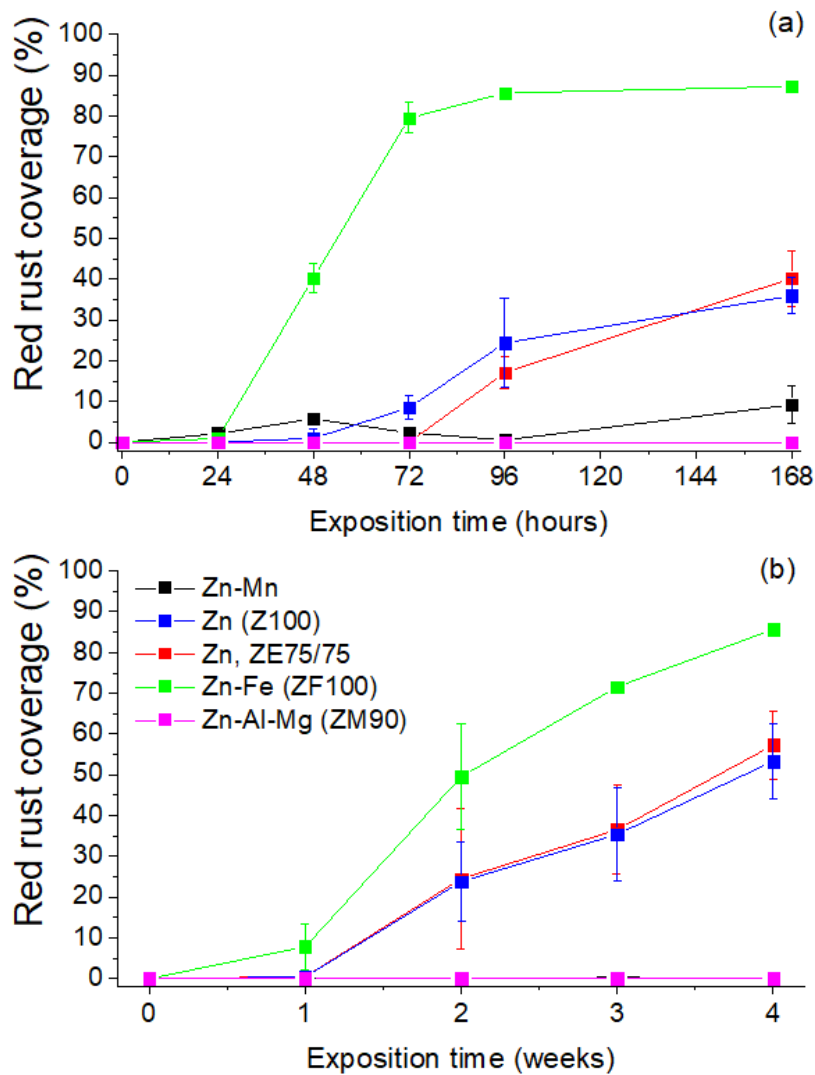


Fig.104: Surface of pulse deposited Zn-Mn (black) covered by red rust during neutral salt spray test (DIN EN ISO 9227) up to 168 hours of exposure (a) and during cyclic corrosion test (VDA 233-102) up to four weeks of exposure (b); comparison with the commercial products Z100 (Zn, hot-dip galvanized, blue), ZE75/75 (Zn, electrogalvanized, red), ZF100 (Zn-Fe, galvanized, green) and ZM90 (Zn-Al-Mg, hot-dip galvanized, magenta)

Measurements of the remaining thickness of the coatings after removal of the corrosion products are summarized in Fig.105. The results obtained after continuous salt spray test (DIN EN ISO 9227) and cyclic corrosion test (VDA 233-102), in Fig.105 (a) and (b) respectively, show a particularly good behaviour of the pulse Zn-Mn deposits in comparison to the commercial coatings. During salt spray test (Fig.105a), the Zn-Fe and Zn deposits show the highest corrosion rate with the consumption of the entire deposit after 24 hours (ZF100), 48 hours (Z100) and 72 hours (ZE75/75). On the other hand, a large portion of the ZM90 and Zn-Mn deposits can still be measured after 96 hours of exposure, with 5.1 and 3.9 μm remaining. Similar results are obtained during exposition in the cyclic corrosion test VDA 233-102 (Fig.105b). While the three ZF100, Z100 and ZE75/75 are fully consumed after 2 weeks, about 2.5 and 5 μm of the ZM90 and Zn-Mn deposits remained uncorroded after 4 weeks.

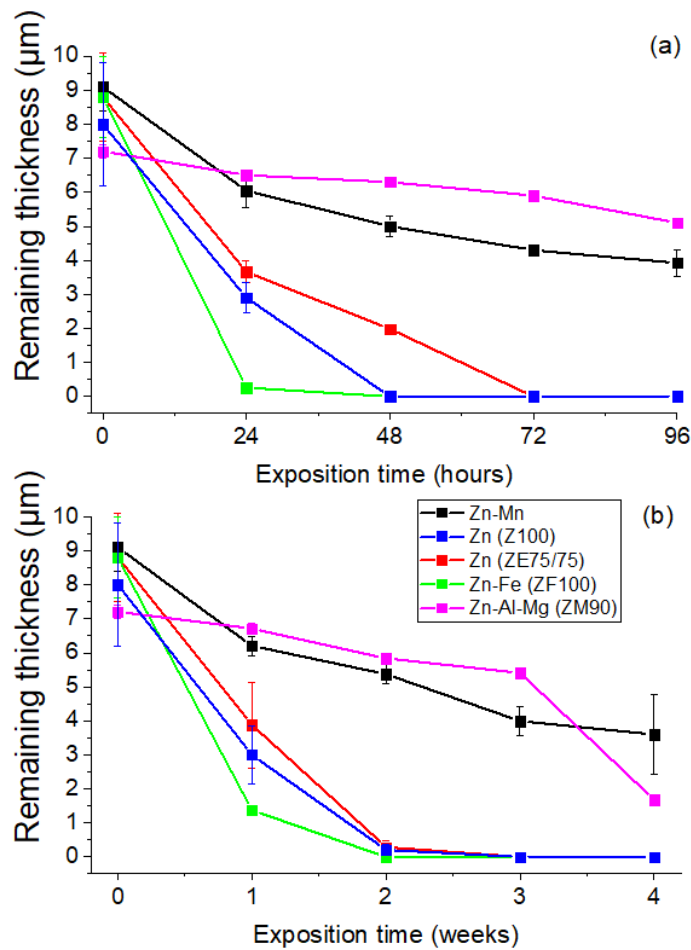


Fig.105: Initial and remaining coating thickness of pulse deposited Zn-Mn (9.1 μm thickness, black) during continuous salt spray test DIN EN ISO 9227 up to 168 hours of exposure (a) and cyclic corrosion test VDA 233-102 up to 4 weeks of exposure (b); comparison with the commercial products Z100 (Zn, hot-dip galvanized, 8.0 μm thickness, blue), ZE75/75 (Zn, electrogalvanized, 8.8 μm thickness, red), ZF100 (Zn-Fe, galvanized, 8.8 μm thickness, green) and ZM90 (Zn-Al-Mg, hot-dip galvanized, 7.2 μm thickness, magenta)

Based on these results and the previously discussed Tafel experiments, the corrosion rates can be summarized for the different deposits in the Table 24.

These results depict the importance of the corrosive environment on the corrosion rate and on the corrosion behaviour of the deposits. While Zn-Mn coatings show the highest corrosion rate under immersion in chloride medium, the lowest corrosion rate is measured under cyclic environment. As a result, the corrosion rate in these three conditions, namely immersion, constant spraying and alternating climate needs to be considered.

Table 24: Corrosion rate of the pulse Zn-Mn and commercial deposits under various exposures

	Immersion in NaCl, from Tafel experiments	Continuous salt spray test (DIN EN ISO 9227)	Cyclic corrosion test (VDA 233-102)
Zn-Mn, 15 wt.% pulse current	1.55 mm/year	0.47 mm/year	0.02 mm/year
commercial Zn (Z100) hot-dip galvanized	1.20 mm/year	1.86 mm/year	0.10 mm/year
commercial Zn (ZE75/75) electrogalvanized	0.86 mm/year	1.24 mm/year	0.11 mm/year
commercial Zn-Fe (ZF100) galvanized	1.02 mm/year	3.12 mm/year	0.39 mm/year
commercial Zn-Al-Mg (ZM90) hot-dip galvanized	0.67 mm/year	0.14 mm/year	0.02 mm/year

4.2.5. Conclusion

In this first section, the corrosion resistance of pulse electrodeposited Zn-Mn deposits was investigated by means of electrochemical and accelerated corrosion tests, namely salt spray test (DIN EN ISO 9227) and cyclic corrosion test (VDA 233-102). In addition, a comprehensive characterization of the corrosion products formed on the samples during the continuous salt spray test was conducted by means of XRD and SEM-EDS analyses on the surface as well as on cross-sections of the specimens.

The results obtained from the potentiodynamic polarization experiments show an impact of Mn addition on the corrosion potential E_{corr} as well as on the corrosion current density i_{corr} . A twofold decrease of the corrosion current density and corrosion rate of the Zn-Mn deposits was observed over pure electrodeposited Zn.

Accelerated corrosion tests revealed promising anticorrosive properties of the pulse Zn-Mn deposits with the late formation of red rust in low amounts. Further analyses of the deposits during continuous salt spray test revealed a decrease of the Mn content on the remaining Zn-Mn deposits over exposition time, supporting the preferential dissolution of Mn during the corrosion of the alloys. Analyses of the corrosion products formed on the surface of the Zn-Mn alloys revealed the simultaneous formation of zinc hydroxychloride (simonkolleite, ZHC) and zinc oxide (ZnO) in a two-path corrosion mechanism. However, it appeared that ZHC is preferentially formed over ZnO due to the preferential dissolution of Mn and the increase of the pH due to hydrogen evolution. Cross-section analyses revealed that the formation of simonkolleite occurs directly on the surface of the Zn-Mn coatings and leads to a compact layer acting as a membrane decelerating the progress of corrosion. In addition, a further reaction of the corrosion products in contact with the corrosive medium and leading to Zn- and Mn-oxides solely was observed.

4.3. Forming behaviour

The forming, and in particular the cold forming behaviour of the alternative Zn-Mn deposits is also of significant concern in the framework of this project. Indeed, the application of metallic coatings

usually occurs directly at the steel supplier's plants. This means that coated steel coils are subjected to various cutting and forming operations in order to obtain the final components. The deposits therefore need to withstand these operations.

Various mechanical properties and forming aspects of the Zn-Mn deposits will be investigated in this section by means of hardness measurements and tensile tests aiming to give some insights on the adhesion of the coatings on the steel substrate.

4.3.1. Hardness

The values of the microhardness for various Zn and Zn-Mn deposits obtained under continuous and pulse modes and various conditions are presented in Fig.106.

It can be observed that the addition of Mn leads to an increase of the hardness, from about 55 Hv for pure Zn up to 85 Hv for deposits containing about 15 wt.% Mn. In addition, a linear increase of the hardness with increase of the Mn content can be observed (Fig.106). Very few studies on the hardness of Zn-Mn alloys can be found in the reference literature. However, Ganesan et al. [97] reported a decrease of the hardness from 79 Hv for pure Zn deposit to 68 Hv for Zn-Mn coatings containing about 15 wt.% Mn.

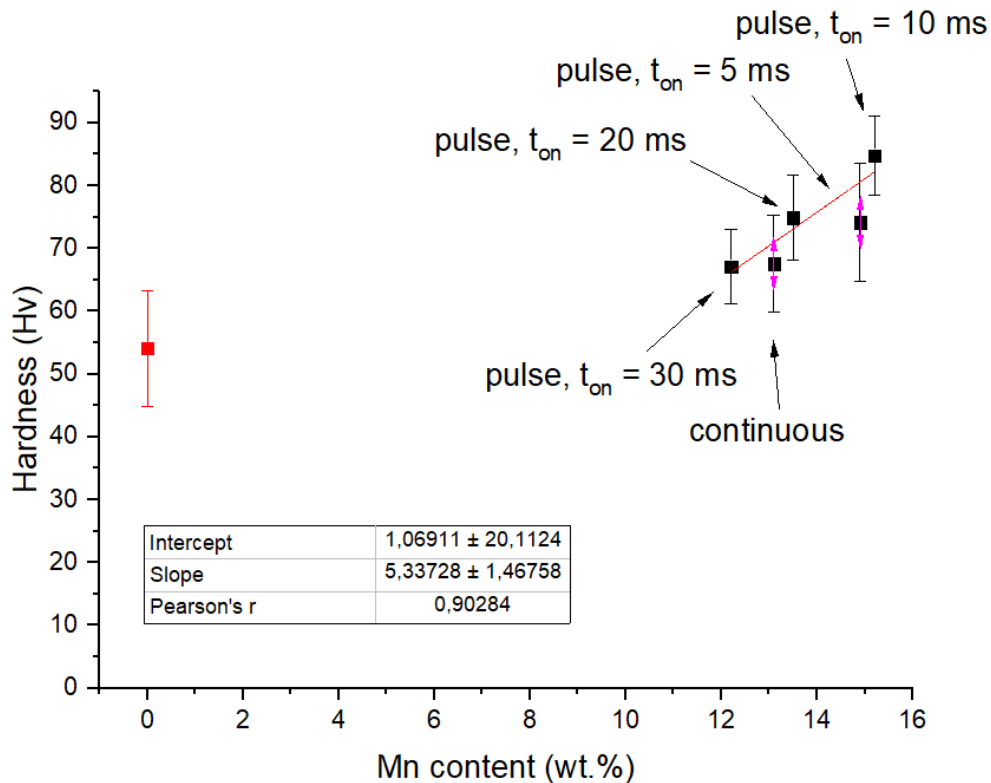


Fig.106: Microhardness of the Zn-Mn deposits (black) obtained under pulse current at various pulse duration and under continuous current and electrodeposited Zn (red)

On the other hand, additional factors such as changes of the grain size are likely to play an important role in the hardness properties. As previously discussed in the section 3.3.4, a decrease of the crystallite size could be observed by decreasing the pulse duration. This decrease of the crystallite size results in an increased hardness in correlation to the Hall-Petch relation given in eq.55 [211].

$$\sigma_y = \sigma_0 + \frac{k_y}{\sqrt{d}} \quad \text{Eq.55}$$

With k_y the strengthening coefficient, σ_0 the lattice resistance against dislocation, d the grain size and σ_y the yield stress. The Hall-Petch strengthening effect implies that the grain boundaries obstruct the movement of dislocations, thus increasing the hardness of the material. Such observations are supported by the findings of Bozzini et al. [226]. The authors reported an increase of hardness in Zn-Mn deposits due to the addition of thiocarbamide additive (TCA), known to stabilize the formation of small crystallites.

Indeed, it appears from the Fig.106 that the deposits obtained with a shorter pulse duration t_{on} present higher hardness values. The microstructural analyses conducted on the coatings deposited under continuous current, presenting the lowest hardness, revealed the presence of large columnar grains (see section 3.2.4, Fig.50). Similar hardness values were measured on pulse deposits obtained at a pulse duration of 30 ms, also composed of relatively large grains (see section 3.3.4, Fig.61). The partial microstructural analyses conducted in chapter 3.3 revealed the smallest grain size for the deposits obtained with a t_{on} of 5 ms (see section 3.3.4, Fig.61), as expected from the literature on the pulse plating. The highest hardness values obtained on alloys deposited with an on-time of 10 ms are therefore surprising. However, additional effects such as surface roughness, defects, heterogeneities, etc. are likely to influence the measurements.

4.3.2. Adhesion of the coatings with the steel substrate

Adhesion under tensile stresses

A representative stress-strain curve obtained at a strain rate of 1 mm/s is presented in Fig.107. An average strain at failure of about $43.1 \pm 0.7\%$ and an UTS (ultimate tensile strength) of about 293 ± 1 MPa were recorded. This results are quite close to those obtained on the raw substrate, with a maximal strain at failure and an UTS of $45.9 \pm 7.6 \%$ and 271 ± 11 MPa, respectively. This observation suggests that the deposit does not influence the mechanical behaviour of the steel substrate, as expected due to the thickness ratio between the deposit ($9.1 \mu\text{m}$ thick) and the substrate (1.5 mm thick).

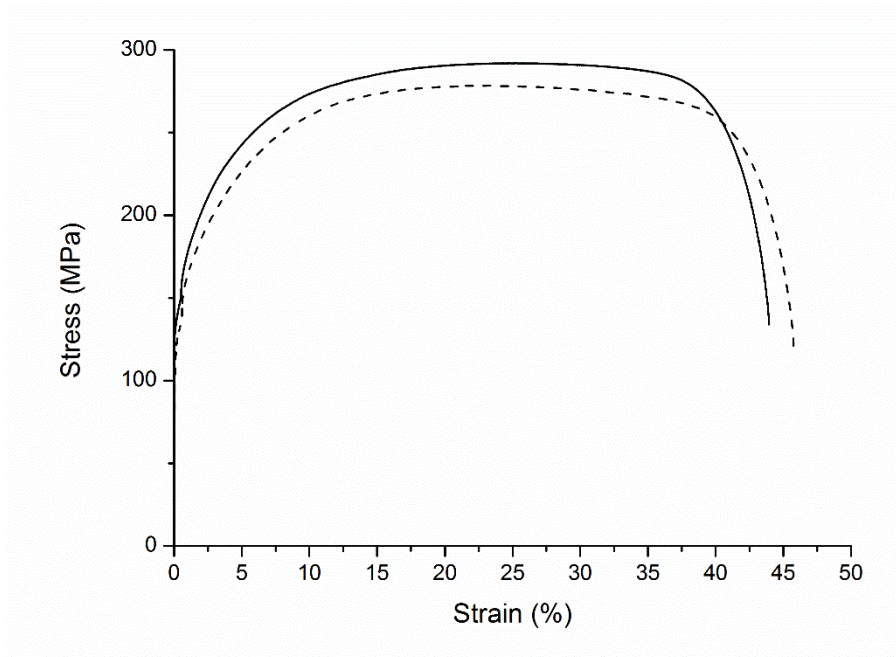


Fig.107: Representative stress-strain curve of the pulse Zn-Mn alloy coatings (solid line) and bare DC06 (dashed line) obtained during tensile testing at 1 mm/s until failure (DIN EN ISO 6892-1)

In order to better understand the mechanical response and the adhesive properties of the Zn-Mn deposit during tensile testing, the morphology of the deposits was investigated by means of SEM-EDS after tensile testing at 1 mm/s until failure.

The deposits presented generally poor adhesive properties with the steel substrate, principally due to the presence of pores at the substrate-coating interface, as discussed previously in section 3.3.4. As a result, two behaviours can be observed. The first one corresponds to a region where the deposit present good adhesive properties. It corresponds therefore to a more representative behaviour of the deposit under tensile stresses. The second one corresponds to regions where the deposit is poorly adherent and therefore strongly delaminated. The micrographs of these two domains are presented in figures Fig.108 and Fig.109, respectively.

In the regions where the deposit present a good adherence to the steel substrate (Fig.108), the Zn-Mn coatings present after tensile test some fine cracks, perpendicular to the tensile direction. The cracks are quite thin, about 3 – 4 μm wide, and do not seem to expose the steel substrate.

In the region where the deposit is poorly adherent to the deposit (Fig.109), the coating clearly shows some flaking and powdering with large chunks of the deposit completely detached from the substrate. The cracks are up to 2.5 μm wide and of various lengths but in any cases not longer than 200 μm . It is important to note in this case that the cracks open up to the steel substrate. From the micrograph obtained at magnification x1000 (Fig.109c), it seems that the cracks propagate along the grain boundaries, or at least along some boundaries between the crystallites. However, the cracks do not systematically propagate perpendicular to the tensile direction but also at an angle of about 45°. This is particularly visible on the Fig.109c.

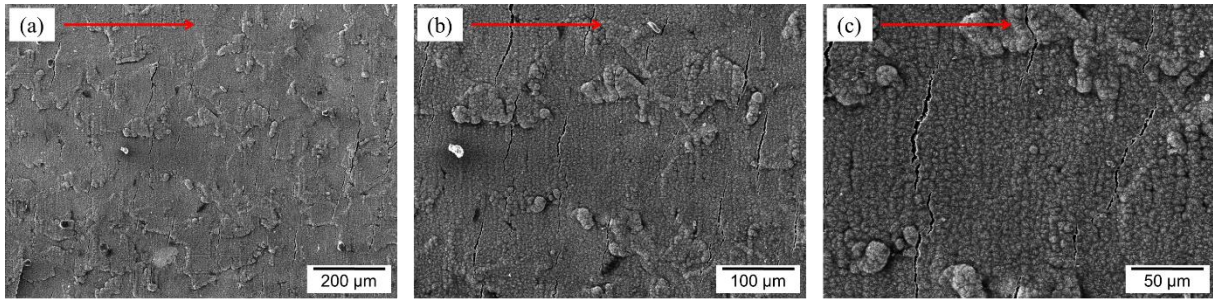


Fig.108: Micrographs of pulse Zn-Mn alloy coatings (9.1 μm thickness) after tensile testing at 1 mm/s until failure (DIN EN ISO 6892-1), tensile direction according to the red arrow. Micrographs obtained in the domain of good adhesion of the deposit at magnifications of x250 (a), x500 (b) and x1000 (c)

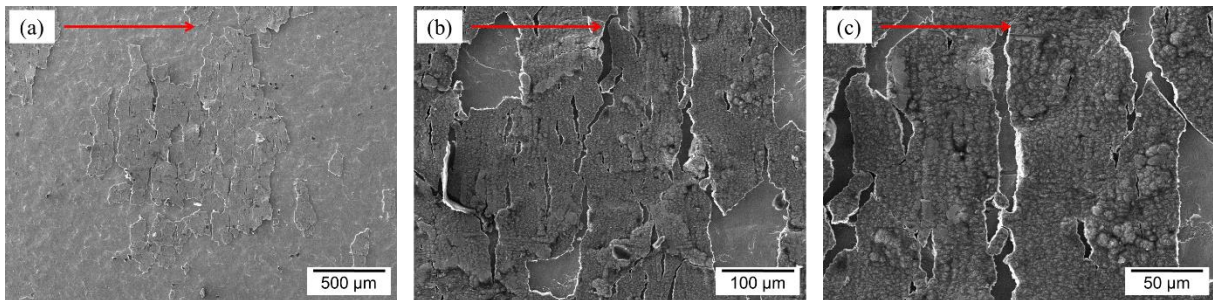


Fig.109: Micrographs of pulse Zn-Mn alloy coatings (9.1 μm thickness) after tensile testing at 1 mm/s until failure (DIN EN ISO 6892-1), tensile direction according to the red arrow. Micrographs obtained in the domain of poor adhesion of the deposit at magnifications of x250 (a), x500 (b) and x1000 (c)

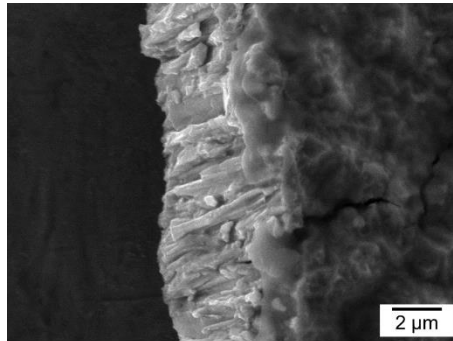


Fig.110: Micrograph of the fracture surface of the pulse Zn-Mn coatings (9.1 μm thickness) after tensile testing at 1 mm/s until failure (DIN EN ISO 6891)

Discussion

During the course of the investigations performed on the pulse Zn-Mn deposits, it quickly appeared that the coatings generally provided unsatisfactory adhesive properties with the steel substrate. In numerous cases, the delamination of large chunks of the deposits could already be observed during the cutting, polishing or milling operations.

A significant example is depicted in the Fig.111a, where the complete delamination of the deposit can be observed during the removal of the mask after coulometry experiments on the corroded samples. The

delamination of the deposit was already discussed after corrosion experiments with the detachment of large chunks during the removal of the corrosion products. Additional examples are depicted in the Fig.111(b) and (c) after press-shearing and after tensile testing, respectively. Some closer SEM micrographs (Fig.109) taken after tensile testing and previously discussed show the importance of the delamination on those samples.

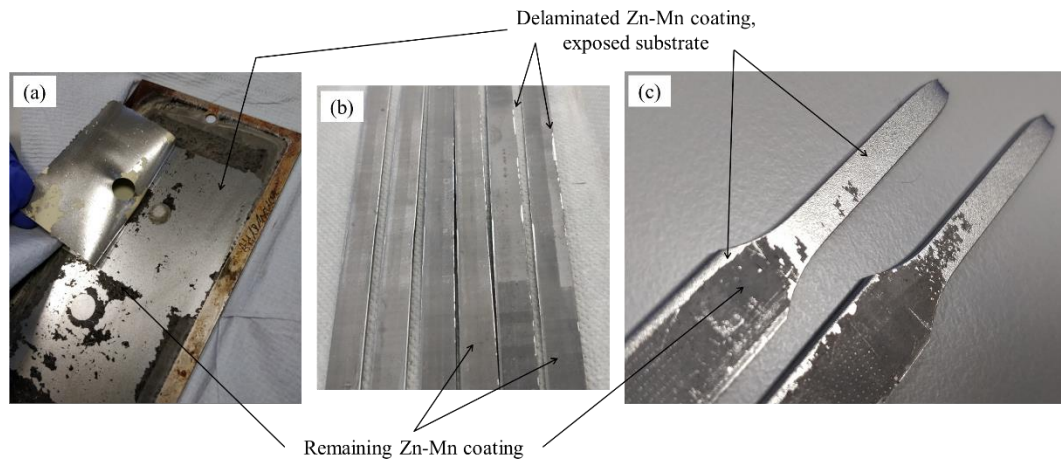


Fig.111: Delamination of the Zn-Mn deposits in various cases: during removal of the sticker mask used for coulometry after exposition to corrosion test and removal of the corrosion products (a), after press-shearing (b) and after press-shearing, milling and tensile testing (c)

The extensive delamination and the poor adhesive properties of the deposits are supposed to originate mostly from the porosity at the deposit – substrate interface, and previously discussed in the section 3.3.4. It is also important to mention that the investigations conducted in this chapter were performed on coatings deposited on unprepared steel substrates.

Further studies of a surface treatment before deposition are needed to be conducted in order to improve the adherence of the deposits on the substrate. Different surface treatments can be explored such as:

- Deposition of a first inner-layer of pure Zn having a better adhesion
- Thermal post-treatment leading to the formation of an interfacial Zn-Fe layer providing a better adhesion
- Chemical treatment (e.g. acidic medium) before the deposition leading to the dissolution of native oxide layers
- Polishing of the steel substrate before the deposition

4.3.3. Comparison with commercial coatings

The formability of the various deposits was at first assessed by means of hardness (Vickers) measurements. The values obtained on the pulse Zn-Mn deposits and on the commercial products are summarized in Table 25.

As previously reported in section 4.3.1, hardness values around 75 Hv were measured on the Zn-Mn deposits. In comparison to the commercial coatings this constitutes a slight increase over the pure Zn

deposits, with hardness values in the 50 – 60 Hv range measured. Although lower hardness values of the Zn-Mn alloys over Zn could be expected from the literature data [97], additional parameters needs to be considered in the case discussed here. Indeed, the grain refinement observed on the Zn-Mn due to the use of pulse currents is likely to result in a higher hardness of the deposits, as suggested by the Hall-Petch relation (eq.55) previously discussed.

Compared to the ZM90, or even the ZF100 deposits, this constitutes a significant decrease from about 100 and 170 Hv, respectively.

These hardness values have a direct impact on the formability of the deposits. Indeed, it is largely known that materials with high hardness present a brittle behaviour while materials with low hardness show a better ductility.

Table 25: Values of microhardness for pulse Zn-Mn and commercial coatings

	Hardness (Hv)
Zn-Mn, 15 wt.% pulse current	74.2 ± 9.4
commercial Zn (Z100), hot-dip galvanized	57.8 ± 4.7
commercial Zn (ZE75/75), electrogalvanized	50.3 ± 3.9
commercial Zn-Fe (ZF100), galvanized	171.5 ± 17.5
commercial Zn-Al-Mg (ZM90), hot-dip galvanized	97.7 ± 7.3

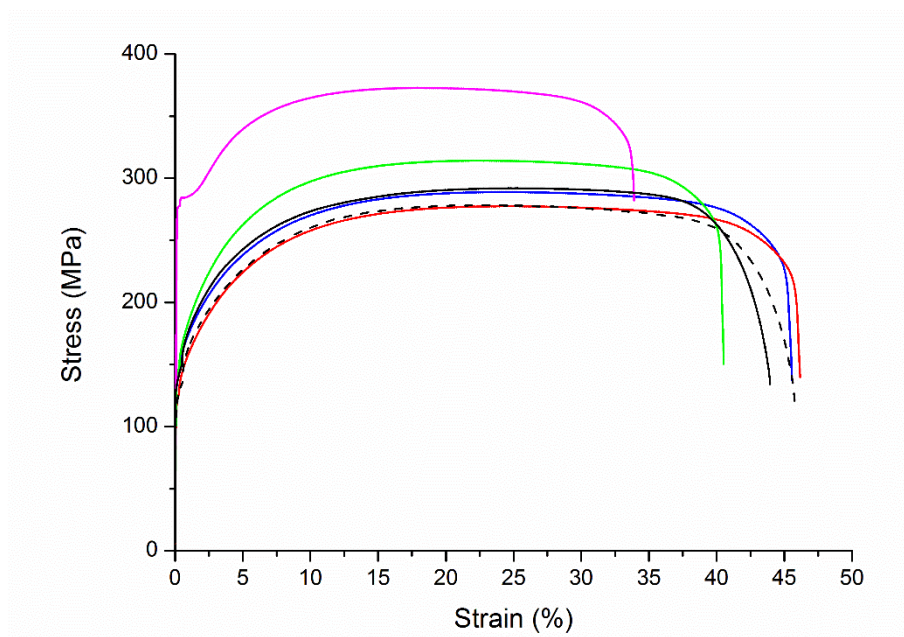


Fig.112: Representative stress-strain curve of the pulse Zn-Mn alloy coatings (black, solid line) and bare DC06 substrate (black, dashed line) as well as of the commercial products Z100 (Zn, hot-dip galvanized, blue), ZE75/75 (Zn, electrogalvanized, red), ZF100 (Zn-Fe, galvanized, green) and ZM90 (Zn-Al-Mg, hot-dip galvanized, magenta) obtained during tensile testing at 1 mm/s until failure (DIN EN ISO 6892-1)

The typical stress-strain curves obtained during tensile testing at 1 mm/s up to failure are summarized in Fig.112. All samples show a similar behaviour in the exception of the ZM90 samples. This is due to the use of a different steel substrate, in this case S220 GD, presenting different mechanical properties as

compared to the substrates used for the Zn-Mn, Z100, ZE75/75 and ZF100 (see Table 15, section 2.8.2 for further details). As a result, the comparison of the ZM90 samples on the basis of the stress-strain curves is not possible.

Still, some information can be obtained from the stress-strain curves of the Zn-Mn, Z100, ZE75/75 and ZF100 samples. The ZF100 coated samples present a lower maximal elongation at failure, about 5% lower than the Zn-Mn, Z100 and ZE75/75 samples. In addition, an increase of the tensile strength was observed. These observations can be explained by the presence of alloying phases at the coating – substrate interface, due to the thermal treatment conducted as part of the annealing process of the ZF100 samples. This result in an increased hardness, lower ductility and higher brittleness of the samples, as previously discussed.

In addition to the stress-strain curves, surface analyses help deliver precious information on the mechanical behaviour of the deposits. Micrographs obtained after tensile testing at 1 mm/s up to failure are presented in Fig.113. As previously discussed, the Zn-Mn deposits (Fig.113a) present in the region of good adherence a good formability with only the formation of very fine cracks perpendicular to the tensile direction. The Z100 (Fig.113b) and ZM90 (Fig.113e) deposits both present cracks and large cracks, respectively, in both cases perpendicular to the tensile direction. In the case of the ZM90 samples, the cracks are large enough to reveal the underlying substrate steel. The ZF100 (Fig.113d) deposits show a brittle behaviour with the presence of multiple cracks, mostly perpendicular to the tensile direction. In addition, an important delamination and the detachment of chunks of the deposit could be observed after tensile testing. The ZE75/75 deposits presented the best mechanical behaviour, with only some very fine cracks, barely distinguishable, oriented parallel to the tensile direction.

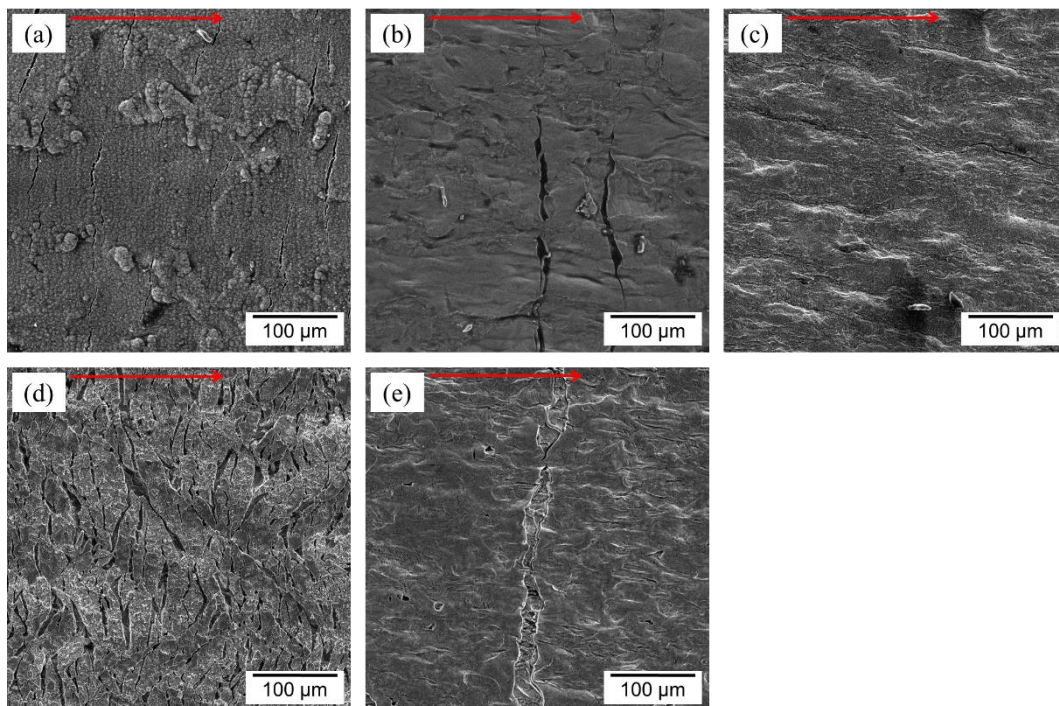


Fig.113: Micrographs of pulse Zn-Mn alloy coatings (a) after tensile testing at 1 mm/s until failure (DIN EN ISO 6892-1); comparison with the commercial products Z100 (Zn, hot-dip galvanized, (b)), ZE75/75 (Zn, electrogalvanized, (c)), ZF100 (Zn-Fe, galvanized, (d)) and ZM90 (Zn-Al-Mg, hot-dip galvanized, (e)); tensile direction according to the red arrow

4.3.4. Conclusion

In this section, the cold formability of the pulse Zn-Mn deposits was assessed by means of hardness measurements and tensile tests. In addition, the adhesive properties of the coatings were investigated.

Hardness measurements revealed an increase of the hardness for the Zn-Mn deposits over pure Zn. Analyses over a range of deposits lead to an apparent increase of the hardness due to the addition of Mn. However, it was demonstrated that additional effects such as the decrease of the grain size could play a significant role in the hardness of the deposits, as supported by the Hall-Petch relation.

Tensile tests carried out on the pulse Zn-Mn deposits exposed some promising forming properties. Indeed, the deposits presented a good behaviour under tensile stresses with the formation of only a few thin cracks and the absence of delamination. These results were however only observed in a few areas where the deposits presented a good adhesion with the steel substrate. In general, a poor adherence of the deposits on the steel substrate could be observed, most likely due to the high porosity at the coating – substrate interface.

4.4. Paintability

After various cutting and forming operations, the coated steel components are systematically submitted to an additional coating process consisting in the application of at least a phosphate conversion layer and an electrophoretic paint also known as E-coat. As a result, the suitability of newly developed materials for such post-processes is of particular importance in the automotive industry.

In this last section, the suitability of the new Zn-Mn deposits for phosphating and electrophoretic coating processes will be assessed. Firstly, the quality and the coverage of the phosphate conversion layer will be investigated by means of SEM-EDS analyses. In a second step, the corrosion behaviour of the Zn-Mn deposits phosphated and e-coated will be determined by means of scribe test.

4.4.1. Analysis of the phosphate conversion layer

SEM micrographs of the phosphated deposits are presented in Fig.114. The formation of a homogeneous layer, about 1 – 2 μm thick, entirely covering the surface can be observed. This layer is composed of well-defined crystals, in the form of platelets (Fig.114c). SEM-EDS analyses carried out on these crystals reveal about 50 at.% O, 35 at.% Zn, 8 at.% P and 7 at.% Mn, likely corresponding to a mixture of hopeith ($\text{Zn}_3(\text{PO}_4)_2$) and hureaulith ($\text{Mn}_2\text{Zn}(\text{PO}_4)_2$). The formation of these products is according to the literature well-known in the case of Zn-based alloys [234, 235] and occurs following the reactions 2 and 3 (page 31), respectively. It can also be observed, especially on the Fig.114a, that the waviness of the deposits does not seem to be significantly affected by the phosphate layer. However, the formation of such a network, with platelet-like crystals seems to lead to an increase of the roughness. This increased roughness is likely to permit a good adhesive base for the electrophoretic paint.

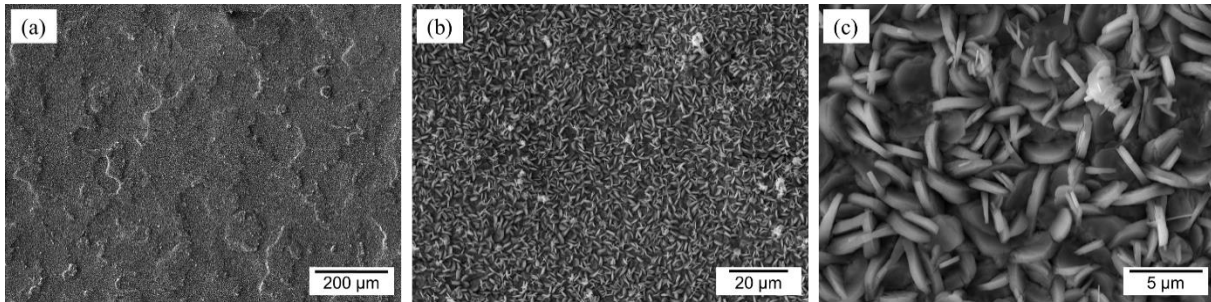


Fig.114: SEM micrographs of the phosphate layer on pulse Zn-Mn deposits at magnifications of x 250 (a), x 2000 (b) and x 10000 (c)

4.4.2. Corrosion resistance of the painted samples

Following the application of the phosphate layer, about 25 μm of the electrophoretic paint was applied on the deposits according to the protocol described in section 2.6.2. The samples were then prepared for cyclic corrosion test VDA 233-102 with a scribe, following the protocol described in section 2.6.3.

The appearance of the painted and scratched samples is depicted in Fig.115. Based on optical analyses, the deposited electrophoretic paint is homogeneous and defect-free, in exception to the edges of the samples. This effect is however expected due to the inhomogeneous, dendritic and cauliflower-like morphology of the deposits (see section 3.5.3 for further details). In these regions, it seems that the E-coat does not fully covers the surface and forms some fine blisters.



Fig.115: Appearance of the pulse Zn-Mn deposits (100 x 200 mm samples) after application of the phosphate conversion layer and the electrophoretic coating (E-coat); samples as prepared for the cyclic corrosion test (VDA 233-102) with scribe

It is also important to note that during the scratching of the samples in order to obtain the scribe, some small parts of the coating could be detached, as depicted in Fig.116. This is due to the poor adhesion of the Zn-Mn deposit on the steel substrate, as discussed in the section 4.3.2. This aspect is of particular importance in the assessment of the corrosion performance of the painted samples. Indeed, due to this delamination, a larger portion of the substrate is exposed to the corrosive medium. As a result, the upcoming results needs to be moderated.

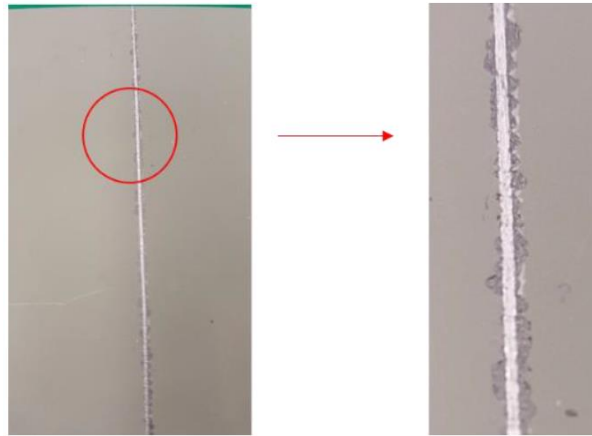


Fig.116: Close-up on the scribe of the Zn-Mn deposits (with phosphate conversion layer and electrophoretic coating) and evidence of the delamination of the entire coating system

The E-coated scribe samples were exposed in the cyclic corrosion test VDA 233-102 for durations up to six weeks. The appearance of the deposits through exposition time is presented in Fig.117.

After a short exposure time (Fig.117a), the formation of a layer of dark-brown corrosion products can be already observed along the scribe. These corrosion products are particularly visible in the regions where chunks of the deposit were removed. Still, one area presenting a good adherence with the substrate can be distinguished, as circled in red on the Fig.117. The formation of corrosion products is in this region barely visible. No significant evolution of the appearance can be observed with increase of the exposition time. A particularly stable behaviour can be observed in the region where the deposit adheres well with the substrate. The most noticeable changes are observed in the regions near the edges of the samples. As previously noticed, the E-coat does not fully cover the surface in those regions, where the deposit also presents some heterogeneities. The early formation, after two weeks, of red rust patches in those areas is therefore not surprising. In the scribe however, the pulse deposits show a good anticorrosive behaviour with the first signs of red rust observed after four weeks in the low-adhesion areas. In the high-adhesion area (circled in red) however, no signs of red rust could be observed up to the sixth week of exposure.

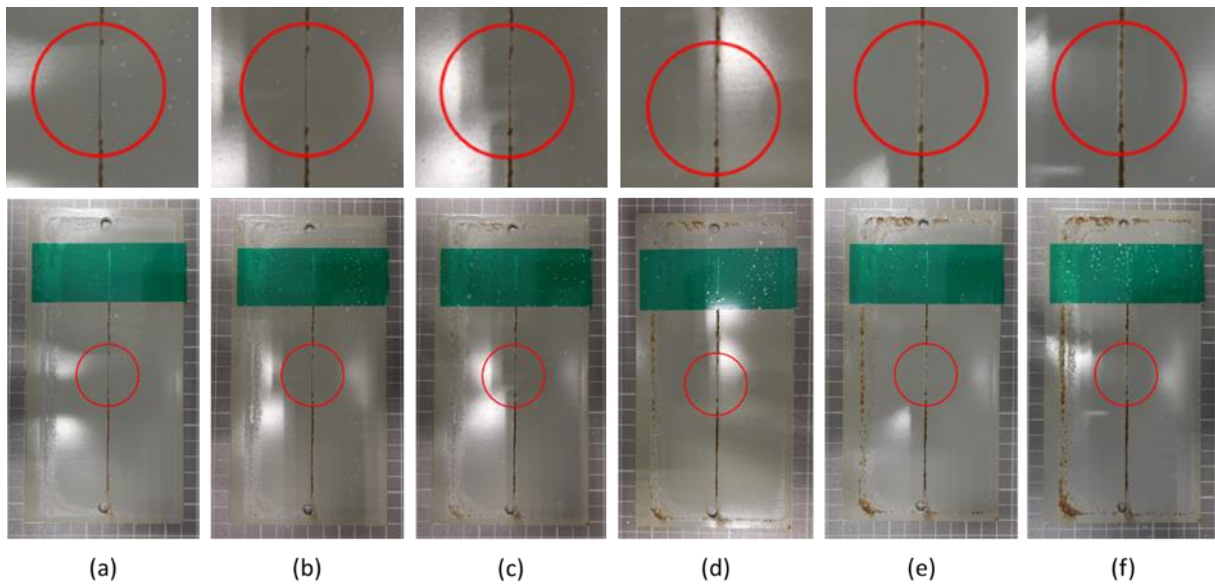


Fig.117: Appearance of E-coated pulse Zn-Mn alloy coatings (scribe samples) after 1 week (a), 2 weeks (b), 3 weeks (c), 4 weeks (d), 5 weeks (e) and 6 weeks (f) of exposure in the cyclic corrosion test VDA 233-102

4.4.3. Comparison with commercial coatings

The phosphatability of the commercial deposits was assessed in a similar manner as for the pulse Zn-Mn deposits. SEM micrographs of the phosphated commercial deposits are presented in Fig.118 while micrographs of the pulse Zn-Mn deposits can be found in Fig.114. All deposits present similar morphologies with the formation of a homogeneous and dense crystalline network. EDS analyses conducted on the surface of the phosphated deposits revealed similar chemical compositions corresponding to the formation of hopeith ($Zn_3(PO_4)_2$) and hureaulith ($Mn_2Zn(PO_4)_2$), already observed on the pulse Zn-Mn deposits and largely reported in the literature for Zn-based alloys [234, 235]. Still, slightly higher amounts of Fe were detected on the phosphated ZF100 deposits, due to the composition of the initial coating. Similarly, traces of Mg and Al were detected on the ZM90 samples.

As it appeared for the Zn-Mn coatings, the phosphate layer did not significantly affect the roughness at large scale (mm), namely the waviness of the commercial deposits. However, an increase of the roughness could be observed on all samples, due to the formation of platelet-like crystals. This increased roughness is expected to form a well-suited base permitting the good adhesion of the electrophoretic paint.

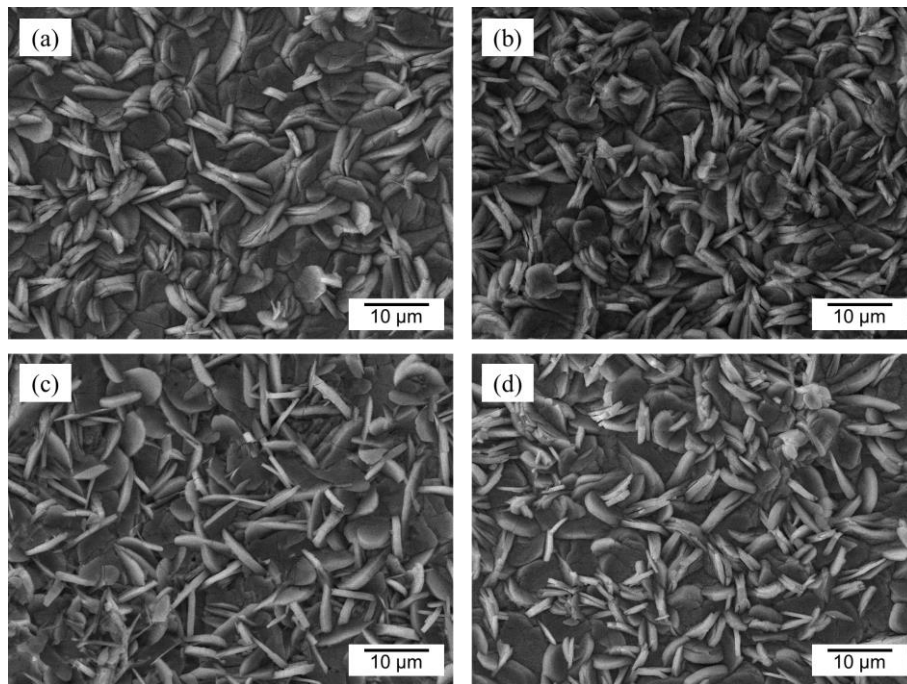


Fig.118: SEM micrographs of the phosphate layer on commercial deposits Z100 (a), ZE75/75 (b), ZF100 (c) and ZM90 (d)

Assessment of the paintability and corrosion resistance of painted commercial products was carried out following the same protocols as those used for the pulse Zn-Mn coatings. However, due to the important number of samples required for such an analysis, these experiments were conducted only on the electrodeposited ZE75/75 deposits. As expected on such well-established products, the deposited electrophoretic paint (E-coat) was homogeneous and defect-free on the entire surface of the samples. The resulting scratching of the samples for the scribe corrosion test was, in comparison to the pulse Zn-Mn deposits, problem-free and did not result in some flaking or delamination.

The E-coated ZE75/75 scribe samples were exposed in the cyclic corrosion test VDA 233-102 for durations of up to six weeks. The appearance of the deposits through exposition time is presented in Fig.119. The formation of white corrosion products can be observed in the scribe after the first week of exposure (Fig.119a). In comparison, dark-brown corrosion products were observed on the Zn-Mn samples. The first small patches of red rust could be observed in the scribe of the ZE75/75 coatings after only two weeks of exposure. On the E-coated Zn-Mn deposits, the first signs of red rust were detected after four weeks of exposure in the low-adhesion areas along the scribe. In the high-adhesion areas, no signs of red rust could be observed up to the sixth week of exposure.

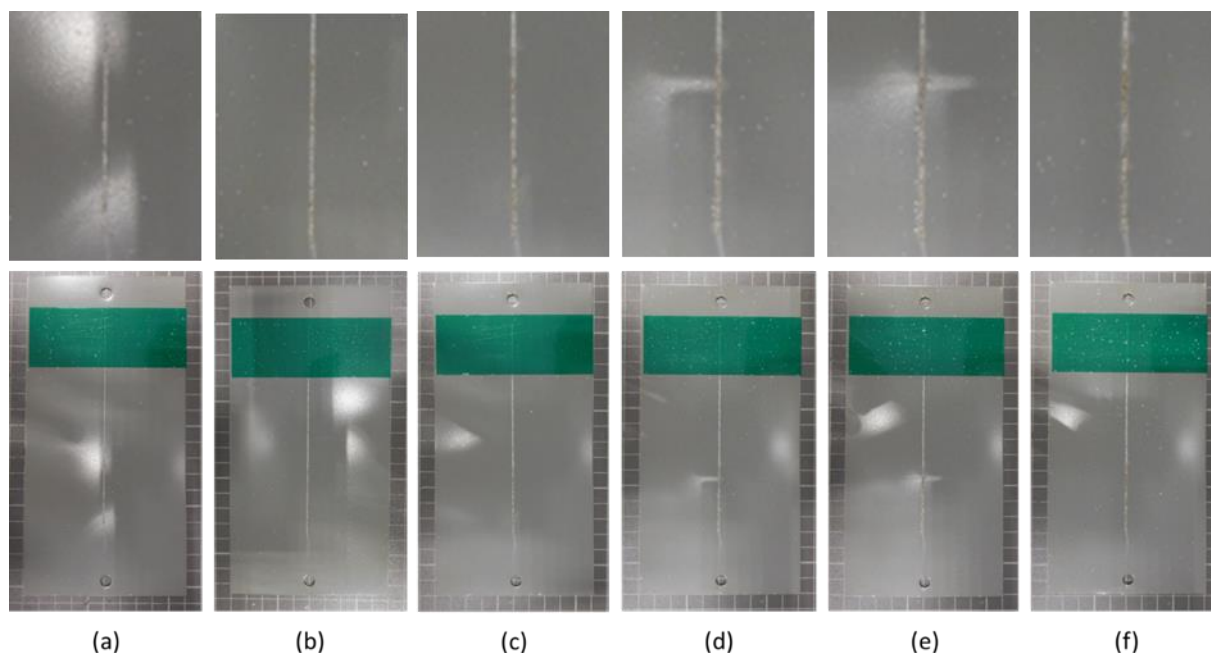


Fig.119: Appearance of E-coated ZE75/75 deposits after 1 week (a), 2 weeks (b), 3 weeks (c) and 4 weeks (d) of exposure in the cyclic corrosion test VDA 233-102

4.4.4. Conclusion

In this third section, the suitability of the pulse Zn-Mn deposits for the phosphating and electrophoretic coating processes was investigated.

SEM-EDS analyses of the samples following the application of a phosphate conversion coating on an industrial line revealed the formation of a homogeneous and compact crystalline network composed of hopeith and hureaulith. These results show the good suitability of the new Zn-Mn deposits for such post-processes.

Application of the electrophoretic paint (E-coat) on the industrial lines lead to the formation of a homogeneous and defect-free E-coat layer. Corrosion tests carried out on E-coated samples with a scribe revealed good anticorrosive properties and the good adhesion of the electrophoretic paint. The first signs of red rust were observed after four weeks of exposure in the cyclic corrosion test (VDA 233-102) in a few areas where the deposits show a poor adhesion to the substrate. In other areas however, no signs of red rust could be observed up to the sixth week of immersion.

4.5. Overall performance (EN) – Performance globale (FR)

In this chapter, the performance of the newly developed pulse Zn-Mn deposits was assessed and compared to commercial coatings Z100 (Zn, hot-dip galvanized), ZE75/75 (Zn, electrogalvanized), ZF100 (Zn-Fe, galvanized) and ZM90 (Zn-Al-Mg, hot-dip galvanized). On the basis of the results

presented and discussed in this chapter, the overall performance of the deposits was assessed by taking several aspects into account:

- The corrosion rate in immersion in a 5 wt.% NaCl electrolyte, from Tafel extrapolation
- The corrosion rate in continuous salt spray test (DIN EN ISO 9227)
- The corrosion rate in cyclic corrosion test (VDA 233-102)
- The formation of red rust during continuous salt spray test (DIN EN ISO 9227)
- The formation of red rust during cyclic corrosion test (VDA 233-102)
- The ductility from hardness measurements

According to these aspects, the following rules were applied:

- Corrosion rates: the formula $\left(\frac{1}{1+CR} \times 100\right)$, meaning that no corrosion would result in the highest score of 100, was systematically applied, with CR the corrosion rate calculated after immersion in 5 wt.% NaCl, continuous salt spray test or cyclic corrosion test
- Red rust formation (SST): the formula $(100 - \text{red rust percentage})$ was applied, with the amount of red rust taken after 96 hours of exposure in the DIN EN ISO 9227 salt spray test
- Red rust formation (VDA): the formula $(100 - \text{red rust percentage})$ was applied, with the amount of red rust taken after two weeks of exposure in the VDA 233-102
- Ductility: the grade is attributed on a linear scale based on the hardest deposit (attributed grade 0)

The overall performance of the coatings investigated in the framework of this work is presented in Fig.120.

The pulse Zn-Mn deposits present remarkable anticorrosive properties in comparison to the commercial deposits, especially during accelerated corrosion tests. These good anticorrosive properties are, as explained in the section 4.2, due to a corrosion mechanism specific to the Zn-Mn alloys, leading to the formation of zinc hydroxychloride (ZHC). Due to a preferential dissolution of Mn, ZHC is rapidly formed on the surface of the deposits and provide a compact layer, significantly reducing the progress of corrosion. As a result, Zn-Mn deposits present a good resistance against the appearance of red rust, characterizing the corrosion of the steel substrate. Analyses of the corrosion rates depicted the importance of the environment on the corrosion behaviour of the deposits. The pulse Zn-Mn deposits showed the highest corrosion rate under immersion in NaCl. However, the deposits presented under continuous salt spray test a lower corrosion rate than the commercial Zn and Zn-Fe coatings, and the lowest corrosion rate overall under cyclic corrosion test.

Regarding the formability, the Zn-Mn deposits present interesting properties in comparison to the commercial coatings. The deposits present slightly higher hardness values in comparison to Zn deposits. However, the values measured are still significantly lower than the ones of the Zn-Fe and Zn-Al-Mg alloys. This increased hardness of the Zn-Mn deposits, expected to result in a lower ductility, does not significantly affect the forming behaviour of the deposits. Under tensile stresses, only a few thin cracks could be observed on the surface of the Zn-Mn deposits, as similarly to the hot-dip galvanized Zn. These results were better than for the electrodeposited Zn deposits where a high crack density could be observed and significantly better than for the ZM90 and ZF100 coatings where large cracks revealing the steel substrate could be observed. On the downside, the Zn-Mn deposits presented in comparisons to commercial coatings poor adherence properties, in the exception of a few areas. However, it has to be remembered that the deposits obtained in this work were deposited on unprepared substrates. As discussed in the section 3.3.5, it appeared that a significant porosity could be observed at the deposit –

substrate interface. Additional experiments should be conducted on those new substrates in order to assess their impact on the adhesive properties.

Few conclusions can be drawn on the phosphatability and the paintability of the deposits. The formation of a dense network composed of hopeith and hureaulith crystals could be observed on the surface of the Zn-Mn alloys. This proves the good suitability of these new deposits for phosphating processes. Similar results were obtained on the commercial coatings. In addition, the deposition of a homogeneous, defect-free electrophoretic paint could be obtained on the Zn-Mn deposits.

Corrosion experiments on painted samples proved the overall good quality of the phosphate and E-coat layers as well as the good anticorrosive properties of the Zn-Mn alloys in the scribe test. On Zn-Mn, the first signs of red rust could be observed in the scribe after four weeks of exposure in the cyclic corrosion test (VDA 233-102). In comparison, the first signs of red rust could be observed after two weeks of exposure on the E-coated ZE75/75 samples.

In conclusion, it was demonstrated that the pulse Zn-Mn deposits present already some very promising properties in comparison to well-established products. However, the results discussed in this chapter also highlight some unsatisfactory properties of the Zn-Mn deposits. As demonstrated in section 4.2, high corrosion rates were obtained on the Zn-Mn deposits when immersed in chloride-containing medium. In addition, the deposits also presented poor adhesive properties that need to be improved. While the improvement of the coating – substrate adhesion is mostly related to the substrate properties and surface state, a further reduction of the corrosion rate of the deposits can be achieved with the help of new composition of the alloy or a new system. The incorporation of nanoparticles in a metallic matrix was suggested in the section 1.4 to be a particularly promising solution for the improvement of the anticorrosive properties of metallic coatings. As a result, the electrodeposition of Zn-Mn- Al_2O_3 coatings will be considered in the next chapter of this work.

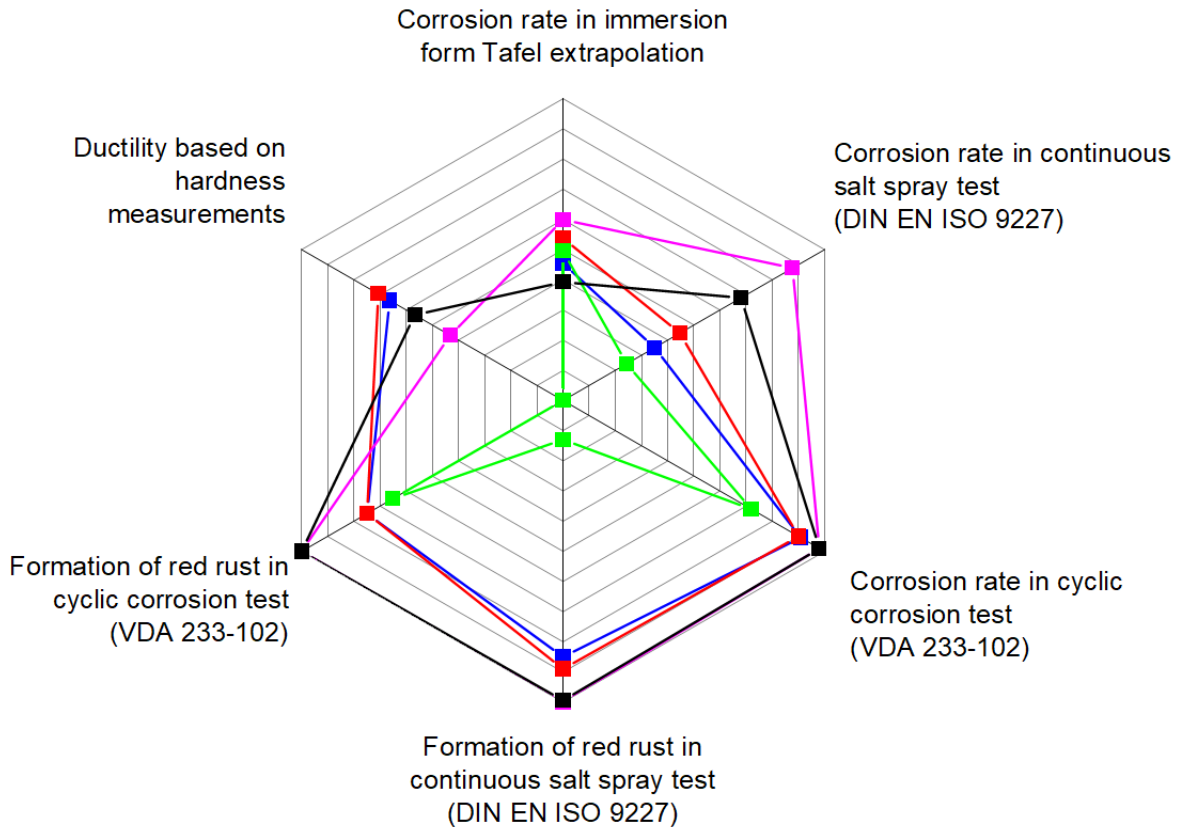


Fig.120: Anticorrosive and forming performance of the pulse Zn-Mn coatings (black); comparison with the commercial products Z100 (Zn, hot-dip galvanized, blue), ZE75/75 (Zn, electrogalvanized, red), ZF100 (Zn-Fe, galvanized, green) and ZM90 (Zn-Al-Mg, hot-dip galvanized, magenta)

Dans ce chapitre, les performances des nouveaux revêtements Zn-Mn impulsionnels ont été évaluées et comparées aux revêtements commerciaux Z100 (Zn, galvanisé à chaud), ZE75/75 (Zn, électrogalvanisé), ZF100 (Zn-Fe, galvannealed) et ZM90 (Zn-Al-Mg, galvanisé à chaud). Sur la base des résultats présentés et discutés dans ce chapitre, la performance globale des dépôts a été évaluée en tenant les aspects suivants en considération :

- La vitesse de corrosion en immersion dans un électrolyte contenant 5 %m de NaCl, après extrapolation selon la méthode de Tafel
- La vitesse de corrosion en brouillard salin continu (SST, DIN EN ISO 9227)
- La vitesse de corrosion en test de corrosion cyclique (VDA 233-102)
- La formation de rouille rouge lors du brouillard salin continu (SST, DIN EN ISO 9227)
- La formation de rouille rouge lors du test de corrosion cyclique (VDA 233-102)
- La ductilité à partir de mesures de dureté

À partir de ces aspects, les règles suivantes ont été appliquées :

- Vitesses de corrosion : la formule $\left(\frac{1}{1+CR} \times 100\right)$ a été systématiquement utilisée, avec CR la vitesse de corrosion calculée après immersion dans NaCl à 5 %m, après brouillard salin continu ou après test de corrosion cyclique
- Formation de rouille rouge (SST) : la formule (100 – pourcentage de rouille rouge) a été utilisée avec le pourcentage de rouille rouge défini après 96 heures d'exposition dans le brouillard salin continu (DIN EN ISO 9227)
- Formation de rouille rouge (VDA) : la formule (100 – pourcentage de rouille rouge) a été utilisée avec le pourcentage de rouille rouge défini après deux semaines d'exposition dans le test de corrosion cyclique (VDA 233-102)
- Ductilité : la note est attribuée sur une échelle linéaire basée sur le revêtement le plus dur auquel la note zéro est attribuée

La performance globale des revêtements étudiés dans le cadre de ce travail est présentée dans la figure Fig.121.

Les revêtements Zn-Mn impulsions présentent des propriétés anticorrosives remarquables en comparaison avec les dépôts commerciaux, en particulier lorsqu'ils sont soumis à des tests de corrosion accélérés. Ces bonnes propriétés anticorrosives sont, comme discuté dans la section 4.2, dues à un mécanisme de corrosion spécifique aux alliages de Zn-Mn, conduisant à la formation de zinc hydroxychlorure (ZHC). Grâce à une dissolution préférentielle du Mn, le ZHC est formé rapidement sur la surface des dépôts et permet la formation d'une couche compacte réduisant l'avancement de la corrosion. Ceci conduit à une très bonne résistance des alliages Zn-Mn contre l'apparition de rouille rouge, caractérisant la corrosion du substrat acier. Les analyses des vitesses de corrosion ont prouvé l'importance de l'environnement sur le comportement en corrosion des dépôts. Les revêtements Zn-Mn impulsions possèdent des vitesses de corrosion les plus élevées sous immersion en milieu NaCl. Cependant, ces mêmes dépôts montrent sous brouillard salin des vitesses de corrosion plus faibles que les alliages de Zn et Zn-Fe, et les vitesses de corrosion les plus faibles sous test de corrosion cyclique.

Concernant la formabilité, les revêtements Zn-Mn ont montré des propriétés intéressantes par rapport aux produits commerciaux. Les dépôts de Zn-Mn présentent des duretés légèrement plus élevée que les revêtements de Zn pur. En revanche, les valeurs obtenues sont de manière significative plus faible que celles mesurées sur les dépôts Zn-Fe et Zn-Al-Mg. Cette augmentation de la dureté par rapport au Zn, bien que supposée conduire à une diminution de la ductilité, n'a pas semblé influencer négativement la formabilité des revêtements de Zn-Mn. Sous contraintes de traction, seulement quelques fissures fines ont pu être observées sur la surface des dépôts de Zn-Mn, similaires à celles observées à la surface du Zn commercial galvanisé à chaud. Ces résultats constituent une amélioration significative par rapport aux dépôts de ZM90 et ZF100 sur lesquels de larges fissures laissant apparaître le substrat ont été observées. D'un autre côté, les dépôts de Zn-Mn ont démontré en comparaison avec les revêtements commerciaux de pauvres propriétés adhésives, à l'exception de quelques zones. Cependant, il doit être rappelé que les revêtements obtenus dans le cadre de ce travail ont été déposés sur des substrats non préparés. Comme discuté dans la section 3.3.5, une importante porosité est observée à l'interface entre le substrat et le revêtement. Des expériences supplémentaires devraient être effectuées sur des substrats ayant subi une préparation de surface différente afin de déterminer l'impact sur l'adhésion des dépôts.

Peu de conclusions peuvent être formulées concernant la phosphatabilité et l'aptitude des revêtements aux opérations de peintures. La formation d'un dense réseau cristallin constitué d'hopéithe et d'uréaulithe a pu être observée sur la surface des alliages de Zn-Mn. Ces observations prouvent la

bonne aptitude de ces nouveaux revêtements pour le procédé de phosphatation, alors que les produits commerciaux ont conduit aux mêmes résultats. De plus, la déposition d'une couche de peinture électrophorèse homogène et sans défauts a pu être observée sur les revêtements de Zn-Mn.

Des tests de corrosion additionnels ont montré de manière générale la bonne qualité des couches de phosphate et de peinture électrophorèse (E-coat) ainsi que le bon comportement anticorrosif des échantillons de Zn-Mn lors d'un test avec rayure. Les premiers signes de rouille rouge ont été observés sur les échantillons de Zn-Mn après quatre semaines d'exposition dans le test de corrosion cyclique (VDA 233-102). En comparaison, les premiers signes de rouille rouge sont apparus sur les échantillons de ZE75/75 recouverts de E-coat après seulement deux semaines dans le test VDA 233-102.

En conclusion, il a été démontré que les revêtements de Zn-Mn impulsionnels présentent d'ores-et-déjà des propriétés particulièrement prometteuses en comparaison avec des produits commerciaux déjà établis. Cependant, les résultats discutés dans ce chapitre ont également mis en évidence des aspects insatisfaisants de ces alliages de Zn-Mn. Comme démontré dans la section 4.2, des vitesses de corrosion élevées ont été obtenues sur les alliages de Zn-Mn lorsqu'ils sont immergés dans un milieu contenant des chlorures. De plus, ces dépôts Zn-Mn ont également présenté une mauvaise adhésion au substrat qu'il sera important d'améliorer. Alors que l'amélioration de l'adhérence entre le substrat et le dépôt relève en grande majorité des propriétés du substrat et de son état de surface, une diminution de la vitesse de corrosion des revêtements peut être obtenue grâce à une nouvelle composition de l'alliage ou un nouveau système. L'incorporation de nanoparticules dans une matrice métallique a été suggérée dans la section 1.4 comme une solution particulièrement prometteuse pour l'amélioration des propriétés anticorrosives de dépôts métalliques. De ce fait, l'électrodéposition de revêtements Zn-Mn- Al_2O_3 sera étudiée dans le chapitre suivant de ce travail.

Suitability of the pulse Zn-Mn deposits for automotive application

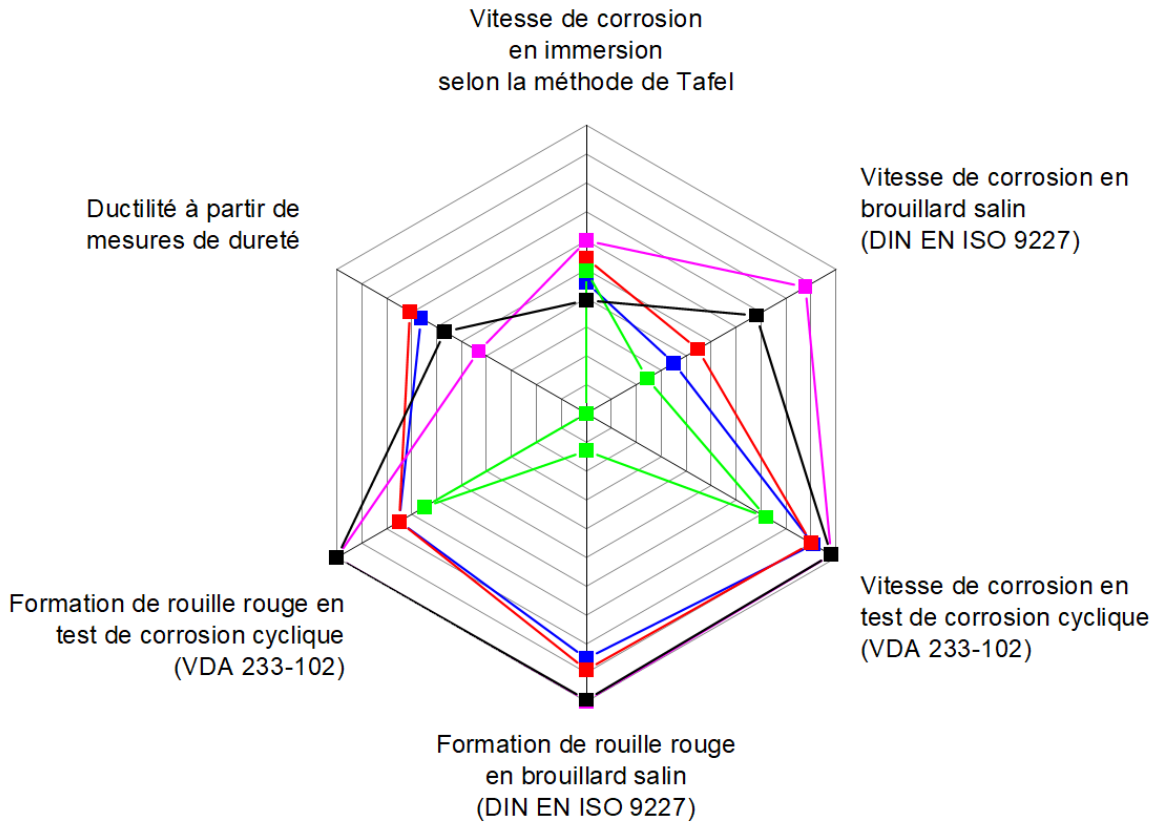


Fig.121: Performance anticorrosive et formabilité des revêtements Zn-Mn impulsionnels (noir) ; comparaison avec les produits commerciaux Z100 (Zn, galvanisé à chaud, bleu), ZE75/75 (Zn, électro galvanisé, rouge), ZF100 (Zn-Fe, galvannealed, vert) et ZM90 (Zn-Al-Mg, galvanisé à chaud, magenta)

5. Towards new coating systems: electrodeposition of ZnMn-Al₂O₃ composite coatings

5.1. Aim and procedure (EN) – But et procédure (FR)

The use of metal matrix composites (MMC) coatings composed of a Zn-Mn alloy as metallic matrix and Al₂O₃ particles as reinforcements was suggested in section 1.4 based on the promising anticorrosive properties of such coating systems. The literature review performed specifically on the composite deposits suggests, due to the addition of particles, an improvement of the homogeneity and morphology of the deposits. This results in a reduced risk for localized or pitting corrosion to occur and leads to lower corrosion rates. In addition, the particles are able to act as a physical barrier against the initiation and progress of corrosion [131-133].

According to the literature, the codeposition of particles inside a metallic matrix is a complex process that can be significantly influenced by many parameters such as the properties and characteristics of the particles, the composition of the electrolyte, the electrical parameters, the hydrodynamic conditions, the geometry of the electrodes and electrochemical cell, etc. It was additionally demonstrated that properties of the metal matrix, such as the texture, play an important role in the mechanism of physical entrapment of the particles [149]. As previously reported, various models have been developed in order to describe and understand the mechanism of particle codeposition. This mechanism can be summarized in five steps including the formation of charged particles in the plating bath, transport of the particles towards the cathode, diffusion through the concentration layer, migration across the electrical double layer and adsorption on the cathode surface [130, 146-148].

Two approaches have to be considered in order to optimize the incorporation and distribution of the particles into the metallic matrix. The first one consists in the use of a surfactant in the plating bath in order to better disperse the particles and avoid aggregation, flocculation and sedimentation. This approach was however discarded during this work in order to simplify the electrodeposition system and avoid the incorporation of unwanted elements in the deposits. Additional parameters related to the electrolyte such as the pH and the amount of particles also have to be taken into account. The second approach consists in the use of pulse currents instead of continuous currents for the electrodeposition. It was demonstrated in sections 3 and 4 that the pulse electrodeposition leads to a significant increase of the deposit homogeneity and yields to a significant improvement of the performance of the deposits. However, some unsatisfactory properties of the pulse Zn-Mn deposits were observed, with namely high corrosion rates in immersion into chloride-containing electrolyte and the presence of porosity at the coating – substrate interface. As a result, the incorporation of nanoparticles into the Zn-Mn metallic matrix was suggested in order to try to improve those properties.

In the framework of this thesis, a particular attention will be given on the successful codeposition of Al₂O₃ particles with a homogeneous dispersion inside the Zn-Mn metallic matrix. The various aspects of ZnMn-Al₂O₃ electrodeposition will be investigated in this section.

A preliminary study of the electroplating bath will be conducted in order to optimize the dispersion and the stability of the particles in the electrolyte. In addition, the influence of the particle on the electrochemical system will also be investigated (section 5.2). In the section 5.3, the effect of the electrical parameters on the composition, morphology and crystallography of the deposits will be studied. Depending on the values of the applied parameters, a more thorough analysis of the deposits

will be carried on in order to determine the amount of particles incorporated and their distribution inside the deposits. Finally, an outlook on the anticorrosive properties of those ZnMn-Al₂O₃ deposits will be given in section 5.4.

L'utilisation de revêtements composites à matrices métalliques (MMC) composés d'un alliage Zn-Mn en tant que matrice métallique et de particules d'alumine Al₂O₃ en tant que renfort a été suggérée dans le chapitre 1.4. Ce système de revêtement a été retenu sur la base de propriétés anticorrosives particulièrement prometteuses. L'étude de l'état de l'art sur ces revêtements composites suggère que l'incorporation de particules permet d'améliorer l'homogénéité ainsi que la morphologie des dépôts de façon significative. Ceci conduit à une diminution du risque de corrosion localisée ou perforante et permet de réduire de manière globale la vitesse de corrosion. De plus, les particules ont aussi la possibilité d'acter en tant que barrière physique contre l'initiation et l'avancement de la corrosion [131-133].

D'après la littérature, la codéposition de particules dans une matrice métallique est un procédé complexe qui peut être influencé de manière significative par de nombreux paramètres tels que les propriétés physicochimiques des particules, la composition chimique de l'électrolyte, les paramètres électriques appliqués, les conditions hydrodynamiques, la géométrie des électrodes et de la cellule de déposition, etc. Il a également été démontré que les propriétés de la matrice métallique telles que la texture jouaient un rôle important dans le mécanisme de piégeage des particules [149]. Tel que mentionné précédemment, de nombreux modèles ont été développés afin de décrire et comprendre le mécanisme de déposition des particules. Ce mécanisme peut être résumé en cinq étapes qui incluent la formation de particules chargées dans l'électrolyte, le transport des particules vers la cathode, la diffusion au travers de la couche de concentration, la migration au travers de la double couche électrique et l'adsorption à la surface de la cathode [130, 146-148].

Deux approches doivent être considérées afin d'optimiser l'incorporation et la distribution des particules dans la matrice métallique. La première consiste à utiliser des surfactants dans l'électrolyte dans le but de mieux disperser les particules et d'éviter les phénomènes d'agrégation, floculation et sédimentation. Cette approche ne sera cependant pas retenue dans le ce travail afin de simplifier le système électrochimique et d'éviter l'incorporation d'éléments indésirables. D'autres paramètres concernant l'électrolyte tels que le pH et la concentration en particules doivent également être pris en compte. La seconde approche consiste à utiliser des courants pulsés en lieu des courants continus traditionnels. Il a été démontré dans les chapitres 3 et 4 que l'électrodéposition impulsienne conduisait à une amélioration significative de l'homogénéité des revêtements ainsi qu'une meilleure performance. Cependant, des propriétés insatisfaisantes ont tout de même été observées avec notamment une vitesse de corrosion élevée en immersion en milieu chloré et une porosité à l'interface entre le dépôt et le substrat. De ce fait, l'incorporation de nanoparticules dans la matrice métallique Zn-Mn a été suggérée dans le but d'améliorer ces propriétés.

Dans le cadre de cette thèse, une attention particulière sera portée à une dispersion homogène des particules dans la matrice Zn-Mn. Les différents aspects concernant l'électrodéposition impulsienne des revêtements ZnMn-Al₂O₃ seront étudiés dans ce chapitre.

Une étude préliminaire du bain d'électrodéposition sera effectuée dans le but d'optimiser la dispersion ainsi que la stabilité des particules dans l'électrolyte (section 5.2). En addition, l'influence des

particules sur le système électrochimique sera également étudiée. Dans la section 5.3, l'effet des paramètres électriques sur la composition, la morphologie et la cristallinité des dépôts sera abordé. En fonction des paramètres appliqués, une analyse plus approfondie des dépôts sera menée afin de déterminer la quantité de particules incorporées ainsi que leur distribution dans les revêtements. Finalement, un aperçu des propriétés anticorrosives de ces nouveaux revêtements ZnMn-Al₂O₃ sera donné dans la section 5.4.

5.2. Preliminary study of the electroplating bath

According to the literature review conducted in section 1.6, the dispersion of the particles in the plating bath is a critical factor for the homogeneous codeposition of MMC coatings. Numerous parameters have an impact on the stability of the electrolyte, such as the concentration of the particles, the pH, the presence or absence of surfactants and their nature, etc.

This section is dedicated to the study of the plating bath charged with rod-shaped particles, presenting an average diameter of about 5 – 10 nm and a length of about 80 nm (see section 2.8.3), with the aim to optimize the dispersion and the stability of the particles. Various protocols will be investigated in order to achieve an optimal dispersion of the particles in an additive-free chloride electrolyte described in Table 11, page 64. The dispersion of the particles and their stability will be assessed by visual inspections and by DLS measurements.

In addition, the impact of the particles on the system will be studied via LSV experiments following the procedures described in 2.2.3.

5.2.1. Dispersion and stability of the plating bath

In order to obtain composite coatings with a homogeneous size distribution of the particles inside the metallic matrix, the size distribution of the particles in the initial plating bath is of capital importance. Moreover, it was demonstrated in the literature that the particle or aggregate sizes influence the amount of particles incorporated [140, 142, 163, 164]. Therefore, it is necessary to monitor the particle size and its distribution in the plating bath.

The use of ultrasonic stirring is quite common during the preparation of electrolytes with particles. In the case of nanoparticle powders, it is well-known that the dispersion mostly consists in strongly bonded aggregates that results in what is called secondary particles of much larger size. Ultrasonic stirring permits the separation of these strongly bonded aggregates into significantly smaller aggregates close to the primary particle size via cavitation as well as fragmentation and erosion mechanisms [236].

Therefore, the use of ultrasonic stirring as a preliminary step was studied with the aim to optimize the dispersion of the particles in the plating bath, at a concentration of 1 g/L of Al₂O₃.

Ultrasound experiments

In order to optimize the dispersion of the Al₂O₃ particles, various parameters were investigated in order to understand how the probe power output, its amplitude and how the duration of the ultrasonication affects the electrolyte.

The results obtained from these various experiments are summarized in Table 26. For each sample treated with ultrasonication, the evolution of the dispersion and sedimentation were assessed on 20 minutes intervals up to 80 minutes after ultrasound treatment. The samples were then graded on the basis of the scale depicted in Fig.122. According to this scale, the highest dispersion and stability is given a grade 1 (Fig.122a). In this case, the particles are well dispersed and no sedimentation is observed. At grade 2 (Fig.122b), the particles are still correctly dispersed but some sedimentation can be observed. At grade 3 (Fig.122c), the particles are poorly dispersed, the electrolyte is partially transparent and significant sedimentation is observed. Finally, the grade 4 (Fig.122d) corresponds to the complete sedimentation of the particles. The electrolyte is in this case limpid.

It is important to note here that sedimentation will occur significantly faster with bigger aggregates. On the opposite, a low sedimentation after a long time will be the sign of a good de-aggregation and dispersion of the particles.

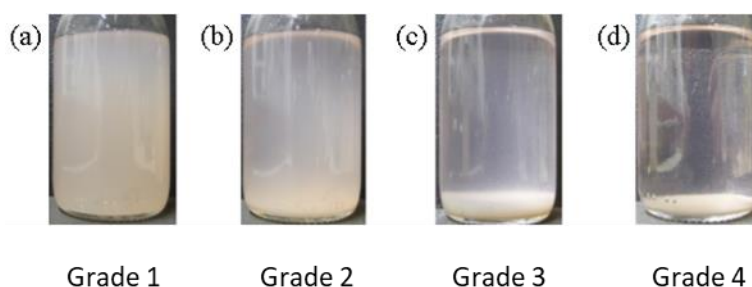


Fig.122: Criterion used for the assessment of the dispersion and stability of the particles in the electrolyte; (a) well dispersed particles without sedimentation = grade 1, (b) dispersed particles with low sedimentation = grade 2, (c) poorly dispersed particles with high sedimentation = grade 3 and (d) full sedimentation = grade 4; photographs taken on a dark background in order to better identify the particles

The stability of the plating bath along time was assessed according to these criteria. An effective ultrasonic pre-treatment results in a good dispersion of the particles (grade 1) that can last over a long period without sedimentation to occur. Given the duration of the deposition process, including the transfer of the electrolyte and the preparation of the samples, the minimal requirement is a low sedimentation after at least 60 minutes at rest.

The results of the Table 26 gives precious information regarding the effect of the ultrasonic parameters on the dispersion and stability of the particles. Firstly, it appears clearly that the use of high power ultrasonic probes is detrimental for the dispersion and the stability of the particles as shown by the evolution observed between the samples e, f and g (Table 26). Similarly, the use of prolonged duration for the ultrasonic treatment does not seem to be particularly beneficial for the plating bath. It seems overall that 30 minutes of ultrasonication lead to a lower stability in comparison to a treatment for 15 minutes. These effects were previously mentioned in the literature [237]. Indeed, it appears that

cavitation effects may occur during prolonged or too intensive sonication, which leads to reagglomeration of the particles and to the formation of dense aggregates [237].

It therefore appears that the conditions used for the sample c (Table 26), with namely 130 W at an amplitude of 50 % during 30 minutes, lead to the best dispersion and stability of the particles up to 60 minutes after the sonication.

Table 26: Dispersion and stability of the particles after sonication under various parameters. Dispersion and stability ranked on the basis of visual assessment with the grading criterion depicted in Fig.122

Sample	Power of the probe (W)	Amplitude (%)	Duration of the sonication (min)	Dispersion and stability of the particles after sonication (grade)				
				0 min	20 min	40 min	60 min	80 min
a	130	25	15	1	1	2	3	3
b			30	1	1	2	3	3
c		50		1	1	2	2	3
d		75	1	2	2	3	3	
e	750	25	15	1	3	3	4	4
f			30	1	3	4	4	4
g		50		1	3	4	4	4

In addition to these preliminary qualitative tests, DLS experiments were conducted in order to obtain a quantitative information on the particle size distribution in the electrolyte. Two kinds of dispersion methods were tested and compared. The first electrolyte was submitted to magnetic stirring for 30 minutes while the second one was sonicated according to the parameters c from the Table 26. The resulting histograms representing the particle size distribution are presented in Fig.123 and Fig.124, respectively.

According to the histograms (Fig.123 and Fig.124), the impact of the sonication is quite significant. With magnetic stirring (Fig.123), a unique population of particles is observed within a large size range from 400 nm up to 20 μ m in diameter. This shows the presence of large aggregates in the electrolyte, with various sizes. After sonication however (Fig.124), two populations of particles can be observed. The first one corresponds to particles, or rather aggregates, presenting a diameter size in the 140 – 200 nm range. The second one corresponds to larger aggregates with a diameter size between 1.4 and 4 μ m. These results show the significant beneficial effect of the sonication on the disaggregation of the particles. Even if two populations are observed, a significant decrease of the average particle size was observed. In addition, it can be supposed in the case of the Fig.124 that the amount of small aggregates is much more significant than the amount of the larger one. Indeed, as mentioned previously in the section 2.2.3, a 1:1 ratio in number amounts for a 1:1000000 ratio in intensity for 5 and 50 nm particles, due to the Rayleigh approximation. This means in this case that the apparent 1:7 ratio in intensity for about 100 and 1000 nm particles amounts for a 1000000:7 ratio in number.

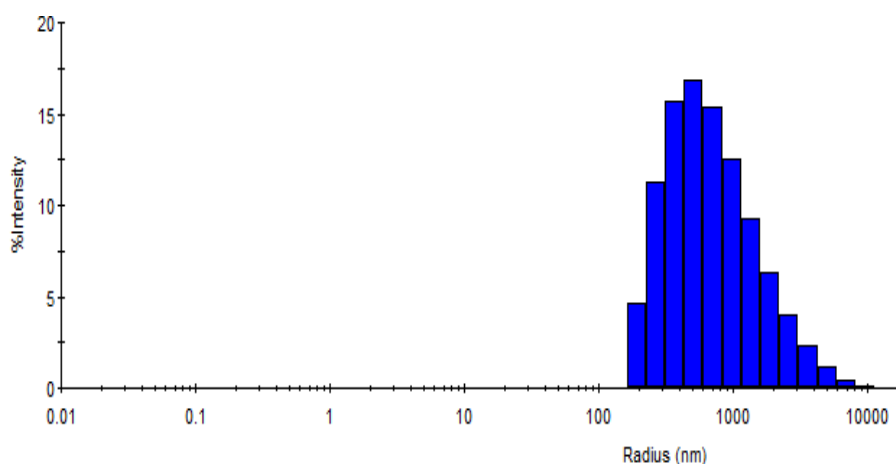


Fig.123: Particle size distribution in the electrolytic bath (1 g/L) submitted to magnetic stirring for 30 min, measurement obtained from DLS analysis on the entire electrolyte

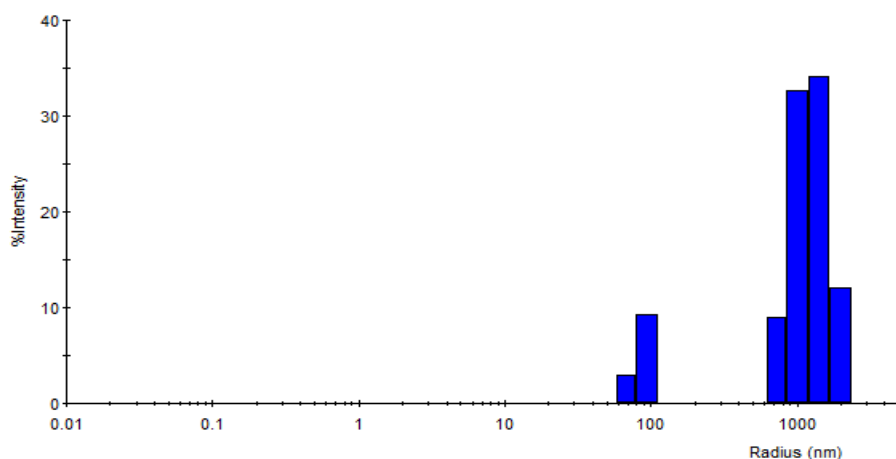


Fig.124: Particle size distribution in the electrolytic bath (1 g/L) submitted to magnetic stirring for 30 min and ultrasonication (130 W, 50 %) for 30 min, measurement obtained from DLS analysis on the entire electrolyte

Improvement of the particle distribution through sedimentation

It was demonstrated in the previous section that the sonication, with appropriate parameters, was largely beneficial in terms of decrease of particle size and stabilization in the electrolyte. However, it was observed that two populations of aggregates were obtained using this technique. As previously mentioned, the objective in this chapter is to achieve the homogeneous incorporation of particles into a metallic Zn-Mn matrix. It is therefore of primary concern to conduct the electrodeposition with an electrolyte as homogeneous as possible.

As a result, an additional step was added after the sonication, which consists in leaving the electrolyte at rest in order to let the sedimentation of the larger aggregates occur. The analysis of the particle size distribution over time after sonication permits to follow the segregation of the large particles and to determine the minimal amount of time required to obtain a monodispersed solution. The histogram presented in Fig.125 shows the particle size distribution after sonication according to the method c

(Table 26) and after two hours at rest. One can observe in comparison to the Fig.124 that a single population of particles is obtained. This resulting population presents an average diameter size slightly over 200 nm in diameter, similarly to the one observed previously.

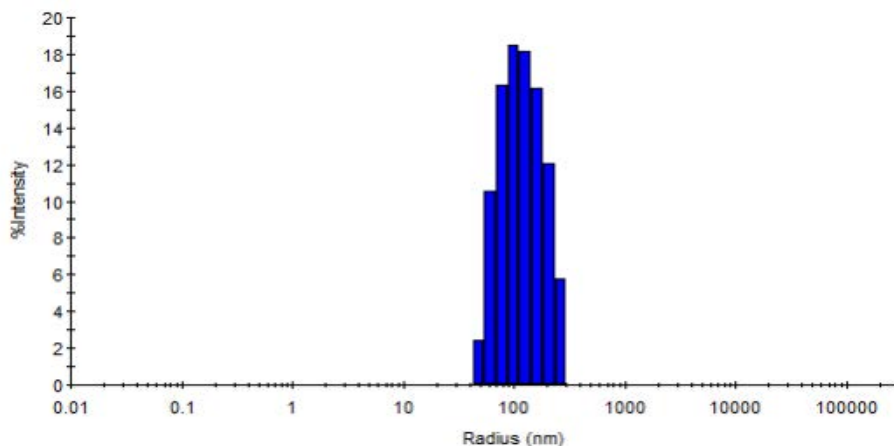


Fig.125: Particle size distribution in the electrolytic bath (1 g/L) submitted to magnetic stirring for 30 min followed by ultrasonication (130 W, 50 %) for 30 min and let to rest for two hours, measurement obtained from DLS analysis on the un-sedimented top-electrolyte

Conclusion

On the basis of this preliminary study of the dispersion of the particles in the plating bath, a protocol was defined for the preparation of the electrolyte.

It was observed that the combined use of magnetic stirring with sonication was leading to the highest dispersion of the particles. Although the use of extended sonication time or high energies was observed to lead to a significant increase of the temperature of the electrolyte, the use of properly tuned parameters permitted to obtain a monodisperse particle distribution with aggregates presenting a diameter of about 200 nm in diameter.

As a result, the following protocol was defined in two steps:

- Sonication at 130 W with an amplitude of 50 % during 30 minutes, coupled with magnetic stirring
- Two hours at rest for sedimentation of larger aggregates to occur

5.2.2. Study of the electrochemical system

Disclaimer: the deposits obtained and investigated in this chapter were obtained on 1 cm² DC06 coupons in a thermostated becher containing about 100 mL of electrolyte.

Influence of the particles

Linear voltammetric studies performed with and without nanoparticles are presented in Fig.126. When the potential is swiped in the negative direction, a first large cathodic peak appears at about -1.2 V, corresponding to the reduction of Zn into Zn²⁺. This observation still corresponds with the voltammetric studies conducted in the section 3.2.1 as well as the literature [115, 118, 160]. A second cathodic peak can be observed at approximately -1.6 V and corresponding to the reduction of Mn into Mn²⁺. This value is in good correlation with the values reported in the literature data [115, 118, 121].

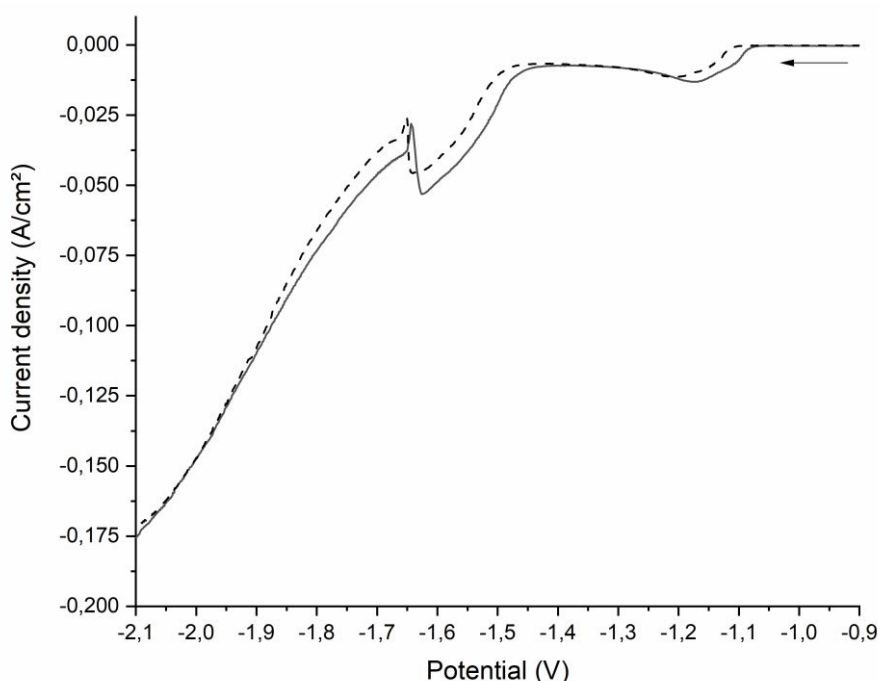


Fig.126: Linear voltammograms obtained during cathodic scan between potentials of -0.6 and -2.2 V on 1 cm² DC06 steel at a scan rate of 10 mV/s in unstirred electrolytes containing 2.8 M KCl, 0.075 M ZnCl₂, 0.6 M MnCl₂, 0.32 M H₃BO₃ and 1 g/L Al₂O₃ nanoparticles (solid line) and without particles (dashed line)

In comparison with the voltammogram obtained without particles (dashed line in Fig.126), the addition of particles does not seem to significantly affect the voltammograms, with only a small positive shift of the reduction peaks, about 0.05 V. In addition, a slight increase of the current density was measured in the electrolyte containing particles. The increase of the current density with increase of the particle content was previously observed in the literature and was related to the adsorption of the Zn²⁺ and Mn²⁺ cations on the surface of the particles [238, 239]. On the other hand, an opposite effect of the particles on the current density was also suggested in the literature. Indeed, it seems that the deposition of the particles on the surface of the deposit may reduce the available surface of the cathode and therefore may result in a decrease of the current density with increasing amount of particles [240, 241].

In the case investigated here, it should be noted that the amount of particles in the electrolyte (1 g/L) is lower than in the reference literature. Therefore, it can be supposed that the amount of particles

incorporated in the deposits is quite low and does not significantly influence the electrochemical system of Zn-Mn.

Influence of the stirring

Similarly, since the electrodeposition of Al₂O₃-ZnMn composites has to be performed with stirring, additional voltammetric studies were conducted in the electrolyte containing 1 g/L Al₂O₃ under various stirring rates up to 1000 rpm. The resulting voltammograms are presented in Fig.127.

As expected, the first cathodic signal, associated to the reduction of the cation Zn at 1.1 V appears as a plateau with a diffusion-limited current density. Consequently, this cathodic signal increases with the stirring rate. Secondly, a shift of the potentials corresponding to the reduction of Mn is observed and becomes quite significant when a stirring rate of 1000 rpm is applied. Since a similar evolution was observed in the absence of particles, the changes depicted in Fig.127 are therefore not related to the incorporation of particles on the cathode. One possible explanation for this increase of the current density could originate from some resistive effects related to the stirring.

As a result, the effect of the stirring needs to be taken into consideration during the electrodeposition. Thus, a fixed applied current density of -0.015 A/cm², corresponding to the continuous electrodeposition of Zn-Mn without stirring, would match under a stirring of 500 rpm with a potential of about -1.15 V, at which only Zn is deposited. Consequently, current densities of -0.045 and -0.055 A/cm² for stirring rates of 500 and 1000 rpm, respectively have to be applied in order to conduct the electrodeposition at a potential around -1.55 V, where Zn-Mn coatings are expected to be obtained.

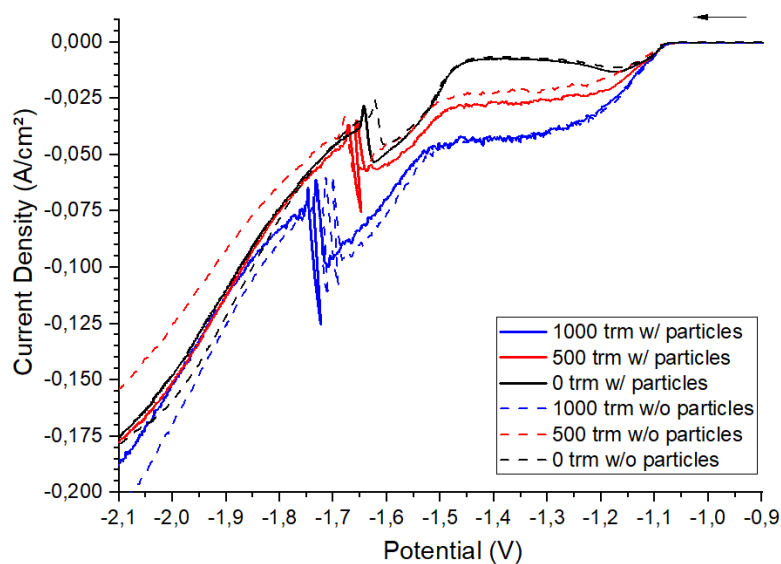


Fig.127: Linear voltammograms obtained during cathodic scan between potentials of -0.6 and -2.2 V on 1 cm² DC06 steel at a scan rate of 10 mV/s in electrolytes containing 2.8 M KCl, 0.075 M ZnCl₂, 0.6 M MnCl₂, 0.32 M H₃BO₃ (dashed lines) and 1 g/L Al₂O₃ nanoparticles (plain lines); voltammograms obtained without stirring (black) and with stirring at 500 rpm (red) and 1000 rpm (blue)

5.2.3. Discussion and conclusion

In this first section, the initial sonication step was developed in order to obtain homogeneous and stabilized electrolytes containing alumina particles. As proven by DLS analyses, combined use of magnetic stirring with sonication with 130 W at an amplitude of 50 % during 30 minutes followed a resting time of two hours permits to obtain a monodisperse distribution of particles presenting a diameter size around 200 nm. Furthermore, the electrolyte prepared following this protocol appears to be stable for at least one hour.

Then, the influence of the particles in the bath and the stirring rate on the electrochemical system were investigated by means of linear voltammetric studies.

No noticeable influence of the particles was observed on the electrochemical system. This absence of effects may be due to the low concentration of particles in the plating bath resulting in a low amount of embedded particles in the coatings. On the other hand, a significant impact of the stirring rate on the electrochemical system was observed, requiring an adjustment of the cathodic growth parameters.

5.3. Electrodeposition of ZnMn-Al₂O₃ coatings under pulse currents

As it was demonstrated in the literature review conducted in section 1.6, the incorporation of nanoparticles in a metallic matrix is a complex process influenced by a large array of parameters related to the particles, the electrolyte, the electrical parameters, etc.

In this section, the electrodeposition of ZnMn-Al₂O₃ composite coatings will be studied from electrolytes containing 1 g/L Al₂O₃ particles stabilized according to the protocol described previously. The influence of the pulse current parameters on the composition, morphology and crystallography of the deposits will be investigated. It is important to note that all deposition experiments conducted in this section will be conducted under constant magnetic stirring at 500 rpm. In the framework of this thesis, the use of pulse currents instead of the continuous current was chosen for the deposition of the Zn-Mn-Al₂O₃ coatings. As already stated in previous sections, the pulse electrodeposition is quite a complex process influenced by various mechanisms. In the case of particle codeposition however, the use of pulse currents provides a significant advantage in comparison to the continuous current. The presence of a relaxation time permits to control and reduce the growth rate of the metallic matrix and to enhance particle incorporation [168]. As a result, the experiments conducted in this section will be strongly focused on the influence of the duty cycle, and by extension on the peak current density and off-time.

While the influence of the particle size is not fully understood, reports from the literature tends towards higher incorporation rates in the case of larger particles [140, 142, 163, 164]. Due to the presence of two distinct particle sizes in the electrolyte used in this work, a specific study on how particles of various sizes are incorporated into the metallic matrix will be firstly conducted. In a second step, deposits will be obtained from stabilized electrolytes with monodispersed particles

5.3.1. Characterization of the metallic matrix

Composition

The influence of the peak current density on the Mn content of the deposits was investigated by means of SEM-EDS, with the Fig.128 showing the dependency of the Mn content on the peak current density. All deposits were obtained at an average current density of 0.045 A/cm², a pulse duration of 5 ms and a stirring rate of 500 rpm.

The results show an increase of the Mn content with the peak current density. This behaviour, corresponding to the normal codeposition mechanism of Zn-Mn [194] was largely observed in the literature and is in good agreement with the observations described in the section 3.3.2 during the electrodeposition of Zn-Mn deposits. A maximal Mn content of 15.2 wt.% was measured on the ZnMn-Al₂O₃ deposits, similar to the Mn content measured on pure Zn-Mn coatings (cf. section 3.3.2). In contrast, depositions at a peak current density $j_p = 0.09$ A/cm² resulted in the formation of a Zn-Al₂O₃ deposit.

As it was demonstrated in Fig.126 that the addition of particles had no effect on the electrolyte, this shift can be attributed to the stirring used for the electrodeposition of the composite coatings, as supported by the findings of the Fig.127.

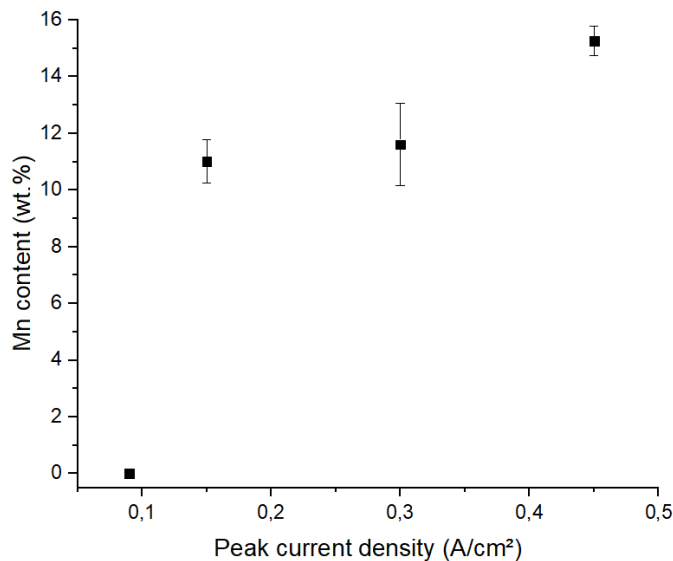


Fig.128: Dependency of the Mn content on the pulse peak current density j_p for an average current density $j_a = 0.045$ A/cm² and a pulse duration t_{on} of 5 ms; deposits obtained in the plating bath presenting the particle distribution presented in Fig.124 with a stirring rate of 500 rpm

Morphology

The influence of the peak current density on the morphology of the deposits is depicted in Fig.129. At low peak current densities $j_p = 0.09$ A/cm² (Fig.129a), the deposits present a rough

morphology with the formation of a cauliflower-like dendrites. This type of morphology was previously observed in the work of Close et al. on Zn-Mn deposits obtained under continuous mode [118]. Further increase of the peak current density to 0.15 A/cm² (Fig.129b, c and d) results in a significant improvement of the morphology. The deposits present a homogeneous morphology with refined and homogeneously distributed crystallites. In comparison to the deposits studied without particles in section 3.3.4 however, no further refinement of the crystallite size on the composite coatings was observed by further increasing the peak current density above 0.15 A/cm².

The presence of some defects is observed on the surface of the ZnMn-Al₂O₃ deposits, especially when peak current densities equal to or above 0.15 A/cm² were used (Fig.129b, c and d). Indeed, numerous pores are observed on the surface of the deposits, as well as some white aggregates, likely corresponding to some Al₂O₃ aggregates.

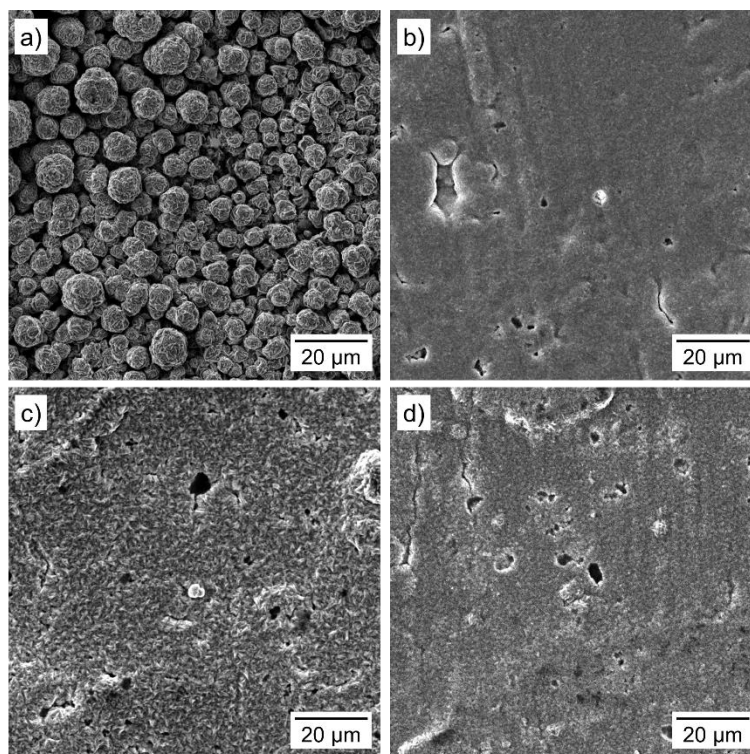


Fig.129: SEM micrographs of the surface of ZnMn-Al₂O₃ deposits obtained by means of pulse plating at an average current density of 0.045 A/cm², a pulse on-time of 5 ms and peak current densities of 0.09 A/cm² containing 0 wt.% Mn (a), 0.15 A/cm² containing 10.6 wt.% Mn (b), 0.30 A/cm² containing 11.0 wt.% Mn (c) and 0.45 A/cm² containing 14.5 wt.% Mn (d); deposits obtained in the plating bath presenting the particle distribution presented in Fig.124

The observation of such a high amount of porosity on the surface of the deposits is quite surprising when considering the findings of the literature. Indeed, the particles are actually expected to fill the pores of the deposits and thus enhance their homogeneity. Still, some hypotheses can be formulated in order to explain these observations:

- On one side, the porosity could originate from some underlying Al₂O₃ aggregates that are still not covered by the growing metallic matrix. The validity of this hypothesis will be tested later via cross-sectional analyses.

- On the other side, detachment or removal of large Al₂O₃ aggregates that were partially entrapped in the metallic matrix could result in such porosity.

Crystallography

The diffraction patterns obtained on the pulse ZnMn-Al₂O₃ deposits at an average current density of 0.045 A/cm, a pulse duration of 5 ms and various peak current densities ranging from 0.15 up to 0.45 A/cm² are presented in Fig.130.

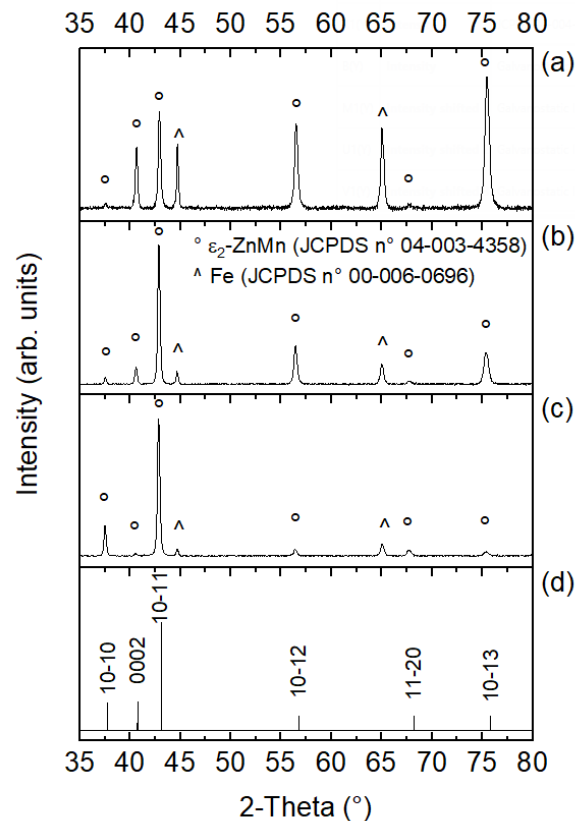


Fig.130: XRD patterns of ZnMn-Al₂O₃ deposits obtained under pulse current at an average current density of 0.045 A/cm², an on-time of 5 ms and a peak current density of 0.45 A/cm² (a), 0.30 A/cm² (b) and 0.15 A/cm² (c); diffraction peaks corresponding to the ϵ_2 -ZnMn (JCPDS n° 04-003-4358); deposits obtained in the plating bath presenting the particle distribution presented in Fig.124

For all three deposits, the main diffraction peaks can be identified to the hexagonal ϵ_2 -ZnMn (JCPDS n° 04-003-4358) phase, as already observed largely on the literature and on the Zn-Mn deposits previously studied in section 3.3.6. Samples deposited at peak current densities of 0.15 and 0.30 A/cm² (Fig.130c and b, respectively) present roughly the same diffractograms with a preferential orientation of the (10.1) and (11.2) planes parallel to the surface of the sample. It is interesting to note here the similarities with the pulse Zn-Mn deposits. Indeed, the deposits studied in the absence of particles (cf. Fig.67 and Fig.71, pages 119 and 123, respectively) presented in almost all cases a preferred orientation with the (10.1) planes parallel to the surface. By increasing the peak current density up to 0.45 A/cm², the deposit

presents a diffractogram with a random orientation as depicted in Fig.130(a). The formation of such a random texture is expected to enhance particle incorporation, as suggested by Camargo et al. [149].

In addition to the ϵ_2 -phase, two additional diffraction peaks located at 46° and 66° are observed, corresponding to the steel substrate.

Efficiency

The faradaic efficiency of the deposits was evaluated by means of the gravimetric method, based on the ratio between the theoretical and the experimental mass deposited. The values obtained on the composite coatings are summarized in the Fig.131.

The results show a clear behaviour in comparison to the one already observed on the pulse Zn-Mn deposits. Increase of the duty cycle, i.e. a decrease of the peak current density, leads to higher faradaic efficiencies. This effect can be explained by the increase of the off-time with lower duty cycles, leading to the partial dissolution of the Zn-Mn coating [211]. Another explanation could originate from the fact that at low duty cycles, higher peak current densities implies a more important contribution of the hydrogen evolution.

Nevertheless, the values measured in the framework of this study are in all cases quite high, with the lowest efficiency evaluated at about 81 % for the deposits obtained at a peak current density of 0.45 A/cm² and the highest efficiency evaluated at 95 % for the deposits obtained at a peak current density of 0.09 A/cm².

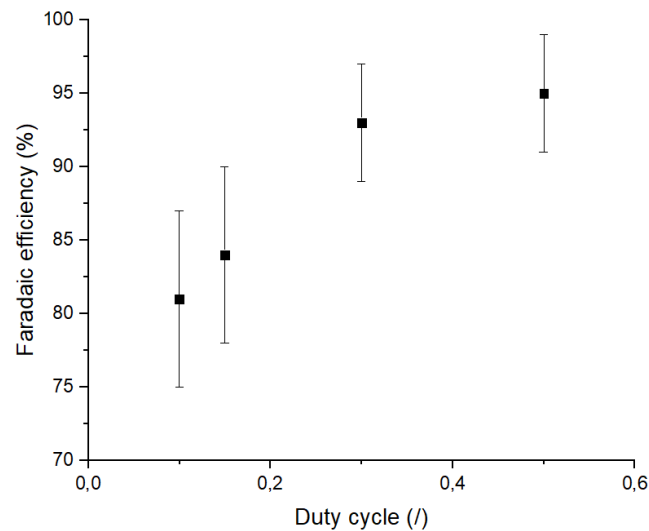


Fig.131: Faradaic efficiencies of the pulse ZnMn-Al₂O₃ deposits determined on the basis of the ration between theoretical and experimental mass of coating deposited

5.3.2. Mechanisms of particle incorporation

The specific incorporation of Al₂O₃ particles of various sizes was investigated by SEM-EDS analyses as well as via cross-sections prepared via the FIB technique. Due to the significant time required to prepare samples via the FIB technique, only the deposits presenting the optimal characteristics, i.e. a high Mn content of ca. 14.5 wt.%, the most homogeneous morphology as well as a random crystallographic orientation were investigated, namely the deposits obtained with an average current density of 0.045 A/cm², a peak current density of 0.45 A/cm² and a pulse on-time of 5 ms.

Al₂O₃ – ZnMn composite coatings obtained bidispersed electrolyte

In this section, the incorporation of Al₂O₃ from a bidispersed electrolyte, i.e. submitted to sonication without resting time, composed of 140 – 200 nm and 1.4 – 4 μm diameter aggregates will be studied. The resulting SEM-EDS micrographs of the surface and cross-sections are presented in Fig.132 and Fig.133, respectively.

The SEM analyses, and especially the EDS mappings conducted on the samples reveals the presence of Al₂O₃ on the surface of the deposits (Fig.132). Indeed, EDS analyses reveal the presence of aluminium in various regions such as in the pores, as depicted by the circled areas A and B on the Fig.132. Additionally, the presence of Al₂O₃ aggregates partially entrapped is recognizable in particular in the circled regions C and D on the Fig.132. These observations seem to confirm one of the hypotheses previously formulated on the incorporation mechanism of the particles. Indeed, it appears that aggregates are entrapped on the surface of the deposit and partially covered by the metallic matrix, resulting in the formation of porosity.

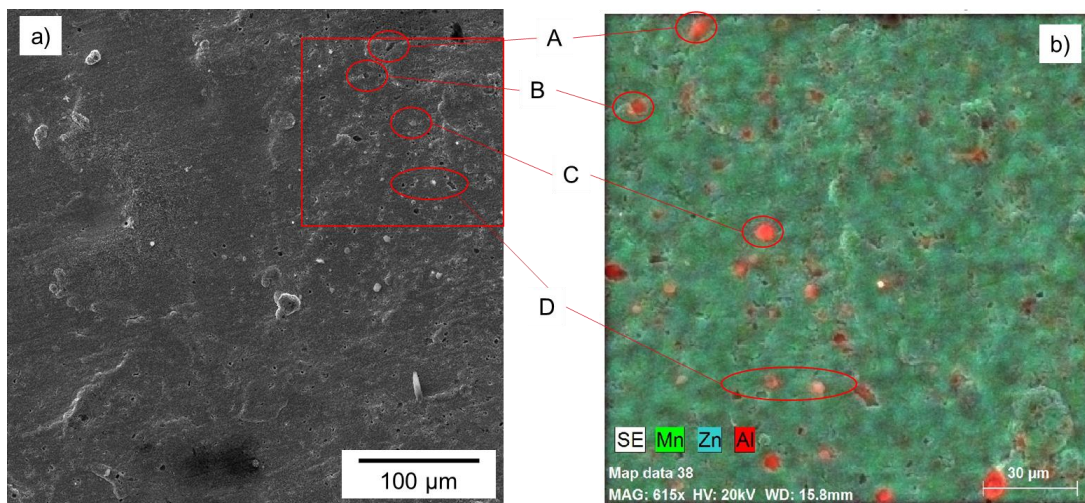


Fig.132: SEM micrograph (a) and EDS mapping (b) of the surface of ZnMn-Al₂O₃ deposits obtained under pulse current at an average current density of 0.045 A/cm², a peak current density of 0.45 A/cm² and a pulse duration of 5 ms; depiction of manganese, zinc and alumina distribution (green, blue and red, respectively)(b)

Similar observations were made on the cross-sections of the composite coatings, as presented in Fig.133. The micrographs of the Fig.133 were acquired in the InLens mode (SE and BSE coupled), permitting to distinguish the porosity from the particles appearing in black and white, respectively.

On the Fig.133a is depicted how small aggregates, presenting an average diameter of 400 nm are incorporated into the metallic matrix. It appears in this case that incorporation mostly occurs at the deposit – substrate interface, although some aggregates could be observed inside the deposit as well as on the surface. A closer look at the aggregates incorporated inside the deposit (Fig.133b) reveals an important porosity around these aggregates forming a sort of particle cloud. The incorporation of larger aggregates are also observed, as depicted in the Fig.133c. In this case, one large aggregate, with a diameter size of about 3 μm , was observed together with a smaller aggregate of about 400 nm diameter. The incorporation of the large aggregates is quite similar as the one previously described for the small aggregates. A large cloud of particles is in this case partially entrapped in the metallic and result in the formation of numerous pores inside and around the aggregate.

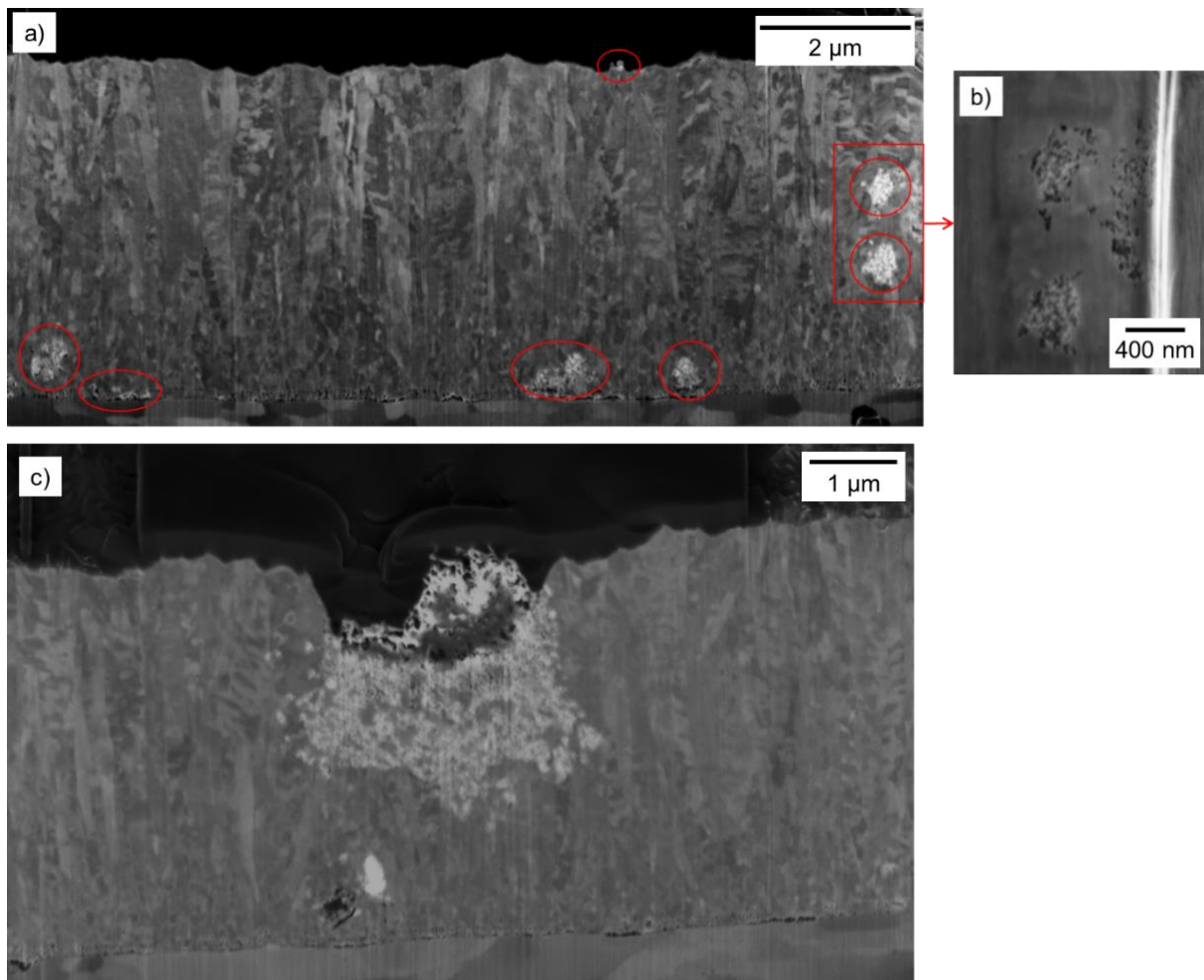


Fig.133: Cross-sectional micrographs of ZnMn-Al₂O₃ deposit obtained under pulse current at an average current density of 0.045 A/cm², a peak current density of 0.45 A/cm² and a pulse on-time of 5 ms, after FIB-SEM milling and polishing; micrographs obtained in the InLens mode; depiction of small aggregates (a) with focus (b), and large aggregates (c)

These micrographs confirm the mechanism of incorporation previously formulated and support previous observations of the deposits morphology. Firstly, some aggregates adhere to the steel surface, whereas other particles are entrapped inside the coating. It seems that the growing metallic matrix requires a significant amount of time in order to cover the aggregate, resulting in the numerous pores around them. However, the deposits still present a remarkable morphology with the absence of porosity inside the metallic matrix. It can also be noticed that the composite coatings present some porosity at the deposit – substrate interface, as already observed on the Zn-Mn deposits (section 3.3.5). Similarly to the pulse Zn-Mn deposits studied in chapter 3, the presence of strata was again observed on the ZnMn-Al₂O₃ coatings.

Interestingly, it can be observed that particles, or aggregates, belonging to each of the population present in the initial plating bath (namely, 140 – 200 nm and 1.4 – 4 µm diameter) could be incorporated inside the metallic matrix. It seems however that a significantly higher amount of small aggregates were incorporated in comparison to the larger ones. This conclusion is in apparent contradiction with the observations of the literature, generally concluding to higher incorporation of larger particles [140, 142, 163, 164]. However, these findings, expressed as atomic or weight percentage of particles, are mostly based on chemical analyses instead of direct observations. Consequently, single large particle would account for higher amount of particles than numerous small particles. Therefore, the results obtained in this first section on polydispersed electrolytes, showing the entrapment of relatively small aggregates, are particularly promising. Additional analyses were as a result conducted on samples obtained from monodispersed electrolytes.

Al₂O₃ – ZnMn composite coatings obtained from monodispersed electrolyte

In this section, the incorporation of Al₂O₃ particles presenting a diameter size of about 200 nm from a monodispersed plating bath, i.e. submitted to sonication and followed by a rest time according to the protocol described in section 5.2, will be studied. Various sections of the deposit were investigated, a schematized in Fig.134. In order to obtain a more representative picture of the particle incorporation inside the metallic matrix, a 3-dimensionnal transverse cut was conducted through the deposit on a distance of 15 µm with the acquisition of a micrograph every 10 nm. Based on these cross-sections, a reconstructed surface could be obtained. The resulting micrographs of the surface, cross-section and reconstructed cross-sections are presented in Fig.135, Fig.136 and Fig.137, respectively.

The SEM micrographs obtained on the surface of the samples in the InLens mode reveals the presence Al₂O₃ in the form of dispersed aggregates as highlighted in light-grey / white on the Fig.135. In comparison to the composite coatings previously investigated (Fig.129d and Fig.132), it appears that the deposits presented in Fig.135 show an improved morphology and a significantly lower amount of porosity.

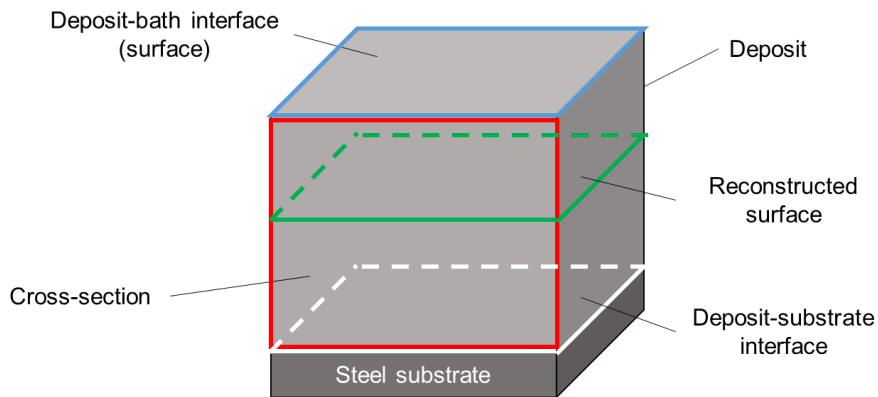


Fig.134: Schematization of the sections studied on the ZnMn-Al₂O₃ deposits after FIB-SEM milling and polishing; normal plane sections such as deposit – bath interface (surface, blue), deposit- substrate interface (white) and reconstructed surface (green); transverse plane sections such as cross-section (red)

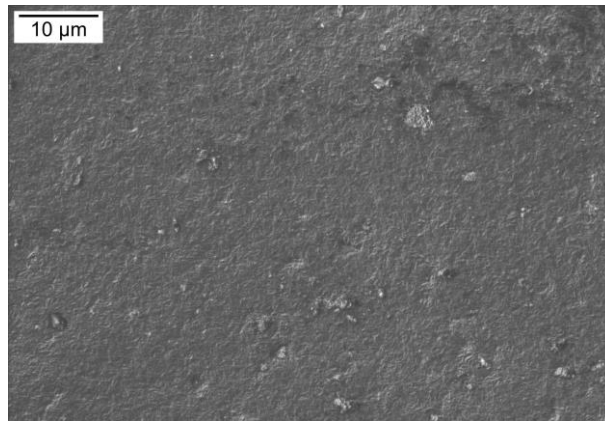


Fig.135: SEM micrograph of the surface of ZnMn-Al₂O₃ deposits obtained by means of pulse plating at an average current density of 0.045 A/cm², a pulse on-time of 5 ms and peak current densities of 0.45 A/cm²; micrograph obtained in the InLens mode

This improvement of the morphology is confirmed by the observations made on cross-sections of the deposits. Across the 15 μm investigated, no aggregates or porosity were observed inside the deposits. A typical cross-section is presented in Fig.136. It can be observed that the vast majority of the particles are located on the surface of the deposits, depicted by the dark-grey dots circled in red on the Fig.136. Black dots are also observed in this region, corresponding to some pores entrapped between the Pt-layer (deposited prior to milling in order to reduce surface roughness and improve the quality of the cross-section) and the deposit. In addition, small amounts of particles were observed near the deposit – substrate interface, also represented in dark-grey. However, the well-known presence of porosity (black spots) in this region circled in blue on the Fig.136, makes the distinction quite difficult. Based on previous observations on Zn-Mn and Zn-Mn-Al₂O₃ deposits, it can be assumed that pores are confined to the deposit – substrate interface.

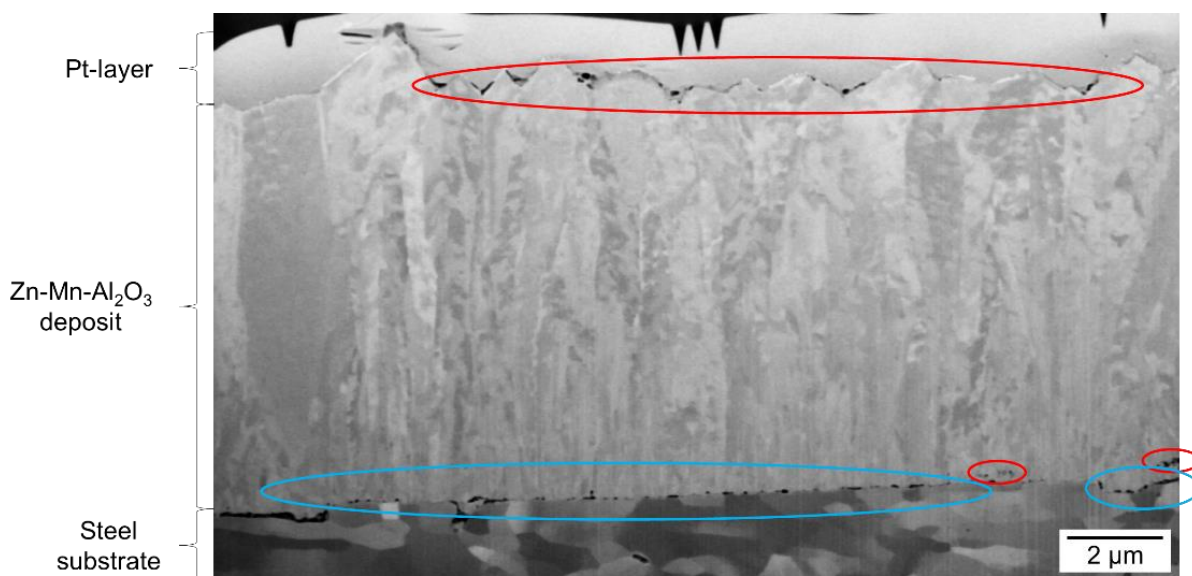


Fig.136: Cross-sectional micrograph of ZnMn-Al₂O₃ deposit obtained under pulse current at an average current density of 0.045 A/cm², a peak current density of 0.45 A/cm² and a pulse on-time of 5 ms, after FIB-SEM milling and polishing; micrograph obtained in the SESI mode; highlight of the location of the particles (red circles) and of the porosity (blue circles)

The reconstructed surface of the Fig.137 lead to similar conclusions. Three examples reconstructed at the deposit – electrolyte interface, in the middle of the deposit (about 2.5 μm deep) and at the deposit-substrate interface are presented in Fig.137(a), (b) and (c), respectively.

The Fig.137a clearly depicts the location of the particles, highlighted in black, on the upper surface of the deposit and more particularly in the cavities formed at the crystallite boundaries. This codeposition of particles on the surface is also enhanced by the random texture of the metallic matrix previously observed in Fig.130 and previously suggested by Camargo et al. [149]. As expected from the cross-sectional analyses, no traces of particles were found inside the deposit (Fig.137b). The reconstruction at the deposit – substrate interface (Fig.137c) reveals the presence of particles in the first nanometres of the coatings and large pores located at the interface. This also confirms the observations previously described.

It is interesting to note that in this case the particles observed on the cross-sections appear to be significantly smaller than the aggregate size measured by DLS in the plating bath.

Some additional features of the metallic matrix could also be observed thanks to this reconstruction:

- A significantly higher amount of crystallites could be observed near the substrate when compared to the surface. This suggests an increase of the crystallite size with increasing coating thickness as already observed on the Zn-Mn coatings obtained under continuous current.
- The presence of strata could again be observed, all oriented perpendicular to the cut direction used during the FIB preparation (Fig.138). This new information further suggests that those strata could be an artefact originating from the milling.

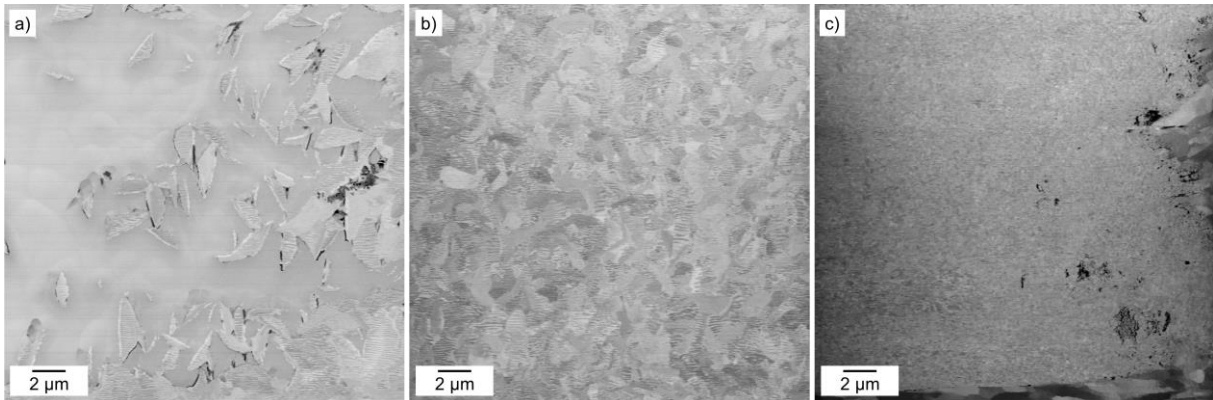


Fig.137: Reconstructed cross-sectional micrograph of ZnMn-Al₂O₃ deposit obtained under pulse current at an average current density of 0.045 A/cm², a peak current density of 0.45 A/cm² and a pulse on-time of 5 ms, after FIB-SEM milling and polishing; micrograph obtained in the SESI mode; micrograph at the deposit – bath interface (a), in the middle of the deposit (b) and at the deposit – substrate interface (c); black dots corresponding to the particles

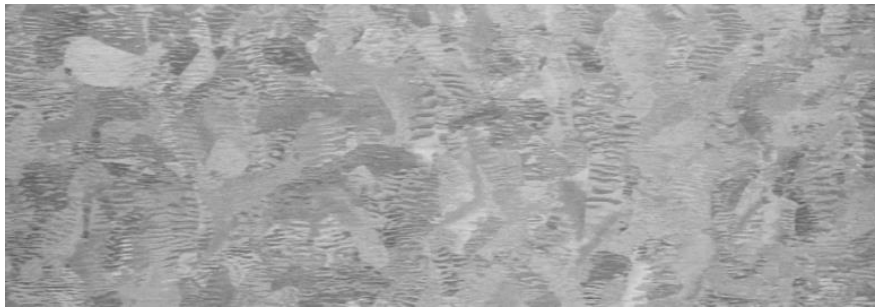


Fig.138: Reconstructed cross-sectional micrograph of ZnMn-Al₂O₃ deposit obtained under pulse current at an average current density of 0.045 A/cm², a peak current density of 0.45 A/cm² and a pulse on-time of 5 ms, after FIB-SEM milling and polishing; micrograph obtained in the SESI mode; micrograph in the middle of the deposit, zoom of the Fig.137b

On the basis of these investigations, it appears that the particles are located to the surface of the deposit and to the coating – substrate interface. These observations show that the incorporation of the particles in the metallic matrix is extremely challenging. This phenomenon can be explained by the growth of the metallic matrix, as depicted in Fig.139.

- During the first steps of the electrodeposition (Fig.139a), the first nuclei of the metallic matrix are formed on the surface of the cathode and some alumina particles are attached on the surface.
- The growth of Zn-Mn nuclei results in the physical entrapment of the particles at the deposit – substrate interface and to the formation of surrounding porosity (Fig.139b).
- Simultaneously, particles are attached on the top of the growing matrix, which pushes them towards the grain boundaries and towards the surface of the deposit (Fig.139c).

In addition, it has to be noted that the both anode and cathode are place vertically, facing each other's in the electrodeposition cell, avoiding the incorporation of the particles via sedimentation effects.

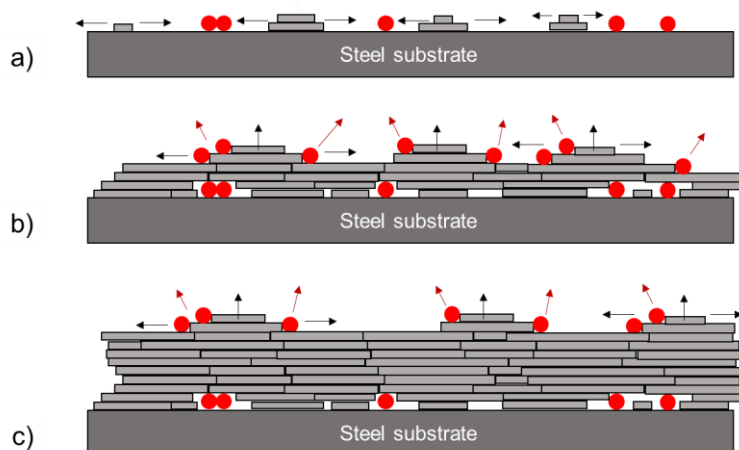


Fig.139: Schematization of particle incorporation during the electrodeposition of Zn-Mn coatings; adsorption of the particles on the surface of the cathode and growth of the first layers of the deposit (a); growth of the Zn-Mn metallic matrix and adsorption of particles on the surface of the deposit, physical entrapment of the particles adsorbed on the steel substrate (b); the particles are pushed towards the surface of the deposits (c)

This codeposition mechanism was previously suggested in the thesis work of Loïc Exbrayat on Zn-CeO₂ composite coatings [242].

Another explanation for the low incorporation rates observed in this work originate from the low amount of porosity in the metallic matrix. Indeed, the presence of pores and cavities inside the deposit provide an additional possibility for the particles to be entrapped.

5.3.3. Discussion and conclusion

In this section, ZnMn-Al₂O₃ composite coatings were obtained through pulse electrodeposition from additive-free chloride electrolytes containing various dispersions of particles (section 5.2).

The characterization of the composite coatings confirms the large impact of the pulse parameters on the properties of the deposit, namely on the composition, morphology and crystallography.

Thanks to properly tuned plating parameters, the deposition of a homogeneous metallic matrix, containing up to 15.2 wt.% Mn was achieved. The results of the investigations also highlight the significant impact of the particle size and distribution in the plating bath on the composite coatings. A bidispersed electrolyte containing large aggregates leads to the formation of numerous pores on the surface of the deposits. In this case, the incorporation of aggregates of various sizes is achieved with the presence of surroundings porosity.

The use of monodispersed electrolytes containing small aggregates leads to a significant reduction of the porosity. A fraction of the particles is entrapped at the coating – substrate interface, while others are pushed towards the surface and the grain boundaries.

5.4. Perspectives on the anticorrosive properties of ZnMn-Al₂O₃ deposits

It was demonstrated in the previous section that Al₂O₃ particles were successfully codeposited inside a Zn-Mn metallic matrix by means of pulse electrodeposition. Depending on the deposition parameters applied, deposits with a Mn content between 11 and 15 wt.% were obtained with the incorporation of particles mostly located near the deposit – substrate interface and on the surface of the coating.

As previously stated, an important aspect of the development process investigated in the framework of this work consists in defining the suitability of the newly developed coatings for an application in the automotive industry.

As a result, some perspectives on the properties of the ZnMn-Al₂O₃ deposits will be tackled in this section. At first, the impact of the particles on the hardness of the deposits will be investigated via Vickers indentation tests. In a second part, an insight on the anticorrosive properties of the deposits, namely on the corrosion potential, corrosion current density and corrosion rate will be given by using the Tafel method.

The deposits investigated in this section were obtained from monodispersed electrolytes (i.e. submitted to sonication and followed by a rest time according to the protocol defined in section 5.2) under constant stirring rate at 500 rpm.

5.4.1. Hardness

The values of the microhardness for ZnMn-Al₂O₃ deposits obtained at peak current densities of 0.15, 0.30 and 0.45 A/cm² are presented in Fig.140.

It appears that the incorporation of Al₂O₃ particles leads to a significant increase of the hardness. Indeed, values in the 160 – 180 Hv range were measured on the composite coatings, in comparison to values around 75 – 90 Hv for the Zn-Mn deposits. As observed in chapter 4.3.1, an increase of the Mn content results in higher hardness values, from about 55 Hv for pure Zn up to 85 Hv for deposits containing 15 wt.% Mn. This behaviour was however not observed on the composite coatings. Indeed, whatever the Mn content (between 11 and 15 wt.%), hardness data are between 160 and 180 Hv with no significant trend.

As previously mentioned in chapter 4.3.1, other aspects such as a decrease of the grain size can influence the hardness. Since the incorporation of alumina particles may impede grain growth [136], the higher hardness values can be to the change of grain size. However, no significant change of the microstructure were observed on the composite coatings (section 5.3.1, Fig.129) in comparison to the Zn-Mn deposits.

Another possibility for this significant increase of the hardness could originate from the location of particles in the metallic matrix. Indeed, the presence of particles at the grain boundaries may obstruct the movement of dislocations, resulting in a higher hardness. Assuming that the particles incorporated in the metallic matrix are homogeneously distributed, as suggested by a relatively low variation of the measurements, it is possible to determine the volume fraction of particles incorporated by applying the rule of mixture.

The rule of mixture is largely used for the prediction of the properties of composite materials. In the case of particles incorporated inside a metallic matrix the rule is described as follow:

$$Hv = f \times Hv_{particles} + (1 - f) \times Hv_{matrix} \quad \text{Eq.56}$$

$$Hv = Hv_{matrix} + f(Hv_{particles} - Hv_{matrix}) \quad \text{Eq.57}$$

With Hv , $Hv_{particles}$ and Hv_{matrix} the hardness of the composite coating, particles and metallic matrix, respectively, and f the volume fraction of the particles.

On the basis of the equation 57, a linear relationship between the hardness of the deposit and the amount of particles incorporated appears, as presented in Fig.140. Assuming hardness values of 75 and 1937 Hv for the Zn-Mn deposit and Al₂O₃ particles, respectively, volume fractions of about 5 and 6 % were obtained. It is however important to note that these results are only some rough estimations of the particle content. Indeed, other aspects of the metallic matrix such as the crystallite size and the Mn content are likely to influence the hardness of the deposits.

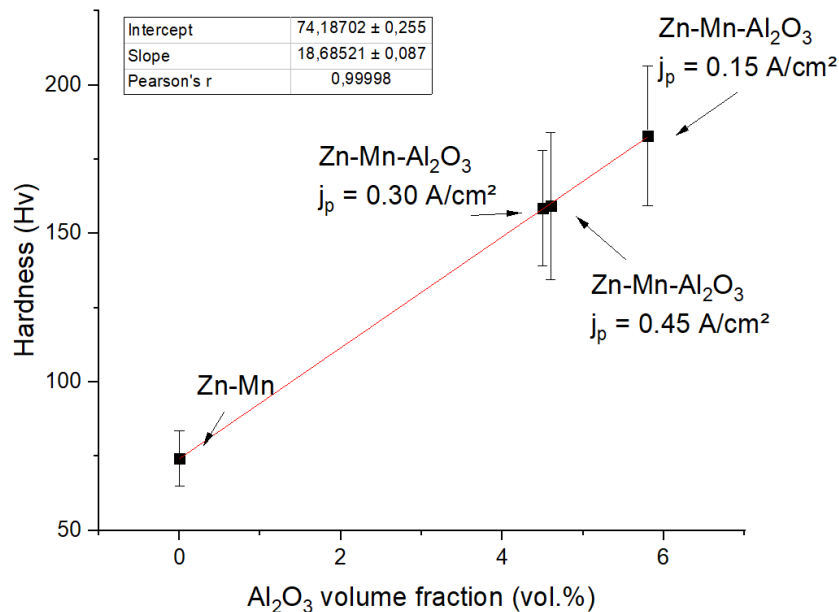


Fig.140: Microhardness of the Zn-Mn and ZnMn-Al₂O₃ deposits obtained under pulse current at various peak current densities, approximation of the amount of particles incorporated based on the rule of mixtures

Significant increase of the hardness for deposits containing particles were numerous reported in the reference literature. Malatji et al. observed an increase of hardness from 132 Hv for pure Zn up to 192 Hv for Zn-Al₂O₃ deposits containing about 2.45 wt.% Al₂O₃ [140]. The application of the rule of mixture on the basis of the hardness measurements of Malatji would result in a volume fraction of particles around 3 %, confirming the validity of the method for a quick estimation of the particle content.

5.4.2. Electrochemical properties

The determination of the corrosion potential E_{corr} and the current density i_{corr} was performed according to the Tafel method from linear scan voltammograms presented in Fig.87. Due to the small size of the samples, the voltammograms were conducted in one single experiment in a 0.5 M NaCl electrolyte. The values for the various deposits, as well as the corrosion rates calculated are summarized in Table 22.

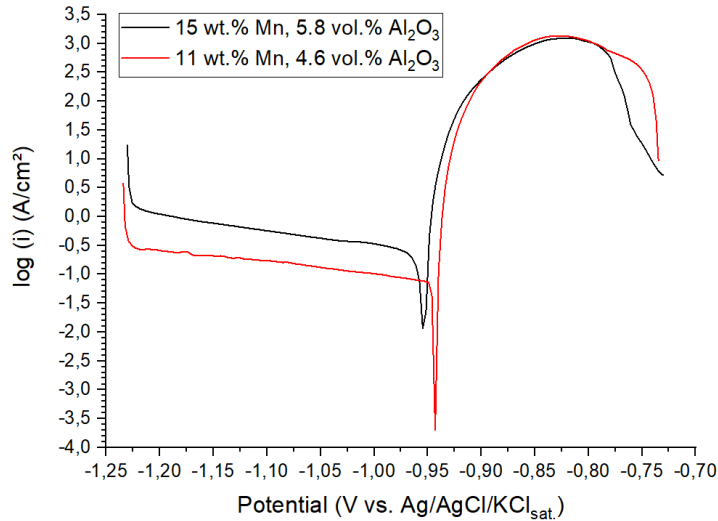


Fig.141: Linear scan voltammograms of 15 wt.% Mn and 5.8 vol.% Al₂O₃ ZnMn-Al₂O₃ (black) 11 wt.% Mn and 4.6 vol.% Al₂O₃ ZnMn-Al₂O₃ (red) and coatings deposited under pulse current

In comparison to the pulse Zn-Mn deposits, a significant increase of the corrosion potential was observed on the composite coatings, independently from the Mn content. Indeed, a shift of about 100 mV was measured between Zn-Mn and ZnMn-Al₂O₃ deposits, both containing 15 wt.% Mn. The second composite coatings, containing about 11 wt.% Mn and a slightly lower amount of particles shows a slight increase of the corrosion potential. This shift is likely explained by a lower Mn content, of about 4 wt.%, as supported by the literature [97, 98, 125] and the previous observations of this work and presented in the section 4.2.1.

Table 27: Corrosion parameters E_{corr} i_{corr} of Zn-Mn and ZnMn-Al₂O₃ coatings deposited under pulse currents. Results obtained from linear scan voltammograms using the Tafel extrapolation method

	E_{corr} (mV)	i_{corr} ($\mu\text{A}/\text{cm}^2$)	Corrosion rate (mm/year)
Zn-Mn, 15 wt.% Mn	-1040 ± 23	105.8 ± 6.4	1.55
ZnMn-Al₂O₃, 15 wt.% Mn, 5.8 vol.% Al₂O₃	-959	146.0	2.13
ZnMn-Al₂O₃, 11 wt.% Mn, 4.6 vol.% Al₂O₃	-943	346.5	5.07

An increase of the corrosion current density was also observed on the composite coatings. For the deposits containing about 15 wt.% Mn, the addition of particles leads to an approximated 50 % increase of the corrosion current density, from 105 up to 146 $\mu\text{A}/\text{cm}^2$. Although the increase of the corrosion rate with incorporation of particles was never reported in the literature, some explanations for this phenomenon can be formulated.

Due to the inert nature of the ceramic oxide particles, the Zn-Mn matrix will be corroded preferentially. In an ideal case where the particles are evenly distributed in the coating a more homogeneous corrosion of the deposit is expected with lower corrosion rates. In the case studied here however, it was demonstrated that the particles were spread on the surface in the form of aggregates, and therefore do not cover the entire surface of the deposit. This inhomogeneous distribution of the aggregates on the surface may lead to a pitting corrosion and to higher corrosion rates. Additional aspects such as porosity in the metallic matrix may also result in an increase of the corrosion rate. A poor cohesion of the particles or aggregates with the matrix could also be an additional hypothesis explaining these results.

It is also important to mention that the measurements presented here were conducted on samples after hardness measurements. Although the indents were confined to a small fraction of the samples, it is likely that these initial experiments negatively impacted the corrosion behaviour of the deposits.

5.4.3. Conclusion and discussion

In this section, some first insights on the properties of the new ZnMn-Al₂O₃ composite coatings were given through some hardness and electrochemical experiments.

Hardness measurements revealed a significant increase of the hardness for the composite coatings in comparison to the Zn-Mn alloys. Due to similar Mn contents between the deposits, this increase of the hardness was assigned to the presence of Al₂O₃ particles probably limiting grain dislocations. An application of the rule of mixture permitted to obtain an estimation of the volume fraction of particles inside the deposits, around 5 and 6 vol.% depending on the deposition parameters.

Electrochemical measurements revealed, for deposits presenting similar Mn contents, a strong increase of the corrosion potential for the composite coatings. An increase of the corrosion rate was also observed for the ZnMn-Al₂O₃ deposits. While this observation is in apparent opposition with the reference literature, an inhomogeneous distribution of the particles, the presence of porosity or a poor cohesion of the particles with the metallic matrix could result in higher corrosion rates. Furthermore, electrochemical experiments conducted after hardness measurements are likely to have negatively impacted the corrosion behaviour of the deposits.

5.5. Conclusion and outlook on the deposition of ZnMn-Al₂O₃ coatings (EN) – Conclusion et perspectives sur la deposition de revêtements ZnMn-Al₂O₃ (FR)

In this last chapter, first attempts on the electrodeposition of ZnMn-Al₂O₃ composite coatings were investigated. In a preliminary study of the electroplating bath, a specific protocol for the dispersion and the stabilization of alumina particles in the electrolyte was defined. Furthermore, the influence of the particles on the electrochemical system was studied. The impact of the pulse parameters on the properties of the metallic matrix as well as the influence of particle dispersion on particle incorporation were also investigated. Based on those studies, some mechanisms of particle incorporation were suggested. Finally, some insights on the properties of such composite deposits were gathered through hardness measurements and electrochemical tests.

The use of ultrasonication combined with magnetic stirring permitted to obtain well-dispersed and stable electrolytes containing 1 g/L of Al₂O₃ nanoparticles. Dynamic light scattering (DLS) experiments proved that electrolytes prepared according to this optimized protocol presented a polydispersed particle distribution with small aggregates between 140 and 200 nm and large aggregates between 1.4 and 4 μ m. The implementation of a sedimentation time following the sonication permitted to obtain a monodispersed suspension of alumina aggregates presenting an average size of 200 nm in diameter.

Linear voltammetric studies carried out in electrolytes containing 1 g/L Al₂O₃ did not show any evidence of an influence of the particles on the electrochemical system, probably due to the low amounts of particles used in this work. However, a rather significant increase of the current density was observed when increasing the stirring rate in the plating bath.

A significant impact of the pulse parameters, and especially of the pulse current density, on the chemical composition, morphology and crystallography of the metallic matrix was observed. Thus, an increase of the pulse current density up to 0.45 A/cm² permitted to obtain deposits containing up to 15.2 wt.% Mn with a mostly homogenous and defect-free surface morphology. In the case of the deposits obtained from bidispersed electrolytes, numerous pores were observed on the surface of the composite coatings. In contrast, these pores were not observed on the coatings deposited from the monodispersed electrolyte. In addition, all deposits obtained at current densities ranging from 0.15 to 0.45 A/cm² exhibit a monophasic ϵ_2 -ZnMn crystallographic composition.

Further analyses of the deposits by means of FIB-SEM on the surface and cross-sections permitted to obtain some information on the mechanisms of codeposition of the particles inside the metallic matrix. The micrographs showed that electrodeposition from polydispersed electrolytes permits to simultaneously codeposit aggregates of various sizes. However, it appeared that the incorporation of large aggregates results in the formation of open porosity. The electrodeposition from monodispersed electrolytes, on the other hand, permitted to reduce significantly the amount of open pores on the deposits. A low amount of entrapped particles was observed at the deposit – substrate interface and on the top surface of the deposit, due to a probable pushing mechanism during the electrocrystallization process.

First analyses of the properties of the ZnMn-Al₂O₃ coatings revealed some interesting perspectives. The composite deposits presented a substantial increase of the hardness in comparison to the Zn-Mn alloys, confirming the successful incorporation of alumina particles inside the metallic matrix. The application of the rule of mixture on the basis of the individual hardness values of each component permitted to estimate the amount of particles incorporated in the deposits, with a maximal amount of 5.8 vol.% obtained in deposits presenting 15.2 wt.% Mn. Electrochemical experiments also revealed some interesting insights on the corrosion behaviour of the composite coatings. An increase of about 100 mV of the corrosion potential was measured on the ZnMn-Al₂O₃ in comparison to the Zn-Mn alloys, in good accordance with the reports of the literature. On the other hand, an increase of the corrosion rate was also measured on the Al₂O₃-containing coatings, likely related to some defects such as porosity, inhomogeneously distributed particles on the surface or poor particle – matrix cohesion.

While these investigations were limited to a few deposition parameters, the studies conducted in this last chapter permitted to gain some insights on the influence of various deposition parameters, with namely particle dispersion in the plating bath and duty cycle, on particle incorporation inside the metallic matrix. First understandings on the how the particles influence some properties of the deposits such as the hardness and the corrosion behaviour were also gathered. Still, further investigations would be necessary in order to optimize further the properties of the deposits and the distribution of the particles.

This includes the use of various pulse durations and relaxation times, more intricate pulse processes as well as a study of the stirring rate. Furthermore, complementary analyses of the behaviour of the composite coatings under accelerated corrosion tests (such as continuous salt spray test or cyclic corrosion test), after mechanical tests, or after phosphating and painting will be of interest.

Dans ce dernier chapitre, des premières tentatives visant à obtenir des revêtements composites de ZnMn-Al₂O₃ ont été investigués. Dans une étude préliminaire du bain électrolytique, le protocole de dispersion ainsi que la stabilité des particules dans l'électrolyte ont été optimisée. De plus, l'impact des particules sur le système électrochimique a été étudié. L'impact des paramètres impulsionsnels sur les propriétés de la matrice métallique ainsi que l'influence de la dispersion des particules sur leur incorporation ont été étudiés. Sur la base de ces études, des mécanismes pour l'incorporation des particules ont pu être proposés. Pour conclure, un aperçu des propriétés de ces revêtements composites a pu être obtenu à l'aide de mesures de dureté ainsi que de tests électrochimiques.

L'utilisation d'ultrasons combinée avec une agitation magnétique ont permis d'obtenir des électrolytes dispersés et stables contenant 1 g/L de nanoparticules d'Al₂O₃. Des mesures par DLS ont démontré que les électrolytes préparés selon ce protocole présentaient une distribution polydispersée avec de petits agrégats de taille comprise entre 140 et 200 nm ainsi que de gros agrégats dont la taille est comprise entre 1.4 et 4 µm. L'implémentation d'un temps de sédimentation suivant le traitement par ultrason a permis d'obtenir une suspension monodispersée de petit agrégats d'alumine dont la taille moyenne est de 200 nm de diamètre.

Les études de voltamétrie linéaire effectuées dans des électrolytes contenant 1 g/L d'Al₂O₃ n'ont pas révélé d'influence des particules sur le système électrochimique, probablement dû aux faibles quantités de particules utilisées dans ce travail. Cependant, une augmentation significative de la densité de courant a pu être observée lors de l'augmentation de l'agitation dans l'électrolyte.

Une influence significative des paramètres impulsionsnels, et en particulier de la densité de courant maximale, sur la composition chimique, la morphologie et la cristallographie de la matrice métallique a été observée. L'augmentation de la densité de courant jusque 0.45 A/cm² a permis d'obtenir des revêtements contenant jusqu'à environ 15 %m de Mn et présentant une morphologie relativement homogène et pratiquement exempte de défauts. En effet, dans le cas des revêtements obtenus à partir d'électrolytes polydispersés, de nombreuses porosités ont pu être observées à la surface des dépôts. En revanche, ces porosités n'ont pas été observées sur les revêtements obtenus à partir d'électrolytes monodispersés. De plus, tous les dépôts obtenus à des densités de courants variant de 0.15 jusque à 0.45 A/cm² ont présenté des cristallographies monophasiques de la phase ε₂-ZnMn.

Des analyses plus poussées des revêtements par FIB-MEB de la surface ainsi que de coupes ont permis d'obtenir des informations sur les mécanismes de codéposition des particules dans la matrice métallique. Les micrographes obtenus ont montré que l'électrodéposition à partir d'électrolytes polydispersés permettait de codéposer des particules ou agrégats de tailles différentes simultanément. Cependant, il est apparu que l'incorporation de gros agrégats conduisait à la formation de porosités ouvertes. L'électrodéposition à partir d'électrolytes monodispersés a permis de réduire de façon significative la quantité de porosités ouvertes dans les dépôts. Une faible quantité de particules a pu également être incorporée à l'interface entre le revêtement et le substrat ainsi qu'à la surface des dépôts, probablement dû à un mécanisme de repoussement lors du procédé d'électrocristallisation.

Les premières analyses de la performance des revêtements de ZnMn-Al₂O₃ ont révélé des propriétés particulièrement prometteuses. Les revêtements composites ont présenté une augmentation substantielle de la dureté en comparaison avec les alliages de Zn-Mn. À l'aide de la loi des mélanges basée sur les mesures de dureté, une approximation de la fraction volumique en particule des revêtements a pu être obtenue, avec une incorporation maximale de 5.8 % vol calculée sur les dépôts contenant 15 % m de Mn. Des mesures électrochimiques ont également permis d'obtenir un aperçu intéressant du comportement en corrosion des revêtements composites. Une augmentation du potentiel de corrosion d'environ 100 mV a été mesurée sur les dépôts ZnMn-Al₂O₃ en comparaison aux alliages de Zn-Mn. D'un autre côté, une augmentation de la vitesse de corrosion a aussi été mesurée sur les dépôts composites, probablement expliquée par la présence de défauts tels que des porosités, une distribution inhomogène des particules ou une faible cohésion entre les particules et la matrice.

Alors que les investigations abordées dans ce chapitre étaient limitées à quelques paramètres de déposition, ces études ont permis d'acquérir de précieux renseignements sur l'influence de divers paramètres, tels que la dispersion des particules dans l'électrolyte et les paramètres impulsionnels, sur l'incorporation des particules dans la matrice métallique. Une première compréhension sur l'influence des particules sur certaines propriétés des dépôts, tels que la dureté et le comportement en corrosion a également pu être obtenue. Néanmoins, des analyses plus poussées seraient nécessaires afin d'optimiser les propriétés des revêtements ainsi que la distribution des particules. Ces études supplémentaires comprennent l'utilisation de diverses durées d'impulsions, divers temps de relaxation, des procédés impulsionnels plus complexes ainsi qu'une étude concentrée sur l'impact de l'agitation. De plus, des analyses complémentaires du comportement des revêtements composites lors de tests de corrosion accélérés (tels que le test de brouillard salin continu ou le test de corrosion cyclique), après des tests mécaniques ou après phosphatation et application de peinture serait de grand intérêt.

Summary and outlook (EN)

In a concern of the automotive manufacturers to decrease the overall weight of passenger vehicles and simultaneously meet increasingly demanding safety requirements, the use of a complex material mix for the body-in-white as well as the chassis of the vehicle is required. Over the large material panel used by the manufacturers, the use of cold formed steels becomes necessary for a wide range of applications. Due to their softer mechanical properties and their ability to deform easily, cold formed steels are required for specific components that need to deform and crumple, therefore permitting the adsorption of large amounts of energy created in the event of a crash. Such steels components can therefore be found in numerous locations on the vehicle, from reinforcements of the chassis to inner-layers of the bodywork. The corrosion of steel components is very likely to arise on passenger vehicles. Due to a continuous exposure to various corrosive environments such as rainwater, humidity, salts and so on during the lifecycle of the vehicle, various forms of corrosion may occur due to contact between different materials or due to some local defects or inhomogeneities on the surface of a single material. In most of the cases, the occurrence of corrosion on the bodywork results in a bad appearance of the vehicle, not acceptable on a brand image point of view. In extreme cases, the corrosion of structural components results in a loss of the mechanical properties and may result in an inappropriate behaviour during a crash.

In order to limit or suppress the occurrence of corrosion, numerous solutions are implemented by the automotive manufacturers. This includes on the one hand the appropriate design of the components and assemblies and on the other hand a proper selection of the materials as well as the definition of a coating system.

This doctorate thesis is specifically focused on the coating system and more precisely on the development of an alternative metallic coating for the sacrificial corrosion protection of cold formed steel components.

Based on a comprehensive review of the literature on the Zn-based coatings, Zn-Mn alloys produced via aqueous electrodeposition were identified as particularly promising for an application as a sacrificial coating in the automotive industry. The influence of the electrodeposition process on the materials properties of the identified Zn-Mn alloys were examined in this work. This includes the comprehensive characterization of the chemical composition, the morphology, the microstructure, the crystallography and the texture of the deposits. In addition, process-relevant properties such as the efficiency, the up-scaling and the stability of the electrodeposition process were investigated. The suitability of the identified Zn-Mn coatings for an application in the automotive industry were also studied in this work. This implies the definition of the anticorrosive performance, the cold forming behaviour and the paintability of the Zn-Mn coatings in comparison with established alloy coatings already commercialized.

The Zn-Mn deposits investigated in this work were obtained from additive-free chloride electrolytes. The electrodeposition from continuous currents, investigated in an early phase, exposed a direct relation between an increase of the cathodic condition (current density or potential) and an increase of the Mn content in the deposits. However, the deposition of high Mn-containing alloys

presenting a satisfactory appearance appeared to be quite challenging due to the high intensity of the hydrogen evolution reaction at high current densities or potentials. Acceptable deposits containing about 13 wt.% Mn were obtained by properly tuning the deposition parameters. In addition, crystallographic analyses revealed monophasic deposits composed of the hexagonal ϵ_2 -ZnMn phase and presenting large columnar grains strongly oriented with the basal plane parallel to the surface.

Nonetheless, numerous aspects and properties of the deposits were insufficient for the application targeted in the framework of this project. Indeed, the high intensity of the HER appeared to be challenging and did not permit to obtain deposits presenting simultaneously high Mn contents and a homogeneous morphology. A porosity could also be observed at the deposit – substrate interface, likely related to hydrogen evolution and the formation of hydrogen bubbles and potentially leading to hydrogen embrittlement in the steel substrate. Finally, a refinement of the microstructure would greatly enhance the properties of the deposits, especially the anticorrosive properties.

In order to solve these issues, the use of pulse plating in place of the traditional continuous plating for the electrodeposition of Zn-Mn alloys was considered. The use of ms-pulse plating permitted a noticeable increase of the Mn content, with up to 15 wt.% depending on the parameters applied. Indeed, it was observed that the pulse parameters, namely the peak current density and the pulse duration t_{on} , could significantly affect the Mn content of the deposits and were related to complex processes:

- The increase of the peak current density results in an increase of the Mn content due to the mechanism of normal codeposition of the Zn-Mn alloys.
- The increase of the peak current density implies a decrease of the duty cycle and therefore an increase of the relaxation time. The use of extended relaxation time however was reported to result in lower amount of Mn.
- On the other hand, the use of short relaxation time induces a faster depletion of the metallic ions near the cathode and also results in a higher intensity of the HER, detrimental to the Mn content.
- The use of extended pulse duration results in a higher intensity of the HER, and is therefore detrimental for the deposition of high Mn-containing alloys.

Similarly, a significant improvement of the deposit morphology was observed with the use of pulse currents. The deposits presented homogeneous morphologies with uniformly distributed crystallites and presented surfaces almost free of defects, cracks and porosity. A decrease of the crystallite size was observed with increase of the peak current density, likely due the preferred nucleation over crystal growth occurring at high current densities. The use of short pulses was also observed to result in finer crystallites, also explained by the promoted creation of new crystallites over the growth of the already existing ones. This decrease of the crystallite size also permitted to decrease the surface roughness of the deposits and enhance the levelling effect.

The use of pulse plating also lead to important changes in the deposit microstructure. In comparison to the large columnar grains obtained with continuous currents, the use of pulse plating resulted in a strong refinement of the microstructure. Interestingly, a transition effect could be observed on the microstructure when decreasing the pulse duration. While the use of short pulses leads to the formation of small and equiaxed grains, the use of longer pulses lead to the formation of a mixture of large columnar as well as small equiaxed grains. In all cases investigated, the presence of porosity at the

deposit – substrate interface were observed. However, no defects or pores were observed inside the deposits.

It was noticed that the pulse parameters had a significant influence on the crystallography and the texture of the deposits. In the range of conditions investigated in this work, both hexagonal ϵ as well as cubic γ phases could be observed over a relatively large range of composition between 9 and 15 wt.% Mn. It appeared that the formation of the γ phase, only formed in a specific domain presenting a relaxation time between 30 and 60 ms, could originate from the metastable hexagonal phase via a slip mechanism. This hypothesis is actually supported by further analyses of the texture of the deposits. Indeed, the presence of a Burgers orientation relationship between the cubic and the hexagonal phases could be observed. Furthermore, it was observed that the majority of the cubic grains were formed at the interface between the bigger hexagonal grains.

It appeared that the pulse electrodeposition process could lead to quite high faradaic efficiencies, depending on the parameters applied. Indeed, the use of relatively short pulses permitting to almost suppress the HER resulted in efficiencies up to 90 %. On the other hand, long pulses during which the intensity of the HER significantly increases lead to low efficiencies around 45 %.

By properly tuning the deposition parameters, monophasic, pore-free and compact deposits containing about 15 wt.% Mn were obtained at high efficiencies. To do so, the following parameters have to be applied:

Average current density, j_a	0.015 A/cm ²
Peak current density, j_p	0.1 A/cm ²
Pulse on-time, t_{on}	5 ms
Duty cycle, γ	0.15
Pulse off-time, t_{off}	28 ms
Frequency, F	30 Hz

Further analyses exposed the high stability of the electrodeposition process. The electrodeposition on various substrate sizes, up to 100 x 200 mm² revealed a homogeneous composition, morphology and crystallography and a reproducible deposition process. The presence of heterogeneities near the edges were systematically observed on the samples. Additional numerical simulations revealed a strong increase of the current density near the edges leading to the formation of dendritic and powdery morphologies as well as a low amounts of Mn. However, it was demonstrated that this edge effect was only limited to a small fraction of the sample, covering an about 5 mm wide strip along the edge.

The anticorrosive performance of the Zn-Mn deposits was assessed via various electrochemical and accelerated corrosion tests such as potentiodynamic polarization, salt spray test (DIN EN ISO 9227) and cyclic corrosion test (VDA 233-102). The results obtained were also compared to a representative selection of commercial alloys already in use in the industry. The pulse Zn-Mn deposits presented highly interesting anticorrosive properties in comparison to the commercial deposits, in particular when exposed to accelerated corrosion tests. This improvement of the corrosion resistance was related to a corrosion mechanism specific to the Zn-Mn alloys. Indeed, during the corrosion of Zn-Mn, the preferential dissolution of Mn results to the formation of a compact and stable corrosion product known

as zinc hydroxychloride (ZHC). The formation of ZHC therefore significantly reduces the progress of corrosion.

It can also be noted that significant variations of the corrosion rates were measured, depending on the environment used for the experiment. While the Zn-Mn deposits presented the highest corrosion rate under immersion in NaCl, they presented the lowest corrosion rate under cyclic corrosion test.

The study of the cold formability also revealed some promising properties for the Zn-Mn alloys. The pulse deposits presented a slight increase of the hardness in comparison to the commercial Zn coatings suggesting a lower ductility of the new deposits. However, tensile experiments did not result in a significant impact on the forming behaviour of the alloys. When submitted to tensile stresses, the Zn-Mn only presented a few thin cracks while commercial electrodeposited Zn coatings presented a high density of fine cracks.

On the other hand, the pulse Zn-Mn deposits developed in the framework of this thesis presented poor adherence properties in comparison to the commercial products, probably related to the presence of porosity at the deposit – substrate interface. However, it needs to be emphasized that the deposits obtained and investigated in this work were obtained on unprepared substrates.

While only a limited amount of experiments was conducted in relation to the phosphatability and the paintability of the new Zn-Mn deposits, some preliminary conclusions can still be obtained. The formation of a dense and homogeneous network of phosphate crystals was obtained on the surface of the Zn-Mn deposits, proving the good suitability of the new alloys for the phosphating process. In addition, the deposition of a homogeneous and pore-free electrophoretic paint (E-coat) could also be achieved on the Zn-Mn coated samples. Preliminary corrosion experiments on E-coated Zn-Mn samples revealed the good quality of the phosphate and E-coat layers as well as the good anticorrosive properties of the entire coating system. Indeed, the first signs of red rust were observed on the Zn-Mn coated samples after four weeks according to the scribe test (VDA 233-102) in comparison to two weeks on the commercial electrocoated Zn samples.

In the present research work, the electrodeposition of Zn-Mn was thoroughly investigated and permitted via pulse currents the deposition of monophasic, homogeneous and compact deposits containing 15 wt.% Mn from additive-free chloride electrolytes. The deposits were comprehensively characterized and presented very interesting anticorrosive properties as well as promising forming behaviour and paintability. However, some challenges were identified. The deposits presented unsatisfactory anticorrosive properties when immersed in NaCl-containing environments and pores were observed at the deposit – substrate interface, resulting in poor adhesive properties.

According to the reference literature, the incorporation of nanoparticles in a metallic matrix could resolve some of the remaining issues observed on the pulse Zn-Mn deposits. Indeed, the homogeneous distribution of inert oxide nanoparticles inside the Zn-Mn metallic matrix is expected to decrease the corrosion rate of the deposit. Furthermore, the entrapment of particles in the porosity of the deposit could also result in an improvement of the deposit – substrate interface.

Based on these considerations, the pulse electrodeposition of Zn-Mn-Al₂O₃ composite coatings was considered as a promising perspective in this work. The influence of the particles, the stirring and the applied pulse parameters on the properties of the metallic matrix were investigated. In addition, a particular attention was given to the homogeneous distribution of the particles in the metallic matrix.

A preliminary study consisting in ultrasonication experiments and dynamic light scattering (DLS) measurements permitted to define a protocol for the dispersion and stabilization of the particles in the plating bath. Depending on the parameters used during the sonication, bidispersed and monodispersed electrolytes were obtained. Further analyses including linear voltammetric experiments revealed that the particles had no impact on the electrochemical system, likely due to the low amounts of particle used, at 1 g/L.

The analyses of the composition and morphology of the composite deposits revealed a behaviour of the metallic matrix quite similar to the one observed during the deposition of pulse Zn-Mn coatings. Increase of the peak current density resulted in an increase of the Mn content, up to 14.5 wt.%. The matrix of the composite deposits also presented similar morphologies to the pure Zn-Mn coatings in the exception of a higher amount of open porosity observed on the surface of the Zn-Mn-Al₂O₃ deposits. This formation of pores could originate from the presence of particle aggregates not fully covered by the metallic matrix, or from the removal of Al₂O₃ aggregates due to hydrodynamic forces. Crystallographic analyses revealed in all cases monophasic deposits composed of the ϵ_2 -ZnMn phase and presenting very similar orientations as the one observed on the pulse Zn-Mn deposits. It has to be mentioned that no signs corresponding to the Al₂O₃ particles were observed during EDS or XRD analyses, most likely due to the low amounts of particle incorporated and below the detection limits of the methods used.

Indeed, further analyses involving FIB-SEM proved the presence of particles and aggregates in the deposits. It appeared from the deposits obtained in bidispersed electrolytes that the incorporation rate of small aggregates was significantly higher than for the large aggregates. In addition, it appeared that the incorporation of the small aggregates while mostly confined near the deposit – substrate interface is much more homogeneous than for the large aggregates. The incorporation of the later takes the form of a large cloud of loosely-bonded particles and results in the formation of numerous pores. Despite the inhomogeneous distribution of the particles in the deposit, a homogeneous microstructure of the metallic matrix was observed as well as the formation of columnar grains.

On the other hand, the deposition from a monodispersed plating bath leads to a significant improvement of the deposit homogeneity. In this case, no porosity or defects were found in the metallic matrix. The analyses of the cross-sections also revealed the presence of a refined and homogeneous microstructure and the formation of columnar grains. A relatively high amount of small aggregates was observed on the surface of the deposits as well as at the deposit – substrate interface. However, no particles or aggregates were observed inside the deposit. This phenomenon is explained by the growth of the metallic matrix. Indeed, some particles adsorbed on the cathode are entrapped by the metallic matrix during the first steps of the deposition due to the preferred nucleation over grain growth. During the growth of the deposit however, the particles adsorbed on the Zn-Mn matrix are pushed towards the grain boundaries and the surface due to the preferred grain growth over nucleation.

It was demonstrated that the incorporation of particles into the metallic Zn-Mn matrix resulted in a significant increase of the deposit hardness. This phenomenon is due to the particles obstructing the movement of dislocations. Electrochemical experiments showed a strong increase of the corrosion potential due to the presence of particles. On the other hand, an increase of the corrosion rate was observed for the composite coatings. Although this observation is in contradiction with the literature, the inhomogeneous distribution of the particles, the presence of porosity or a poor adherence of the particles with the metallic matrix could explain such a behaviour.

The investigations conducted in the framework of this work on the Zn-Mn- Al_2O_3 composite coatings revealed some interesting insights on the impact of the various process parameters on the incorporation of particles inside the metallic matrix. Furthermore, some first investigations highlighted very promising mechanical and electrochemical properties with namely an increased hardness as well as higher corrosion potential. However, it appeared that the homogeneous incorporation of particles was particularly challenging and could result, if not appropriate, to some defects and an increase of the corrosion current. Further experiments would therefore be necessary in order to improve particle distribution and to enhance the properties of the deposits.

With the aim of developing alternative anticorrosive coating for the automotive industry, two promising approaches were investigated in the framework of this doctorate thesis.

On the one hand, the pulse electrodeposition process of Zn-Mn was comprehensively studied and the deposits thoroughly characterized. In addition, these new alloys were tested according to various standardized methods in order to determine their corrosion resistance, formability and paintability. While a good overview of the properties of the Zn-Mn deposits was gathered in this work, further investigations would be required in order to consider the Zn-Mn alloys at an industrial scale. First of all, a study focused on the relation between the substrate and the deposit would be of interest in order to improve the adhesive properties of the deposits. These experiments could include substrates of various nature and compositions as well as various pre-treatments of the substrate prior to deposition. Based on those experiments, additional mechanical and corrosion tests could be considered in order to conclude on the beneficial or detrimental impact of the substrate on the adhesive properties. In addition, further investigations of the suitability of the Zn-Mn deposits for further post-processes involved in the automotive industry such as laser cutting, welding, bonding, etc. would be of interest.

On the other hand, the electrodeposition of new Zn-Mn- Al_2O_3 composite coatings was attempted. In this first preliminary study, some insights on how the electrodeposition process and the applied parameters impact the properties of the metallic matrix as well as the incorporation of particles were obtained. However, further research work on the electrodeposition process will be required in order to fully master the deposition of ZnMn- Al_2O_3 coatings. This includes the study of the plating bath with parameters such as the pH and the use of surfactant, the zeta-potential of the particles, the study of the deposition under continuous currents, how the stirring rate influence particle incorporation, etc. Based on these investigations, a comprehensive characterization of the most promising deposits will be required, including the corrosion resistance of the deposits under accelerated corrosion tests such as the salt spray test and the cyclic corrosion test, their formability, phosphatibility as well as paintability.

Based on the understandings gathered in this work on the pulse electrodeposition of Zn-Mn alloys, another interesting approach could be focused on the electrodeposition of multilayer coatings. Some

concepts were suggested in the framework of this thesis, such as the deposition of coatings presenting a gradient of the composition, or coatings presenting an additional oxide layer. The deposition of such coatings could be achieved via more complex pulse processes such as superimposed or reversed pulse plating.

Résumé et perspectives (FR)

Avec pour objectifs de réduire la masse globale des véhicules de tourisme ainsi que de remplir les strictes exigences de sécurité, l'utilisation d'un mélange complexe de matériaux pour la caisse en blanc et le châssis des véhicules est nécessaire. Parmi le large choix de matériaux utilisé par les constructeurs d'automobiles, l'utilisation d'aciers mis en forme à froid devient une véritable nécessité pour un large nombre d'applications. De par leur capacité à se déformer facilement, ces aciers formés à froid sont requis pour des composants qui doivent se déformer permettant ainsi d'absorber de larges quantités d'énergie en cas de crash. De tels composants peuvent ainsi être trouvés à de nombreux endroits sur le véhicule, des renforcements du châssis jusqu'à la carrosserie. La corrosion de ces composants en acier est fortement probable sur des véhicules de tourisme. De par leur exposition continue à des environnements corrosifs tels que l'eau de pluie, l'humidité, les sels de déneigement, etc., de nombreuses formes de corrosion peuvent survenir par contact entre deux matériaux de composition différente, ou dû à des défauts ou hétérogénéités de surface sur un matériau seul. Dans la majorité des cas, l'apparition de corrosion sur la carrosserie résulte en une mauvaise apparence du véhicule, inacceptable pour l'image de la marque. Dans certains cas extrêmes cependant, la corrosion de composants structurels peut conduire à une perte des propriétés mécaniques et peut mener à un comportement inapproprié en cas d'accident.

Afin de limiter, voire supprimer l'apparition de corrosion, de nombreuses solutions sont implémentées par les constructeurs automobiles. Ceci inclut d'un côté l'utilisation d'un design approprié des composants et des assemblages et d'un autre côté une sélection adéquate des matériaux ainsi que des revêtements.

Cette thèse de doctorat se concentre particulièrement sur le système de revêtements utilisé dans l'industrie automobile est plus spécifiquement sur le développement de nouveaux revêtements métalliques pour la protection sacrificielle contre la corrosion d'aciers formés à froid.

Sur la base d'une étude détaillée de la littérature sur les revêtements à base de zinc, les alliages de Zn-Mn déposés par électrodéposition en phase aqueuse ont été identifiés comme particulièrement prometteurs pour une application comme revêtement sacrificiel dans l'industrie automobile. L'influence du procédé d'électrodéposition sur les propriétés des dépôts Zn-Mn a été étudiée dans ce travail. Ceci inclut une caractérisation détaillée de la composition chimique, de la morphologie, de la microstructure, de la cristallographie et de la texture des revêtements. De plus, les propriétés relatives au procédé telles que l'efficacité, l'aptitude au changement d'échelle et la stabilité du procédé d'électrodéposition ont été analysées. L'aptitude des revêtements de Zn-Mn pour une application dans l'industrie automobile a également été étudiée dans cette thèse. Ceci implique la détermination des propriétés anticorrosives, le comportement lors de la mise en forme à froid ainsi que l'aptitude aux opérations de peinture, en comparaison avec des revêtements déjà commercialisés.

Les revêtements de Zn-Mn étudiés dans ce travail ont été obtenus à partir d'électrolytes chlorés en l'absence d'additifs. L'électrodéposition via l'utilisation de courants continus, étudiée dans une première phase, a permis de mettre en évidence une relation directe entre une augmentation de la densité de courant ou du potentiel et une augmentation de la teneur en manganèse dans les dépôts. Cependant, l'obtention de revêtements présentant une teneur en Mn élevée s'est révélée particulièrement complexe

de par la haute intensité de la réaction d'hydrogène lorsque de fortes densités de courants ou de forts potentiels sont appliquées. Néanmoins, l'utilisation de paramètres spécialement définis a permis d'obtenir des revêtements présentant des propriétés acceptables contenant environ 13 %m de Mn. De plus, des analyses cristallographiques ont révélées des dépôts monophasés composés de la phase hexagonale ϵ_2 -ZnMn et présentant de grands grains colonnaires fortement orientés avec le plan basal parallèle à la surface.

Néanmoins, de nombreux aspects et de nombreuses propriétés de ces revêtements sont insuffisants pour l'application visée dans le cadre de ce projet. En effet, la forte intensité de la réaction d'hydrogène est contraignante et ne permet pas d'obtenir des dépôts présentant simultanément de forts taux de Mn et une morphologie homogène. Une porosité a pu également être observée à l'interface entre le revêtement et le substrat, probablement dûe à l'évolution d'hydrogène et la formation de bulles et conduisant à une pénétration dans le substrat. Finalement, un affinement de la microstructure permettrait une significative amélioration des propriétés des revêtements, en particulier la résistance contre la corrosion.

Afin de résoudre ces problèmes, l'utilisation de courants impulsions au lieu des traditionnels courants continus pour l'électrodéposition des alliages de Zn-Mn a été considérée. L'utilisation de courants impulsions a permis une notable augmentation de la quantité de Mn, jusque 15 %m en fonction des paramètres appliqués. En effet, il a été observé que les paramètres impulsions, en particulier la densité de courant maximale et la durée des impulsions, pouvaient affecter de manière significative la teneur en Mn des dépôts, dû à des procédés complexes :

- L'augmentation de la densité de courant maximale résulte en une augmentation de la teneur en Mn dû au mécanisme de codéposition normale des alliages de Zn-Mn.
- L'augmentation de la densité de courant maximale implique une diminution du rapport cyclique et de ce fait une augmentation du temps de relaxation. L'utilisation de temps de relaxation prolongés conduit en revanche à des taux de Mn plus faibles.
- D'un autre côté, l'utilisation de temps de relaxation courts induit une déplétion plus rapide des ions métalliques à proximité de la cathode et résulte ainsi en une plus forte intensité de l'évolution d'hydrogène, néfaste à l'obtention de forts taux de Mn.
- L'utilisation de pulse longues conduit à une augmentation de l'intensité de la réaction d'hydrogène et est de ce fait néfaste à la déposition de revêtements présentant de forts taux de Mn.

De manière similaire, une amélioration significative de la morphologie des revêtements a été observée lors de l'utilisation de courants impulsions. Les dépôts présentent des morphologies homogènes avec une distribution uniforme des cristallites ainsi qu'une quasi-absence de défauts, fissures et porosités. Une diminution de la taille des cristallites a été observée avec une augmentation de la densité de courant maximale, probablement lié à une favorisation de la nucléation par rapport à la croissance des grains. L'utilisation d'impulsions courtes a également permis d'obtenir des cristallites plus petites, d'une manière similaire du fait d'une nucléation favorisée. De par cette diminution de la taille des cristallites, une diminution de la rugosité de surface des revêtements a pu être observée.

L'utilisation de courants impulsions a également conduit à d'importants changements dans la microstructure des dépôts. En comparaison aux larges grains colonnaires obtenus par courant continu,

la déposition via courants pulsés a résulté en un fort affinement de la microstructure. De façon intéressante, une transition a pu être observée sur la microstructure lorsque la durée des impulsions diminue. Alors que l'utilisation d'impulsions courtes conduit à la formation de petits grains équiaxes, l'utilisation d'impulsions longues résulte en une microstructure mixte composée de petits grains équiaxes ainsi que de gros grains colonnaires. Dans tous les cas, la présence de porosités à l'interface entre le dépôt et le substrat a pu être étudiée mais aucunes porosités à l'intérieur des revêtements.

Il a été observé que les paramètres impulsionnels avaient une grande importance sur la cristallographie ainsi que la texture des revêtements. Dans le domaine de conditions étudiées au cours de ce travail, deux phases ont pu être observées, l'une hexagonale ϵ et l'autre cubique γ , sur une large plage de compositions entre 9 et 15 %m de Mn. Il est apparu que la formation de la phase γ , seulement formée dans un domaine spécifique avec un temps de relaxation compris entre 30 et 60 ms, pouvait provenir de la phase hexagonale métastable via un mécanisme de glissement. Cette hypothèse est supportée par des analyses plus poussées de la texture des dépôts. En effet, la présence d'une relation d'orientation de Burgers entre la phase cubique et la phase hexagonale a pu être observée. De plus, il a été mis en évidence que la majorité des grains de la phase cubique étaient formés à la jonction entre les grains de la phase hexagonale.

Il est apparu que le procédé d'électrodéposition impulsionnelle pouvait conduire à des rendements faradiques élevés en fonction des paramètres appliqués. En effet, l'utilisation d'impulsions courtes permettant de supprimer complètement l'évolution d'hydrogène conduit à de forts rendements, jusque 90 %. D'un autre côté, des impulsions longues durant lesquelles l'intensité de la réaction d'hydrogène augmente de façon significative conduisent à des rendements particulièrement faibles, autour de 45 %.

En sélectionnant de manière appropriée les paramètres de déposition, des revêtements monophasiques, non-poreux, compacts et contenant près de 15 %m de Mn ont pu être obtenus avec des rendements élevés. Pour ce faire, les paramètres suivants doivent être appliqués :

Densité de courant moyenne, j_a	0.015 A/cm ²
Densité de courant maximale, j_p	0.1 A/cm ²
Durée des impulsions, t_{on}	5 ms
Rapport cyclique, γ	0.15
Temps de relaxation, t_{off}	28 ms
Fréquence, F	30 Hz

Des analyses complémentaires ont également mis en évidence la très bonne stabilité du procédé d'électrodéposition. La déposition des alliages de Zn-Mn sur des substrats de tailles variées, jusqu'à 100 x 200 mm² a révélé des compositions, morphologies et cristallographies homogènes ainsi qu'un procédé reproductible. La présence d'hétérogénéités à proximité des bords a pu être systématiquement observée sur les échantillons. Des analyses poussées impliquant des dépôts en cellule de Hull ainsi que des simulations numériques ont révélé une forte augmentation de la densité de courant près des bords, conduisant à la formation de morphologies dendritiques et poudreuses ainsi que de faibles taux de Mn. Cependant, il a été démontré que cet effet de bord était seulement limité à une faible surface des échantillons, couvrant une bande d'environ 5 mm de large le long du bord.

Les propriétés anticorrosives des revêtements de Zn-Mn ont été évalués via divers tests électrochimiques et tests de corrosion accélérés tels que la polarisation potentiodynamique, le test de brouillard salin (DIN EN ISO 9227) et le test de corrosion cyclique (VDA 233-102). Les résultats obtenus ont également été comparés à une sélection représentative d'alliages commerciaux d'ores et déjà utilisés dans l'industrie. Les dépôts de Zn-Mn impulsionnels ont démontré des propriétés anticorrosives extrêmement intéressantes par rapport aux produits commerciaux, en particulier lors d'une exposition à des tests de corrosion accélérés. Cette amélioration de la résistance à la corrosion est expliquée par les mécanismes de corrosion spécifiques aux alliages de Zn-Mn. En effet, lors de la corrosion du Zn-Mn, la dissolution préférentielle du Mn conduit à la formation d'une couche stable et compacte de produits de corrosion connue sous le nom de zinc hydroxychlorure (ZHC). La formation de ZHC permet en conséquence de réduire de façon significative la progression de la corrosion.

Il peut également être remarqué qu'une variation significative des vitesses de corrosion a été mesurée, dépendant largement de l'environnement utilisé lors de la mesure. Alors que les alliages de Zn-Mn ont démontré la vitesse de corrosion la plus élevée lors d'un test d'immersion en milieu contenant du NaCl, ils ont présenté la vitesse de corrosion la plus faible lors du test de corrosion cyclique.

L'étude de la formabilité à froid a aussi révélé des propriétés particulièrement prometteuses pour les alliages de Zn-Mn. Les dépôts impulsionnels ont démontré une légère augmentation de la dureté en comparaison avec les revêtements commerciaux de Zn, ce qui suggère une diminution de la ductilité pour les nouveaux dépôts. Cependant, les essais de traction réalisés n'ont pas mis en évidence un impact quelconque sur le comportement des alliages lors de la mise en forme. Lorsque soumis à des contraintes de traction, les dépôts de Zn-Mn ont seulement montré de fines fissures alors que les revêtements électrodéposés de Zn commerciaux présentaient une forte densité de fissures.

D'un autre côté, les revêtements de Zn-Mn impulsionnels développés dans le cadre de cette thèse ont présenté de manière générale des propriétés adhésives faibles en comparaison aux produits commerciaux, principalement dues aux importantes quantités de porosités situées à l'interface entre le dépôt et le substrat. Cependant, il doit être rappelé que les revêtements étudiés dans ce travail ont été obtenus sur des substrats non préparés.

Bien que peu d'analyses aient pu être effectuées concernant la phosphatibilité et l'aptitude aux opérations de peinture des nouveaux revêtements de Zn-Mn, des premières conclusions ont tout de même été obtenues. La formation d'un dense et homogène réseau de cristaux de phosphates a pu être observé sur la surface des dépôts de Zn-Mn, prouvant ainsi la bonne aptitude des revêtements au procédé de phosphatation. De plus, la déposition d'une couche de peinture électrophorèse (E-coat) homogène et absente de défauts a également pu être obtenue. Des premiers essais de corrosion sur des échantillons de Zn-Mn recouvert de peinture électrophorèse ont pu révéler la très bonne qualité des couches de phosphate et de E-coat ainsi que le bon comportement anticorrosif du système de revêtement. En effet, des premiers signes de rouille rouge ont été observés sur les échantillons Zn-Mn après quatre semaines d'exposition au test de corrosion cyclique avec griffure (VDA 233-102). En comparaison, les premiers signes de rouille rouge sur les échantillons commerciaux de Zn électrodéposés ont été observés après seulement deux semaines d'exposition.

Dans ce travail de recherche, l'électrodéposition du Zn-Mn a été exhaustivement étudiée et a permis d'obtenir à partir d'électrolytes chlorés en l'absence d'additifs des revêtements monophasiques, homogènes et compact présentant une teneur en manganèse de 15 %m. Les dépôts ont été minutieusement caractérisés et ont démontré des propriétés anticorrosives particulièrement intéressantes ainsi qu'une capacité à la mise en forme à froid et une aptitude aux opérations de peinture prometteuse. Cependant, certaines limites ont pu être identifiées. Les revêtements présentent un comportement anticorrosif insatisfaisant lors d'une immersion en milieu contenant du NaCl, et une forte porosité est systématiquement observée à l'interface entre le dépôt et le substrat, conduisant à une faible adhésion.

D'après la littérature, l'incorporation de nanoparticules dans une matrice métallique devrait permettre de résoudre certains problèmes rencontrés avec les revêtements de Zn-Mn impulsionnels. En effet, la distribution homogène de nanoparticules d'oxydes inertes dans la matrice métallique de Zn-Mn est supposée permettre une diminution de la vitesse de corrosion des dépôts. De plus, le piégeage des particules dans les porosités des dépôts devrait permettre d'améliorer l'interface entre le substrat et le revêtement.

Sur la base de ces considérations, l'électrodéposition impulsienne de revêtements composites de Zn-Mn-Al₂O₃ a été considérée comme une alternative prometteuse dans ce travail. L'influence des particules, de l'agitation et des paramètres électriques sur les propriétés de la matrice métallique ont été investigués. De plus, une attention particulière a été portée sur la distribution homogène des particules dans la matrice métallique.

Une étude préliminaire consistant à des expérimentations par ultrasons et des mesures par diffusion dynamique de la lumière (DLS) ont permis de définir un solide protocole permettant la dispersion et la stabilisation des particules dans l'électrolyte. En fonction des paramètres utilisés lors de la sonication, des électrolytes bidispersés et monodispersés ont pu être obtenus. Des analyses plus poussées incluant de la voltamétrie linéaire ont révélé l'absence d'une influence des particules sur le système électrochimique, probablement due aux faibles concentrations en particules utilisées, de l'ordre de 1 g/L.

L'analyse de la composition et de la morphologie des revêtements composites révèle un comportement de la matrice métallique similaire à celui observé lors de la déposition impulsienne du Zn-Mn. L'augmentation de la densité de courant maximale conduit à une augmentation de la teneur en manganèse, jusque 14.5 %m. La matrice du revêtement composite présente également des morphologies similaires à celles obtenues sur les dépôts Zn-Mn à l'exception d'une quantité de porosités plus élevée à la surface des composites. Cette formation de porosités est susceptible de provenir d'agrégats de particules partiellement recouverts par la matrice métallique ou de d'agrégats retirés par les forces hydrodynamiques. Les analyses cristallographiques ont révélé dans tous les cas des alliages monophasiques composés de la phase hexagonale ϵ_2 -ZnMn et présentant des orientations très proches de celles observées sur les revêtements Zn-Mn impulsionnels. Il est également intéressant de mentionner que aucun signe des particules, aussi bien par EDS que DRX, n'a pu être observé, probablement dû aux faibles quantités de particules incorporées.

En effet, des analyses plus poussées par des moyens FIB-MEB ont prouvé la présence de particules et agrégats dans les revêtements. Il est apparu que les dépôts obtenus dans des électrolytes

bidispersés présentait une incorporation plus rapide des agrégats de petite taille en comparaison aux larges agrégats. De plus, il a été observé que les petits agrégats étaient principalement confinés à l'interface entre le substrat et le dépôt et présentaient une distribution nettement plus homogène que pour les gros agrégats. L'incorporation de ces derniers résulte dans la formation d'un large nuage de particules peu cohésif ainsi que la formation de nombreuses porosités. Malgré une distribution inhomogène des particules dans le revêtement, une microstructure homogène de la matrice métallique a pu être observée ainsi que la formation de grains colonnaires.

D'un autre côté, l'électrodéposition depuis un électrolyte monodispersé conduit à une amélioration significative de l'homogénéité des dépôts. Dans ce cas, aucune porosité ou défaut ont pu être identifiés dans la matrice métallique. Les analyses des coupes ont également montré la présence d'une microstructure plus fine et plus homogène ainsi que la formation de grains colonnaires. Une quantité relativement élevée d'agrégats de petite taille a pu être observée en surface ainsi qu'à l'interface entre le dépôt et le substrat. Cependant, aucune particule ou agrégat n'a pu être observée à l'intérieur du dépôt. Ce phénomène est expliqué par la croissance de la matrice métallique. En effet, une fraction des particules absorbées sur la cathode se retrouvent piégées par la matrice métallique durant les premières étapes de l'électrodéposition dû à une nucléation préférée à la croissance des grains. Durant la croissance du revêtement cependant, les particules adsorbées en surface de la matrice Zn-Mn sont repoussées vers les joints de grains et vers la surface due à une croissance de grain préférée à la nucléation.

Il a été démontré que l'incorporation des particules dans la matrice métallique de Zn-Mn conduisait à une augmentation notable de la dureté des revêtements. Ce phénomène est dû à la présence des particules, bloquant le mouvement des dislocations. Des mesures électrochimiques ont montré une forte augmentation du potentiel de corrosion causé par l'incorporation des particules. D'un autre côté, une augmentation de la vitesse de corrosion a également été observée. Bien que cette observation soit en contradiction avec la littérature, une distribution inhomogène des particules, la présence de porosités ou une faible adhérence des particules avec la matrice métallique peuvent expliquer un tel comportement.

Les analyses réalisées dans le cadre de ce travail sur les revêtements composites Zn-Mn-Al₂O₃ ont révélé un aperçu intéressant sur l'impact de divers paramètres du procédé d'électrodéposition sur l'incorporation des particules dans la matrice métallique. De plus, des premières études ont montré des propriétés mécaniques et électrochimiques particulièrement prometteuses, avec notamment une augmentation de la dureté ainsi qu'une augmentation du potentiel de corrosion. Cependant, il est apparu qu'une incorporation homogène des particules était particulièrement exigeante et pouvait conduire à la formation de défauts et par conséquent une augmentation du courant de corrosion. Des expériences supplémentaires seraient de ce fait nécessaires afin d'augmenter la distribution des particules ainsi que d'améliorer la performance des revêtements.

Dans le but de développer de nouveaux revêtements anticorrosifs pour l'industrie automobile, deux approches extrêmement intéressantes ont été étudiées dans le cadre de cette thèse de doctorat.

D'une part, l'électrodéposition impulsionnelle du Zn-Mn a été investiguée de manière détaillée et les revêtements précisément caractérisés. De plus, ces nouveaux revêtements ont pu être testés en accord avec de nombreuses méthodes normalisées dans le but de déterminer leur résistance à la corrosion, leur

aptitude à la mise en forme et leur aptitude aux opérations de peinture. Alors qu'un aperçu très détaillé des propriétés des alliages de Zn-Mn a été obtenu dans ce travail, des études supplémentaires sont nécessaires avant de pouvoir considérer une application des alliages de Zn-Mn à une échelle industrielle. Tout d'abord, une étude concentrée sur la relation entre le substrat et le revêtement serait d'un grand intérêt afin d'optimiser les propriétés adhésives des dépôts. Ces expériences supplémentaires pourraient inclure des substrats de différentes natures et compositions ainsi que diverses méthodes de prétraitement. Sur la base de ces expériences, des tests mécaniques et de corrosion additionnels devraient être considérés afin de déterminer l'impact positif ou négatif du substrat sur les propriétés adhésives. De plus, des analyses supplémentaires concernant l'aptitude des revêtements aux diverses opérations requises dans l'industrie automobile telles que la découpe au laser, la soudure, le collage, etc. seraient à prendre en compte.

D'autre part, l'électrodéposition de nouveaux revêtements composite Zn-Mn- Al_2O_3 a été tentée. Dans cette étude préliminaire, des premières connaissances sur l'impact du procédé d'électrodéposition et des paramètres appliqués sur les propriétés de la matrice métallique ainsi que sur l'incorporation des particules ont pu être obtenues. Cependant, d'additionnels travaux de recherche concentrés sur le procédé d'électrodéposition seront requis pour obtenir une maîtrise complète de la déposition des composites Zn-Mn- Al_2O_3 . Ces travaux comprennent une étude de l'électrolyte et des paramètres tels que le pH et l'utilisation de surfactants, une étude de l'électrodéposition sous courants continus, de l'influence de l'agitation sur l'incorporation des particules, etc. D'après ces recherches, une caractérisation minutieuse des dépôts les plus prometteurs sera requise, comprenant également la résistance à la corrosion, la formabilité et l'aptitude aux opérations de phosphatation et de peinture.

Sur la base des connaissances amassées au cours de ce travail sur l'électrodéposition d'alliages de Zn-Mn, un autre axe de recherche pourrait être concentré sur l'électrodéposition de revêtements multicouches. Certains concepts ont été suggérés dans le cadre de cette thèse, tel que la déposition de revêtements présentant un gradient de composition, ou des revêtements présentant une surcouche d'oxydes. L'obtention de tels dépôts pourrait être envisagée grâce à des procédés impulsionsnels plus complexes tels que l'électrodéposition impulsionsnelle super-imposée ou renversée.

Appendix

Appendix 1: Promising coating systems

Additional coatings concepts were considered in the framework of this work for the improvement of anticorrosive coatings in the automotive industry and resulted in some patent applications, as summarized in the Table 9, section 1.4.1.

Zn-Co-Fe alloys

One solution proposed involves the alloying of Zn, Co and Fe in order to form Zn-Co-Fe ternary alloys coatings [91]. The alloying of Zn with Co was already extensively studied in the literature. It was widely reported that the addition of Co significantly improves the anticorrosive properties. The addition of Co into Zn deposits was quite extensively studied in the literature. De Lima-Neto et al. demonstrated the beneficial impact of the Co on corrosion resistance in chloride medium [243], also proved by Gharahcheshmeh and Sohi [244], Panagopoulos et al. [245] and Bajat et al. [246, 247]. The improvement provided by the addition of Co seems to be linked to its specific corrosion mechanism, making the coating more noble resulting in lower corrosion rates [243]. From the literature, two cases were observed. The first case concerns the improvement of corrosion resistance obtained at high Co contents, 18% obtained by De Lima-Neto [243]. The second case observed concerns Zn-Co coatings with low amounts of cobalt, forming deposits with a single phase structure and a refined morphology, providing the highest corrosion resistance [244, 246]. The corrosion mechanisms of Zn-Co coatings were investigated by Ortiz et al. [53]. Zn-Co forms zinc hydroxychlorides and zinc oxide ZnO at early stages, followed by layered double hydroxides $Zn_2Co_3(OH)_{10} \cdot 2H_2O$ and cobalt chloride $CoCl_2 \cdot H_2O$ after long exposures. The addition of Fe together with Zn and Co was considered because of two aspects. At first, the addition of Fe should reduce the corrosion potential of the alloy and thus diminish the corrosion rate. On a second note, the addition of Fe could lead to the formation of additional phases presenting a higher melting temperature that could make these coatings eligible for hot forming operations. A few of these alloys were investigated in the literature. Bhat and Hedge reported for ternary Zn-Co-Fe alloys, with 0.62 wt.% Co and 6.1 wt.% Fe a corrosion resistance 30 times higher than for the Zn-Co alloys [248]. The authors linked the increase of corrosion resistance to the improved homogeneity of the deposits and to some changes of the phase composition. Abou-Krisha et al. [249, 250] investigated Zn-Co-Fe deposits containing high amounts of Co and Fe with from 8 to 21 % Co and 22 to 25 % Fe. An improvement of the homogeneity of the deposits was observed, together with a reduction of the grain size, resulting in better anticorrosive properties compared to the Zn-Co or Zn-Fe deposits. Higher Co contents, up to 40 wt.% Co [251] provides better corrosion resistance than low Co alloys. The electrodeposition of Zn-Co-Fe deposits may result, according to the literature, to the formation of various phases such as $Zn_{0.35}Co_{0.65}$, $Zn_{21}Fe_5$ and Fe-Co [250]. These alloys present melting temperatures significantly higher than of pure zinc (693 K) with values of 1400 K, 1550 K and 1750 K for $Zn_{21}Fe_5$, $Zn_{0.35}Co_{0.65}$ and Fe-Co, respectively. These higher melting temperatures could constitute a significant improvement for the hot forming properties of these coatings by potentially impeding the formation of cracks due to LME.

High entropy alloys – HEA

The use of high entropy alloys (HEA) was also considered in this work. HEA consist in the alloying of at least five metallic elements such as aluminium, cobalt, chrome, copper, steel, hafnium, manganese, molybdenum, niobium, nickel, tantalum, vanadium, wolfram or zirconium. Each of these elements, known as primary elements, should account for at least 5 at.% of the alloy and no more than 35 at.%. In addition to the primary elements, the addition of so called secondary elements is possible, such as carbon, nitrogen, rhenium, ruthenium or silica. The amount of each of the secondary element should not exceed 5 at.%.

On the basis of the literature, a particular interest was found in the Co-Cr-Fe-Mn-Ni based alloys. The following composition was identified as especially promising:

- 10 – 35 at.% Co
- 15 – 30 at.% Cr
- 10 – 30 at.% Fe
- 5 – 25 at.% Mn
- 10 – 30 at.% Ni

It was already reported that high entropy alloys of the Co-Cr-Fe-Mn-Ni basis were leading to the formation of mixed crystallographies consisting of mixture between face- and body-centered cubic structures (FCC and BCC, respectively). In particular, it was reported that a quasi-equi-molar composition of the alloy, i.e. about 18 – 22 at.% per element, was leading to the formation of a monophasic face-centered cubic structure [252]. These peculiar properties of the HEA permit to obtain a much simpler crystallography in comparison to binary or ternary phases usually observed when mixing two or three elements.

In the case of HEA, the formation of these FCC and/or BCC phases leads to a significant increase of the thermal resistance, caused by the absence of phase transformation. Similarly, it was reported that the oxidation mechanisms could be drastically reduced due to a decrease of the diffusion mechanisms inside the alloys. HEA of the Co-Cr-Fe-Mn-Ni basis also presented extremely high melting temperatures, over 1600 °C and exceptional mechanical properties such as superplasticity with a maximal elongation reaching from 405 % up to 800 % at temperatures between 800 and 1000 °C [252]. In addition, numerous reports stated some other interesting properties of the HEA such as good anticorrosive properties, fracture toughness, hardness and wear resistance [252].

Such promising properties would therefore make high entropy alloys good candidates as a replacement for Zn-based deposits for anticorrosive applications in the automotive industry.

Zn-Mo and Zn-Mn-Mo alloys

Another solution involves the incorporation of Mo together with Zn and/or Mn in order to produce Zn-Mo or Zn-Mn-Mo alloy coatings [94]. The use of Mo alloyed with Zn or Zn-based alloys was investigated in the last years. Szczygiel et al. deposited Zn-Ni-Mo as well as Zn-Co-Mo deposits [253]. The authors reported deposits with smoother surface when Mo was added and an increase of the microhardness. The impact of Mo addition on the corrosion behaviour appears to be complex and related to the phases formed as the presence of Mo improves the anticorrosive properties of Zn-Co alloys but impedes those of Zn-Ni alloys. Investigations of the corrosion behaviour of Zn-Co-Mo was performed by Winiarski et al. [254]. The authors observed a passive layer composed Zn(OH)₂, zinc and

molybdenum (IV) oxides and hydroxides as well as cobalt oxide Co_3O_4 [255, 256]. The particular advantages of molybdenum compounds were emphasized. At initial stages, zinc hydroxide is formed together with zinc hydroxy carbonates and ZHC. Increased exposure leads to the transformation of the hydroxides into the more stable ZnO [255]. The electrodeposition of Zn-Mn-Mo alloy coatings with up to 20.5 wt.% Mn and 7.1 wt.% Mo leads to the formation of compact and pore-free layers [257]. The corrosion protection of Zn-Mn-Mo containing 0.5% Mn and 0.5% Mo in chloride electrolyte was improved by 50% in comparison to pure Zn deposits. In other works from Kazimierczak on Zn-Mo, a refinement of the deposits was observed as well as an increase of the microhardness [258, 259].

The use of high entropy alloys (HEA) was proposed in this work. HEA are materials consisting in at least five principal elements in approximate similar amount, between 5 and 35 at.% and possible secondary elements of with a maximal 5 at.% content [260]. The primary elements may consist of Al, Co, Cr, Cu, Fe, Hf, Mn, Mo, Nb, Ni, Ta, V, W or Zr while the secondary elements may consist of C, N, Re, Ru or Si. Among the possibilities offered by such alloys, the Co-Cr-Fe-Mn-Ni based alloys were identified as particularly promising [94] with the following composition: 10 – 35 at.% Co, 15 – 30 at.% Cr, 10 – 30 at.% Fe, 5 – 25 at.% Mn and 10 – 30 at.% Ni. This particular composition was reported to lead to the formation of single body centered cubic (BCC) or face centered cubic (FCC) phases [252]. A reduced number of phases is particularly advantageous for the corrosion resistance of the deposits, reducing the variations in corrosion behaviour between the phases. Besides, the presence of both Ni and Cr were reported to improve the corrosion resistance of the layers. The Co-Cr-Fe-Mn-Ni alloys were also reported to show a significant increase of the melting temperature, above 1600°C, significantly reducing the risk for LME to occur. They also provide outstanding thermal stability due to the absence of phase transformation and low thermal diffusion. Additionally, these alloys demonstrate superplasticity permitting to reach 405 to 800% elongation for temperatures between 800 and 1000°C, as well as high hardness and wear properties.

Another concept considered in this work concerns the use of layers with variation of the composition. A first possibility consists in a Zn-Mn alloy coatings with increase of the Mn content with increase of the thickness [94]. This solution offers the advantage of providing a high Mn content at the outer surface of the deposit, rapidly dissolving into Mn^{2+} and permitting the formation of a compact layer of ZHC corrosion products. The opposite solution of preferring a high Mn content at the substrate-coating interface was also suggested [94]. In this case, the high Mn content near the substrate steel would result in the formation of Zn-Mn phases of higher melting temperature that would act as a protective layer against LME during hot forming operations.

Zn-Mn with Ce-containing nanoparticles

The use of cerium-based particles was already reported in the literature. In particular, the use of ceria CeO_2 was stated to provide promising anticorrosive properties [158, 261]. The particular mechanism leading to this improvement of the corrosion resistance is still not fully understood. However, it seems that cerium-containing compounds generally impede the cathodic reaction by reducing the available surface on the substrate. As a result, the corrosion rate can be strongly reduced [262]. Amongst these Ce-containing compounds, examples such as Ce_2O_3 , CeCl_3 , $\text{Ce}(\text{NO}_3)_3$, $\text{Ce}_2(\text{SO}_4)_3$ or CeN were already reported [263]. In addition, CeO_2 particles were reported to provide good barrier properties due low thermal diffusivity and high thermal expansion coefficient [264].

Zn-Mn with active nanocontainers

The use of corrosion inhibitors into anticorrosive layers was reported to significantly increase the lifetime of the steel substrates by actively inhibiting the progress of corrosion [265-267]. The incorporation of polymeric micelles into Zn and Zn-Co electrodeposits was studied by Koleva et al. [268] and Boshkov et al. [269]. The authors observed an increase of the anticorrosive properties in the deposits mixed with polymeric micelles. It was reported this combination together the Zn-based metallic matrix form a dual protective layer composed of a low solubility ZHC layer and polymer inhibiting the progress of corrosion towards the substrate. However, it was reported that the direct incorporation of the inhibitors into the metallic matrix could lead to some damages of the matrix and/or to the degradation of the inhibitors [270-272]. As a result, encapsulation of the inhibitors prior incorporation into the matrix can help to solve these drawbacks. Encapsulation also offers some advantages such as a controlled release of the inhibitor through a pH dependent decomposition of the outer shell of the container. The release of the inhibitor can in such a case decrease the corrosion rate locally. The use of nanocontainers for the corrosion protection of steels or galvanized steels was investigated by Kamburova et al. [273]. The authors used polymeric nanocontainers, benzotriazole (BTA) inhibitor into poly(acrylic acid) – PAA and poly(diallyldimethylammonium chloride) – PDAD deposited onto hematite, and observed an improvement of the anticorrosive properties of the Zn coatings.

Appendix 2: Mathematical models describing the behavior of metal electrodeposition with inclusion of particles

Model	Characteristics and assumptions	Deposit and process conditions			
		System	Particles size, μm	Current density, j , mA/cm^2	Rotation speed ω , rpm
Guglielmi, 1972 [151]	Describes both adsorption and electrophoresis. The particles are covered by adsorbed metal ions. Particles characteristics and electrolyte conditions are accounted semi-empirically. The effect of flow is not considered.	Ni-TiO ₂ Ni-SiC	1-2	20-100	Not given
Celis et al., 1987 [274]	Uses probability concept to describe the amount of particles that can be incorporated at a given current density. Mass transport of particles is proportional to the mass transport of ions to the working electrode. Volume ratio of particles in the metal deposit increases under charge transfer control and decreases under mass transport control	Cu-Al ₂ O ₃ Au-Al ₂ O ₃	0.05	0-90	400-600
Fransaer et al., 1992 [153]	Uses trajectories to describe the codeposition of non-Brownian particles. Involves two steps: (1) reduction of metal ions (described by Butler-Volmer expression); (2) codeposition of particle (described by trajectory expression)	Cu-PS Ni-SiC	11 0.01-10	0-80 0-200	0-700 0-2000
Hwang et al., 1993 [275]	An improvement of Guglielmi's model. Uses three modes of current density (low, intermediate, high) to distinguish the reduction of adsorbed ion on particles. Involves three steps: (1) convection of particles to surface; (2) loose adsorption on the surface; (3) irreversible incorporation of particles by reduction of adsorbed ions.	Co-SiC	3	1-60	400
Vereecken et al., 2000 [276]	The transport of particles to the surface is controlled by convective-diffusion. The influence of particle gravitational force and hydrodynamics is accounted for at various current densities. Valid only when the particle size is smaller than the diffusion layer thickness.	Ni-Al ₂ O ₃	0.3	5-40	500-2000
Bercot et al., 2002 [277]	An improvement of Guglielmi's model, which incorporates a corrective factor (a 3 rd order polynomial equation) to account for the effects of adsorption and hydrodynamic conditions.	Ni-PTFE	0.5	10-70	400-1000

Appendix 3: Numerical modeling of the cell geometries

In order to try to understand the specificities related to the geometry of the electrochemical cell and the samples, a numerical model of the electrodeposition process was developed. Based on the results obtained, some improvements of the electrochemical cell were suggested. In addition, some insights on the edge effects observed on the deposits could be gathered.

The COMSOL Multiphysics platform was used for the numerical analysis.

The basic model geometry used for the numerical simulation is shown in Fig.142. The anode is a planar dissolving anode of surface $200 \times 200 \text{ mm}^2$, according to the real system described in chapter 2.2.2. The cathode is a planar piece to be coated with a surface ranging from $40 \times 40 \text{ mm}^2$ up to $90 \times 190 \text{ mm}^2$ in order to account for the various sample sizes. The cathode has a thickness of 1.5 mm and is bordered by an isolated edge of 5 mm width representing the isolating tape used in the real system. An inter-electrode distance of 50 mm was used. The overall dimensions of the cell are $200 \times 200 \times 100 \text{ mm}^3$ (H / L / W).

In order to gather more information from the numerical models, two approaches were developed in the framework of this thesis. A first 2-dimensional model and a 3-dimensional one. In both cases, a deforming geometry was used in order to account for the increased thickness on the cathode.

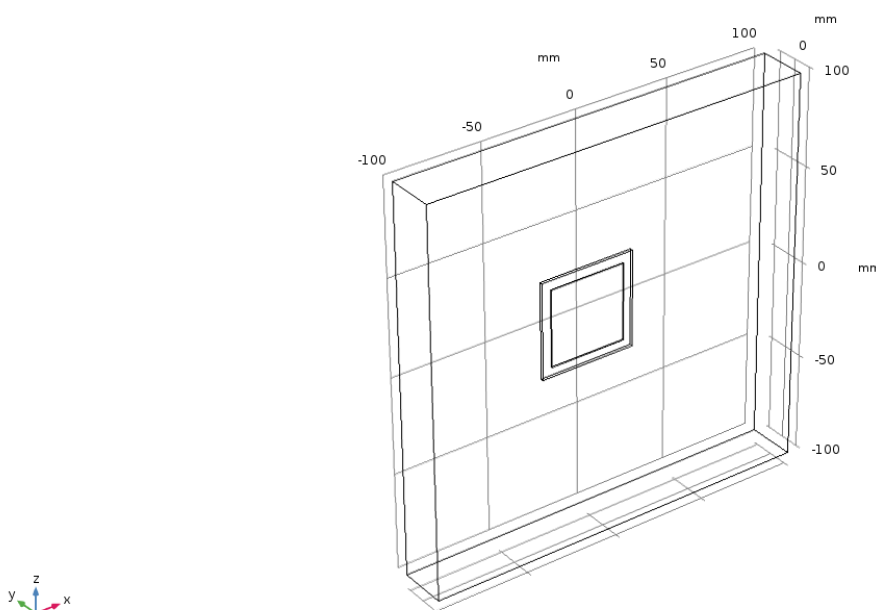


Fig.142: Model geometry (3-dimensional) used for the numerical simulation

As usual in the case of numerical simulations, some assumptions need to be made in order to simplify the system. This permits to save a considerable calculation time. In the case simulated in this work, the following assumptions were made:

- The conductivity of the metal for anode and cathode (no values are required) is considered very high compared to that of the electrolyte. This implies that the resistance of the electrolyte is important.

Appendix

- The electric potential in metallic parts is considered constant. The variations in the activation overpotential are as a result caused by the variations of the potential in the electrolyte at the surface of the electrodes.
- The anode is considered as a boundary in the simulation (no thickness). This assumption is valid in cases where the anode is extremely thin compared to the overall geometry.
- The composition of the electrolyte is considered to be constant through both space and time.
- Mass transport and concentration overpotential are not considered.
- Electrodes kinetics and activation overpotential are considered.

This implies from the chart depicted in Fig.143 that a “secondary current distribution” model will be used.

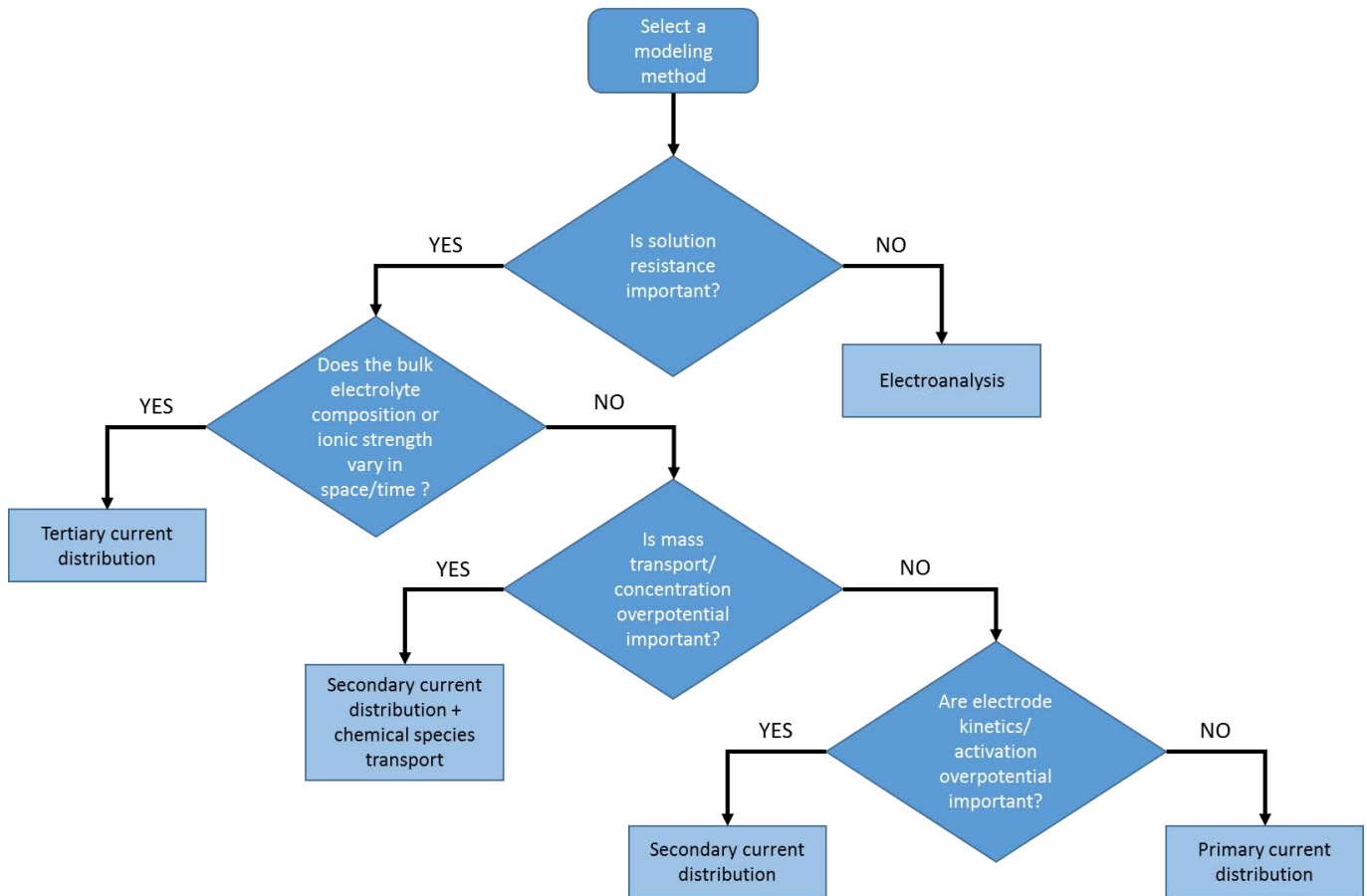


Fig.143: Chart for the selection of the proper modelling method

The electrolyte potential Φ_l is determined from the following equations 58 and 59:

$$i_l = -\sigma_l \nabla \Phi_l \quad \text{Eq.58}$$

$$\nabla \cdot i_l = 0 \quad \text{Eq.59}$$

Appendix

With i_l the electrolyte current density vector and σ_l the electrolyte conductivity, assumed to be constant and equal to 220 mS/cm.

A “default” insulation condition is applied for all boundaries except anode and cathode. The main electrode reaction on both anode and cathode is the zinc dissolution / deposition reaction according to equation 60:



The overpotential η is determined according to the equation 61:

$$\eta = \Phi_{s,0} - \Phi_l - E_{eq,Zn} \quad \text{Eq.61}$$

With the equilibrium potential $E_{eq,Zn} = -0.76$ V.

A Butler-Volmer expression is used to model the reaction, giving the local current density according to equation 62:

$$i_{loc,Zn} = i_{0,Zn} \left(\exp\left(\frac{\alpha_a F \eta_{Zn}}{RT}\right) - \exp\left(\frac{\alpha_c F \eta_{Zn}}{RT}\right) \right) \quad \text{Eq.62}$$

With the anodic and cathodic transfer coefficients α_a and α_c equal to 0.5 and the exchange current density $i_{0,Zn}$ equal to 28 $\mu\text{A}/\text{mm}^2$.

The rate of deposition at the cathode and the rate of dissolution at the anode is calculated according to the equation 63:

$$v = \frac{i_{loc,Zn} \times M}{n \times F \times \rho} \quad \text{Eq.63}$$

With M the molar mass of Zn equal to 68.35 g/mol, ρ the density of Zn equal to 7134 kg/m^3 and n the number of participating electrons equal to 2.

A “default” boundary condition sets the electric potential to zero at the anode (ground). An average current density, constant, $i_{l,average}$ is set at the cathode.

In addition to the zinc deposition reaction, a second reaction is added at the cathode in order to model the hydrogen evolution reaction (HER), according to 64:



A cathodic Tafel equation is used to model the kinetics of the HER, setting the local current density $i_{loc,Zn}$ according to the equation 65:

$$i_{loc,Zn} = -i_{0,H} \times 10^{-\eta^H/Az} \quad \text{Eq.65}$$

Appendix

With the exchange current density $i_{0,H}$ equal to $1 \cdot 10^{-8} \text{ A/m}^2$ (Advances in Corrosion Engineering, Lecture 9: Exchange Current Density – Polarization Relationships, NPTEL Web Course). The HER does not contribute to the rate of Zn deposition, but it contributes to the total current density at the cathode.

A time-dependent model is finally used for the calculation.

Appendix 4: Transmission Electron Microscopy – TEM

During transmission electron microscopy, an incident beam of electrons is focused on an ultra-thin specimen in a similar manner than during SEM, as previously described. However, during TEM the detectors are placed on the other side of the specimen (facing the source) in order to collect transmitted electrons passing through the sample. The interactions between the incident beam and the material lead to the transmission of: transmitted electrons, secondary electrons (SE), Auger electrons, inelastic electrons, elastically scattered electrons and transmitted X-rays.

The secondary electrons give information on the morphology of the specimen. Materials with heavier elements (high Z) tend to appear darker due to the increased absorption of electrons. In a similar way, crystallized materials also appears darker due to the increased diffraction of electrons [278]. The transmitted X-rays are used for EDS analysis in the same way as during SEM.

TEM analysis offers various advantages over SEM. At first, because the energy of the incident beams are considerably higher with accelerating voltages in the 40 – 100 kV range, the spatial resolution is significantly increased at about 0.1 nm. The elemental detectability is also improved, with 0.1 – 1 wt.% depending on the specimen. Finally, the volume of interaction is also significantly reduced with about $10^{-8} \mu\text{m}^3$ [278].

References

1. Mercedes-Benz. *1886: Benz Patent-Motorwagen*. 11/09/2017]; Available from: https://www.mercedes-benz.de/content/germany/mpc/mpc_germany_website/de/home_mpc/passengercars/home/world/mythos/gallery_of_legends.flash.html#1886.
2. AG, Z.F., *Weight-Saving ZF Technology for the Chassis*. 2015.
3. Euro NCAP - *Protocols*. 20/07/2017]; Available from: <https://www.euroncap.com/en/for-engineers/protocols/>.
4. NHTSA - *Road safety*. 20/07/2017]; Available from: <https://www.nhtsa.gov/road-safety>.
5. Review, A.T. *Walking Through History - Mercedes-Benz Museum, Stuttgart*. 11/09/2017]; Available from: <https://autotechreview.com/features/walking-through-history-mercedes-benz-museum-stuttgart?showall=1>.
6. *New Trends and Developments in Automotive Industry*. 2011: InTech.
7. *Innovative lightweight construction of the future Mercedes C 180*. 20/07/2017]; Available from: <http://www.car-engineer.com/innovative-lightweight-construction-future-mercedes-c-180/>.
8. Zhang, X.G., *Corrosion and Electrochemistry of Zinc*. 1996.
9. *Substances restricted under REACH*. [cited 2016 18.10.2016]; Available from: <https://echa.europa.eu/addressing-chemicals-of-concern/restrictions/substances-restricted-under-reach>.
10. *Kathodische Tauchlackierung*. [cited 2016 18.10.2016]; Available from: <http://www.chemie.de/lexikon/Kathodische-Tauchlackierung.html>.
11. Sankara Narayanan, T.S.N., *Surface pretreatment by phosphate conversion coatings - A review*. *Reviews on Advanced Materials Science*, 2005. **9**: p. 130-177.
12. Pietschmann, J., *Industrielle Pulverbeschichtung. Grundlagen. Verfahren. Praxiseinsatz. 4. Auflage*, ed. S. Vieweg. 2013.
13. Krylova, I., *Painting by electrodeposition on the eve of the 21st century*. *Progress in Organic Coatings*, 2001. **42**: p. 119-131.
14. Arlt, K., *Cathodic deposition of paint*. *Electrochimica Acta*, 1993. **39**(8/9): p. 1189-1193.
15. Almeida, E., et al., *Cataphoretic and autophoretic automotive primers A comparative study*. *Progress in Organic Coatings*, 2003. **46**: p. 8-20.
16. LeBozec, N., N. Blandin, and D. Thierry, *Accelerated corrosion tests in the automotive industry: A comparison of the performance towards cosmetic corrosion*. *Materials and corrosion*, 2008. **59**(11).
17. Automobilindustrie, V.d., *VDA 621-415 - Prüfung des Korrosionsschutzes von Kraftfahrzeuglackierungen bei zyklisch wechselnder Beanspruchung*. 1982.
18. Normung, D.I.f., *DIN EN ISO 9227: Corrosion tests in artificial atmospheres - Salt spray tests*. 2015.
19. Close, D., et al. *Challenges in Corrosion Protection for Press-Hardened Steels*. in *9. Erlanger Workshop Warmblechumformung*. 2014. Meisenbach Bamberg.
20. Normung, D.I.f., *DIN EN ISO 8407: Corrosion of metals and alloys - Removal of corrosion products from corrosion test specimens*. 2014.
21. Fujita, S. and D. Mizuno, *Corrosion and corrosion test methods of zinc coated steel sheets on automobiles*. *Corrosion Science*, 2007. **49**(1): p. 211-219.
22. Normung, D.I.f., *DIN EN ISO 11997-1: Paints and vernishes - Determination of resistance to cyclic corrosion conditions - Part 1: Wet (salt fog)/dry/humidity*. 2006.
23. Edavan, R.P. and R. Kopinski, *Corrosion resistance of painted zinc alloy coated steels*. *Corrosion Science*, 2009. **51**(10): p. 2429-2442.
24. Bandyopadhyay, N., et al., *Corrosion behaviour of galvanized steel sheet*. *Surface and Coatings Technology*, 2006. **200**(14-15): p. 4312-4319.
25. Hosking, N.C., et al., *Corrosion resistance of zinc-magnesium coated steel*. *Corrosion Science*, 2007. **49**(9): p. 3669-3695.
26. Roudabush, L., H. Townsend, and D. McCune, *Update on the Development of an Improved Cosmetic Corrosion Test by the Automotive and Steel Industries*. SAE Technical Papers, 1993.
27. Automobilindustrie, V.d., *VDA 233-102 - Klimawechseltest*. 2013.
28. Group, V., *STD 423-0014: Accelerated corrosion test: Atmospheric corrosion*. 2015.

29. ArcelorMittal. *Zinc coatings and thin organic coatings*. 14.11.2017]; Available from: <http://automotive.arcelormittal.com/europe/products/UHSS/Usibor/EN>.
30. UK, C.S.P., *Protected with strength - Solutions in Galvatite hot-dip galvanized steel*. 2004.
31. Metal, N.S.S., *DURGRIP Hot dip galvanized sheet steel*. 2016.
32. Metal, N.S.S., *Coated Steel Sheets - Hot-dip Galvanized Sheets, Electrogalvanized Sheets and Precoated Sheets*. 2012.
33. Metal, N.S.S., *Quality Characteristics of SuperDyma - Hot-dip Zn-Al-Mg-Si Alloy Coated Steel Sheets*. 2012.
34. Steel, N. *ZAM - Hot dip Zinc-6%Aluminium-3%Magnesium alloy coated steel sheet*. 14.11.2017]; Available from: <http://www.nisshin-steel.co.jp/en/products/emarket/01zam/01zam01.htm>.
35. POSCO. *Electrical Galvanized Steel*. 14.11.2017]; Available from: <http://www.posco.com/homepage/docs/eng5/jsp/product/info/s91e2000010c.jsp?mdex=posco13F>.
36. POSCO. *Galvanized Steel*. 14.11.2017]; Available from: <http://www.posco.com/homepage/docs/eng5/jsp/product/info/s91e9000010c.jsp?mdex=posco13E>.
37. Flachstahl, S. *Feuerverzinkte Produkte*. 14.11.2017]; Available from: <https://www.salzgitter-flachstahl.de/de/produkte/feuerverzinkte-produkte.html>.
38. Flachstahl, S. *StronSal beschichtete Produkte*. 14.11.2017]; Available from: <https://www.salzgitter-flachstahl.de/de/produkte/stronsalr-beschichtete-produkte.html>.
39. Flachstahl, S. *Elektrolytisch verzinkte Produkte*. 14.11.2017]; Available from: <https://www.salzgitter-flachstahl.de/de/produkte/elektrolytisch-verzinkte-produkte.html>.
40. SSAB. *Protection against rust with zinc coating*. 14.11.2017]; Available from: <https://www.ssab.com/products/steel-categories/metal-coated-steels/coatings/zinc-coating>.
41. SSAB. *Galfan - Enhanced formability and corrosion resistance*. 14.11.2017]; Available from: <https://www.ssab.com/products/steel-categories/metal-coated-steels/coatings/galfan-coating>.
42. SSAB. *Excellent corrosion protection for painted steel parts*. 14.11.2017]; Available from: <https://www.ssab.com/products/steel-categories/metal-coated-steels/coatings/galvannealed-coating>.
43. Steel, T., *MagiZinc - For superior corrosion protection*. 2012.
44. Steel, T. *Metallic coated*. 14.11.2017]; Available from: <https://www.tatasteeleurope.com/en/products-and-services/flat/metallic-coated>.
45. thyssenkrupp. *Our sheet and coated products*. 14.11.2017]; Available from: <https://www.thyssenkrupp-steel.com/en/products/sheet-coated-products/>.
46. GmbH, V.S. *corrender*. 14.11.2017]; Available from: <http://www.voestalpine.com/corrender>.
47. GmbH, V.S., *Hot-dip galvanized steel strip - Technical Terms of Delivery*.
48. GmbH, V.S., *Electrolytically galvanized steel strip - Technical Terms of Delivery*.
49. Seminar, G.O. *Inspection Course - Galvanizing Process - Surface Preparation*. 05.12.2016]; Available from: <http://www.galvanizeit.org/inspection-course/galvanizing-process/surface-preparation>.
50. *Standard Reduction Potentials by Value*. [cited 2016 18.10.2016]; Available from: http://chem.libretexts.org/Reference/Reference_Tables/Electrochemistry_Tables/P2%3A_Standard_Reduction_Potentials_by_Value.
51. Salgueiro Azevedo, M., et al., *Corrosion mechanisms of Zn(Mg, Al) coated steel in accelerated tests and natural exposure: 1. The role of electrolyte composition in the nature of corrosion products and relative corrosion rate*. *Corrosion Science*, 2015. **90**: p. 472-481.
52. Duchoslav, J., et al., *Evolution of the surface chemistry of hot dip galvanized Zn–Mg–Al and Zn coatings on steel during short term exposure to sodium chloride containing environments*. *Corrosion Science*, 2015. **91**: p. 311-320.
53. Ortiz, Z.I., et al., *Characterization of the corrosion products of electrodeposited Zn, Zn–Co and Zn–Mn alloys coatings*. *Corrosion Science*, 2009. **51**(11): p. 2703-2715.
54. Ramanauskas, R., et al., *Corrosion resistance and microstructure of electrodeposited Zn and Zn alloy coatings*. *Surface and Coatings Technology*, 1997. **92**: p. 12-21.
55. Ramanauskas, R., et al., *Characterization of the corrosion behaviour of Zn and Zn alloy electrodeposits: atmospheric and accelerated tests*. *Corrosion Science*, 1998. **40**(2/3): p. 401-410.
56. Suzuki, I., *The behavior of corrosion products on zinc in sodium chloride solution*. *Corrosion Science*, 1985. **25**(11): p. 1029-1034.

57. El-Lateef, H.M.A.B.D., A.-R. El-Sayed, and H.S. Mohran, *Role of nickel alloying on anodic dissolution behavior of zinc in 3.5% NaCl solution. Part II: Potentiodynamic, potentiostatic and galvanostatic studies*. Transactions of Nonferrous Metals Society of China, 2015. **25**(9): p. 3152-3164.
58. Amadeh, A., B. Pahlevani, and S. Heshmati-Manesh, *Effects of rare earth metal addition on surface morphology and corrosion resistance of hot-dipped zinc coatings*. Corrosion Science, 2002. **44**: p. 2321-2331.
59. Prosek, T., et al., *Composition of corrosion products formed on Zn–Mg, Zn–Al and Zn–Al–Mg coatings in model atmospheric conditions*. Corrosion Science, 2014. **86**: p. 231-238.
60. Zhang, X., C. Leygraf, and I. Odnevall Wallinder, *Atmospheric corrosion of Galfan coatings on steel in chloride-rich environments*. Corrosion Science, 2013. **73**: p. 62-71.
61. Pourbaix, M., *Atlas of electrochemical equilibria in aqueous systems*. 1966.
62. Salgueiro Azevedo, M., et al., *Corrosion mechanisms of Zn(Mg,Al) coated steel: 2. The effect of Mg and Al alloying on the formation and properties of corrosion products in different electrolytes*. Corrosion Science, 2015. **90**: p. 482-490.
63. Pritzel dos Santos, A., et al., *Comparative study of the corrosion behavior of galvanized, galvanized and Zn55Al coated interstitial free steels*. Surface and Coatings Technology, 2015. **279**: p. 150-160.
64. Dosdat, L., et al., *Corrosion Resistance of Different Metallic Coatings on Press-Hardened Steels for Automotive*. steel research international, 2011. **82**(6): p. 726-733.
65. Ramanauskas, R., et al., *Effect of Corrosion Products on the Atmospheric Corrosion of Electrodeposited Zinc and Zinc alloy Coatings*. Corrosion, 2000. **56**(6): p. 588-597.
66. de Azevedo Alvarenga, E. and V. de Freitas Cunha Lins, *Atmospheric corrosion evaluation of electrogalvanized, hot-dip galvanized and galvanized interstitial free steels using accelerated field and cyclic tests*. Surface and Coatings Technology, 2016.
67. Kawafuku, J., *Properties of Zinc Alloy Coated Steel Sheets Obtained by Continuous Vapor Deposition Pilot-Line*. SAE Technical Papers, 1991.
68. Schuhmacher, B., et al., *Innovative steel strip coatings by means of PVD in a continuous pilot line: process technology and coating development*. Surface and Coatings Technology, 2003. **163-164**: p. 703-709.
69. Morishita, M., et al., *Improvement in the corrosion resistance of zinc-plated steel by electrodeposition of magnesium from a molten salt*. ISIJ International, 1996. **36**(6): p. 714-719.
70. Morishita, M., K. Koyama, and Y. Mori, *Self-Healing Ability of Zinc-Plated Steel Coated with Magnesium Electrodeposited from a Molten Salt*. Materials Transactions, 1997. **38**(8): p. 719-723.
71. Morishita, M., K. Koyama, and Y. Mori, *Inhibition of Anodic Dissolution of Zinc-plated Steel by Electrodeposition of Magnesium from a Molten Salt*. ISIJ International, 1997. **37**(1): p. 55-58.
72. Lindström, R., L.-G. Johansson, and S. J-E, *The influence of NaCl and CO₂ on the atmospheric corrosion of magnesium alloy AZ91*. Materials and corrosion, 2003. **54**: p. 587-594.
73. Jönsson, M., D. Persson, and D. Thierry, *Corrosion product formation during NaCl induced atmospheric corrosion of magnesium alloy AZ91D*. Corrosion Science, 2007. **49**(3): p. 1540-1558.
74. Vlot, M., N.V. Landschoot, and R. Bleeker, *Magzinc (ZnAlMg) Coatings versus galvanized*.
75. Prosek, T., et al., *Corrosion performance of Zn-Al-Mg coatings in open and confined zones in conditions simulating automotive applications*. Materials and Corrosion, 2009: p. NA-NA.
76. Sriraman, K.R., et al., *Characterization of corrosion resistance of electrodeposited Zn–Ni Zn and Cd coatings*. Electrochimica Acta, 2013. **105**: p. 314-323.
77. Autengruber, R., G. Luckeneder, and A.W. Hassel, *Corrosion of press-hardened galvanized steel*. Corrosion Science, 2012. **63**: p. 12-19.
78. Chen, Z., et al., *A review on the mechanical methods for evaluating coating adhesion*. Acta Mechanica, 2013. **225**(2): p. 431-452.
79. Ye, M., et al., *Characterization and adhesion strength study of Zn coatings electrodeposited on steel substrates*. Surface and Coatings Technology, 1998. **105**: p. 184-188.
80. Marder, A.R., *The metallurgy of zinc-coated steel*. Progress in Materials Science, 2000. **45**: p. 191-271.
81. Herring, H.D. *Grain Size and Its Influence on Materials Properties*. The Heat Treat Doctor, 2005. 2.
82. Krajewski, W.K., et al., *Property enhancement by grain refinement of zinc-aluminium foundry alloys*, in *4th International Conference on Advances in Solidification Processes (ICASP-4)*. 2016, IOP Conference Series: Materials Science and Engineering. p. 6.
83. Alger, M., *Polymer Science Dictionary. Third Edition*, ed. Springer. 2017.

84. Panagopoulos, C.N., et al., *Mechanical behaviour of Zn–Fe alloy coated mild steel*. Materials & Design, 2009. **30**(10): p. 4267-4272.
85. Song, G.M., et al., *Interface fracture behavior of zinc coatings on steel: Experiments and finite element calculations*. Surface and Coatings Technology, 2006. **201**(7): p. 4311-4316.
86. Tzimas, E. and G. Papadimitriou, *Cracking mechanisms in high temperature hot-dip galvanized coatings*. Surface and Coatings Technology, 2001. **145**: p. 176-185.
87. Shah, S., J. Dilewijns, and R. Jones, *The structure and deformation behavior of zinc-rich coatings on steel sheets*. Galvatech '92, 1992.
88. Ghiotti, A., et al., *Tribological performances of Zn-based coating in direct hot stamping*. Tribology International, 2014. **78**: p. 142-151.
89. Kondratiuk, J., et al., *Zinc coatings for hot sheet metal forming: Comparison of phase evolution and microstructure during heat treatment*. Surface and Coatings Technology, 2011. **205**(17-18): p. 4141-4153.
90. Fan, D.W. and B.C. De Cooman, *State-of-the-Knowledge on Coating Systems for Hot Stamped Parts*. steel research international, 2012. **83**(5): p. 412-433.
91. Claudel, F., et al., *DE102017002385 (A1) - Verfahren und Karosseriehalbzeug zum Herstellen eines Karosseriebauteils für einen Kraftwagen*, D.P.-u. Markenamt, Editor. 2018, Daimler AG.
92. Claudel, F., et al., *DE102017003234 (A1) - Karosserieteil für einen Personenkraftwagen, Verfahren zum Beschichten eines solchen Karosserieteils und Verfahren zum Herstellen einer Beschichtung für ein solches Karosserieteils*, D.P.-u. Markenamt, Editor. 2018, Daimler AG.
93. Claudel, F., et al., *DE102017011553 (A1) - Beschichtung aus einer konfigurationsentropiestabilisierten Legierung, Karosserieteil mit einer solchen Beschichtung, Verfahren zur Herstellung eines Karosserieteils mit einer solchen Beschichtung, sowie Verwendung einer solchen Beschichtung zum Beschichten eines Karosserieteils*, D.P.-u. Markenamt, Editor. 2019, Daimler AG.
94. Claudel, F., et al., *DE102017010175 (A1) - Stahlflachprodukt und aus einem Stahlflachprodukt hergestelltes Stahlbauteil*, D.P.-u. Markenamt, Editor. 2019, Daimler AG.
95. Claudel, F., et al., *DE102017011557 (A1) - Beschichtung für ein Karosserieteil mit einer Legierung aus Zink und Mangan, Karosserieteil mit einer solchen Beschichtung und Verfahren zum Herstellen eines beschichteten Karosserieteils mit einer solchen Beschichtung*, D.P.-u. Markenamt, Editor. 2019, Daimler AG.
96. Boshkov, N., *Galvanic Zn–Mn alloys—electrodeposition, phase composition, corrosion behaviour and protective ability*. Surface and Coatings Technology, 2003. **172**(2-3): p. 217-226.
97. Ganesan, S., G. Prabhu, and B.N. Popov, *Electrodeposition and characterization of Zn-Mn coatings for corrosion protection*. Surface and Coatings Technology, 2014. **238**: p. 143-151.
98. Bučko, M., et al., *Initial corrosion protection of Zn–Mn alloys electrodeposited from alkaline solution*. Corrosion Science, 2011. **53**(9): p. 2861-2871.
99. Boshkov, N., S. Vitkova, and K. Petrov, *Corrosion products of zinc-manganese coatings: part I - investigations using microprobe analysis and x-ray diffraction*. Metal Finishing, 2001. **99**(9): p. 56-60.
100. Bozzini, B., et al., *Electrodeposition and Plastic Behavior of Low-Manganese Zinc-Manganese Alloy Coatings for Automotive Applications*. Automotive Finishing, 1999.
101. Sylla, D., et al., *Electrodeposition of Zn–Mn alloys on steel using an alkaline pyrophosphate-based electrolytic bath*. Surface and Coatings Technology, 2005. **200**(7): p. 2137-2145.
102. Sagiyama, M., et al., *Electrodeposition of zinc-manganese on steel strip*. Plating and surface finishing, 1987. **74**(11): p. 77-82.
103. Gabe, D.R., G.D. Wilcox, and A. Jamani, *Zinc-Manganese Alloy Electrodeposition*. Metal Finishing, 1993.
104. Gabe, D.R., *Protective layered electrodeposits*. Electrochimica Acta, 1994. **39**(8-9): p. 1115-1121.
105. Boshkov, N., K. Petrov, and S. Vitkova, *Corrosion products of zinc-manganese coatings - Part III: Double-protective action of manganese*. Metal Finishing, 2002. **100**(6): p. 98-100.
106. Müller, C., M. Sarret, and T. Andreu, *ZnMn alloys obtained using pulse, reverse and superimposed current modulations*. Electrochimica Acta, 2003. **48**(17): p. 2397-2404.
107. Shivakurama, S., et al., *Influence of condensation product on electrodeposition of Zn-Mn alloy on steel*. Indian Journal of Chemical Technology, 2008. **15**: p. 29-35.
108. Diaz Ballote, L., R. Ramanauskas, and P. Bartolo-Pérez, *Mn Oxide Film As Corrosion Inhibitor of Zn-Mn Coatings*. Corrosion Reviews, 2000. **18**(1).

109. Pistofidis, N., et al., *Microstructure of zinc hot-dip galvanized coatings used for corrosion protection*. Materials Letters, 2006. **60**(6): p. 786-789.
110. Bakhtiari, A., *Effects of a small addition of Mn on modifying the coating thickness, structure and corrosion resistance of hot-dip galvanized coatings*. Metallurgical and Materials Engineering, 2012. **18**(1): p. 1-7.
111. Wang, Y. and J. Zeng, *Effects of manganese addition on microstructures and corrosion behavior of hot-dip zinc coatings of hot-rolled steels*. Surface and Coatings Technology, 2014. **245**: p. 55-65.
112. *Mn-Zn (Manganese-Zinc)*. Landolt-Börnstein New Series IV/5.
113. Münz, R., et al., *Zinc/manganese multilayer coatings for corrosion protection*. Thin Solid Films, 2004. **459**(1-2): p. 297-302.
114. Paunovic, M. and M. Schlesinger, *Fundamentals of electrochemical deposition - second edition*, ed. W. Interscience. 2006.
115. Bučko, M., et al., *Electrodeposition of Zn–Mn alloys at high current densities from chloride electrolyte*. Journal of Solid State Electrochemistry, 2013. **17**(5): p. 1409-1419.
116. Tkalenko, D.A., V.I. Pokhmurs'kyi, and M.D. Tkalenko, *Surface properties of metals and overvoltage of hydrogen release from electrolytes*. Materials Science, 1997. **33**(6).
117. Danaee, I. and S. Noori, *Kinetics of the hydrogen evolution reaction on NiMn graphite modified electrode*. Journal of Hydrogen energy, 2011. **36**.
118. Close, D., et al., *Electrodeposition, microstructural characterization and anticorrosive properties of Zn–Mn alloy coatings from acidic chloride electrolyte containing 4-hydroxybenzaldehyde and ammonium thiocyanate*. Surface and Coatings Technology, 2016. **298**: p. 73-82.
119. Müller, C., M. Sarret, and T. Andreu, *Electrodeposition of Zn–Mn alloys at low current densities*. Journal of the Electrochemical Society, 2002. **149**.
120. Eyraud, M., et al., *Morphology and composition of electrodeposited zinc-manganese alloys*. Plating and surface finishing, 1995. **82**(1): p. 63-70.
121. Sylla, D., et al., *Electrodeposition of Zn–Mn alloys on steel from acidic Zn–Mn chloride solutions*. Thin Solid Films, 2003. **424**(2): p. 171-178.
122. Savall, C., et al., *Morphological and structural characterisation of electrodeposited Zn–Mn alloys from acidic chloride bath*. Materials Science and Engineering: A, 2006. **430**(1-2): p. 165-171.
123. Loukil, N. and M. Feki, *Zn–Mn alloy coatings from acidic chloride bath: Effect of deposition conditions on the Zn–Mn electrodeposition-morphological and structural characterization*. Applied Surface Science, 2017. **410**: p. 574-584.
124. Loukil, N. and M. Feki, *Synergistic effect of triton X 100 and 3-hydroxybenzaldehyde on Zn–Mn electrodeposition from acidic chloride bath*. Journal of Alloys and Compounds, 2017. **719**: p. 420-428.
125. Diaz-Arista, P., et al., *Electrodeposition and characterization of Zn–Mn alloy coatings obtained from a chloride-based acidic bath containing ammonium thiocyanate as an additive*. Surface and Coatings Technology, 2009. **203**: p. 1167-1175.
126. Chandrasekar, M.S. and M. Pushpavanam, *Pulse and pulse reverse plating—Conceptual, advantages and applications*. Electrochimica Acta, 2008. **53**(8): p. 3313-3322.
127. Paunovic, M., M. Schlesinger, and D.D. Snyder, *Fundamental considerations*, in *Modern Electroplating, Fifth Edition*. 2010, John Wiley & Sons, Inc.
128. Danilov, F.I., V.V. Gerasimov, and D.A. Sukhomlin, *Pulsed electrodeposition of Zinc-Manganese Alloys*. Russian Journal of Electrochemistry, 2001. **37**(3): p. 308-310.
129. Müller, C., M. Sarret, and T. Andreu, *Electrodeposition of ZnMn Alloys Using Pulse Plating*. Journal of The Electrochemical Society, 2003. **150**(11): p. C772.
130. Walsh, F.C. and C. Ponce de Leon, *A review of the electrodeposition of metal matrix composite coatings by inclusion of particles in a metal layer: an established and diversifying technology*. Transactions of the IMF, 2014. **92**(2): p. 83-98.
131. Sajjadnejad, M., et al., *Preparation and corrosion resistance of pulse electrodeposited Zn and Zn–SiC nanocomposite coatings*. Applied Surface Science, 2014. **300**: p. 1-7.
132. Sajjadnejad, M., et al., *Direct current electrodeposition of Zn and Zn–SiC nanocomposite coatings*. Transactions of the IMF, 2014. **92**(4): p. 227-232.
133. Bagheri, P., et al., *Ni–TiO₂ nanocomposite coating with high resistance to corrosion and wear*. Surface and Coatings Technology, 2010. **204**(23): p. 3804-3810.

134. Sajjadnejad, M., M. Ghorbani, and A. Afshar, *Microstructure-corrosion resistance relationship of direct and pulse current electrodeposited Zn-TiO₂ nanocomposite coatings*. *Ceramics International*, 2015. **41**(1): p. 217-224.
135. Praveen, B.M. and T.V. Venkatesha, *Electrodeposition and Corrosion Resistance Properties of Zn-Ni/TiO₂ Nano composite Coatings*. *International Journal of Electrochemistry*, 2011. **2011**: p. 1-4.
136. Praveen, B.M. and T.V. Venkatesha, *Electrodeposition and properties of Zn-nanosized TiO₂ composite coatings*. *Applied Surface Science*, 2008. **254**(8): p. 2418-2424.
137. Erten, Ü., et al., *Structural and electrochemical characterization of Zn-TiO₂ and Zn-WO₃ nanocomposite coatings electrodeposited on St 37 steel*. *Journal of Applied Electrochemistry*, 2015. **45**(9): p. 991-1003.
138. de la Fuente, D., J.G. Castano, and M. Morcillo, *Long-term atmospheric corrosion of zinc*. *Corrosion Science*, 2007. **49**: p. 1420-1436.
139. Zhou, X. and Y. Shen, *Beneficial effects of CeO₂ addition on microstructure and corrosion behavior of electrodeposited Ni nanocrystalline coatings*. *Surface and Coatings Technology*, 2013. **235**: p. 433-446.
140. Malatji, N., et al., *Multifaceted incorporation of Zn-Al₂O₃/Cr₂O₃/SiO₂ nanocomposite coatings: anti-corrosion, tribological, and thermal stability*. *The International Journal of Advanced Manufacturing Technology*, 2015. **82**(5-8): p. 1335-1341.
141. Fayomi, O.S.I., A.P.I. Popoola, and C.A. Loto, *The effect of particulate strengthening on microstructure and mechanical characterization of binary-modified composites on mild steel*. *Journal of Composite Materials*, 2014. **0**: p. 1-12.
142. Zheng, H.-Y. and M.-Z. An, *Electrodeposition of Zn-Ni-Al₂O₃ nanocomposite coatings under ultrasound conditions*. *Journal of Alloys and Compounds*, 2008. **459**(1-2): p. 548-552.
143. Müller, C., M. Sarret, and M. Benballa, *Complexing agents for a Zn-Ni alkaline bath*. *Journal of Electroanalytical Chemistry*, 2002. **519**(1-2): p. 85-92.
144. Kuo, S.-L., et al., *Nano-particles dispersion effect on Ni/Al₂O₃ composite coatings*. *Materials Chemistry and Physics*, 2004. **86**(1): p. 5-10.
145. Shrestha, N.K., et al., *Composite coatings of nickel and ceramic particles prepared in two steps*. *Surface and Coatings Technology*, 2001. **140**(2): p. 175-181.
146. Low, C.T.J., R.G.A. Wills, and F.C. Walsh, *Electrodeposition of composite coatings containing nanoparticles in a metal deposit*. *Surface and Coatings Technology*, 2006. **201**(1-2): p. 371-383.
147. Kerr, C., et al., *The Electrodeposition of Composite Coatings based on Metal Matrix-Included Particle Deposits*. *Transactions of the IMF*, 2000. **78**(5): p. 171-177.
148. Azizi, M., W. Schneider, and W. Plieth, *Electrolytic co-deposition of silicate and mica particles with zinc*. *Journal of Solid State Electrochemistry*, 2005. **9**(6): p. 429-437.
149. Camargo, M.K., et al., *Ultrasound assisted electrodeposition of Zn and Zn-TiO₂ coatings*. *Electrochimica Acta*, 2016. **198**: p. 287-295.
150. Pavlatou, E.L. *Composite electrodeposition*. in *COST MP 1407 training school*. 2017. Schwäbisch Gmund.
151. Guglielmi, G., *Kinetics of the Deposition of Inert Particles from Electrolytic Baths*. *Journal of Electrochemical Society*, 1972. **119**(8): p. 1009-1012.
152. Hovestad, A., R.J.C.H.L. Heesen, and L.J.J. Janssen, *Electrochemical deposition of zinc-polystyrene composites in the presence of surfactants*. *Journal of Applied Electrochemistry*, 1999. **29**: p. 331-338.
153. Fransaeer, J., J.P. Celis, and J.R. Roos, *Analysis of the Electrolytic Codeposition of Non-Brownian Particles with Metals*. *Journal of the Electrochemical Society*, 1992. **139**(2): p. 413-425.
154. Ltd, E. *AN004 Zeta potential - electrophoresis, electroacoustics and streaming potential*. [cited 2016 12.11.2016]; Available from: <http://88.208.209.19/~escbu/wp-content/uploads/2016/08/AN004-Zeta-potential-electrophoresis-electroacoustics-and-streaming-potential-rev-0.pdf>.
155. Pellicer, E. *Electrodeposited composites*. in *COST MP 1407 training course*. 2016. Brno.
156. Vathsala, K. and T.V. Venkatesha, *Zn-ZrO₂ nanocomposite coatings: Electrodeposition and evaluation of corrosion resistance*. *Applied Surface Science*, 2011. **257**(21): p. 8929-8936.
157. Kammona, O., et al., *Synthesis of polymeric and hybrid nanoparticles for electroplating applications*. *Electrochimica Acta*, 2009. **54**(9): p. 2450-2457.
158. Ranganatha, S., et al., *Electrochemical studies on Zn/nano-CeO₂ electrodeposited composite coatings*. *Surface and Coatings Technology*, 2012. **208**: p. 64-72.

159. Muresan, L.M., *Electrodeposited Zn-Nanoparticles Composite Coatings for Corrosion Protection of Steel*, in *Handbook of Nanoelectrochemistry*. 2016, Springer. p. 333-353.
160. Gomes, A. and M.I. da Silva Pereira, *Pulsed electrodeposition of Zn in the presence of surfactants*. *Electrochimica Acta*, 2006. **51**(7): p. 1342-1350.
161. Tuaweri, T.J. and G.D. Wilcox, *Behaviour of Zn-SiO₂ electrodeposition in the presence of N,N-dimethyldodecylamine*. *Surface and Coatings Technology*, 2006. **200**(20-21): p. 5921-5930.
162. Hovestad, A. and L.J.J. Janssen, *Electrochemical codeposition of inert particles in a metallic matrix*. *Journal of Applied Electrochemistry*, 1995. **25**: p. 519-527.
163. Tulio, P.C., S.E.B. Rodrigues, and I.A. Carlos, *The influence of SiC and Al₂O₃ micrometric particles on the electrodeposition of ZnNi films and the obtainment of ZnNi-SiC and ZnNi-Al₂O₃ electrocomposite coatings from slightly acidic solutions*. *Surface and Coatings Technology*, 2007. **202**(1): p. 91-99.
164. Vlasa, A., et al., *Electrodeposited Zn-TiO₂ nanocomposite coatings and their corrosion behavior*. *Journal of Applied Electrochemistry*, 2010. **40**(8): p. 1519-1527.
165. Müller, C., M. Sarret, and M. Benballa, *ZnNi/SiC composites obtained from an alkaline bath*. *Surface and Coatings Technology*, 2002. **162**: p. 49-53.
166. Hino, M., M. Hiramatsu, and K. Murakami, *Electroplated Zn-Ni-SiO₂ composite coatings treated with a silane coupling agent to replace chromating*. *Acta Metallurgica Sinica*, 2004. **18**(3): p. 416-422.
167. Wang, Y.L., et al., *Electrodeposition and characterization of Al₂O₃-Cu(Sn), CaF₂-Cu(Sn) and talc-Cu(Sn) electrocomposite coatings*. *Surface and Coatings Technology*, 1998. **106**: p. 162-166.
168. Lajevardi, S.A. and T. Shahrabi, *Effects of pulse electrodeposition parameters on the properties of Ni-TiO₂ nanocomposite coatings*. *Applied Surface Science*, 2010. **256**(22): p. 6775-6781.
169. Close, D., *Alternative protective coatings for hot stamped automotive body parts*, in *Pôle M4 - matière, matériaux, métallurgie, mécanique*. 2018, Université de Lorraine.
170. Hegde, A.C., K. Venkatakrishna, and N. Eliaz, *Electrodeposition of Zn-Ni, Zn-Fe and Zn-Ni-Fe alloys*. *Surface and Coatings Technology*, 2010. **205**(7): p. 2031-2041.
171. Normung, D.I.f., *DIN 50957-1. Testing of electrolytes used for electro-deposited metallic coatings - Test involving electro-deposition - Part 1: Standard Hull cell*. 2016.
172. Perez, N., *Electrochemistry and Corrosion Science - Second Edition*, ed. Springer. 2016.
173. Instruments, M., *Dynamic Light Scattering: An Introduction in 30 Minutes*, in *Technical Note*.
174. Cantoni, M., *3D Microscopy and FIB Nanotomography*. Ecole Polytechnique Federale de Lausanne - EPFL.
175. Sturm, S. *Electron microscopy methods*. in *COST MP 1407 training course*. 2017. Schwäbisch Gmünd.
176. Maitland, T. and S. Sitzman, *Electron Backscatter Diffraction (EBSD) Technique and Materials Characterization Examples*, in *Scanning Microscopy for Nanotechnology - Techniques and Applications*, Springer, Editor. 2006.
177. physics, K.L.-I.f.n.a.r. *X-ray diffraction - Bruker D8 Discover*. 02.08.2017]; Available from: <https://fys.kuleuven.be/iks/nvsf/experimental-facilities/x-ray-diffraction-2013-bruker-d8-discover>.
178. Normung, D.I.f., *DIN EN ISO 25178-2. Geometrical product specifications - Surface texture: Areal - Part 2: Terms, definitions and surface texture parameters*. 2012.
179. Jung, S., *Oberflächenbeurteilung (Rauheitsmessung)*. 2012, Institut für Maschinenelemente - Universität Stuttgart.
180. AG, D., *DBL 4093 - Karosserieteile aus pressgehärteten Stahlblechen*, in *9.4 Galvanostatische Auflösung des ZnFe-Überzugs*. 2015.
181. *ASTM G 102-89*.
182. Normung, D.I.f., *DIN EN ISO 6892-1. Metallic materials - Tensile testing - Part 1: Method of test at room temperature*. 2009.
183. Normung, D.I.f., *DIN EN ISO 7438. Metallic materials - Bend test*. 2016.
184. Automobilindustrie, V.d., *VDA 238-100 - Plate bending test for metallic materials*. 2010.
185. ArcelorMittal. *High formability steels for drawing*. 15.02.2017]; Available from: <http://automotive.arcelormittal.com/europe/products/DS/DD/EN>.
186. Normung, D.I.f., *DIN EN ISO 10130: Cold rolled low carbon steel flat products for cold forming - Technical delivery conditions*. 2007.
187. GmbH, v.S. *Produktinformationsportal > Elektrolytisch verzinktes Stahlband > Weichstähle > DC 06 B+* *ZE*. 15.02.2017]; Available from: <https://www.voestalpine.com/pro/PROMain?mid=60&pkat=13399&t=1487164907876>.

188. outokumpu. *The effects of alloying elements*. 15.02.2017]; Available from: <http://www.outokumpu.com/en/products-properties/more-stainless/the-effects-of-alloying-elements%E2%80%8B/pages/default.aspx>.
189. Inc., G.M., *The Effects of Alloying Elements in Steel*.
190. Ispatguru. *Interstitial Free Steels*. 15.02.2017]; Available from: <http://ispatguru.com/interstitial-free-steels/>.
191. ArcelorMittal. *Major metallurgical families and characterization*. [cited 11.02.2019].
192. Garza, L.G. and C.J. Van Tyne, *Friction and formability of galvanized interstitial free sheet steel*. Journal of Materials Processing Technology, 2007. **187-188**: p. 164-168.
193. Claudel, F., et al., *Pulse electrodeposition and characterization of Zn–Mn coatings deposited from additive-free chloride electrolytes*. Journal of Applied Electrochemistry, 2019.
194. Brenner, A., *Electrodeposition of Alloys, Vol. II*. 1963.
195. Okamoto, H. and L.E. Tanner, *Mn-Zn (Manganese-Zinc)*. Binary Alloy Phase Diagrams, II Ed., 1990. **3**: p. 2625-2629.
196. Nayana, K.O. and T.V. Venkatesha, *Synergistic effects of additives on morphology, texture and discharge mechanism of zinc during electrodeposition*. Journal of Electroanalytical Chemistry, 2011. **663(2)**: p. 98-107.
197. Nayana, K.O. and T.V. Venkatesha, *Bright zinc electrodeposition and study of influence of synergistic interaction of additives on coating properties*. Journal of Industrial and Engineering Chemistry, 2015. **26**: p. 107-115.
198. Greul, T., et al., *Epitaxial growth of zinc on ferritic steel under high current density electroplating conditions*. Electrochimica Acta, 2013. **113**: p. 797-802.
199. Raciassi, K., et al., *Effect of surface preparation on zinc electrodeposited texture*. Surface and Coatings Technology, 2005. **197(2-3)**: p. 229-237.
200. Saltykova, N.A., *Electrodeposition of Platinum Metals and Alloys from Chloride Melts*. Journal of Mining and Metallurgy, 2003. **39(1-2)**: p. 201-208.
201. Silva Filho, J.F. and V.F.C. Lins, *Crystallographic texture and morphology of an electrodeposited zinc layer*. Surface and Coatings Technology, 2006. **200(9)**: p. 2892-2899.
202. Youssef, K.M., C.C. Koch, and P.S. Fedkiw, *Influence of pulse plating parameters on the synthesis and preferred orientation of nanocrystalline zinc from zinc sulfate electrolytes*. Electrochimica Acta, 2008. **54(2)**: p. 677-683.
203. Vasilakopoulos, D., M. Bouroushian, and N. Spyrellis, *Texture and morphology of pulse plated zinc electrodeposits*. Journal of Materials Science, 2006. **41(10)**: p. 2869-2875.
204. Mirkova, L., et al., *Hydrogen evolution and permeation into steel during zinc electroplating: effect of organic additives*. Journal of Applied Electrochemistry, 2001. **31**: p. 647-654.
205. Oriani, R.A., *Hydrogen - The Versatile Embrittler*. Corrosion, 1987. **43(7)**: p. 390-397.
206. Smialowski, M., *Hydrogen in Steel*. 1962: Pergamon.
207. Paatsch, W., *Untersuchungen zur Wasserstoffversprödung vergüteter Stähle bei der galvanotechnischen Beschichtung - Teil I: Wasserstoffpermeationsversuche*. Metalloberfläche, 1978. **32(12)**: p. 546-550.
208. Monev, M., et al., *Effect of brighteners on hydrogen evolution during zinc electroplating from zincate electrolytes*. Journal of Applied Electrochemistry, 1998. **28**: p. 1107-1112.
209. Park, H. and J. Szpunar, *The role of texture and morphology in optimizing the corrosion resistance of zinc-based electrogalvanized coatings*. Corrosion Science, 1998. **40(4/5)**: p. 525-545.
210. Ashton, R.F. and M.T. Hepworth, *Effect of Crystal Orientation on the Anodic Polarization and Passivity of Zinc*. Corrosion, 1986. **24(2)**: p. 50-53.
211. Hansal, W.E.G. and S. Roy, *Pulse Plating*. 2012: Eugen G. Leuze Verlag KG.
212. Puippe, J.C. and N. Ibl, *Influence of charge and discharge of electric double layer in pulse plating*. Journal of Applied Electrochemistry, 1980. **10**: p. 775-784.
213. Ibl, N., *Some theoretical aspects of pulse electrolysis*. Surface Technology, 1980. **10(2)**: p. 81-104.
214. Datta, M. and D. Landolt, *Experimental investigation of mass transport in pulse plating*. Surface Technology, 1985. **25(2)**: p. 97-110.
215. Gamburg, Y.D. and G. Zangari, *Theory and Practice of Metal Electrodeposition*. 2011: Springer.
216. Chène, O. and D. Landolt, *The influence of mass transport on the deposit morphology and the current efficiency in pulse plating of copper*. Journal of Applied Electrochemistry, 1989. **19(2)**: p. 188-194.
217. *CRC Handbook of Chemistry and Physics*, ed. D.R. Lide. 2003: CRC Press.

218. Frade, T., et al., *Pulsed-reverse current electrodeposition of Zn and Zn-TiO₂ nanocomposite films*. Surface and Coatings Technology, 2010. **204**(21-22): p. 3592-3598.
219. Youssef, K.M.S., C.C. Koch, and P.S. Fedkiw, *Influence of Additives and Pulse Electrodeposition Parameters on Production of Nanocrystalline Zinc from Zinc Chloride Electrolytes*. Journal of The Electrochemical Society, 2004. **151**(2): p. C103.
220. El-Sherik, A.M., U. Erb, and J. Page, *Microstructural evolution in pulse plated nickel electrodeposits*. Surface and Coatings Technology, 1996. **88**: p. 70-78.
221. Paatsch, W., *Electroplating With Current Pulses. II. Zinc Precipitation*. Metalloberfläche, 1987. **41**(1): p. 39-43.
222. Raeissi, K., et al., *The effect of γ -fiber texture intensity of carbon steel substrate on zinc hetero-epitaxial growth*. Surface and Coatings Technology, 2006. **201**(6): p. 3116-3122.
223. Paravano, N. and V. Caglioti, *Structure and chemical composition of some [manganese-zinc and cobalt-zinc] alloys*. Mem. Accad. Italia Chim., 1932. **3**(3): p. 5-21.
224. Bozzini, B., P.L. Cavallotti, and F. Pavan, *Metastable intermetallics in the Zn-Mn system obtained by electrodeposition*. Journal de Chimie Physique, 1997. **94**: p. 1009-1013.
225. Bozzini, B., et al., *Zn-Mn Alloy Electrodeposition on Steel*. Transactions of the IMF, 1997. **75**(5): p. 175-180.
226. Bozzini, B., et al., *Electrodeposition of Zn-Mn alloys in the presence of thiocarbamide*. Surface and Coatings Technology, 2002. **154**: p. 294-303.
227. Bučko, M., et al., *The influence of anion type in electrolyte on the properties of electrodeposited ZnMn alloy coatings*. Surface and Coatings Technology, 2013. **228**: p. 221-228.
228. Fels, C.C. and W. Plieth, *Zink-Mangan-Legierungselektrolyten im Test*. JOT Journal für Oberflächentechnik, 2001. **41**(11): p. 64-67.
229. Dencheva, S. and G. Kirov, *Crystal morphology of Simonkolleite (Zn₅(OH)₈Cl₂(H₂O)): a SEM study*. 2014.
230. Chen, Z.Y., D. Persson, and C. Leygraf, *Initial NaCl-particle induced atmospheric corrosion of zinc—Effect of CO₂ and SO₂*. Corrosion Science, 2008. **50**(1): p. 111-123.
231. Mouanga, M., P. Berçot, and J.Y. Rauch, *Comparison of corrosion behaviour of zinc in NaCl and in NaOH solutions. Part I: Corrosion layer characterization*. Corrosion Science, 2010. **52**(12): p. 3984-3992.
232. Mouanga, M., et al., *Effects of some additives on the corrosion behaviour and preferred orientations of zinc obtained by continuous current deposition*. Journal of Applied Electrochemistry, 2006. **37**(2): p. 283-289.
233. Charlot, G., *Les réactions chimiques en solution aqueuse et caractérisation des ions*, ed. Masson. 1983, Paris.
234. Satoh, N., *Effects of heavy metal additions and crystal modification on the zinc phosphating of electrogalvanized steel sheet*. Surface and Coatings Technology, 1987. **30**(2): p. 171-181.
235. Su, H.-Y. and C.-S. Lin, *Effect of additives on the properties of phosphate conversion coating on electrogalvanized steel sheet*. Corrosion Science, 2014. **83**: p. 137-146.
236. Chung, S.J., et al., *Characterization of ZnO nanoparticle suspension in water: Effectiveness of ultrasonic dispersion*. Powder Technology, 2009. **194**: p. 75-80.
237. Vasylykiv, O. and Y. Sakka, *Synthesis and Colloidal Processing of Zirconia Nanopowder*. Journal of the American Ceramic Society, 2001. **84**(11): p. 2489-2494.
238. Ataee-Esfahani, H., et al., *Influence of SiC nanoparticles and saccharin on the structure and properties of electrodeposited Ni-Fe/SiC nanocomposite coatings*. Journal of Alloys and Compounds, 2009. **484**(1-2): p. 540-544.
239. Benea, L., et al., *Composite Electrodeposition to Obtain Nanostructured Coatings*. Journal of the Electrochemical Society, 2001. **148**(7): p. 461-465.
240. Vaezi, M.R., S.K. Sadrnezhaad, and L. Nikzad, *Electrodeposition of Ni-SiC nano-composite coatings and evaluation of wear and corrosion resistance and electroplating characteristics*. Colloids and Surfaces A: Physicochemical and Engineering Aspects, 2008. **315**(1-3): p. 176-182.
241. Exbrayat, L., et al., *Role of Ceria Nanoparticles on the Electrodeposited Zinc Coating's Growth: Interest of a TEM-Scale Investigation*. ECS Electrochemistry Letters, 2014. **3**(9): p. D33-D35.
242. Exbrayat, L., *Nouveaux revêtements nanocomposites Zn/CeO₂: élaboration, caractérisation, propriétés*, in *Laboratoire des Sciences de l'Ingénieur pour l'Environnement*. 2014, Université de la Rochelle.

243. De Lima-Neto, P., et al., *Corrosion Study of Electrodeposited Zn and Zn-Co Coatings in Chloride Medium*. Journal of Brazilian Chemical Society, 2007. **18**(6): p. 1164-1175.
244. Gharahcheshmeh, M.H. and M.H. Sohi, *Study of the corrosion behavior of zinc and Zn-Co alloy electrodeposits obtained from alkaline bath using direct current*. Materials Chemistry and Physics, 2009. **117**(2-3): p. 414-421.
245. Panagopoulos, C.N., D.A. Lagaris, and P.C. Vatista, *Adhesion and corrosion behaviour of Zn-Co electrodeposits on mild steel*. Materials Chemistry and Physics, 2011. **126**(1-2): p. 398-403.
246. Bajat, J.B., et al., *Corrosion stability of Zn-Co alloys deposited from baths with high and low Co content - The influence of deposition current density*. Surface and Coatings Technology, 2010. **204**(16-17): p. 2745-2753.
247. Bajat, J.B., S. Stankovic, and B.M. Jokic, *Electrochemical deposition and corrosion stability of Zn-Co alloys*. Journal of Solid State Electrochemistry, 2009. **13**(5): p. 755-762.
248. Bhat, R.S. and A.C. Hedge, *Electroplating and Corrosion study of Zn-Co, Zn-Fe and Zn-Co-Fe Alloys*. Analytical & Bioanalytical Electrochemistry, 2012. **4**(6): p. 593-609.
249. Abou-Krishna, M.M., et al., *Electrochemical behavior of Zn-Co-Fe alloy electrodeposited from a sulfate bath on various substrate materials*. Arabian Journal of Chemistry, 2015.
250. Abou-Krishna, M., et al., *Electrochemical behavior and corrosion resistance of electrodeposited nanoparticles Zn-Co-Fe alloy*. Anti-Corrosion Methods and Materials, 2016. **63**(1): p. 29-35.
251. Lodhi, Z.F., et al., *Corrosion resistance of Zn-Co-Fe alloy coatings on high strength steel*. Surface and Coatings Technology, 2009. **203**(10-11): p. 1415-1422.
252. Tsai, M.-H. and J.-W. Yeh, *High-Entropy Alloys: A Critical Review*. Materials Research Letters, 2014. **2**(3): p. 107-123.
253. Szczygieł, B., A. Laszczyńska, and W. Tylus, *Influence of molybdenum on properties of Zn-Ni and Zn-Co alloy coatings*. Surface and Coatings Technology, 2010. **204**(9-10): p. 1438-1444.
254. Winiarski, J., et al., *The influence of molybdenum on the corrosion resistance of ternary Zn-Co-Mo alloy coatings deposited from citrate-sulphate bath*. Corrosion Science, 2015. **91**: p. 330-340.
255. Winiarski, J., W. Tylus, and B. Szczygieł, *EIS and XPS investigations on the corrosion mechanism of ternary Zn-Co-Mo alloy coatings in NaCl solution*. Applied Surface Science, 2016. **364**: p. 455-466.
256. Winiarski, J., et al., *The influence of molybdenum on the electrodeposition and properties of ternary Zn-Fe-Mo alloy coatings*. Electrochimica Acta, 2016. **196**: p. 708-726.
257. Kazimierczak, H., et al., *Electrodeposition of Zn-Mn-Mo layers from citrate-based aqueous electrolytes*. Electrochimica Acta, 2016. **202**: p. 110-121.
258. Kazimierczak, H., et al., *Characterisation of Zn-Mo alloy layers electrodeposited from aqueous citrate solution*. Journal of Alloys and Compounds, 2013. **578**: p. 82-89.
259. Kazimierczak, H., et al., *Microstructure and micromechanical properties of electrodeposited Zn-Mo coatings on steel*. Journal of Alloys and Compounds, 2015. **636**: p. 156-164.
260. Youssef, K.M., et al., *A Novel Low-Density, High Hardness, High-entropy Alloy with Close-packed Single-phase Nanocrystalline Structures*. Materials Research Letters, 2014. **3**: p. 95-99.
261. Exbrayat, L., et al., *Corrosion behaviour in saline solution of pulsed-electrodeposited zinc-nickel-ceria nanocomposite coatings*. Materials and Corrosion, 2017. **68**(10): p. 1129-1142.
262. Nemes, P.I., et al., *Influence of the electrodeposition current regime on the corrosion resistance of Zn-CeO₂ nanocomposite coatings*. Surface and Coatings Technology, 2014. **252**: p. 102-107.
263. Stoffer, J.O., et al., *US 7,241,371 B2 - Additive-assisted, cerium-based, corrosion-resistant e-coating*, U.S. Patent, Editor. 2007, The Curators of University of Missouri.
264. Cao, X.Q., R. Vassen, and D. Stoeber, *Ceramic materials for thermal barrier coatings*. Journal of the European Ceramic Society, 2004. **24**(1): p. 1-10.
265. Brooman, E.W., *Modifying organic coatings to provide corrosion resistance: Part I - Background and general principles*. Metal Finishing, 2002. **100**(1): p. 48-53.
266. Brooman, E.W., *Modifying organic coatings to provide corrosion resistance: Part II - Inorganic additives and inhibitors*. Metal Finishing, 2002. **100**(5): p. 42, 44-47, 49-53.
267. Brooman, E.W., *Modifying organic coatings to provide corrosion resistance: Part III - Organic additives and conducting polymers*. Metal Finishing, 2002. **100**(6): p. 104-110.
268. Koleva, D., et al., *Application of PEO₁₁₃-b-PS₂₁₈ nano-aggregates for improved protective characteristics of composite zinc coatings in chloride-containing environment*. Surface and Coatings Technology, 2010. **204**(23): p. 3760-3772.

269. Boshkov, N., et al., *Corrosion behavior and protective ability of Zn and Zn–Co electrodeposits with embedded polymeric nanoparticles*. Applied Surface Science, 2008. **254**(17): p. 5618-5625.
270. Zheludkevich, M.I., et al., *Anticorrosion Coatings with Self-Healing Effect Based on Nanocontainers Impregnated with Corrosion Inhibitor*. Chemistry of Materials, 2007. **19**(3): p. 402-411.
271. Zheludkevich, M.I., J. Tedim, and M.G.S. Ferreira, *"Smart" coatings for active corrosion protection based on multi-functional micro and nanocontainers*. Electrochimica Acta, 2012. **82**(1): p. 314-323.
272. Sonawane, S.H., et al., *Improved active anticorrosion coatings using layer-by-layer assembled ZnO nanocontainers with benzotriazole*. Chemical Engineering Journal, 2012. **189-190**: p. 464-472.
273. Kamburova, K., et al., *Design of polymeric core-shell nanocontainers impregnated with benzotriazole for active corrosion protection of galvanized steel*. Colloids and Surfaces A: Physicochemical and Engineering Aspects, 2016. **499**: p. 24-30.
274. Celis, J.P., J.R. Roos, and C. Buelens, *A Mathematical Model for the Electrolytic Codeposition of Particles with a Metallic Matrix*. Journal of the Electrochemical Society, 1987. **134**(6): p. 1402-1408.
275. Hwang, B.J. and C.S. Hwang, *Mechanism of Codeposition of Silicon Carbide with Electrolytic Cobalt*. Journal of the Electrochemical Society, 1993. **140**(4): p. 979-984.
276. Vereecken, P.M., I. Shao, and P.C. Searson, *Particle Codeposition in Nanocomposite Films*. Journal of the Electrochemical Society, 2000. **147**(7): p. 2572-2575.
277. Bercot, P., E. Pena-Munoz, and J. Pagetti, *Electrolytic composite Ni-PTFE coatings: an adaptation of Guglielmi's model for the phenomena of incorporation*. Surface and Coatings Technology, 2002. **157**(2-3): p. 282-289.
278. Sturm, S. (*Scanning*) *Transmission electron microscopy*. in *COST MP 1407 training course*. 2017. Schwäbisch Gmünd.